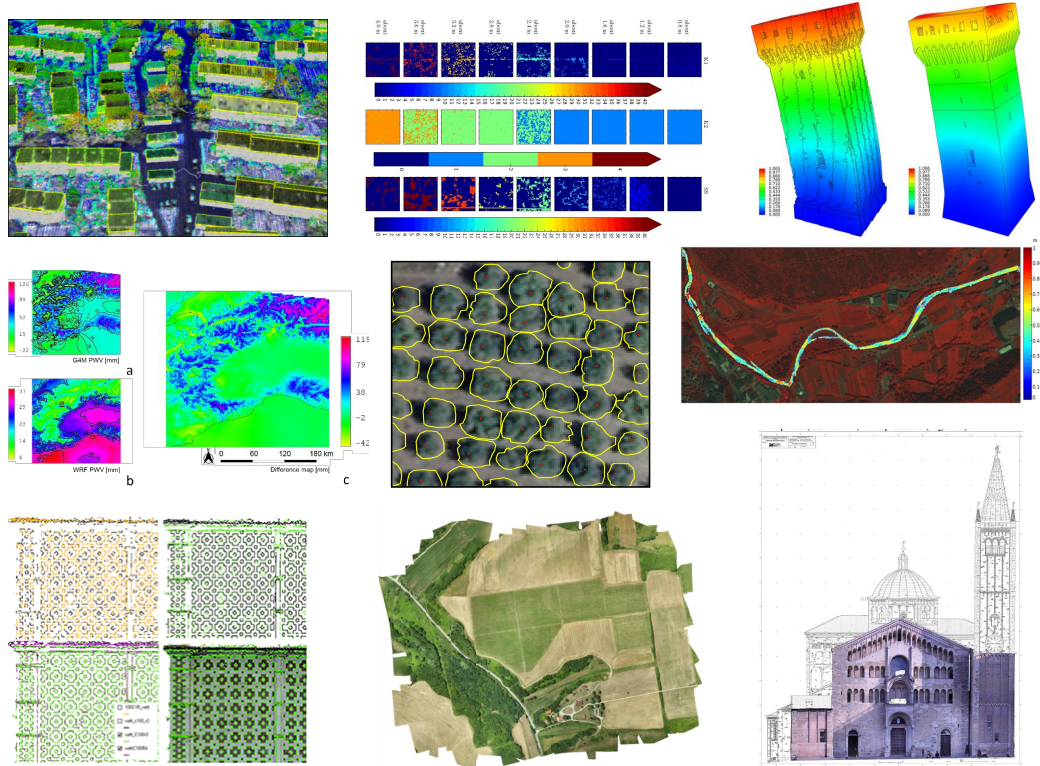


Antonio Vettore editor

RICERCHE DI GEOMATICA 2017



GEOMATICS RESEARCH 2017



STUDI PRESENTATI ALLA TREDICESIMA EDIZIONE DEL PREMIO AUTeC
STUDIES PRESENTED TO THE THIRTEENTH EDITION OF THE AUTeC AWARD

Associazione **U**niversitari di **T**opografia e **C**artografia



RICERCHE DI GEOMATICA 2017

*

GEOMATICS RESEARCH 2017

*STUDI PRESENTATI ALLA DODICESIMA EDIZIONE DEL PREMIO AUTEc
STUDIES PRESENTED AT THE TWELFTH EDITION OF AUTEc AWARD*

Questo volume raccoglie gli articoli che hanno partecipato al **Premio AUTEc 2017**. Il premio è stato istituito nel 2005 e, fino al 2015, veniva conferito ogni anno ad una tesi di Dottorato giudicata particolarmente significativa sui temi di pertinenza del SSD ICAR/06 (Topografia e Cartografia) nei diversi Dottorati di Ricerca attivi in Italia.

A partire dal 2016 si è deciso di differenziare la competizione sulla base dell'affinità tra gli argomenti sviluppati e di attribuire fino a tre premi uno per ciascuna delle tre sezioni tematiche proprie del settore:

1. Geodesia, GNSS, Navigazione
2. Fotogrammetria e Laser Scanner
3. GIS, Remote Sensing

Ciascun candidato riassume in un articolo i punti salienti della propria tesi. Gli articoli vengono sottoposti al giudizio di una Commissione giudicatrice costituita dai membri della Giunta AUTEc vigente nell'anno in cui si conferisce il premio e eventualmente alti esperti del settore. Nell'anno 2017 la Commissione è risultata composta dai professori Caterina Balletti Università Iuav di Venezia, Donatella Dominici dell'Università dell'Aquila, Eva Savina Malinverni dell'Università Politecnica delle Marche, Domenico Visintini dell'Università di Udine, Luca Vittuari dell'Università di Bologna e Ambrogio Manzino del Politecnico di Torino.

Il premio AUTEc 2017 è stato così assegnato:

- per la sezione tematica **Geodesia, GNSS, Navigazione** alla Dott.ssa Ilaria Ferrando, che ha conseguito il Dottorato di Ricerca presso l'Università di Genova, per la tesi dal titolo: "GNSS CONTRIBUTION TO MONITOR SEVERE RAINFALLS: AN INNOVATIVE PROCEDURE FOR WIDE AND OROGRAPHICALLY COMPLEX AREA WITH EXISTING INFRASTRUCTURES";
- per la sezione tematica **Fotogrammetria e Laser Scanner** alla Dott.ssa Irene Aicardi, che ha conseguito il Dottorato di Ricerca presso il Politecnico di Torino, per la sua tesi dal titolo "UAVS FOR SPATIAL DATA ACQUISITION: SENSORS EVALUATION, FLIGHT DESIGN AND PLANNING, MULTI-TEMPORAL SOLUTIONS";
- per la sezione tematica **GIS, Remote Sensing** alla Dott.ssa Martina Di Rita, che ha conseguito il Dottorato di Ricerca presso l'Università La Sapienza di Roma con la sua tesi dal titolo "NEW TRENDS FOR DSMS GENERATION FROM OPTICAL AND SAR SATELLITE IMAGERY: DEFINITION AND IMPLEMENTATION OF AN INNOVATIVE STRATEGY".

Il premio e la pubblicazione degli articoli in un volume e-book vogliono essere un riconoscimento degli Universitari del SSD ICAR/06 per il lavoro di questi giovani ricercatori e una motivazione per continuare le loro ricerche.



*The volume contains the papers submitted for applying to the **AUTEc Award 2017**. The award was established in 2005 and until 2015 it has been assigned annually to the most scientifically-sound Ph.D. thesis realized in one of the Italian Doctoral Courses pertaining to the scientific sector ICAR/06 (Surveying and Mapping). Since 2016, up to three awards have been established, each one related to one of the following thematic sections:*

- *Geodesy, GNSS, Navigation*
- *Photogrammetry and Laser Scanner*
- *GIS, Remote Sensing*

Candidates are invited to summarize the main outcomes of their research in a paper. Then, articles are examined by a Commission composed by current members of the AUTEc Executive Board. In 2018, the Commission was composed by Professors Caterina Balletti from the University Iuav of Venice, Donatella Dominici from University of L'Aquila, Eva Savina Malinverni from the Polytechnic of Marche, Domenico Visintini from University of Udine, Luca Vittuari from the University of Bologna and Ambrogio Manzino from the Polytechnic of Turin.

The winners of the AUTEc Award 2017 are:

- *Section "Geodesy, GNSS, Navigation": Dr. Ilaria Ferrando who followed the Doctoral Course at the University of Genova, for her thesis entitled "GNSS contribution to monitor severe rainfalls: an innovative procedure for wide and orographically complex area with existing infrastructures";*
- *Section "Photogrammetry and Laser Scanner": Dr. Irene Aicardi, who followed the Doctoral Course at the Polytechnic of Turin, for her thesis entitled "UAVs for spatial data acquisition: sensors evaluation, flight design and planning, multi-temporal solutions";*
- *Section "GIS, Remote Sensing": Dr Martina Di Rita., who followed the Doctoral Course at the University of Roma La Sapienza, for her thesis entitled "New trends for DSMs generation from optical and SAR satellite imagery: definition and implementation of an innovative strategy".*
-

AUTEc Awards and "Ricerche di Geomatica" e-book, which are both promoted by ICAR/06 academics and AUTEc associates, aim at rewarding young researchers for their efforts in challenging studies and stimulating their future works.

*Prof. Antonio Vettore
AUTEc Coordinator 2018-2019*



Associazione Universitari di Topografia e Cartografia

AUTEc (Associazione Universitari di Topografia e Cartografia) si è costituita a Bologna il 9 febbraio 1998. Possono iscriversi a questa Associazione i docenti universitari inquadrati nel Settore Scientifico Disciplinare ICAR/06 - Topografia e Cartografia (Settore Concorsuale 08/A4 - Geomatica).

L' **AUTEc** si propone i seguenti obiettivi:

- creare un luogo di incontro per discutere problemi di sviluppo della ricerca, di allocazione delle risorse e di promozione di iniziative didattiche di formazione;
- coordinare le iniziative nei riguardi di Enti ed Organismi nazionali ed internazionali, comunitari e non, con i quali intercorrono rapporti, per sviluppare e promuovere una politica di richieste e di scelte coordinata;
- promuovere quanto necessario per migliorare la qualità dell'insegnamento delle discipline del settore e il loro impatto sulla realtà produttiva del Paese;
- diffondere in maniera sistematica le informazioni che riguardano il settore.

AUTEc è retta da un Coordinatore nazionale coadiuvato dalla Giunta. Le cariche si rinnovano ogni biennio. Hanno rivestito la carica di Coordinatore AUTEc i professori:

Riccardo Galetto, ordinario dell'Università degli Studi di Pavia, nel biennio 1998-1999;
Giorgio Bezoari, ordinario del Politecnico di Milano, nel biennio 2000-2001;
Bruno Astori, ordinario del Politecnico di Torino, nel biennio 2002-2003;
Anna Spalla, ordinario dell'Università degli Studi di Pavia, nei bienni 2004-2005 e 2006-2007;
Benedetto Villa, ordinario dell'Università degli Studi di Palermo, nei bienni 2008-2009 e 2010-2011;
Gabriele Bitelli, ordinario dell'Università degli Studi di Bologna, nei bienni 2012-2013 e 2014-2015.

Dal 2016 riveste la carica di Coordinatore il prof. Antonio Vettore, ordinario dell'Università degli Studi di Padova.

AUTEc is the Italian Association of the academics (University Professors and Researchers) belonging to the Scientific Sector ICAR/06 - Surveying and Mapping. It was founded in Bologna, February 9, 1998.

AUTEc has the following objectives:

- *to create a meeting place to discuss issues related to research development, resource allocation and promotion of educational training in the scientific sector;*
- *to co-ordinate actions and to promote a common policy towards national and international entities and organizations;*
- *to promote what is necessary to improve both the quality of teaching of the disciplines of the scientific sector and their impact on the national productive reality;*
- *to disseminate information related to the scientific sector in a systematic manner.*

AUTEc is governed by a National Coordinator assisted by an Executive Board. The positions are renewed every two years.

The position of AUTEc Coordinator was covered by:

Riccardo Galetto, Full Professor at the University of Pavia, in the period 1998-1999;
Giorgio Bezoari, Full Professor at the Polytechnic of Milan in 2000-2001;
Bruno Astori, Full Professor at the Polytechnic of Turin in 2002-2003;
Anna Spalla, Full Professor at the University of Pavia, in the two-year periods 2004-2005 and 2006-2007;
Benedetto Villa, Full Professor at the University of Palermo, in the two-year periods 2008-2009 and 2010-2011;
Gabriele Bitelli, Full Professor at the University of Bologna, in the two-year periods 2012-2013 and 2014-2015;

Since 2016 holds the position of Coordinator Antonio Vettore, Full Professor at the University of Padova.



Indice

*

Index

	Sezione Tematica 1 Geodesia, GNSS, Navigazione * <i>Thematic Section 1</i> <i>Geodesy, GNSS, Navigation</i>	p. 9
FERRANDO Ilaria	GNSS CONTRIBUTION TO MONITOR SEVERE RAINFALLS: AN INNOVATIVE PROCEDURE FOR WIDE AND OROGRAPHICALLY COMPLEX AREA WITH EXISTING INFRASTRUCTURES	p. 11
	Sezione Tematica 2 Fotogrammetria e Laser Scanner * <i>Thematic Section 2</i> <i>Photogrammetry and Laser Scanner</i>	p. 23
ALICANDRO Maria	OPTIMIZATION AND AUTOMATION OF THE POST-PROCESSING HIGH RESOLUTION UAV PHOTOGRAMMETRIC DATA	p. 25
AICARDI Irene	UAVS FOR SPATIAL DATA ACQUISITION: SENSORS EVALUATION, FLIGHT DESIGN AND PLANNING, MULTI-TEMPORAL SOLUTIONS	p. 35
BRUNO Nazarena	FROM SURVEY TO ANALYSIS FOR CULTURAL HERITAGE MANAGEMENT: A NEW PROPOSAL FOR DATABASE DESIGN IN BIM	p. 47
RAVANELLI Roberta	3D MODELLING BY LOW-COST RANGE CAMERAS: METHODS AND POTENTIALITIES	p. 59
ROTONDI Andrea	UAV MONITORING TO SUPPORT PRECISION FARMING: A STUDY-CASE IN THE LAND OF THE CESANESE DEL PIGLIO	p. 71
SELVAGGI Ilenia	SURVEYING AND THREE-DIMENSIONAL MODELING FOR PRESERVATION AND STRUCTURAL ANALYSIS OF CULTURAL HERITAGE	p. 81
	Sezione Tematica 3 GIS e Remote Sensing * <i>Thematic Section 3</i> <i>GIS and Remote Sensing</i>	p. 93
BELFIORE Oscar Rosario	REMOTE SENSING TECHNIQUES FOR MAPPING AGROFORESTRY PARAMETERS: APPLICATIONS FOR INDIVIDUAL TREE CROWN DETECTION	p. 95
DI RITA Martina	NEW TRENDS FOR DSMS GENERATION FROM OPTICAL AND SAR SATELLITE IMAGERY: DEFINITION AND IMPLEMENTATION OF AN INNOVATIVE STRATEGY	p. 107



GOTTARDI Caterina	BEYOND THE MAP. NUMERICAL AND COMPARATIVE ANALYSIS FOR THE STUDY OF HISTORICAL CARTOGRAPHY	p. 119
LAMBERTI Alessandro	INNOVATIVE USE AND INTEGRATION OF REMOTE SENSED GEOSPATIAL DATA FOR 3D CITY MODELING AND GIS URBAN APPLICATIONS	p.131
NIROUMAND JADID Milad	RIVERS HYDROMORPHOLOGICAL CHARACTERIZATION FROM HIGH RESOLUTION REMOTELY SENSED DATA	p. 141
PIERDICCA Roberto	SENSEABLE SPACES: FROM A THEORETICAL PERSPECTIVE TO THE APPLICATION IN AUGMENTED ENVIRONMENTS	p. 153



Associazione **U**niversitari di **T**opografia **e** **C**artografia

Sezione Tematica 1 Geodesia, GNSS, Navigazione

*

*Thematic Section 1
Geodesy, GNSS, Navigation*

GNSS CONTRIBUTION TO MONITOR SEVERE RAINFALLS: AN INNOVATIVE PROCEDURE FOR WIDE AND OROGRAPHICALLY COMPLEX AREA WITH EXISTING INFRASTRUCTURES

Ilaria Ferrando

DICCA - Dipartimento di Ingegneria Civile, Chimica e Ambientale, Università degli Studi di Genova,
via Montallegro 1, 16145 Genova, Italia - ilaria.ferrando@edu.unige.it

KEY WORDS: GNSS, Zenith Total Delay (ZTD), Precipitable Water Vapour (PWV), Severe Meteorological Events, GIS

ABSTRACT:

The paper presents an innovative methodology for monitoring the content of Precipitable Water Vapour (PWV) in atmosphere for wide and orographically complex area. The water vapour content is strictly related to the occurrence of rains, hence the knowledge of PWV can be useful to interpret and monitor severe meteorological events. An automatic procedure has been conceived for producing 2D PWV maps with high spatial and temporal resolution starting from Zenith Tropospheric Delay (ZTD) estimations, obtained from GNSS Permanent Stations (PSs) network compensation, and from Pressure (P) and Temperature (T) observations, all collected by existing infrastructures. In the present work both a 1D approach to analyse ZTD and PWV time series and a 2D approach to localize severe meteorological events in time and space are presented. The procedure is then applied to a wide and orographically complex area, to study two severe meteorological events occurred in Genoa with reliable results. The introduction of the Heterogeneity Index (HI), accounting the spatial variability of PWV, allows to individuate the correct timing and location of severe meteorological events.

1. INTRODUCTION

The typical application of GNSS (Global Navigation Satellite System) technology is obtaining the coordinates of a receiver by means of spatial triangulation, knowing the satellites orbits and positions. The positioning precision is affected by different sources of bias, primarily produced by the crossing of the atmosphere, due to ionospheric and tropospheric refraction, and by structural and non-structural issues (receiver/satellite clock errors, multipath, code/phase range, etc.). The Ionosphere is a dispersive layer, thus its effect depends on the frequency of the electromagnetic signal. The ionospheric bias can be easily modelled and eliminated by means of proper L1 and L2 phase combinations (iono-free model) transmitted by GNSS satellites and using the dispersion relations for Ionosphere (Spilker, 1980; Brunner and Gu, 1991). The tropospheric bias can't be reduced by means of any combination, hence it has to be taken into account. The tropospheric effect produces a bias in each satellite-receiver observation that can be related with the so-called Zenith Total Delay (ZTD), computed in the zenith direction above the GNSS station, by means of an appropriate mapping function. On the one hand, the estimation of ZTD and its time and space variability could help to enhance the positioning precision; on the other hand, the monitoring of ZTD could be useful to study and interpret severe meteorological events, as previous studies demonstrated (Bouma and Stoew, 2001; De Pondeca and Zou, 2001; Basili et al., 2003; Bock et al., 2008; Boniface et al., 2009; Bennitt and Jupp, 2012; Crespi et al., 2004; Piccardo and Sguerso, 2007; Sguerso et al., 2013, 2015; Tsuda et al., 2013). Considering the atmosphere as a biphasic fluid composed by a mix of dry and wet gases, ZTD may be split in its two components, the Zenith Hydrostatic Delay (ZHD) and the Zenith Wet Delay (ZWD). ZHD is due to the mix of dry gases in atmosphere, is dominant (it covers about the 90% of the total tropospheric delay) and can be easily modelled by means of relations involving the atmospheric pressure and depending on latitude and elevation of the GNSS station. ZWD is due to the water vapour refractivity caused by the dipole moment of water vapour molecules and it can't be easily modelled, therefore it is

typically obtained by difference between ZTD and ZHD. ZWD is closely related to the value of Precipitable Water Vapour (PWV). PWV represents the maximum amount of condensable water due to the water vapour contained in an imaginary unitary-base column that extends from the GNSS receiver height to the upper limit of the troposphere. This quantity can be considered the upper limit of the precipitable water, if the triggering conditions for water condensation are present.

PWV can be estimated above a GNSS Permanent Station (PS), by means of the relations by Bevis et al. (1992 and 1994), involving ZTD integrated with Pressure (P) and Temperature (T) observed close to the GNSS receiver.

Starting from Bevis' assumptions, a GIS procedure called G4M (GNSS for Meteorology) has been conceived to produce 2D PWV maps with high spatial and temporal resolution, using as input data GNSS, P and T sparse observations not necessarily co-located, coming from existing infrastructures.

In the present work both a 1D approach to analyse ZTD and PWV time series, and a 2D approach to produce PWV maps and to interpret their evolution are presented. The final goal is to better localize severe meteorological events in time and space for near real-time applications by means of PWV estimations.

2. GNSS METEOROLOGY

The most common instruments to measure the vertical and horizontal distribution of water vapour are radiosonde and Water Vapour Radiometers (WVR).

Radiosonde provides a good vertical resolution but it is an expensive technique, available for a restricted number of launches. Regarding the WVR, there are two main categories of instruments: the upward (UL) and the downward looking (DL). The UL WVR is a ground-based instrument measuring the microwave radiation produced by atmospheric water vapour and estimating the Integrated Water Vapour (IWV) and the Integrated Liquid Water (ILW) content along a given line of sight. The DL WVR is a space-based instrument measuring the absorption lines in the radiation from the hot background provided by the Earth. UL units can provide a good temporal coverage but they are

lacking in spatial coverage, whereas DL units have the opposite characteristics. Moreover, geostationary satellites, such as Meteosat, return images of the water vapor content, but relative to the top of the cloud layer.

GNSS signals are delayed by water vapour, dry gases, hydrometeors and other particulates in atmosphere (Neill, 1996; Solheim et al., 1999), with different effect in the Ionosphere and in the Troposphere. Thus, the GNSS technology allows to estimate the content of PWV along the zenith direction above a GNSS PS, from the ground to the upper limit of the troposphere, observing the delay of the electromagnetic GNSS signal, integrated with P and T data on the ground, as described in the following section.

2.1 Tropospheric delay estimation

The Troposphere is the closest layer to Earth, from the ground up to about 12 km, and it is the most interesting layer for GNSS signal transmission because it is the zone of active weather, where all the clouds types and meteorological precipitations develop. A mix of dry gases and water vapour constitutes it. The Troposphere's refraction is frequency independent and it is only due to temperature, pressure and relative humidity. The water vapour dipole moment contributes to atmosphere's refractivity and it is common to treat it separately from non-dipole component. The two components are commonly referred to as the wet (ZWD) and hydrostatic (ZHD); both of them assume smaller values along the zenith direction and increase with the inverse of the elevation angle's sine. The hydrostatic component is dominant and contributes for about the 90% on the total effect. On spite of the smaller effect, the wet component represents the main source of bias for its larger variability and more difficult predictability with respect to theoretical models and meteorological measurements from surface (Resch, 1984; Tralli et al., 1988).

Having surface pressure measurements, Saastamoinen (1972) showed that it is possible to model ZHD with reliable accuracy (in the order of a few millimeters), as long as the accuracy of pressure measurement is higher than 0.3 hPa.

Elgered et al. (1991) proposed the following relation

$$ZHD = \frac{(2.2779 \pm 0.0024) \cdot P_s}{f(\varphi, H)} \quad (1)$$

where ZHD is measured in mm, P_s is the surface level pressure (in hPa) and $f(\varphi, H)$ is a function accounting for the gravitational acceleration variation depending on the latitude φ and the height H on the ellipsoid (measured in km).

$$f(\varphi, H) = 1 - 0.00266 \cdot \cos(2\varphi) - 0.00028 \cdot H \quad (2)$$

Davis et al. (1985) suggested

$$ZWD = 10^{-6} \cdot \left(k_2' \cdot \int \frac{P_v}{T} dz + k_3 \cdot \int \frac{P_v}{T^2} dz \right) \quad (3)$$

where P_v is the partial pressure of water vapour (in hPa), T is the atmospheric temperature (in K) and

$$k_2' = 17 \pm 10 \quad \left[\frac{K}{hPa} \right] \quad (4)$$

$$k_3 = (3.776 \pm 0.03) \cdot 10^5 \quad \left[\frac{K^2}{hPa} \right]$$

The predictability of ZWD by means of models and surface measurements is much lower than the ZHD one. For this reason, for GNSS Meteorology applications, ZWD is typically obtained by difference between ZTD and ZHD.

ZTD can be estimated by adjustment of GNSS receivers networks, in order to correct the delay computed in a defined time

span (generally, two hours or lower) with a tropospheric model adopted in standard atmosphere conditions.

Also international and national agencies deal with the estimation of tropospheric models by elaborating GNSS Permanent Stations network (PSs) and interpolating their local estimations (Bosy et al., 2012; Karabatić et al., 2011; Pacione and Vespe, 2003; Yao et al., 2015). The spatial and temporal resolutions are suitable for climate or meteorological analysis on wide area, but are too low for the monitoring of an intense localized event, as the purpose of the author.

2.2 Precipitable Water Vapour estimation

Once ZWD has been obtained, it is possible to estimate PWV, using the relation proposed by Bevis et al. (1992)

$$PWV = \Pi \cdot ZWD \quad (5)$$

where Π is a function of the physical parameters and the weighted mean temperature of the atmosphere T_m .

The proposed relation for Π is

$$\frac{1}{\Pi} = 10^{-6} \cdot \left(k_2' + \frac{k_3}{T_m} \right) \cdot R_v \cdot \rho \quad (6)$$

where R_v is the specific gas constant for water vapour and ρ is the density of water.

Davis et al. (1985) defined the weighted mean T_m as

$$T_m = \frac{\int \frac{P_v}{T} dz}{\int \frac{P_v}{T^2} dz} \quad (7)$$

representing the average temperature of atmosphere weighted by the pressure of water vapour, and depending on surface temperature, Troposphere's temperature profile and vertical distribution of water vapour. As already stated, it is difficult to estimate the partial pressure of vapour P_v and the temperature T, thus an approximate expression for the weighted mean temperature T_m has been found (Bevis et al., 1992):

$$T_m = 70.2 + 0.72 \cdot T_s \quad (8)$$

The previous (1-8) equations represent the basic equations of GNSS Meteorology and demonstrate the possibility of retrieve PWV spatio-temporal distribution in the atmosphere by means of GNSS observations.

2.3 PVW Variance Propagation

PWV variance propagation has been performed by the author to understand the role of each component and its uncertainty, and to evaluate the final rms (σ) of PWV.

Assuming ZTD rms equal to 3 mm (as suggested by Bevis et al., 1992), a latitude of 45° and a height of 1000 m known with high precision ($\sigma_\varphi = \sigma_z = 0$), a precautionary value of $\sigma_P = 1$ hPa, considering that PSs and meteorological stations are not co-located, the ZHD and ZWD variance results equal to $5.185 \cdot 10^{-3}$ mm² and to 14.185 mm² respectively.

Supposing ρ and R_v known with high precision ($\sigma_\rho = \sigma_{R_v} = 0$), assuming $T_m = 279$ K, $\sigma^2_{T_m} = 1$ K, the typical values for k_2' , k_3 and their relative σ (Bevis et al, 1992) and a conservative value of 250 mm for ZWD, it follows $\sigma_{PWV} = 0.736$ mm.

2.4 PWV sensitivity analysis

To evaluate how much PWV is sensitive to the variation of the parameters involved, a sensitivity analysis has been carried out using a MATLAB code. The code is intended to produce two graphs representing the variation of PWV and σ_{PWV} varying one of the parameters. The tolerance interval is discretized in seven

points, to compute the corresponding PWV in: the default value and in the default value $\pm 3 \cdot \sigma$, $\pm 2 \cdot \sigma$ and $\pm \sigma$.

Table 1 reports PWV and σ_{PWV} sensitivity to the variation of the different parameters inside their tolerance intervals, assuming $\varphi = 45^\circ$, $z = 1000$ m, the default values for the variables ($k'_2 = 17$ K/mbar, $k_3 = 3.776 \cdot 10^5$ K²/mbar, $T_m = 281.27$ K, $P = 1013.25$ hPa, $ZTD = 2.5$ m) and the corresponding σ (as reported in equation (4) and section 2.3).

PWV and σ_{PWV} variations are quite limited if the five variables variations are limited inside the corresponding tolerance intervals. P and ZTD are the most influencing parameters on PWV values. In fact, a variation of about 6 hPa in P produces a variation of PWV of about 2 mm; a variation of 9 mm in ZTD produces a variation of 3 mm in PWV.

Variab.	Conf. interval	PWV		σ_{PWV}	
		[mm]		[mm]	
		Min	Max	Min	Max
k'_2	(7;27)	31.0	31.5	$6.9 \cdot 10^{-1}$	$7.0 \cdot 10^{-1}$
k_3	(3.68;3.87) $\cdot 10^5$	30.5	32.0	$6.7 \cdot 10^{-1}$	$7.1 \cdot 10^{-1}$
T_m	(279.1;283.4)	31.0	31.5	$6.9 \cdot 10^{-1}$	$7.0 \cdot 10^{-1}$
P	(1010;1016)	30.0	32.2	$6.9 \cdot 10^{-1}$	$7.0 \cdot 10^{-1}$
ZTD	(2.491;2.500)	29.7	32.7	$6.8 \cdot 10^{-1}$	$7.0 \cdot 10^{-1}$

Table 1. PWV and σ_{PWV} sensitivity as each parameter changes around the default value

3. DATA NETWORKS AND DATABASE

The GNSS Meteorology applications that have 2D PWV maps as final product mainly exploit existing national networks or specifically designed high dense (1-2 km) GNSS networks (Sato et al., 2013).

An element of innovation in this field has been introduced by Andrea Walpersdorf, who proposed to use existing regional, national and international GNSS PSs for the retrieval of ZTD, to be used in climatological applications (Sguerso et al., 2013).

The present research proposes to estimate PWV using these GNSS networks, together with NOAA existing network of P and T observations. Note that GNSS receivers and P and T sensors are not necessarily co-located. To overcome the low density and the sparseness of the networks, their different configurations and distribution, a simplified mathematical model was conceived (Sguerso et al., 2014). A detailed description of networks and data follows.

3.1 GNSS Permanent Stations Network

GNSS data of 181 PSs, belonging to global (IGS and EUREF), trans-national (GAIN), national (France: RENAG and RGP; Switzerland: AGNES; Italy: GEODAF and RING) and regional (Piemonte and Liguria) networks, covering the French-Italian neighbouring area, have been used to estimate a set of homogeneous tropospheric parameters (ZTDs, horizontal North-South and East-West tropospheric gradients) through common elaboration techniques and procedures. The average data spacing is 40 km. The total extent is depicted in Figure 1.

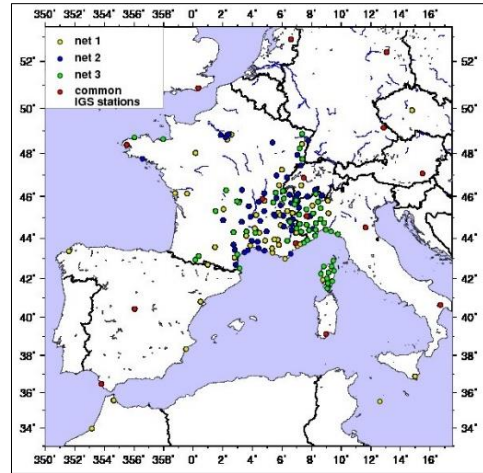


Figure 1. Total extent of GNSS PSs network

The GAMIT/GLOBK software ver. 10.4 and 10.6 (Herring et al., 2010, 2015) was employed to elaborate the GNSS data. Due to computational limits of GAMIT/GLOBK software, the PSs network has been split in three sub-networks according to decreasing station age (net1, net2 and net3, respectively), to obtain stable network geometries. A common set of 15 stations was included in each sub-network in order to achieve a stable reference frame. Within these 15 stations, 13 belong to IGS and 2 to EUREF networks.

To estimate the total amount of ZTD, several IGS stations at large distances (more than 1500 km, according to Tregoning et al., 1998) from the local network were included in each analysis.

3.2 ZTD estimations and validation

The ZTDs and the gradients were estimated for each station, simultaneously with a daily positioning solution for 24 hours sessions and were extracted from the ambiguity free solution, in order not to introduce biases in ZTDs (Santerre, 1991; Walpersdorf et al., 2007). The settings implemented for the ZTD estimations are described in Sguerso et al. (2013, 2015).

The ZTD estimations have been validated by means of two strategies: an intra-net comparison of ZTDs from the 13 IGS and the 2 EUREF common PSs, and a comparison with IGS's official ZTD estimations. Both of them result extremely useful to check the coherence of tropospheric parameters evaluated in different networks and to understand how much the network, in which a PS is included, can influence the determination of the tropospheric parameters.

3.2.1 Intra-net comparison: The 15 common PSs have been used to verify the internal consistency between the three networks calculations.

Table 2 reports the average differences and standard deviation values for the entire year 2011, for the 15 PSs. Table 3 reports the average and maximum number and percentage of outliers.

Intra-net comparison (2011)		
	With outliers	Without outliers
Average difference [mm]	net1-net2 = 0.4	net1-net2 = 0.4
	net1-net3 = 1.4	net1-net3 = 1.4
	net2-net3 = 0.9	net2-net3 = 0.9
Standard deviation [mm]	net1-net2 = 1.8	net1-net2 = 1.6
	net1-net3 = 2.0	net1-net3 = 1.7
	net2-net3 = 1.9	net2-net3 = 1.6
Max and min differences [mm]	net1-net2 = (-48;26)	net1-net2 = (-6;8)
	net1-net3 = (-67;56)	net1-net3 = (-5;8)
	net2-net3 = (-70;55)	net2-net3 = (-6;7)

Table 2. Comparison of ZTDs for the common 15 PSs for 2011

Intra-net comparison (2011)	
Without outliers	
Average number of outliers	net1-net2 = 58 (1.4%)
	net1-net3 = 69 (1.6%)
	net2-net3 = 66 (1.6%)
Maximum number of outliers	net1-net2 = 82 (1.9% SFER)
	net1-net3 = 182 (4.5% TORI)
	net2-net3 = 175 (4.3% TORI)

Table 3. Average and maximum number of outliers

The average difference values are quite small and almost the same considering or excluding the outliers. The standard deviations slightly decrease removing the outliers. Instead, the maximum and minimum values of the differences reduce substantially if the outliers are removed. This means that the ZTD estimates are coherent between the three sub-networks, with differences within the typical errors of 3-5 mm.

The average number of outliers is almost the same in the three comparisons, with slightly better results for net1-net2; the same behaviour is confirmed in the maximum number of outliers.

3.2.2 Comparison with IGS's official ZTD estimates: The comparison with IGS's official troposphere product was performed for year 2002 on 16 PSs; the ZTD estimates were extracted from net1 elaboration.

Globally, the comparison shows total differences with a mean bias of -3.6 mm and a standard deviation of 4.5 mm. The persistent bias could be related to the different network configurations, to the lack of constrain in any a priori position in the regional network elaboration, and to possible differences in the troposphere models used in the two solutions. Additionally, the different time spans at which the two ZTD estimations are carried out (5 minutes for IGS solutions and 2 hours for GAMIT solutions) could influence the results. Nevertheless, the observed constant bias does not diminish the capacity of investigating the evolution of ZTD in time.

3.3 ZTD DataBase

The two-hourly ZTD estimations and three-hourly tropospheric gradients for the 181 PSs have been included in the RENAG DataBase (DB). A first release containing ZTD and gradients from January 1998 to May 2012 was already available (Sguerso et al., 2013). A recent update was performed until December 2015. The complete DB, that will contain two-hourly ZTD estimates and couples of N-S and E-W gradients over 18 years, will be available soon. The DB will allow ZTD/gradient trend estimation and conversion from ZTD to PWV, if integrated with P and T observations.

3.4 Pressure and Temperature data

Following the criterion of exploiting existing infrastructures, a selected number of NOAA P and T stations in the French-Italian border region has been chosen. P and T sensors are not always co-located. Moreover, occasional lack of P or T data may happen due to maintenance or malfunction of the stations. For these reasons, the density of the networks varies in time.

4. ZTD AND PWV 1D ANALYSIS

As mentioned in section 2, starting from the two-hourly ZTD estimates, it is possible to calculate two-hourly PWV introducing P and T observations in the same site or nearby the PSs. The availability of ZTD long time series integrated with P and T historical data, allows to obtain PWV, which is useful for the interpretation of severe meteorological events.

In the following, an application for the city of Genoa (Italy) is shown. Genoa has been chosen because historically and recently hit by intense meteorological events (e.g. 4th November 2011 and 9th October 2014).

Two PSs are present in Genoa: GENO and GENU. GENO is an IGS PS and it is located on the Navy Hydrographic Institute building, whereas GENU is one of the six PSs belonging to the Regione Liguria positioning service, and it is located on a building of DICCA Department of the University of Genoa.

GENO and GENU PSs are not equipped with P and T sensors, thus P and T data have been extracted from two Meteorological Stations (MSs) of the University of Genoa, near the PSs: the Meteorology Observatory and the Villa Cambiaso stations (hereafter DISTAV and DICCA MS respectively). Figure 2 shows the positions of the two meteorological stations, with respect to GENO and GENU PSs, which are a few km apart.



Figure 2. Genoa PSs and MSs

DISTAV MS provides hourly mean, maximum and minimum temperature and barometric pressure data from January 2002 to December 2015 at MS height (58.3 m above mean sea level). DICCA MS registers temperature, humidity, pressure, solar radiation, wind velocity and rain data since 1989 with half-hour time step, referred to MS height (40 m above mean sea level).

4.1 ZTD Time Series

In order to identify ZTD patterns related to intense precipitation events, data from 1998 for GENO and from 2009 for GENU have been analysed. The annual two-hourly ZTD time series allow to compute a climatological average of ZTD, by averaging the corresponding two-hourly estimations at the same time and the same day of different years. The climatological average can be compared with the ZTD evolution of individual years, in order to identify specific behaviours related to intense rainfalls.

In the present thesis, the climatological averages for GENO and GENU have been compared to the ZTD evolution over the year 2011. In Figure 3, the blue dots represent the climatological averages and the red dots the year 2011. The climatological averages present slightly different behaviors, probably due to the different time spans over which were computed. The 2011 ZTD time series result almost identical for the two PSs. This demonstrates that the two PSs inspect the same portion of Troposphere.

Focusing on 4th November 2011 rain event and on GENO, Figure 4 represents the climatological average of ZTD time series with error bars (black lines) related to the root mean square differences of the individual years with respect to the climatological average, superposed on the 2011 time series. Several episodes of 2011 ZTD are significantly higher than the climatological average. Among them, the Genoa storm of 4th November 2011, which is highlighted by the black vertical bars.

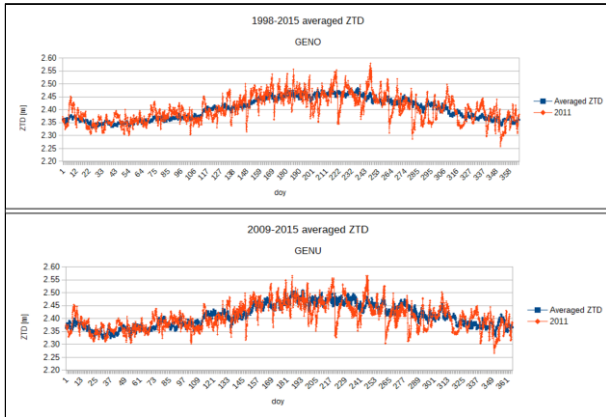


Figure 3. GENO and GENU ZTD climatological average (blue) and 2011 time series (red)

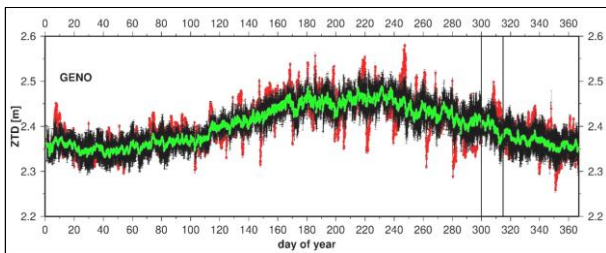


Figure 4. ZTD 2011 (red) and climatological average (green) with error bars (black) on GENO

A zoom on 4th November is depicted in Figure 5. The vertical bars underline the 4-hour interval with most of the rainfall. ZTD was significantly higher than the climatological average for about 30 hours, starting about 12 hours before the maximum of rainfall on 4th November (doy 308).

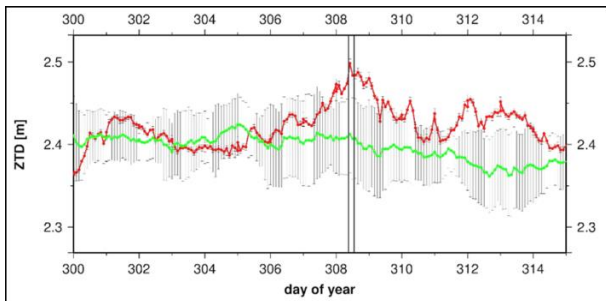


Figure 5. Zoom of ZTD time series during 4th November 2011 Genoa storm

4.2 PWV Time Series

The same approach of time series analysis was extended to PWV, to obtain a closer link to potential rain. The PWV time series from 2002 to 2015 for GENO and from 2009 to 2015 for GENU were produced, and the PWV climatological averages were computed. Focusing on 4th November 2011 rain event, Figure 6 represents the average PWV time series (in blue) and the 2011 PWV time series (in red), together with the error bars (light grey lines), showing the root mean square differences of the individual years with respect to the climatological average. There are several episodes which overcome the value of climatological average. Among them, the Genoa storm of 4th November 2011.

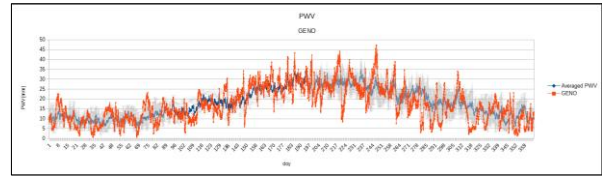


Figure 6. Climatological average (blue), 2011 PWV (red) and error bars

A zoom on shorter time span, from doys 225 (13rd August) to doys 333 (29th November), is represented in Figure 7. The two events in the circles, referring to 4th September 2011 (green circle) and to 4th November 2011 (red circle), are taken as example of the overcoming of the threshold represented by the climatological average error bars.

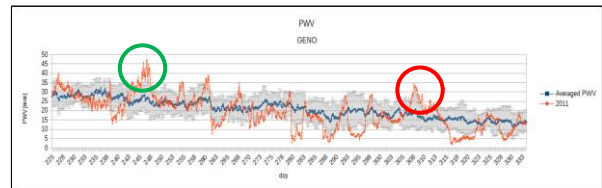


Figure 7. Zoom of PWV time series

The total amounts of rain were substantially different in the two cases. In fact, on 4th September the amount of rain was very limited and not likely to produce a meteorological alert, whereas on 4th November the amount of rain was considerably higher. Omitting considerations on the triggering conditions, which are more related to an atmospheric physics study, the presented approach, based on the overcoming of a threshold, seems not exhaustive for individuating the occurrence of severe meteorological events. The 1D approach is still valid to characterize the pattern of PWV and it can represent a new source of available data, to deepen the knowledge of meteorological phenomena and their evolution in time and space. Even so, this strategy could be applied to other test cases in order to improve the method and identify other eventual indicators. However, a 2D methodology has been conceived to monitor the evolution of PWV in time and space.

5. PWV 2D PROCEDURE

A GIS procedure has been conceived to realize 2D maps to monitor the evolution of PWV content in atmosphere. Using the commands of GRASS GIS ver. 6.4 and map algebra, the GNSS Meteorology equations (1-8) were simply implemented. In order to transform local ZTD, P and T information to 2D PWV maps, a simplified mathematical model, conceived to describe the atmosphere's physics, including data interpolation, was performed. Hence, the interpolated P, T and PWV maps were compared with the fields coming from the meteorological simulation, to check the adequacy of the proposed procedure. Then, an indicator for severe rainfalls was identified.

5.1 Data interpolation

A major issue was to identify the most appropriate interpolation technique to create PWV maps from ZTD, P and T data, in a quick and automatic way for near-real time application, in order to support the monitoring of intense meteorological events. The main difficulties were due to the sparse distribution of P, T and ZTD data and the different networks configurations, combined with high resolution and wide orographically complex computational region.

The meteorological event of Genoa on 4th November 2011 was a first case study to compare the interpolation techniques.

117 PSs on the French-Italian neighbouring area extracted from RENAG DB and 27 NOAA meteorological stations were employed to compare Inverse Distance Weighted (IDW), Regularized Spline with Tension (RST), kriging (krig) and Triangulated Irregular Network (TIN) interpolation techniques with low resolution.

Figure 8 depicts the distribution of the GNSS PSs, P and T networks as black, red and blue dots respectively. The mean spacing between GNSS PSs is about 40 km, while P and T stations are sparser, with a mean spacing of about 150 km.

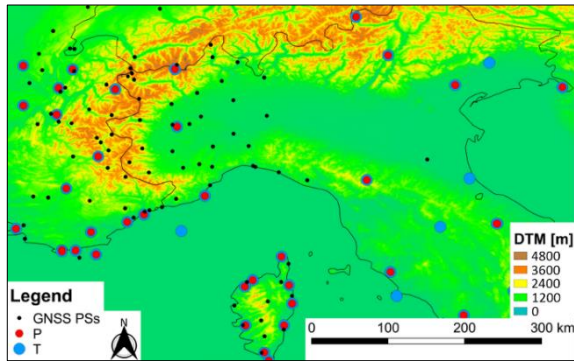


Figure 8. Distribution of GNSS, P and T stations

5.1.1 ZTD interpolation: The comparison of interpolation techniques was performed on a wide computational area with a resolution of 6' (about 10 km) on ΔZTD data, representing the differentiation in time of ZTD with respect to a “calm” moment (Ferrando et al., 2017).

The geostatistical behavior of the observed data was analysed, computing the variogram of ΔZTD in R environment (2008), to verify the correctness of the grid size of the interpolation maps. Figure 9 depicts the empirical points and the variogram model of ZTD data relative to 03/11/2011 04 UTC with respect to 03/11/2011 02 UTC.

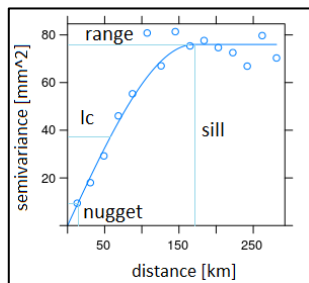


Figure 9. Variogram of ΔZTD

The variogram model that best fit the empirical data is a spherical function. The correlation length (indicated in Figure 9 as l_c) can be estimated to about 50-60 km, while the mean distance between PSs is around 40-60 km. So similar magnitudes indicate an appropriate density for the considered “regional” GNSS network, but represent the upper limit of the sampling.

ΔZTD data have been interpolated via IDW, RST, krig and TIN. In particular, for the IDW technique, three different tests have been performed using 3, 6 and 12 nearest points, indicated as IDW3, IDW6 and IDW12 respectively. Concerning RST, the smoothing parameter has been set close to zero to make the interpolated surface passing on the sampled points. The Regression Kriging (RK) was employed, also to evaluate the data correlation with elevation.

In order to define which interpolation technique could be the most representative of the ZTD spatial distribution, 12 PSs of the 117, called Check Points (CPs), were excluded by the interpolation dataset and were used to verify the results. The

comparisons were carried out on the CPs, along a transept representative of the complex orography of the area to focus the attention on the altimetric differences, and through a 2D difference map between interpolated surfaces to analyze the global behavior in the study area.

Table 4 reports the minimum, maximum, mean and standard deviation of each techniques calculated on the 12 CPs.

	Min	Max	Mean	Std
IDW3	-14.9	3.1	-0.6	5.2
IDW6	-14.0	3.2	-0.7	5.0
IDW12	-14.1	4.4	-0.6	5.2
RST	-10.9	4.0	-0.6	4.1
krig	-11.3	4.0	-0.7	4.0
TIN	-11.5	3.4	-0.9	4.4

Table 4. Evaluation of different interpolation methods compared with observed values at 12 test PSs (in mm)

The values are very similar for every interpolation method, with differences between interpolated surface values and the observed values of the “check points” are always within the mean $\pm 3\sigma$. Kriging and RST seem to behave slightly better, having lower values of standard deviation.

Figure 10 depicts the trace of the transept and the values of ΔZTD along it, produced applying the previous interpolation techniques. The results are quite similar, apart from IDW3 which has a trend in steps. Excluding IDW3, the maximum differences between interpolated and true values of ΔZTD are generally less than 4 mm, which is comparable to the standard deviation noise.

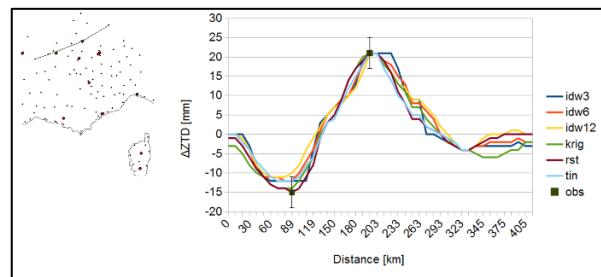


Figure 10. Transept position (on the left) and values of ΔZTD along it (on the right), from South/West to North/East

Figure 11 depicts the 2D interpolation surface of ΔZTD between using IDW6, and the differences of the various interpolation techniques in respect to IDW6.

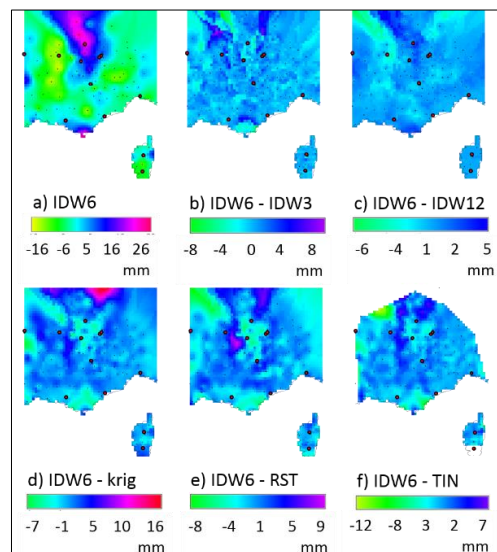


Figure 11. Map of ΔZTD created by IDW6 interpolation and difference maps between IDW6 and the other techniques

The interpolated maps seem quite similar, with main differences located at the boundary. Excluding the boundary area, the maximum differences range between -7 (IDW6-TIN) and 9 (IDW6-RST) mm. Systematic patterns are present only for IDW6-IDW3.

However, RST and kriging have been considered not suitable for near real-time applications, due to the needed calibration of their parameters (tension and smoothing for RST and the variogram for kriging), which are very sensitive to the network's configuration that can vary in time due to temporary lack of data. IDW6 parameters are less sensitive, assuming almost standard values. TIN has no parameter to be defined and shows high adaptability to different network configurations. Hence IDW6 and TIN can be successfully used for near real-time applications.

5.1.2 P and T data interpolation: P and T 2D maps were generated applying an interpolator involving a simplified mathematical model conceived by the research group (under evaluation for a patent).

Generally, P and T 2D maps could be obtained from meteorological models, but the present procedure is intended to be totally independent from weather models. Hence, interpolation of data coming from NOAA's DB of P and T meteorological stations has been carried out. In this way, the procedure results could be used as starting conditions for existing meteorological models or as comparison with them, to better understand the meteorological phenomena.

P and T data have been interpolated via IDW, RST, TIN and RK. Then, the same approach used for ZTD has been extended to P and T fields: comparisons were carried out both along a transept and 2D differences maps, to evaluate both the local and the global behaviour in the study area.

Despite the difficulties due to the sparse distribution of P and T data and the considerable orographic effect, the simplified mathematical model seems effective in reproducing P and T fields. All the tested interpolators show similar results, with higher differences located in high altitude areas, both for P and T and in the edge regions, due to the different behaviours of the tested interpolators.

For further details on the comparison results, refer to Ferrando et al. (2016).

5.2 Comparison with meteorological simulation

The interpolated P, T and PWV maps were compared with the fields coming from a meteorological simulation generated by using the entire set of existing observations.

The simulation maps were produced using the mesoscale Weather Research and Forecasting (WRF) model. The simulation settings are summarized in Cassola et al. (2015).

Again, as already done in the comparison between ZTD, P and T fields interpolated with different methods, the comparisons were carried out along a transept and through 2D difference maps.

For P and T fields, the comparison along the transept has been carried out between interpolated fields, meteorological simulation and observed data, which showed a good accordance, confirming that it is possible to obtain P and T fields even from sparse data. The comparison through 2D difference maps provides similar results in the entire study area. A deeper analysis on the results is presented in Ferrando et al. (2016).

The attention is here focused on the comparisons on PWV maps, whose validation is a recent progress but, for the sake of completeness, is here reported..

The WRF and G4M PWV data have been produced with a spatial resolution of 3.3 km and temporal resolution of 1 hour. As a consequence of what emerged from the comparison between interpolators, TIN was used to produce PWV maps.

Figures 12a and 12b depict the G4M and WRF PWV maps produced for 4th November 2011, 10 UTC; Figure 12c shows the PWV difference map. The contour lines on Figures 12a and 12b correspond to PWV values of 20, 25, 30, and 35 mm.

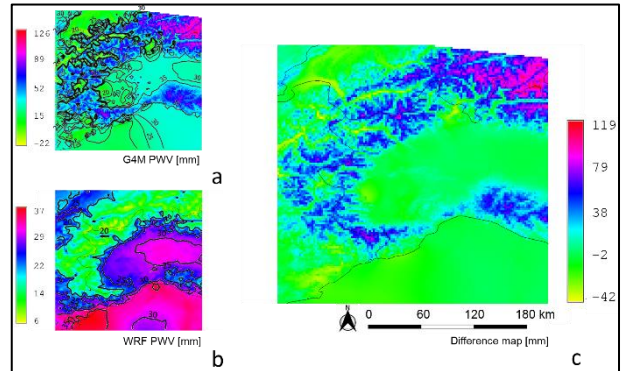


Figure 12. PWV map from the G4M procedure (a), WRF simulation (b) and difference map (G4M-WRF) (c)

The unrealistic negative PWV values in Figure 12a may be due to the effect of P overestimation and/or ZTD underestimation in localized areas. The PWV negative values have been sorted in 5 classes (from 0 to -22 mm with steps of 5 mm) and then compared with the Digital Terrain Model (DTM), to assess the influence of elevation on the unrealistic values of PWV. What firstly emerged is the non-significance of negative PWV values from a statistical point of view; in facts, they are limited to 1.6% of the total cells. They are typically located in elevation ranges from 0 to 1000 m in areas where an abrupt variation of elevation is present (e.g., valleys).

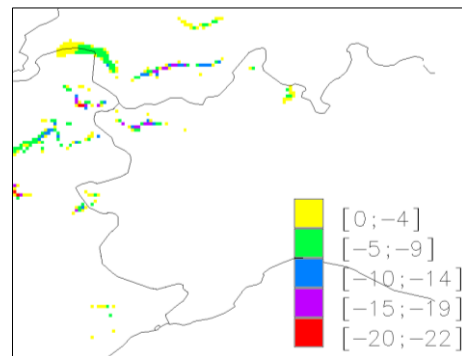


Figure 13. Distribution of PWV negative values

Two-hourly PWV time series for 3rd and 4th The PWV difference map shows large differences in high-altitude areas, whereas the differences are negligible for flat land and on the sea. The average and root-mean-square (rms) of the PWV differences are 8 mm and 24 mm, respectively. The PWV differences might be due to observation and/or interpolation errors of P and T fields, generated by the simplified mathematical model, and of the ZTD maps, in addition to WRF uncertainties.

To asses if the encountered discrepancies are significant and to determine their effect on the interpretation of the meteorological phenomenon, two strategies have been introduced: (1) the analysis of the PWV time series for PSs at different elevations, and (2) the study of PWV along a section crossing complex topographic areas.

GENO (110 m a.s.l.), TORI (261 m a.s.l.), GRAS (1270 m a.s.l.), and AGNE (2300 m a.s.l.) two-hourly PWV time series of G4M and WRF PWV have been analysed from 3rd November 2011 00 UTC to 4th November 2011 22 UTC. The two series show slight differences (few millimeters), as reported in Figure 14. This highlights the correct interpretation of the PWV temporal

evolution by G4M, in spite of the influence of orography on PWV.

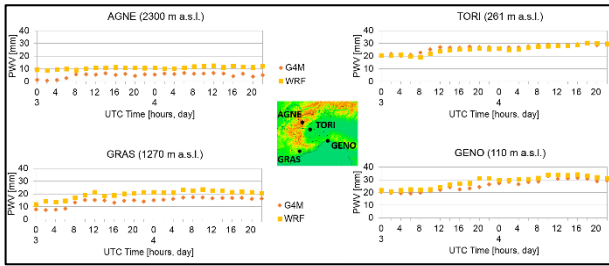


Figure 14. Two-hourly PWV time series for 3rd and 4th November 2011, for GENO, TORI, GRAS and AGNE

Then, a section of the G4M and WRF PWV maps passing through the Alps was studied. The position of the section and obtained PWV values are depicted in Figure 15. A strong orographic effect is evident in the G4M PWV map.

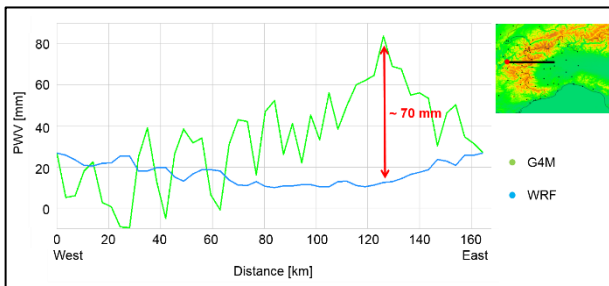


Figure 15. G4M and WRF PWV values along a transept

5.3 ΔPWV maps

To remove the orographic effect, the ΔPWV map was introduced. The ΔPWV consists of time differentiation of PWV maps with respect to a “calm” moment, when the PWV content in the atmosphere is limited. This allows to remove the orographic effect, which is constant in time, and to highlight PWV variations. Figure 16 reports the ΔPWV trend relative to the same section of Figure 15. The removal of the orographic effect and a reduction of the differences between the curves, from more than 20 mm (on average) to approximately 2–3 mm, are evident.

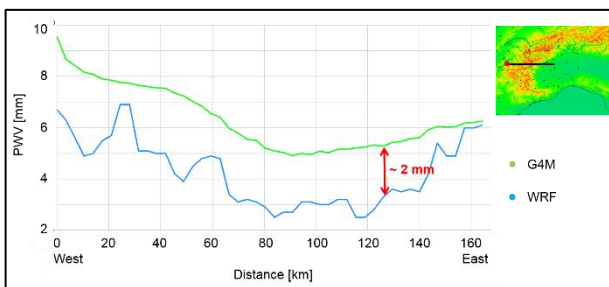


Figure 16. G4M and WRF ΔPWV values along a transept

The same effect can be globally observed in the entire study area by creating a difference map of the G4M and WRF ΔPWV maps, as shown in Figure 17c. The ΔPWV maps from G4M and WRF are depicted in Figures 17a and 17b. In spite of the differentiation in time, several differences between the two ΔPWV maps are visible, but a substantial reduction with respect to the values reported in Figure 12 can be observed. The ΔPWV differences range from -17 to 6 mm, with a mean value of -1 mm and standard deviation of 2.8 mm.

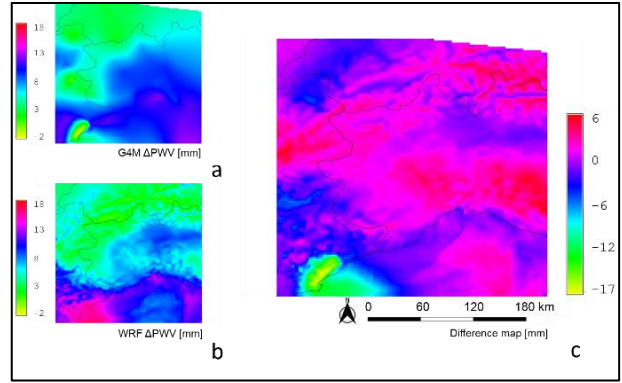


Figure 17. ΔPWV map from the G4M procedure (a), WRF simulation (b) and difference map (G4M-WRF) (c)

5.4 An indicator for severe rainfalls: Heterogeneity Index

In order to detect remarkable features in the PWV evolution, which can potentially precede severe meteorological events, and to better correlate the PWV content to the occurrence of rain, the spatial variability of PWV has been considered as a promising indicator. Indeed, the overcoming of a threshold of PWV seems a not sufficient parameter, as shown in the 1D analysis. Moreover, the ΔPWV map does not help in defining where a severe event could take place. An example is reported in Figure 18a (relative to 4th November 2011, 10 UTC), where a severe event occurred in circle 1 and no rain occurred in circle 2, although both locations are characterized by a high ΔPWV. The hourly cumulated rain observed on 4th November 2011, at rain gauges in circles 1 and 2 is reported in Figure 19b and 19a, respectively.

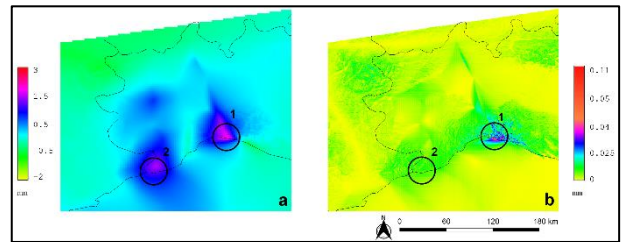


Figure 18. ΔPWV is not sufficient to determine if a severe event may occur in circles 1 or 2 (a), whereas HI highlights circle 1, where the severe event occurred (b)

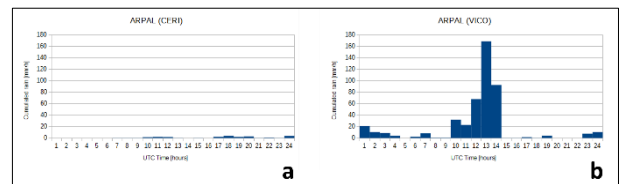


Figure 19. Hourly cumulated rain observed on 4th November 2011, at rain gauges in circles 1 (right) and 2 (left)

To localize intense meteorological events in time and space, an index accounting for the spatial ΔPWV variability, the HI, has been conceived. The index represents ΔPWV “block standard deviation” obtained by resampling of ΔPWV maps to a coarser grid (1 km) and computing the value of the standard deviation, using the GRASS module *r.resamp.stats*. Thus, each pixel of the HI map represents the empirical standard deviation of the 16 ΔPWV map pixels included in it. The 1 km resolution was deemed to be an appropriate resolution for the present case study, because it is comparable to the spatial scales of the analyzed meteorological phenomenon. Figure 18b shows high HI values

only in circle 1, where the event occurred, and not in circle 2, where no rain occurred.

As will be shown in the next section, HI seems a promising indicator to localize in time and space the occurrence of heavy rains. Thus, HI could be useful to an early-warning system based on near real-time PWV maps, as an independent contribute to meteorological alerts.

In the near future, the correlation between rainfall and HI peaks will be studied in depth, paying particular attention to the localized spatial and temporal distribution of heavy rainfall.

6. APPLICATION ON A REAL TEST CASE

During the morning of 4th November 2011, a stationary and self-healing storm developed over the city of Genoa, causing a huge amount of rain with intensities of up to 169 mm/hour near the city center. In some areas of Genoa, almost 400 mm rain fell over the entire day and ~300 mm rain fell from 09 to 13 UTC. This severe meteorological event led to the flooding of the Bisagno River and its tributary Fereggiano, causing the death of six people and much damage.

Figure 20 shows the reflectivity map observed by the Bric della Croce (Turin) meteorological radar at 11:35 UTC, where the localized distribution of intense rainfall around Genoa (circle 1) and moderate values elsewhere (e.g., circles 2 and 3) are evident.

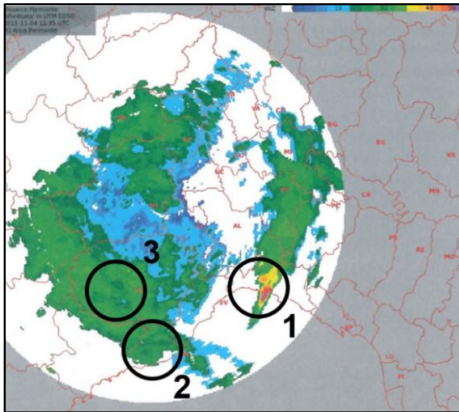


Figure 20. Reflectivity map observed by the Bric della Croce meteorological radar at 11:35 UTC on 4th November 2011

The application of the G4M procedure to this severe meteorological event based on a posteriori and simulated near real-time approaches is presented in the following Sections 6.1 and 6.2.

G4M procedure was also applied to the severe meteorological event occurred on Genoa on 9th October 2014 with satisfactory results.

6.1 PWV a posteriori monitoring

PWV maps were realized, with a time step of 2 hours to analyze the meteorological phenomenon and its evolution in space and time, from 02 UTC on 3rd November 2011 to 00 UTC on 5th November 2011, using the G4M procedure. The existing infrastructure used in the elaboration consisted of 117 PSs with a mean spacing of 40 km and 35 meteorological stations with a mean spacing of approximately 150 km. The computational region has been discretized with a resolution of 6' (nominal WGS84 datum; ~10 km). To remove the orographic effect from PWV maps and to easily visualize the PWV evolution in time, ΔPWV maps were produced in reference to a “calm” moment in which it did not rained, i.e. 02 UTC on 3rd November 2011.

Figure 21 shows the sequence of ΔPWV maps for 4th November 2011, from 00 to 22 UTC. The increase in the amount of water

vapor over time in the study area is evident. The Genoa event (black circle in Figure 21) occurred between 9:00 and 13:00 UTC.

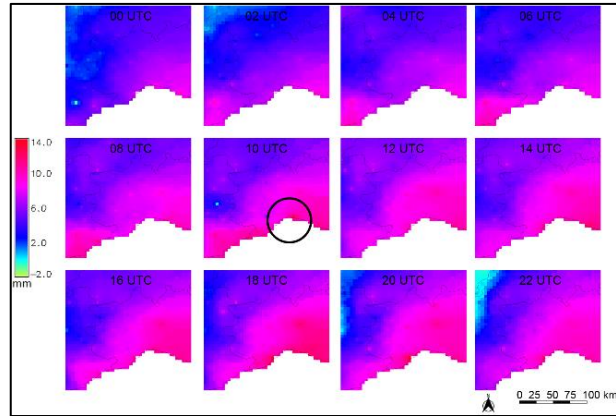


Figure 21. ΔPWV maps for 4th November 2011 (00-22 UTC). The circle indicates the position and time of the higher value.

Higher temporal and spatial resolutions will allow to better localize the event, as discussed in the next section.

However, the PWV value is useful for estimating the maximum amount of rain that can precipitate under triggering conditions. A very rough evaluation of the maximum rain intensity may be obtained by assuming that the raindrops fall with a velocity of 9 m/s (characteristic value for the velocity of large raindrops; see Gunn and Kinzer, 1949) from a typical condensation level altitude of 3000 m; it takes 666 s for the rain drops to reach the ground. Assuming that the PWV remains nearly constant for one hour and that all of the water vapor condenses, the following factor $k = 3600/666 = 5.4$, can be considered as multiplying factor relating the PWV values to the maximum amount of potential rain. Thus, the PWV value of 42 mm obtained for 10:00 UTC on November 4, 2011, can be converted into approximately 230 mm/h of potential rain. The DICCA pluviometer at the University of Genoa observed only 75 mm from 9:00 to 10:00 UTC but the Vicomorasso pluviometer in the Bisagno basin between 13 and 14.00 UTC observed 165 mm (see Figure 19b; more details in ARPAL, 2012). Hence, such a rough potential rain computation could be useful for a decision support system based on GNSS meteorology to establish risk thresholds under different rain scenarios.

6.2 PWV near real-time monitoring

The G4M procedure was employed to interpret meteorological events by simulating a near real-time analysis. Indeed, the proposed near real-time analysis is an a posteriori analysis, but it is considered a useful test to evaluate the feasibility of the procedure and its application in near real-time, mainly concerning needed data, computational time, and additional information provided with respect to the a posteriori analysis. Considering the limited time and space scales of severe meteorological events, typically characterized by short durations (15–30 minutes) and extreme localization (on the order of a few kilometers), a time span of 6 minutes and spatial resolution of 250 m were chosen.

Due to computational limitations in GAMIT software, a 4-hour analysis period and a smaller PSs network were considered. The network consists of the 15 PSs common to the three subnetworks (described in Section 3.1), 14 PSs of the Regione Piemonte network, 6 PSs of the Regione Liguria network, and the EUREF GENO and IGS AJAC PSs as additional stations, as shown in Figure 22.

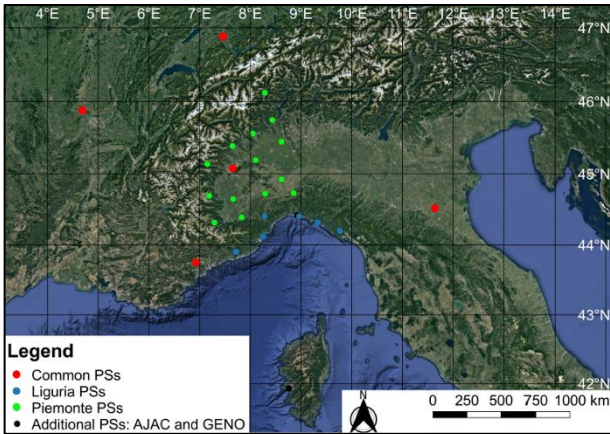


Figure 22. GNSS PSs network for near real-time monitoring

Figure 23 shows a test performed on the accordance of 6 minutes and 2 hours ZTD estimates.

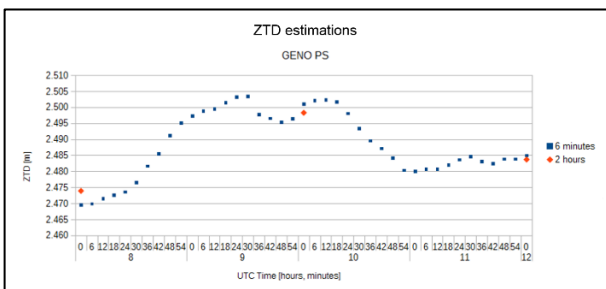


Figure 23. Comparison between 6 minutes and 2 hours ZTD estimates

Slightly different ZTD estimations, in the order of few mm, can be appreciated. Concerning the ZTD rms comparison, higher differences appear, mainly located near the start and the end of session. For this reason, only the three central hours of session have been taken into account, removing the first and the last half hours of the 4 hours session. In general, high rms values could be related to the higher correlation between ZTD estimation in short time span elaborations. Nevertheless, it seems that higher rms values do not influence the interpretation of the time evolution of the investigated meteorological phenomenon. Thus, 6 minutes PWV maps have been obtained starting from 6 minutes ZTD estimations for the severe event occurred on Genoa on 4th November 2011.

Concerning the environmental data, P and T data have been obtained by interpolation of NOAA data, supposing a linear behavior of the temporal evolution of P and T between two sampled data.

A 30-minute extraction of the 6 minutes Δ PWV maps, from 09 to 11:30 UTC on 4th November 2011, is represented in Figure 24.

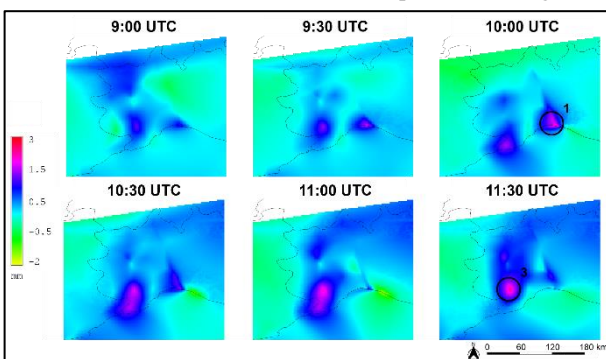


Figure 24. 30-minutes extraction of the 6 minutes Δ PWV maps

The Δ PWV maps were obtained by differentiation in time with respect to 8:30 UTC on November 4, 2011, representing relative “calm” conditions with respect to the rain peak. The Δ PWV maps highlight both positive and negative time differences, corresponding to an increase and decrease in the water vapor amount in the atmosphere, the last one due to rainfall.

In addition to the Δ PWV peak of Genoa, another peak with analogous values is evident in the area around Mondovì (circle 3 in Figure 24), where an intense meteorological event might occur.

HI maps were produced with a spatial resolution of 1 km and a time resolution of 6 minutes from 8:30 to 11:30 UTC on 4th November 2011. A 30-minute extraction from 09 to 11:30 UTC is presented in Figure 25.

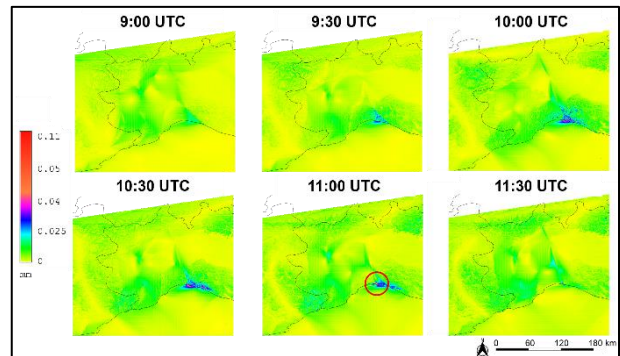


Figure 25. 30-minutes extraction of the 6 minutes HI maps

As expected, the HI maps allow to localize the intense meteorological event, assuming values close to zero for the whole area, except for Genoa, where the event occurred (red circle in Figure 25).

Instead, the Δ PWV peak observed in circle 3 in Figure 24 does not correspond to a high HI value in Figure 25, as expected based on the moderate radar reflectivity in that area (Figure 20).

The timings of the highest HI values (approximately at 11 UTC) in the analyzed time window are in accordance with the highest rain values. HI seems to predict the maximum observed rain, between 11 and 12 UTC, several tens of minutes before. Thus, the locally strong spatial variation in Δ PWV seems to be correlated to the intense meteorological event considered in this study.

The correspondence between HI and the rain peaks will be studied in detail in the near future.

CONCLUSIONS AND FUTURE PERSPECTIVES

The present work focuses on the possibility of obtaining 2D PWV maps starting from GNSS, P and T data coming from existing infrastructure. ZTD is estimated in homogeneous GNSS regional networks, P and T are extracted from international stations in different discrete points. ZTD estimates and P and T observations from international measuring stations are located at different discrete points, with a mean spacing of 40 and 150 km, respectively.

Based on Bevis et al. (1992), a procedure called G4M has been conceived to produce 2D PWV maps with high spatio-temporal resolution (up to 6 min and 250 m for PWV, 1 km for HI).

G4M is based on a simplified mathematical model conceived by the research group, which is able to effectively describe the 2D P and T fields, despite difficulties due to the sparse distribution of observed data.

The procedure was applied to an area approximately covering northwestern Italy, to study a severe meteorological event that occurred in Genoa on 4th November 2011.

The strength and originality of the G4M procedure are based on the use of existing infrastructure, the independence from meteorological models, the possibility of automation, the high adaptability to different network configurations, and the ability to produce high-resolution 2D PWV maps, even from sparse input data.

A comparison has been carried out both in 1D and 2D on the different interpolation techniques for ZTD, P and T in order to state the most appropriate interpolation technique in sight of applying the G4M procedure in near real-time. Moreover, P, T and PWV fields obtained via G4M have been validated by comparison with those originating from WRF meteorological simulations.

The study of PWV time series for PSs at different altitudes, the evaluation of PWV behavior along a section crossing complex topography, and the computation of difference maps between G4M and WRF PWV fields led to understand that the encountered differences do not influence the interpretation of the meteorological phenomenon evolution in time. Hence, the procedure can be considered effective. The emerged key role of orography can be roughly removed by introducing the Δ PWV map, representing the differentiation of the PWV in time with respect to a “calm” moment. The observation of different PWV values over time provides the spatial and temporal evolution of the PWV, allowing for easier monitoring of the atmosphere.

The HI, conceived by the research group, allows to localize of severe meteorological events in time and space, accounting for the spatial variability of Δ PWV. It allows to discriminate between locations and times characterized by high Δ PWV values based on spatial Δ PWV heterogeneity, which seems to be correlated with the intense meteorological event considered in this study.

The G4M procedure has been applied both to a posteriori and simulated near real-time strategies using 2-hour and 6-minute ZTD, P, and T data. The simulated near real-time strategy and the analysis of HI evolution during the analysed event seem to be promising for a future early-warning system based on G4M. In fact, because the entire G4M procedure is independent from meteorological models, it could be innovatively integrated into them, supporting now-casting.

Systematic application of G4M procedure to different case studies (intense and moderate events, lacking/false meteorological alerts) to statistically evaluate the reliability of HI and its performance is planned for the near future. Moreover, the relationship between HI and rain peaks will be studied in depth.

ACKNOWLEDGEMENTS

I wish to thank:

- prof. Bianca Federici and prof. Domenico Sguerso for supervising this thesis;
- prof. Toshitaka Tsuda and prof. Giovanna Venuti for being the external reviewers of this PhD thesis;
- prof. Andrea Walpersdorf for hosting me at ISTerre to work with her on RENAG Database update;
- prof. Andrea Mazzino and Dr. Federico Cassola for sharing the meteorological simulation data.

REFERENCES

ARPAL (2012) Genoa November 4-9, 2011 meteo-hydrological event report. Quaderni ARPAL, n.2 (in Italian; https://www.arpal.gov.it/images/stories/meteo/Documenti_sito/QuadernoArpalGenovaSettembre_WEB.pdf)
 Basili P., Bonafoni S., Ferrara R., Ciotti P., Fionda E., Betti B., Prini R., Tornatore V., Crespi M., Di Paola S., Baiocchi V.,

Radicioni F. (2003). Assessment of precipitable water vapour by use of a local GPS network and microwave ground-based radiometer. 11th International Conference on Antennas and Propagation (ICAP 2001), vol. 2001, p. 72-76, Institute of Electrical and Electronics Engineers Inc., ISBN: 0852967330, doi: 10.1049/cp:20010241
 Bennitt G.V., Jupp A. (2012). Operational Assimilation of GPS Zenith Total Delay Observations into the Met Ofce Numerical Weather Prediction Models. *Monthly Weather Review*, 140, pp. 2706–2719
 Bevis M., Businger S., Herring T., Rocken C., Anthes R., Ware R. (1992). GPS meteorology – Remote sensing of atmospheric water vapor using the Global Positioning System. *Journal of Geophysical Research*, 97, pp. 15787–15801
 Bevis M., Businger S., Chiswell S., Herring T., Anthes R., Rocken C., Ware R. (1994). GPS meteorology: Mapping zenith wet delays onto precipitable water. *Journal of applied meteorology*, 33, pp. 379–386
 Bock O., Bouin M.N., Doerfing E., Collard P., Masson F., Meynadier R., Nahmani S., Koité M., Balawan K.G.L., Didé, F., Ouedraogo D., Pokperlaar S., Ngamini J.B., Lafore J.P., Janicot S., Guichard F., Nuret M. (2008). West African Monsoon observed with ground-based GPS receivers during African Monsoon Multidisciplinary Analysis (AMMA). *Journal of Geophysical Research*, 113, doi: 10.1029/2008JD010327
 Boniface K., Ducrocq V., Jaubert G., Yan X., Brousseau P., Masson F., Champollion C., Chéry J., Doerfing E. (2009). Impact of high-resolution data assimilation of GPS zenith delay on Mediterranean heavy rainfall forecasting. *Annales Geophysicae*, 27(7), pp. 2739–2753, doi: 10.5194/angeo-27-2739-2009
 Bosy J., Kaplon J., Rohm W., Sierny J., Hadas T. (2012). Near real-time estimation of water vapour in the troposphere using ground GNSS and the meteorological data. *Annales Geophysicae; Katlenburg-Lindau* 30.9: 1379
 Bouma H.R., Stoew B. (2001). GPS observations of daily variations in the atmospheric water vapor content. *Physics and Chemistry of the Earth, Part A: Solid Earth and Geodesy*, 26, pp. 389–392
 Cassola F., Ferrari F., Mazzino A. (2015). Numerical simulations of Mediterranean heavy precipitation events with the WRF model: a verification exercise using different approaches. *Atmospheric Research*, 164-165, pp. 210-225
 Crespi M., Luzietti L., Frattale Mascioli F., Rizzi A. (2004). Impiego meteorologico del GPS per la previsione di precipitazioni critiche. In: 8° Conferenza Nazionale ASITA. Federazione Italiana delle Associazioni Scientifiche per le Informazioni Territoriali ed Ambientali, Roma, 14-17 dicembre, 2004
 Davis J.L., Herring T.A., Shapiro I.I., Rogers A.E.E., Elgered G. (1985). Geodesy by interferometry: effects of atmospheric modeling errors on estimates of baseline lengths. *Radio Science* 20, pp. 1593-1607
 De Ponte M.S.F.V., Zou X. (2001). A Case Study of the Variational Assimilation of GPS Zenith Delay Observations into a Mesoscale Model. *Journal of Applied Meteorology*, 40, pp. 1559–1576
 Elgered G., Davis J.L., Herring T.A., Shapiro I.I. (1991), Geodesy by radio interferometry: Water vapor radiometry for estimation of the wet delay, *J. Geophys. Res.*, 96, pp. 6541-6555
 Ferrando I., Federici B., Sguerso D. (2017). Zenith total delay interpolation to support GNSS monitoring of potential precipitations. *GEAM - Geingegneria Ambientale e Mineraria*, Anno LIV, n. 2, pp. 85-90

- Ferrando I., De Rosa P., Federici B., Sguerso D. (2016). Spatial interpolation techniques for a near real-time mapping of Pressure and Temperature data. *PeerJ Preprints* 4:e2223v2 <https://doi.org/10.7287/peerj.preprints.2223v2>
- GRASS Development Team. (2010). Geographic Resources Analysis Support System (GRASS) Software, Version 6.4.0. Open Source Geospatial Foundation <http://grass.osgeo.org>
- Gunn R., Kinzer G.D. (1949). The terminal velocity of fall for water droplets in stagnant air. *Journal of Meteorology*, 6(4), pp. 243-248
- Herring T.A., King R.W., McClusky S.C. (2010). GAMIT Reference Manual–Release 10.4. Department of Earth, Atmospheric, and Planetary Sciences, Massachusetts Institute of Technology. ed. USA
- Herring T.A., King R.W., McClusky S.C. (2015). GAMIT Reference Manual–Release 10.6. Department of Earth, Atmospheric, and Planetary Sciences, Massachusetts Institute of Technology. ed. USA
- Karabatić A., Weber R., Hayden T. (2011). Near real-time estimation of tropospheric water vapour content from ground based GNSS data and its potential contribution to weather now-casting in Austria. *Advances in Space Research*, Volume 47, Issue 10, Pages 1691-1703
- Pacione R., Vespe F. (2003). GPS Zenith Total Delay Estimation in the Mediterranean Area for Climatological and Meteorological Applications. *Journal of Atmospheric and Oceanic Technology*, Vol. 20, 1034.
- Piccardo D., Sguerso D. (2007). Il contributo del GPS nelle previsioni di eventi meteorologici significativi. *Atti della 11° Conferenza Nazionale ASITA*, Torino, 6-9 novembre 2007, vol. 2, pp. 1775-1780
- R Development Core Team. (2008). R: A language and environment for statistical computing. R Foundation for Statistical Computing, Vienna, Austria. ISBN 3-900051-07-0, <http://www.R-project.org>
- Resch G.M. (1984). Water vapor radiometry in geodetic applications, *Geodetic Refraction*, pp. 53-84
- RENAG DataBase
ftp://renag.unice.fr/products/GPS_climatology_Sguerso_Labbouz_Walpersdorf
- Saastamoinen J. (1972). Introduction to practical computation of astronomical refraction. *Bulletin Géodésique*, 106, pp. 383-397
- Santerre R. (1991). Impact of GPS satellite sky distribution. *Manuscripta Geodaetica*, 16, pp. 28-53
- Sato K., Realini E., Tsuda T., Oigawa M., Iwaki Y., Shoji Y., Seko H. (2013). A high-resolution Precipitable Water Vapor monitoring system using a dense network of GNSS receivers. *Journal of Disaster Research*, 8(1), pp. 37-47
- Sguerso D., Labbouz L., Walpersdorf A. (2013). 14 years of GPS tropospheric delays in the French-Italian border region: a data base for meteorological and climatological analyses. *The International Archives of the Photogrammetry, Remote Sensing and Spatial Information Sciences*, XL-5/W3, 7-14, doi:10.5194/isprsarchives-XL-5-W3-7-2013
- Sguerso D., Federici B., Agrillo G., Ferrando I. (2014). Il contributo della geomatica alla valutazione delle allerte meteorologiche. *Newton's Bulletin*, ISSN 1810-8563, Volume: Il prof. Sansò e l'evoluzione della geodesia in Italia, CD-ROM, pp. 1-11
- Sguerso D., Labbouz L., Walpersdorf A. (2015). 14 years of GPS tropospheric delays in the French–Italian border region: comparisons and first application in a case study, *Applied Geomatics*, DOI 10.1007/s12518-015-0158-z, ed. Springer Verlag, Online ISSN 1866-928X, pp. 1-13
- Sieczka M. and GRASS Development Team 2006. r.surf.nnbathy GRASS Software, Version 6.4. Open Source Geospatial Foundation
- Solheim F.S., Vivekanandan J., Ware R.H., Rocken C. (1999). Propagation delays induced in GPS signals by dry air, water vapor, hydrometeors, and other particulates. *Journal of Geophysical Research*, 104, pp. 9663-9670
- Spilker J.J. (1980). Signal structure and performance characteristics, *Navigation*, 1, Institute of Navigation, pp. 29-54
- Tralli D.M., Dixon T.H., Stephens S. (1988). The effect of wet tropospheric path delays on estimation of geodetic baselines in the Gulf of California using the Global Positioning System, *J. Geophys. Res.*, 93, pp. 6545-6557
- Tregoning P., Boers R., O'Brien D. (1998). Accuracy of absolute precipitable water vapor estimates from GPS observations. *Journal of Geophysical Research: Atmospheres*, 103(D22), pp. 28701-28710
- Tsuda T., Sato K., Realini E., Oigawa M., Iwaki Y., Shoji Y., Seko H. (2013). A real-time monitoring system of Precipitable Water Vapor (PWV) using a dense GNSS receiver network. *Journal of Disaster Research*, vol.8 No.1, pp. 155-156
- Walpersdorf A., Bouin M.N., Bock O., Doerflinger E. (2007). Assessment of GPS data for meteorological applications over Africa: Study of error sources and analysis of positioning accuracy. *Journal of Atmospheric and Solar-Terrestrial Physics*, 69(12), pp. 1312-1330
- Yao Y., Xu C., Shi J., Cao N., Zhang B., Yang J. (2015). ITG: A New Global GNSS Tropospheric Correction Model. *Sci. Rep.* 5, 10273; doi: 10.1038/srep10273.



Associazione **U**niversitari di **T**opografia **e** **C**artografia

Sezione Tematica 2 Fotogrammetria e Laser Scanner

*

*Thematic Section 2
Photogrammetry and Laser Scanner*

OPTIMIZATION AND AUTOMATION OF THE POST-PROCESSING HIGH RESOLUTION UAV PHOTOGRAMMETRIC DATA

M. Alicandro^{1,*}

¹ DICEAA, Dept. Of Civil, Architectural and Environmental Engineering, 67100 LAquila, Italy maria.alicandro@univaq.it

KEY WORDS: Photogrammetry, UAV, Image Enhancement, Automated image data analysis

ABSTRACT:

The photogrammetry technique has undergone strong evolution in the last few decades, both in terms of data processing and acquisition mode, to allow obtaining detailed 3D models useful for a detailed survey and to support the management and recovery of cultural heritage and buildings. However, despite recent developments, the main outputs of the photogrammetry process are raster data and point clouds characterized by high informative content, but they are not typically extracted automatically. In addition, these data are characterized by big volume and complexity that make it difficult to use, in fact, they are classified as "Big Data." The research activity carried out in this Ph.D. thesis, based on the need to optimize the use of data from the "renewed photogrammetry process", involved the automated and optimized procedures for the automatic vectorization of photogrammetric data, characterized by a very high geometric resolution. The proposed analyses and experiments were carried out considering two cases study different application scale and type of information content: a cultural heritage of the city of L'Aquila "St. Maria of Collemaggio" church and a historic centre "Aielli". In the first case study, vectorization interested the particular mosaic of the main facade by experimenting with innovative artificial intelligence algorithms that improved the images filtering. In the second case study, starting from the Digital Elevation Model (DEM), automated procedures have been implemented and optimized for the vectorization of the geomorphologic characteristics of the building, useful for the conservation, restoration and sustainable recovery of cultural heritage and historical centres. The vector data has made it easier to obtain more readable data, making it easy to read and facilitate interchange with other analytic applications in different fields of application. In addition, the vector data, compared to the raster data, allows to have lighter databases in terms of memory occupation and to meet the less stringent production requirements in terms of VOLUME, one of the three properties of the big data.

1. INTRODUCTION

The photogrammetry technique has undergone strong evolution in the last few decades, both in terms of data processing and acquisition mode, to allow obtaining detailed 3D models useful for a detailed survey and to support the management and recovery of cultural heritage and buildings. The main advantages were introduced by Computer Vision in the automation of most of the processes, drastically reducing the processing time of photogrammetric data, without however losing a high precision of the result. Simultaneously, with the development of UAVs (Unmanned Aerial Vehicle), the technique, which took the name of UAV Photogrammetry, allows to perform surveys in a short time (more than one hectare of surface in less than 10 minutes) and at low cost (compared to aerial photogrammetry), allowing the acquisition of very high resolution data and to investigate inaccessible and dangerous areas, such as the red areas of earthquake craters, or high and hidden details such as towers or roofs (Dominici et al., 2012).

Although Computer Vision is born for automation purposes, compared to the photogrammetric technique closest to the precision of the final metric data (Hartley and Mundy, 1993), its contribution in the photogrammetric process has been of fundamental importance to return interest towards a technique almost completely replaced by scanning laser in 3D modeling (Remondino et al., 2014). Specifically, the purpose of Computer Vision is to determine the greatest amount of information from images through automated processing without taking into account the use of the final product by users. On the other hand, photogrammetry, being a three-dimensional metric process, must

guarantee the requirements for precision, reliability and robustness in processing (Granshaw and Fraser, 2015). Despite the different objectives, the two techniques are based on the same criterion for the reconstruction of three-dimensional models: an iterative bundle adjustment (Triggs et al., 1999). Substantially, the Computer Vision has developed "Structure From Motion" techniques for the reconstruction of a 3D scene (Structure) without the knowledge of the interior orientation parameters of the camera (non-calibrated camera) basing the reconstruction on the long sequences of images (Motion) with different points of view (Barazzetti et al., 2011) and Dense Matching algorithms (Remondino et al., 2014, Hirschmuller, 2008, Furukawa and Ponce, 2010, Pierrot-Deseilligny and Paparoditis, 2006) that, once generated a sparse pattern of points (called a sparse point cloud), allow a detailed reconstruction of the final model. Actually most of the 3D modeling software use these techniques (Szeliski, 2010) as Pix4D, Agisoft, APERO-MICMAC, etc. The high degree of automation introduced by Computer Vision is a clear advantage over the classic photogrammetric approach (Westoby et al., 2012), making the technique more accessible for important applications such as 3D modeling of the territory and documentation of structures and infrastructures.

Furthermore, the use of UAV, as survey platform, equipped with photogrammetric instrument, remote controlled (automatic or semiautomatic mode), define a new survey technique, namely "UAV Photogrammetry" (Eisenbeis, 2009). The main advantages of this technique (high resolution photogrammetric 3D model, drop survey time, low costs, no danger in hazard contexts), the repeatability and the possibility of mounting other sensors make UAV photogrammetry a complete and versatile survey technique. UAV Photogrammetry opens new application scenar-

*Corresponding author

ios in the field of close-range photogrammetry, combining aerial and terrestrial photogrammetry (Eisenbeis, 2009), such as Precision Farming (Honkavaara et al., 2013), geology (Aicardi et al., 2016, Chiabrando et al., 2010, Piras et al., 2016), emergency management (Baiocchi et al., 2013, Chou et al., 2010, Dominici et al., 2016, Gomez and Purdie, 2016), traffic management (Puri et al., 2007), cultural heritage (Cabuk et al., 2007).

The photogrammetric process allows to obtain different metrically correct and georeferenced products, such as 3D models, point clouds, orthomosaics and Digital Elevation Models (DEMs), able to describe in a particular and continuous way the object investigated. However, by their nature, these data do not allow to derive the information about the characteristics of surveyed objects in a quantitative manner (total built area, areas and lengths of details, measurements, material characteristics, etc.), because any point or pixel (depending on the output returned) corresponds to a different information that must be queried individually. Automated feature detection is yet manual, time-consuming procedure and an active area of research (Vasuki et al., 2014). The raster to vector conversion is not direct, but transformations, namely segmentation, must be performed on the input data to convert the pixel values into features. Segmentation consists of partitioning images into distinct and homogeneous regions based on a distinguishable characteristic. The grouping into regions (clusters) is based on criteria of homogeneity and discontinuity between the values of pixels. Taking an R image, segmentation is the process that distinguishes the image in n regions R_i :

$$\bigcup_{i=1}^n R_i = R \quad (1)$$

were R_i is a set $\forall i = 1, 2, \dots, n$

$$R_i \cap R_j = \emptyset \quad \forall i, j \text{ with } i \neq j$$

$$Q(R_i) = TRUE \quad \forall i = 1, 2, \dots, n$$

$$Q(R_i \cup R_j) = FALSE \quad \forall R_{neighboring} \quad R_i, R_j.$$

Where $Q(R_k)$ is any predicate that indicates any distinctive property of the regions.

The segmentation algorithms derive from the Pattern Recognition and Computer Vision for the analysis of images in different application fields: from medicine to telecommunications (Schiewe, 2002). In the literature different types of segmentations have been proposed, each one is used for different purposes and applicable to several types of images. In general, segmentation techniques can be divided into two large groups based on the principle of discontinuity or homogeneity, the first subdivide the images based on abrupt changes in the analyzed properties of the images, while the latter are based on the search for regions with similarity (Matta, 2014). In geomatics, the main segmentation algorithms can be divided into two categories: pixel-oriented, based on individual pixel classifications and may be unsupervised or supervised and object-oriented, which instead are able to group characteristics by aggregation in similar regions or polygons. In this case, different strategies are used: point-based, edge-based, region-based or combined (Schiewe, 2002). In many case, especially in Remote Sensing data, the presence of noise in the images can affect the distinction thresholds for segmentation. To overcome this, it's possible to use derivative filters that allow a better reading of the data. (Roushdy, 2006, Shrivakshan et al., 2012). Filters most used in the field of edge recognition are Robert, Pre-witt, Sobel filters and the Canny algorithm based on the analysis

of the gradient and the Laplacian filters (Zero Crossing) (Maini and Aggarwal, 2009). Remote sensing data are the most complex to treat (Schiewe, 2002) because of their heterogeneity (presence of different objects and shapes), the nature of sensor used and the different scale. The literature provides several approaches to obtain vector data in the field of Remote Sensing. In (Schiewe, 2002) the main advantages and limitations of object-oriented segmentation techniques to multispectral images are analyzed. Another case is reported in (Baiocchi et al., 2014) for the thematic classification of Worldview2 images, characterized by 8 spectral bands and a geometric resolution of 0.5m. Other examples are based on the same approach for the restitution of land use and forest maps, always through the treatment of multispectral data from satellite (Chirici et al., 2009, Pastore et al., 2010). Another interesting application example for the extraction and vectorial reconstruction of buildings starting from DEM data proposed by (Forlani et al., 2003): the restitution of the roof discontinuity plans to analyze the vector forms; also in this case the analysis was performed on data with a geometric resolution of 1 m coming from LIDAR techniques. When these techniques are applied to data coming from the close-range photogrammetry, characterized by a very high geometric resolution (centimeter) and a low radiometric resolution (number of available RGB bands limiting the treatment in case of amateur camera), the results of classifications cannot be so satisfying and failing in vectorization. The aim of this study is to investigate the possible improvement of the vector conversion of the data obtained from the photogrammetric processes. In particular, this study is focused on two contexts characterised by different application scale and type of information content. In the first case study, the restitution involved the vectorization of a facade of a cultural heritage, a "St. Maria of Collemaggio" church. In the second case, instead, the vectorizations of morphological features pertaining to a historical minor centre Aielli(AQ) in the Abruzzi region will be presented starting from a very high resolution DEM.

2. CASE STUDIES

This section is dedicated to the presentation of two case studies, analysing the entire supply chain of the renewed photogrammetric process (from the data acquisition phase through UAV to the 3D model restitution) up to the treatment for raster to vector conversion. In particular, as case studies have been considered a prestigious building, symbol of the city of L'Aquila, the "Basilica of Santa Maria di Collemaggio" and a historical minor center, the village of "Aielli" (AQ). These areas, different in terms of application scale and type of information to be returned, require a different approach and processing strategies. Then, after analyzing the phases of the survey and the restitution of the photogrammetric models, in the first case study will be presented a methodology of vector conversion of the church faade. In the second case, the analysis will concern the vectorization of useful information for a sustainable redevelopment of minor historical centers.

2.1 "St. Maria of Collemaggio" church

2.1.1 Photogrammetry survey. The survey was carried out with a mini UAV Anteos A2-Mini / B, with on board a Canon S100 digital compact camera, the characteristics are shown in Table 1.

Starting from the knowledge of the relationships that exist between the characteristics of the sensor (focal length and sensor size), the flight altitude and the Ground Sample Distance (GSD),

UAV Type		Mini UAV Quadcopter	
Optical Sensor	Camera	Canon S100	
	GSD	12 MP	
	Focal length	5,2 mm	
	Sensor size	Width	7,6 mm
		Height	5,7 mm
	Pixel size	1,9 μ m	

Table 1. Sensor parameters and instrument

(Kraus, 1994), two flight have been planned with a vertical route and a horizontal acquisition to reconstruct the church facades. Due to the particular structure of the Anteos A2-Mini/B, it was mandatory to apply a Field Of View (FOV) direction of 16,5 with respect to the horizontal direction in order to exclude any part of the UAV in the photograms. For the first flight, the distance of the UAV from the facades have been of 30 m, knowing the camera parameters (focal length = 5,2 mm and sensor size = 7,6 x 5,7 mm) used, a Ground sample Distance (GSD) equal to 1 cm has been obtained. Applying the correction due to the oblique acquisition, the maximum and minimum variation of GSD was equal to 0.5 cm. In order to limit the effect of the oblique image, it is generally necessary to increase the overlap between images and to improve their redundancy (Rupnik et al., 2014). Then, 14 waypoints are obtained imposing an overlap of 90 %. For the second flight, the narrow distance of the faade was the main issue to plan a flight with the same parameters of the first flight. Imposing the distance from the faade equal to 10 m, the GSD is equal to 0,36 cm cm with 0,1 cm of variation for the oblique acquisition. 291 images were acquired to cover the entire church. After the creation of an accurate flight planning, the flights can be executed following the pre-imposed route to collect the images for further elaboration. In addition, 52 natural GCPs easily identifiable and well distributed on the structure have been measured in a local reference system. A TS30 Total Station has been used obtaining a precision of the coordinates values equal to a few millimetres. The local reference system has been measured with GNSS in static mode in order to georeference the final model in WGS84. The data elaboration has been carried out using Agisoft Photoscan (Agisoft Photoscan Manual, 2016) which allows to obtain the 3D model following the Structure From Motion workflow (Westoby et al., 2012) and the Dense Matching approach. Initially, the matching features allow to detect the tie-point between adjacent images using descriptors and detectors algorithm (Remondino and Fraser, 2006). Subsequently, bundle adjustment retrieves the camera position for all images and the calibration parameters of the camera, allowing the generation of sparse 3D point clouds. Thanks to high number of tie-points, a statistical adjustment is implemented. The values of camera calibration can be achieved in an automatic way (Fraser, 1997) considering those values as variables in the resolution of the collinearity equations. Then, the insertion of GCPs along with the tie-points allows to georeference and to scale the 3D models and to refine the output of the bundle adjustment. The other collected points are used as Check Points (CPs) to compare the results with the ground truth. The results are exposed in the Table 2. Several combination of GCPs and CPs are reported to control the final precision (Figure 1).

Once obtained the orientation parameters with dense matching algorithm (Agisoft Photoscan, 2011), a depth map is calculated in medium quality to reconstruct the dense cloud. Finally, the mesh is created by using the arbitrary mode as method of reconstruction to extract detailed information on the facades of the building. The

Case 1	GCPs	CPs
Number	7	45
Res. (m)	0.036	0.062
Res. (pix)	1.36	1.40
Case 2	GCPs	CPs
Number	11	41
Res. (m)	0.032	0.039
Res. (pix)	1.32	1.41
Case 3	GCP	CPs
Number	20	32
Res. (m)	0.027	0.047
Res. (pix)	1.36	1.41

Table 2. Residual values for different distribution of GCPs and CPs in the bundle adjustment.

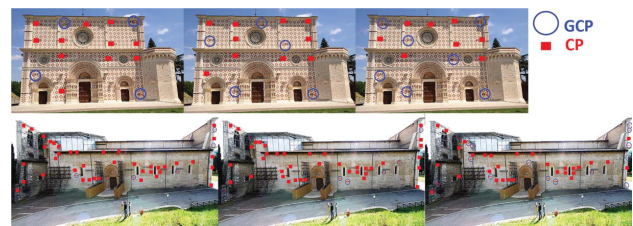


Figure 1. Several distribution of GCPs and CPs

result is a 3D model, subsequently texturized. The main results of the processing phase are the georeferenced 3D model, orthophoto (Figure 2) and DEM.



Figure 2. faade orthophoto of St. Maria of Collemaggio

2.1.2 Post-elaboration of photogrammetric output. In this case study, the vector conversion involved the edge extraction of the characteristic faade of the church. For this purpose, usually *object-oriented* techniques and filter are employed. But as already mentioned, the selection of the separation threshold with the classical filters is still a critical issue. The following figure 3, 4, 5 and 6 illustrate some examples of classical filters application results.

To enhance the threshold distinction, a new approach has been tested, using experimental filters: Active Connection Matrix (ACM) developed by the Semeion Research Center for the Science of Communication and until now experimented only in

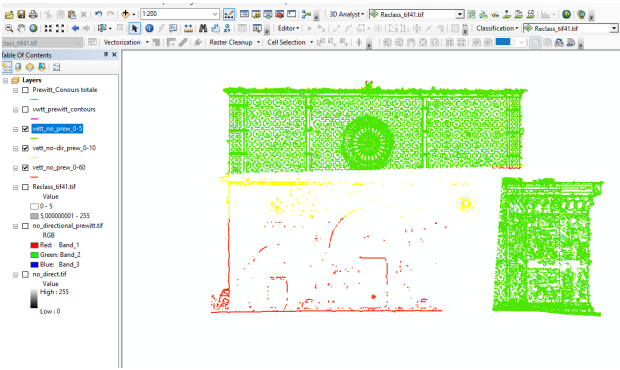


Figure 3. Prewitt Filter of ortophoto

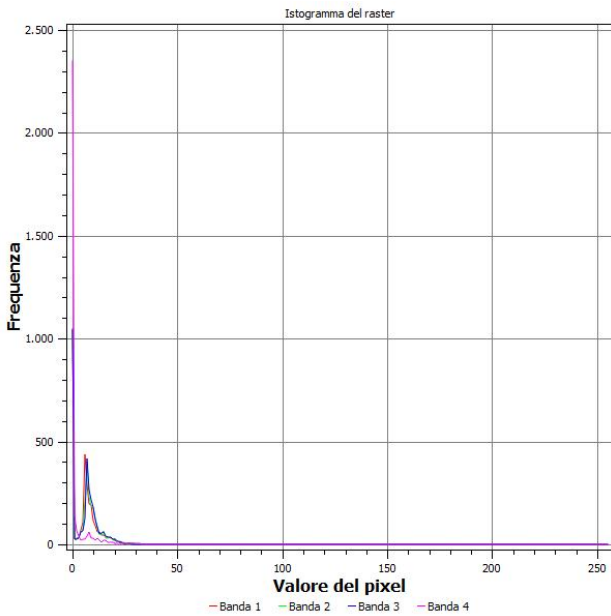


Figure 4. Prewitt Filter histogram

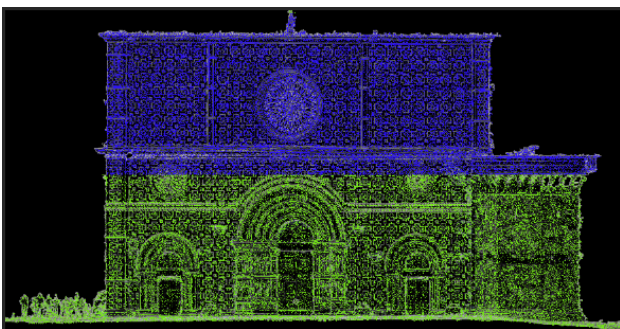


Figure 5. Laplacian Filter on ortophoto

medical field. In this algorithm the images are considered as a connected matrix of elements that develop over time. Then to the original dimensions of the images two other dimensions are added: the local connection between the pixels ω and the time (t) according to the equation 2:

$$PIXEL^{originale}(x_1, x_2, x_3, x_D) = PIXEL^{ACM}(x_1, x_2, x_3, x_D, w, t) \quad (2)$$

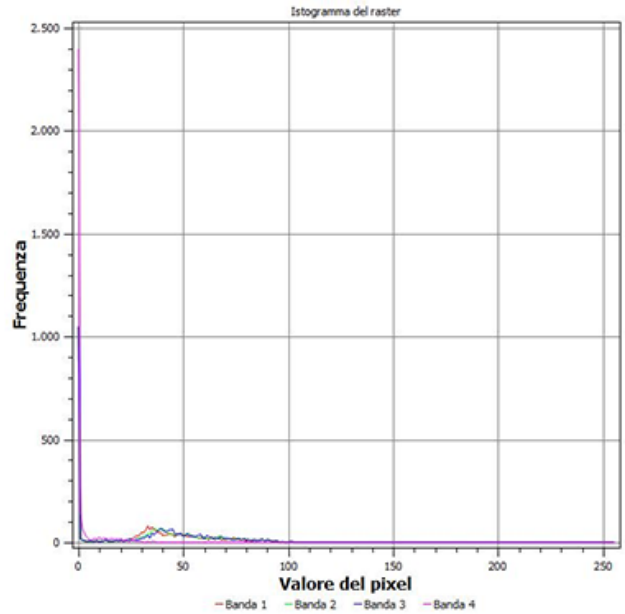


Figure 6. Laplacian filter histogram

These systems remodel any digital image through three operations: 1. transform the original image into a connected pixel network ω ; 2. apply to the transformed image operations that directly or indirectly transmit the original brightness of the pixels and / or their connections t ; 3. terminate when the cost function is satisfied that is when the transformation process stabilizes. The ACM systems are subdivided into three classes according to the variables, the pixels connection, the units or both that are considered constrained/unconstrained (Figure 7). "Each image to N dimensions, transformed into a connected network of units that develop over time, through local operations, deterministic and iterative, can show, in a larger dimensional space, morphological and dynamic regularities that in their original dimensions would not be visible or quantifiable as noise". (Buscema, 2006)

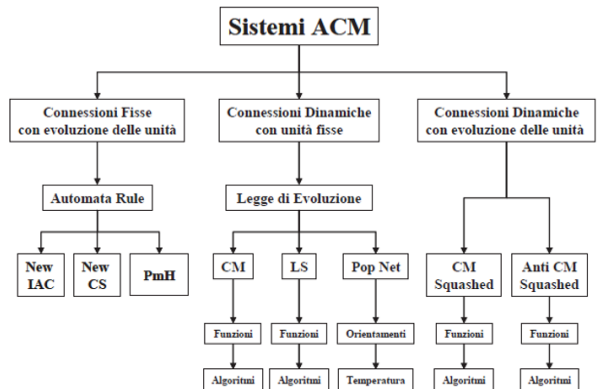


Figure 7. ACM Filters

Among all the tested filters, the New Constraint Satisfaction Networks (New CS), which is a fixed connection system, allowed to obtain a binary image and a perfect threshold distinction.

A two-dimensional image can be expressed as a pixel matrix according to equation 2, in which the radiometric values are considered the evolutionary units (u) in the ACM systems. Therefore

substituting this notation in 2, an active array of connections is defined through the following system of equations:

$$\begin{aligned}
 u_{i,j}^{[n+1]} = & f(u_{i,j}^{[n]}, u_{i-1,j-1}^{[n]}, u_{i,j-1}^{[n]}, u_{i+1,j-1}^{[n]}, u_{i-1,j}^{[n]}, \\
 & u_{i+1,j}^{[n]}, u_{i-1,j+1}^{[n]}, u_{i,j+1}^{[n]}, u_{i+1,j+1}^{[n]}, \\
 & w_{(i,j),(i,j-1)}^{[n]}, w_{(i,j),(i-1,j-1)}^{[n]}, w_{(i,j),(i+1,j-1)}^{[n]}, w_{(i,j),(i-1,j)}^{[n]}, \\
 & w_{(i,j),(i+1,j)}^{[n]}, w_{(i,j),(i-1,j+1)}^{[n]}, w_{(i,j),(i,j+1)}^{[n]}, w_{(i,j),(i+1,j+1)}^{[n]})
 \end{aligned} \quad (3)$$

and

$$\begin{aligned}
 w_{(i,j),(i-1,j-1)}^{[n+1]} &= g(u_{i,j}^{[n]}, u_{i-1,j-1}^{[n]}, w_{(i,j),(i-1,j-1)}^{[n]}) \\
 w_{(i,j),(i,j-1)}^{[n+1]} &= g(u_{i,j}^{[n]}, u_{i-1,j-1}^{[n]}, w_{(i,j),(i,j-1)}^{[n]}) \\
 w_{(i,j),(i+1,j-1)}^{[n+1]} &= g(u_{i,j}^{[n]}, u_{i+1,j-1}^{[n]}, w_{(i,j),(i+1,j-1)}^{[n]}) \\
 w_{(i,j),(i-1,j)}^{[n+1]} &= g(u_{i,j}^{[n]}, u_{i-1,j}^{[n]}, w_{(i,j),(i-1,j)}^{[n]}) \\
 w_{(i,j),(i+1,j)}^{[n+1]} &= g(u_{i,j}^{[n]}, u_{i+1,j}^{[n]}, w_{(i,j),(i+1,j)}^{[n]}) \\
 w_{(i,j),(i-1,j+1)}^{[n+1]} &= g(u_{i,j}^{[n]}, u_{i-1,j+1}^{[n]}, w_{(i,j),(i-1,j+1)}^{[n]}) \\
 w_{(i,j),(i,j+1)}^{[n+1]} &= g(u_{i,j}^{[n]}, u_{i,j+1}^{[n]}, w_{(i,j),(i,j+1)}^{[n]}) \\
 w_{(i,j),(i+1,j+1)}^{[n+1]} &= g(u_{i,j}^{[n]}, u_{i+1,j+1}^{[n]}, w_{(i,j),(i+1,j+1)}^{[n]})
 \end{aligned} \quad (4)$$

$$\begin{aligned}
 \forall u_{i,j}^{[n]} \\
 e \\
 \forall w_{(i,j),(i,j+k,j+z)}^{[n]} \\
 |(i,j,x+k,j+z) \in I_x^G = \\
 = \{(i,j,x+k,j+z) | 0 < \text{dist}(i,j,x+k,j+z) \leq G\}
 \end{aligned} \quad (5)$$

with fixed initial value $u_{i,j}^{[0]} = u_{x_s}^{[0]}$;
 $w_{(i,j),(i,j,x+k,j+z)}^{[0]} = w_{x,x_s}^{[0]}$.

Where subscripts x are the pixel position i, j , while subscript s is the pixel position respect to a neighbourhood I_x^G of radius G . G is the number pixel, neighbourhood the central pixel, affected by elaboration.

In fixed connection systems, units or pixels evolve at each processing cycle (n) on values calculated in the previous cycle using fixed connections:

$$u_{i,j} = u_x^{[n+1]} = f(u_x^{[n]}, \dots, u_{x_s}^{[n]}, \dots, w_{x,x_s}^{[0]}) \quad (6)$$

Where $w_{x,x_s}^{[0]}$ represents the connection between the pixel $x = (i, j)$ and its neighbour $x_s = (i+k, j+z)$ calculated at time 0. In this case the connections act only as an impulse and constraint to the evolution of pixels. 2D image becomes a matrix with R rows and C columns, in which each cell is an autonomous unit $u_{i,j} = u_{i,j}^{[0]} = u_x^{[0]}$, connected with the 8 units of its neighbourhood with symmetrical weight $w_{(i,j),(i+k,j+z)}^{[0]} = w_{x,x_s}^{[0]}$. The Automata Rule (AR) algorithm defines the connection among pixel through non-linear transformations of the different brightness of the pixels. Considering that each unit can assume $[0, 1]$, a parameter is defined to control the connections strength σ , making the algorithm sensitive to differences in the images; can take values between $0 \leq \sigma \leq 2N$, with N the discrete number of brightness levels that each unit can assume in the range of data values (for example 2^8). Thus, the Gaussian transformation relative to brightness values among adjacent pixels is defined:

$$R_{(i,j),(i+k,j+z)} = e^{-(\sigma u_{i,j} - \sigma u_{i+k,j+z})^2} \quad (7)$$

Defined its minimum value $\varepsilon = e^{-\sigma^2}$, it is possible to scale and add a constant such that the value of the projection can take a value into $[-c, c]$ (for example $c = 5$) facilitating the calculations and obtaining:

$$R'_{(i,j),(i+k,j+z)} = \frac{c}{1-\varepsilon} (2 * R_{(i,j),(i+k,j+z)} - \varepsilon - 1) \quad (8)$$

At this point the value of connections is defined through a hyperbolic tangent:

$$w_{(i,j),(i+k,j+z)}^{[0]} = w_{(x,x_s)}^{[0]} = \text{Tanh}(R'_{(i,j),(i+k,j+z)}) \quad (9)$$

The AR defines connections as close to 1 if the brightness values of the connected units are similar and tends -1 the more they are not. (Buscema, 2006). In Figure 8 are reported several analysis

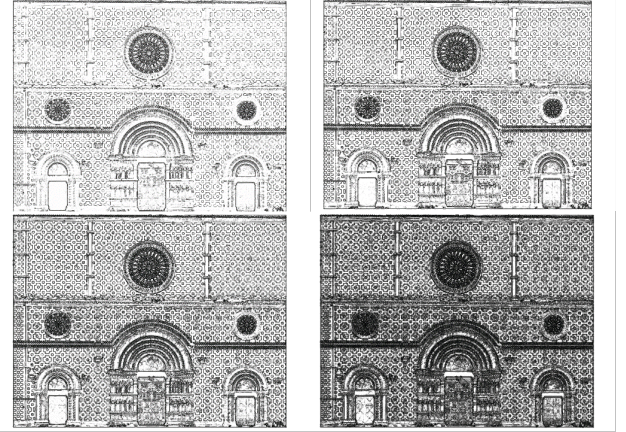


Figure 8. Automata Rule with different σ ; upper left $\sigma : 10$, upper right $\sigma : 15$; bottom left $\sigma : 20$; bottom right $\sigma : 40$.

varying σ : for weak connections ($\sigma = 10$), there is a loss of information, while for high σ , the strength of connection between the pixels tends to create very noisy images. Therefore, 15 was chosen as the final value of the AR. Once defined the connections, New Cs determines the evolution of pixels (Figure 9). The New CS is a changed version of the Constraint Satisfaction Networks (McClelland et al, 1988) and the central idea is to consider each pixel-agent of the matrix a "hypothesis", which can be gradually "true" or "false", in ratio to the brightness value of each pixel-agent. The cost function of the New CS system tends to "make true" the hypothesis of the matrix:

$$\begin{aligned}
 \text{Maxf}(\text{Pixel}) = \\
 \text{f}(\text{Pixel}) = \frac{1}{2} * \sum_x \sum_{I_x} u_x * u_{x_s} * w_{x,x_s}
 \end{aligned} \quad (10)$$

where: Pixel = all pixels; x = position of central pixel; I_x = neighbourhood; u_x = value of central pixel $[0, 1]$; w_{x,x_s} = x e x_s connection.

The optimization rule of each pixel is based on Boolean functions, NOT (XOR), AND and CONTEST. The following equation 11 is for the NOT(XOR) function:

$$(u_x u_{x_s}) + (\bar{u}_x \bar{u}_{x_s}) = \text{State} \quad (11)$$

and in tabular form (Table 3):

The parameter that allows to define the binary image is the number of cycles (C). The following are some images and their his-

Center	Neighbors	State
1	1	1
1	0	0
0	1	0
0	0	1

Table 3. NOT(XOR) Function

tograms of the orthophoto processing for cycles 1, 30, 60 and 100 (Figure 9). To create the final vector (Figure 10), the image was

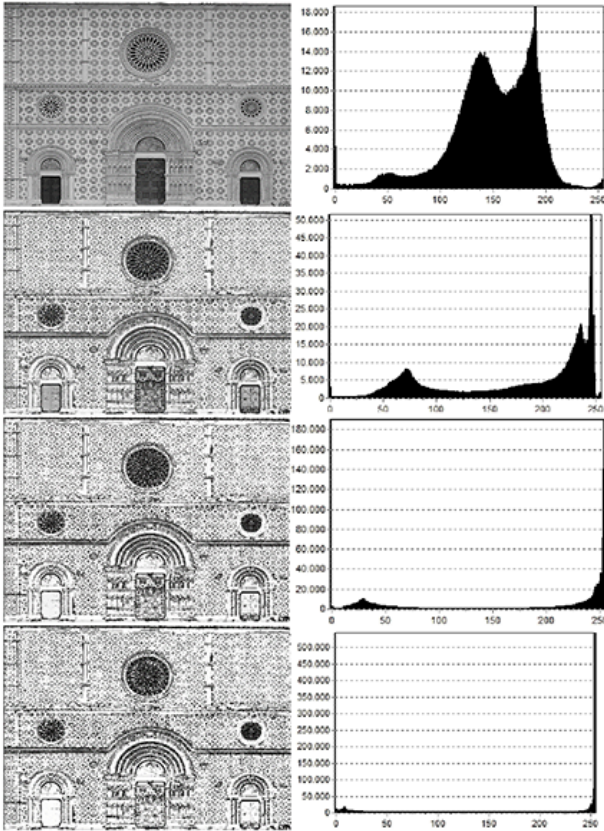


Figure 9. New CS elaboration. On the left the images; on the right the histograms. From top to bottom, the image changes according to the number of cycles. ($c=10$, $c=30$, $c=60$; $c=100$. Values of grayscale pixels from 0 to 255 in x axis, while in the y axis are shown the pixel numbers of the image. Ordinate scale is different, but is not confusing because the objective is to highlight the separation of the pixels distribution within the binary image.

processed using the ArcSCAN tool in the GIS environment.

The image processed, however, was not the full resolution orthophoto due to the limit of the software, but the resolution was 2 cm. To evaluate the impact of the resolution, the partial mosaic, with a full resolution (1 cm) was further analyzed with the same parameters obtaining the following result .

It can be concluded that the increase of σ makes it possible to increase the visible details but with the maximum limit of 30, in which an increase of noise is observed. Finally, a further test was performed varying the neighbourhood of pixels with the creation of greater connections during processing. In Figure XXX the results performed for the values $I = 2$, $I = 3$ and $I = 4$, in which the neighborhood of pixels are respectively 24, 48 and 80.



Figure 10. Vector conversion

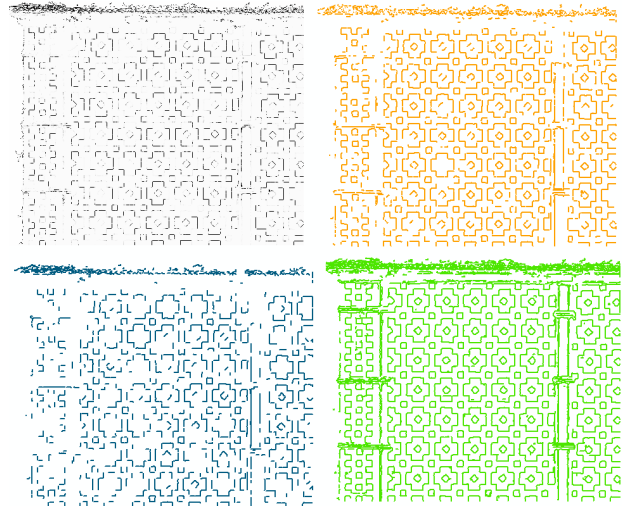


Figure 11. Vectorization to the original resolution. upper left $\sigma=10$ upper right $\sigma: 15$;bottom left $\sigma: 20$; bottom right $\sigma: 30$.

Analyzing the results it's possible to conclude that increasing the I there are more details in the vectorialitation but also an increase of noise. A good compromise is the result obtained with $\sigma = 20$ and with $I = 3$.

2.2 "Aielli", Minor Historical Centre

2.2.1 Photogrammetric Survey.

A multi-rotor Flynovex equipped with a Sony alpha 6000 camera has been used in order to carry out this case study. Table 4 shows the main characteristics of UAV and of the optical sensor. In the following, the main steps to obtain a metric 3D model are presented: the flight planning, the data acquisition and the final step of elaboration. As in the previous case study, a flight planning has been generated. Imposing the GSD equal to 2 cm, a flight altitude of about 75 m has been obtained. In order to avoid the occlusion problems due to the shadow and the nadiral acquisition (Brito, 2000, Nex and Remondino, 2014), a high overlap of 80 % between images has been imposed and a second flight has been planned with an oblique acquisition of 10° . The oblique acquisition affects negatively the GSD value (Hhle, 2008), but, in our case study, the maximum

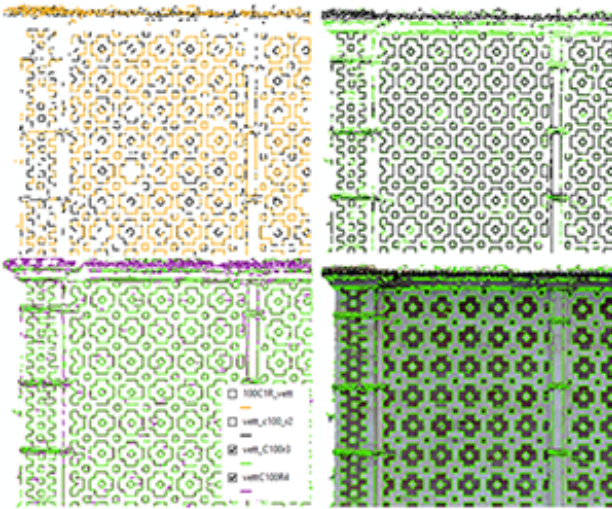


Figure 12. Vectorization varying I . In particular, the images have been overlapped to highlight the differences. upper left $I = 1$ and $I + 1 = 2$; upper right $I : 2$ and $I + 1 = 3$; bottom left $I = 3$ and $I + 1 = 4$; bottom right overlapping between $I = 3$ and $\sigma = 20$ and orthophoto.

	Type of UAV	Mini-UAV Hexa-copter
Optical Sensor	Camera	Sony alpha 6000
	Resolution	24 MP
	Focal length	16 mm
	Sensor width	24 mm
	dimensions height	16 mm
	Pixel dimension	4.3 m
	Weight	345 g

Table 4. Parameters and instrumentation features.

variation was 0.4 cm. In addition, 35 natural Ground Control Points (GCPs) have been collected for georeferencing and for scaling the final model. The GCPs have been measured with a Leica GNSS receiver in Real Time Kinematic (RTK), obtaining the 3D WGS84 coordinates with about a centimetre precision. The data elaboration has been carried out using Agisoft Photoscan. In order to assess the bundle adjustment results, Table 6 contains the global residual values of the bundle adjustment. Only 16 surveyed points are used as GCPs, while the other points are used as CPs. It is possible to see that the GCPs residual is smaller with respect to the CPs ones. This is due to the high redundant adjustments influence on GCPs coordinate values, which may induce an overestimation of the precision.

GCPs	Error (m)	Error (pix)
16	0.05	1.30
CPs	Error (m)	Error (pix)
19	0.09	1.42

Table 5. Final residuals of the bundle adjustment.

Also in this case the results of data processing are a metrically correct 3D model with a resolution of 2 cm, the orthophotos and finally the Digital Model of Elevations (DEM) with a resolution of 6 cm. In the particular case of application, dedicated to analyse of a sustainable urban redevelopment, different post-processing techniques were applied to obtaining vector informa-

tion related to the morphological characteristics (slopes and aspect). As shown in Figure 13, the very high original resolution does not allow to evaluate the general slope and aspect of the roofs, but returns information about the slope of tiles, chimney pots, eaves and so on.

2.2.2 Post-elaboration of photogrammetric output. A preliminary investigation was made for the choice of the optimal resolution, which does not create too much noise in the vector return phase and at the same time does not lose too much information on the analysed areas. The optimal resolution was chosen by creating slope maps at various resolutions (Figure 13) with 0.06 m, 0, 10 m, 0.20 m and 0.30 m sampling. Conversely, with resolutions too high 0.30 m, there is a loss of information mainly in the border areas of the buildings, which are obviously characterized by a steep slope (in the figure represented in red by the areas with a slope of 60-90 °). After the first step, the vector

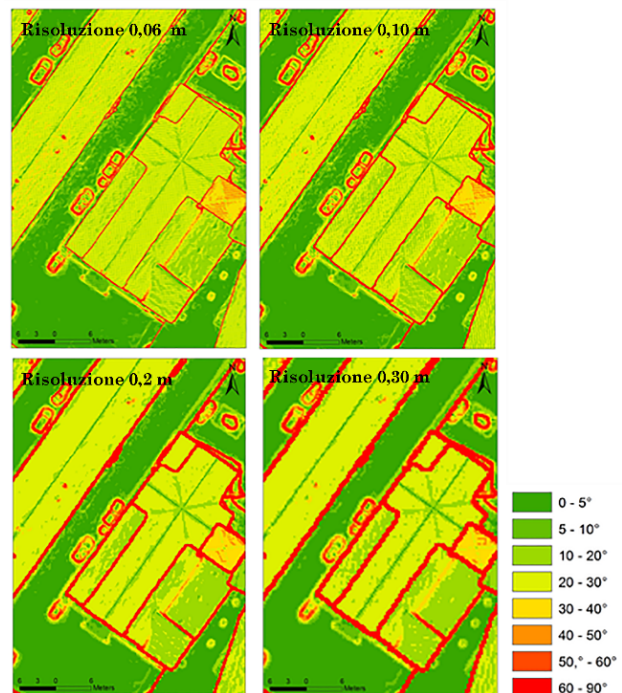


Figure 13. DEM resolution. Upper left: original resolution 0.06cm; upper right 0, 10cm; bottom left 0.20cm; bottom right 0.30.

morphological analysis was automated in GIS environment with ArcMap Model Builder (Figure 14). Once chosen the appropriate DEM resolution, the "Slope" and "Aspect" algorithms were applied (Burrough et al., 2015) to extract the morphological information. Then, the "Raster to Polygon" tool allowed the vector conversion grouping in polygons with similar slope the pixel values of the dataset, after a reclassification of the values into integers according as shown in Figure 14. The slope classes have been chosen as follows: class 1 has been generated with slope values of 0-5deg which can be considered with zero slope and class 8 groups the high slope considered high for the purpose of application. For the aspect maps, indeed, the classes have been imposed by the algorithm.

The obtained vectors are still very noisy due to the high segmentation of the polygons and for the presence of noise residues generated by trees and cars. To further filter the data, the "Eliminate"

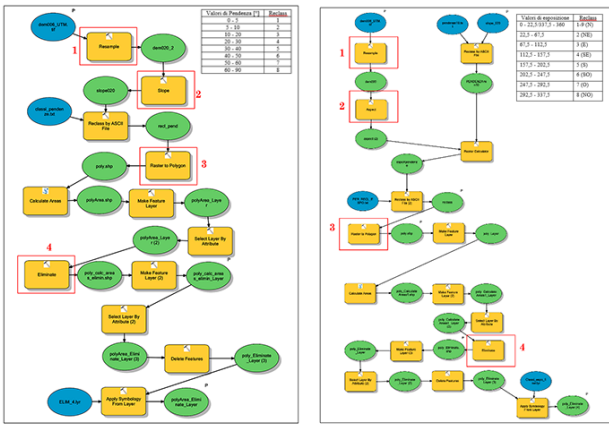


Figure 14. Slope (right) and aspect(left) flowchart.

algorithm in ArcToolbox was used providing more satisfactory results. The tool groups polygon fragments, imposing a threshold, with adjacent polygons that have a larger area. The selection was made for areas smaller than $5 m^2$. The other processes are ancillary for the vector conversion in GIS environment, as for example the area calculation operation, at the end of the polygonization process, is a necessary condition for the "Eliminate" tool. The final maps are shown in Figure



Figure 15. Slope (right) and aspect(left) maps.

The aspect map was compared with a map obtained with a manual vector map and the Table shows the difference between the areas calculated. The analysis was performed considering the relative error, expressed as percentage, between the calculated difference and the total area of the building.

3. CONCLUSION

The strong automation in the photogrammetry and the use of new acquisition platforms (UAV) allowed to the technique to come back to be considered a relevant technique of survey. The results obtained were analyzed, noting that the automation still makes it possible to obtain precise 3D model for the purposes of the survey and above all that the process outputs, even if characterized by a high information content, do not allow direct automatic extraction of descriptive information (features). Moreover, these data

Building	Area [m ²]	Aspect Area [m ²]	Delta [m ²]	Delta [%]
Building L West side	506.57	490.82	15.75	3.21
Building L North side	32.44	34.53	-2.09	-6.05
Building L Est side	449.58	451.09	-1.51	-0.33
Church 1	168.35	151.27	17.08	11.29
Church 2	239.84	222.93	16.91	7.59
Church 3	22.18	21.14	1.04	4.92
Church 4	36.12	34.5	1.62	4.70

Table 6. Comparison of polygons.

are characterized by a high memory occupation. For this reason we investigated procedures for the vector conversion of the high information content of photogrammetric data, characterized by a very high geometric and a low radiometric resolution. To achieve this goal, innovative algorithms of artificial intelligence have been tested that have allowed to improve the image filtering and procedures have been implemented automatically for the vector conversion of interesting features and parameters for conservation, restoration and sustainable restoration of cultural heritage and historical centres. The vector conversion allowed to obtain more usable data, facilitating its readability and simplifying the exchange with other analysis applications in different fields of application. Furthermore, the vector data allows to have lighter databases, in terms of memory occupancy, and to meet the needs of production of data less heavy in terms of VOLUME, one of the three properties of "BIG DATA" (Gandomi and Haider, 2015). The developed procedures were tested on two case studies, different for scale of restitution (cultural heritage and historical centre) and types of information to be returned, which confirmed its validity of application. In the first case, the use of innovative filters allowed to generate binary images with a net separation threshold, compared to the classic filters used to define edges. In the second case study, relating to the minor historical centres, the automatic restitution procedures were optimized for obtaining vector maps relating to slopes and exposures, useful for sustainable redevelopment. As regards future developments, the presence of a net threshold in the vectorization of particulars facilitates the subsequent phase. With the performed experiments, it has been noticed that the filter is influenced by the resolution of the initial image and therefore this variability must be analysed further. Although the vectorization has given interesting results in the morphological characterization of the building, useful for rapid cartographic updates and to directly have the characteristic data of the roofs, it is advisable to carry out further investigations in order to obtain the geometric characteristics with greater precision. Future application on 3D point clouds and other types of data (thermal, multispectral, etc.) will be experimented to increase the information obtainable.

ACKNOWLEDGEMENTS

I would like to thank the Semeion research centre for supporting this work.

REFERENCES

Agisoft Photoscan Manual, 2016.

- Aicardi, I., Chiabrando, F., Lingua, A. M., Noardo, F., Piras, M. and Vigna, B., 2016. A methodology for acquisition and processing of thermal data acquired by UAVs: a test about subfluvial springs investigations. *Geomatics, Natural Hazards and Risk* pp. 1–13.
- Baiocchi, V., Brigante, R., Dominici, D., Milone, M. V., Mormile, M. and Radicioni, F., 2014. Automatic three-dimensional features extraction: The case study of LAquila for collapse identification after April 06, 2009 earthquake. *European Journal of Remote Sensing* 47, pp. 413–435.
- Baiocchi, V., Dominici, D. and Mormile, M., 2013. UAV application in post-seismic environment. *Int. Arch. Photogramm. Remote Sens. Spatial Inf. Sci., XL-1 W 2*, pp. 21–25.
- Barazzetti, L., Forlani, G., Remondino, F., Roncella, R. and Scaioni, M., 2011. Experiences and achievements in automated image sequence orientation for close-range photogrammetric projects. pp. 80850F–80850F–13.
- Brito, J., 2000. OCCLUSION DETECTION IN DIGITAL IMAGES THROUGH BAYESIAN NETWORKS. *INTERNATIONAL ARCHIVES OF PHOTOGRAMMETRY AND REMOTE SENSING* 33(B3/1; PART 3), pp. 101–108.
- Burrough, P. A., McDonnell, R., McDonnell, R. A. and Lloyd, C. D., 2015. *Principles of geographical information systems*. Oxford University Press.
- Buscema, Paolo, M., 2006. *Sistemi ACM e Imaging Diagnostico*. Springer-Verlag, Milan.
- Cabuk, A., Deveci, A. and Ergincan, F., 2007. Improving heritage documentation. *GIM International*.
- Chiabrando, F., De Bernardi, M. and Roggero, M., 2010. Impiego di aerei ultraleggeri e camere di medio formato per la fotogrammetria aerea a grande scala. *BOLLETTINO DELLA SOCIETÀ ITALIANA DI FOTOGAMMETRIA E TOPOGRAFIA* 4, pp. 75–95.
- Chirici, G., Di Martino, P., Garf, V., Ottaviano, M., Tonti, D., Giongo Alves, M., Santopuoli, G. and Marchetti, M., 2009. Tecniche avanzate di cartografia degli ambienti forestali su base tipologica in Italia centrale. In: *Atti del Terzo Congresso Nazionale di Selvicoltura. Accademia Italiana di Scienze Forestali, Taormina*, pp. 989–994.
- Chou, T.-Y., Yeh, M.-L., Chen, Y. C. and Chen, Y. H., 2010. *Disaster monitoring and management by the unmanned aerial vehicle technology*. na.
- Dominici, D., Baiocchi, V., Zavino, A., Alicandro, M. and Elaiopoulos, M., 2012. MICRO UAV FOR POST SEISMIC HAZARDS SURVEYING IN OLD CITY CENTER OF L'AQUILA. Roma.
- Dominici, D., Massimi, V. and Alicandro, M., 2016. The role of geomatics for the cultural heritage. Giorgio Monti, Gianfranco Valente, Roma, pp. 173–188.
- Eisenbeis, H., 2009. *UAV photogrammetry*. ETH Zurich, Switzerland:.
- Forlani, G., Nardinocchi, C., Scaioni, M. and Zingaretti, P., 2003. Building reconstruction and visualization from lidar data. *International Archives Of Photogrammetry Remote Sensing And Spatial Information Sciences* 34(5/W12), pp. 151–156.
- Fraser, C. S., 1997. Digital camera self-calibration. *ISPRS Journal of Photogrammetry and Remote Sensing* 52(4), pp. 149–159.
- Furukawa, Y. and Ponce, J., 2010. Accurate, dense, and robust multiview stereopsis. *IEEE transactions on pattern analysis and machine intelligence* 32(8), pp. 1362–1376.
- Gandomi, A. and Haider, M., 2015. Beyond the hype: Big data concepts, methods, and analytics. *International Journal of Information Management* 35(2), pp. 137–144.
- Gomez, C. and Purdie, H., 2016. UAV-based Photogrammetry and Geocomputing for Hazards and Disaster Risk Monitoring A Review. *Geoenvironmental Disasters* 3(1), pp. 23.
- Granshaw, S. I. and Fraser, C. S., 2015. Editorial: Computer Vision and Photogrammetry: Interaction or Introspection? *Photogrammetric Record* pp. 3–7.
- Hartley, R. I. and Mundy, J. L., 1993. Relationship between photogrammetry and computer vision. In: *Optical engineering and photonics in aerospace sensing*, International Society for Optics and Photonics, pp. 92–105.
- Hirschmuller, H., 2008. Stereo processing by semiglobal matching and mutual information. *IEEE Transactions on pattern analysis and machine intelligence* 30(2), pp. 328–341.
- Honkavaara, E., Saari, H., Kaivosoja, J., Pnen, I., Hakala, T., Litkey, P., Mkyne, J. and Pesonen, L., 2013. Processing and assessment of spectrometric, stereoscopic imagery collected using a lightweight UAV spectral camera for precision agriculture. *Remote Sensing* 5(10), pp. 5006–5039.
- Hhle, J., 2008. Photogrammetric Measurements in Oblique Aerial Images. *Photogrammetrie, Fernerkundung, Geoinformation : Organ der Deutschen Gesellschaft fuer Photogrammetrie und Fernerkundung e.V., PHOTOGRAMMETRIE, FERNERKUNDUNG, GEOINFOR* (1), pp. 7–14.
- Kraus, K., 1994. *Fotogrammetria Vol.1*. Vol. 1, Libreria universitaria Levrotto & Bella, Torino.
- Maini, R. and Aggarwal, H., 2009. Study and comparison of various image edge detection techniques. *International journal of image processing (IJIP)* 3(1), pp. 1–11.
- Matta, S., 2014. Review: Various image segmentation techniques. *Swati Matta(IJCSIT) International Journal of Computer Science and Information Technologies* 5(6), pp. 7536–7539.
- Nex, F. and Remondino, F., 2014. UAV for 3d mapping applications: a review. *Applied Geomatics* 6(1), pp. 1–15.
- Pastore, V., Sole, A. and Telesca, V., 2010. Classificazione object-oriented e tecniche di segmentazione per la derivazione di cartografia di uso/copertura del suolo multiscala.
- Pierrot-Deseilligny, M. and Paparoditis, N., 2006. A multiresolution and optimization-based image matching approach: An application to surface reconstruction from SPOT5-HRS stereo imagery. *Archives of Photogrammetry, Remote Sensing and Spatial Information Sciences*.
- Piras, M., Taddia, G., Forno, M. G., Gattiglio, M., Aicardi, I., Dabove, P., Russo, S. L. and Lingua, A., 2016. Detailed geological mapping in mountain areas using an unmanned aerial vehicle: application to the Rodoretto Valley, NW Italian Alps. *Geomatics, Natural Hazards and Risk* pp. 1–13.
- Puri, A., Valavanis, K. P. and Kontitsis, M., 2007. Statistical profile generation for traffic monitoring using real-time UAV based video data. In: *Control & Automation, 2007. MED'07. Mediterranean Conference on*, IEEE, pp. 1–6.
- Remondino, F. and Fraser, C., 2006. Digital camera calibration methods: considerations and comparisons. Vol. Vol. XXXVI.

Remondino, F., Spera, M. G., Nocerino, E., Menna, F. and Nex, F., 2014. State of the art in high density image matching. *The Photogrammetric Record* 29(146), pp. 144–166.

Roushdy, M., 2006. Comparative study of edge detection algorithms applying on the grayscale noisy image using morphological filter. *GVIP journal* 6(4), pp. 17–23.

Rupnik, E., Nex, F. and Remondino, F., 2014. Oblique multi-camera systems-orientation and dense matching issues. *The International Archives of Photogrammetry, Remote Sensing and Spatial Information Sciences* 40(3), pp. 107.

Schiewe, J., 2002. Segmentation of high-resolution remotely sensed data-concepts, applications and problems. *International Archives of Photogrammetry Remote Sensing And Spatial Information Sciences* 34(4), pp. 380–385.

Shrivakshan, G. T., Chandrasekar, C. and others, 2012. A comparison of various edge detection techniques used in image processing. *IJCSI International Journal of Computer Science Issues* 9(5), pp. 272–276.

Szeliski, R., 2010. *Computer vision: algorithms and applications*. Springer Science & Business Media.

Triggs, B., McLauchlan, P. F., Hartley, R. I. and Fitzgibbon, A. W., 1999. Bundle adjustment modern synthesis. In: *International workshop on vision algorithms*, Springer, pp. 298–372.

Vasuki, Y., Holden, E.-J., Kovesi, P. and Micklethwaite, S., 2014. Semi-automatic mapping of geological structures using uav-based photogrammetric data: An image analysis approach. *Computers & Geosciences* 69, pp. 22–32.

Westoby, M. J., Brasington, J., Glasser, N. F., Hambrey, M. J. and Reynolds, J. M., 2012. Structure-from-Motionphotogrammetry: A low-cost, effective tool for geoscience applications. *Geomorphology* 179, pp. 300–314.

UAVS FOR SPATIAL DATA ACQUISITION: SENSORS EVALUATION, FLIGHT DESIGN AND PLANNING, MULTI-TEMPORAL SOLUTIONS

I. Aicardi ^{1*}

¹ Department of Environmental, Land and Infrastructure Engineering, Politecnico di Torino, Corso Duca degli Abruzzi 24, 10129 Torino, Italy, (irene.aicardi, andrea.lingua)@polito.it

KEY WORDS: Photogrammetry, UAVs, sensors, automation, multi-temporal

ABSTRACT:

During past years, UAVs (Unmanned Aerial Vehicles) have become very popular and, for this reason, my research activities were concentrated on the use of these systems as geomatic tools for measurements taken in monitoring and change-detection scenarios. The interest in these aerial platforms is due to their capability of performing aerial surveys in an easy and flexible way using low-cost sensors. Three fundamental topics related to the use of UAVs were investigated: the evaluation of navigation sensors, the photogrammetric flight design and planning and the an automatic procedure for the usage of multi-temporal data. All the addressed issues used applications based on different geomatics techniques related to photogrammetry, positioning, navigation and topography. The first part was devoted to the analyses of on-board and external installable sensors to evaluate their accuracy. The navigation platform of a UAV was analysed to investigate the reliability of the internal GNSS (Global Navigation Satellite System) receiver and the IMU (Inertial Measurement Unit) platform. Then, external sensors were analysed to assess if it is possible to improve positioning and attitude information. The second part of the thesis was related to the investigation of the flight planning for photogrammetric purposes. Different features of the flight (such as overlaps, cross and border strips) were evaluated by analysing the final block orientation in relation to different parameter configurations. This was undertaken following a simulation approach and the results were evaluated through real case studies. Finally, the last part was related to the development of an automatic technique to co-register multi-temporal high-resolution image blocks from UAVs without the introduction of GCPs. The proposed strategy was instead based on the use of a reference epoch (considered fixed) and the registration of the others according to it.

1. INTRODUCTION

UAVs are now well-established platforms for aerial activities. Despite the fact that these systems were developed for military purposes, the availability of low-cost sensors and platforms has laid the foundation for an increasing interest also in the civil field, especially for environmental and cultural heritage scenarios.

In the civil field (ENAC, 2015; NASA, 2015), the most investigated categories are mini and micro UAVs (payload <30 Kg) both fixed wings and multi-rotors for their ease of use, low-cost and transportability to perform surveys in different areas. On the other hand, their small size requires specifically designed sensors that have to be both reliable and lightweight enough to respect the limits of the payload.

The UAVs competence to carry out flights without a pilot on-board, their adaptability to different kind of missions and the opportunity to design platforms with changeable sizes, weights and costs demonstrate the great potential for the development of unmanned platforms for monitoring applications at different scales (Aicardi et al., 2016b; Aicardi et al., 2016d; Masini et al., 2015; Ramsey et al., 2014). The ability to perform automatic flights with a relative low-cost technology has generated interest among the photogrammetric community; many studies and tests have been carried out in the photogrammetric field.

However, specific guidelines for performing flights and for the collection and processing of the data for metrical purposes have not been well established and there is still the need to assess the real achievable accuracy (in terms of flight navigation and final products). This is due to the fact that the end user's interest is

more focused on the use of these platforms and many of them do not spend time investigating the on-board sensors. Also, for the use of external devices, most users do not investigate their performance but prefer off-the-shelf solutions whose specifications are declared by the manufacturer.

With regards to flight planning, also in this case most of the operators consider predefined rules without investigating a lot the parameters that can improve the final results (also because some of the users are not photogrammetry experts). This is also because the major part of the available photogrammetric and Computer Vision software packages propose predefined workflows in which the user cannot easily interact. This trend is also due to the need for automation both in the survey and in the processing (Behling et al., 2014; El-Omari, 2011; Frueh et al, 2004; Matikainen et al., 2004; Wong, 2007). More automatic strategies for the flight and an autonomous processing workflow are requested by the user to save time and energy otherwise spent on the control of each single step since, in most cases, what matters is the final result.

Considering UAVs platforms, a lot of civil applications require a good reliability of the acquired data and also the needed accuracy is increasing thanks to the advantages offered by new hardware components and software solutions.

In this regards, the development of integrated photogrammetric Computer Vision approaches allows us to process an aerial photogrammetric block of images, but their theoretical basis and their requirements need to be investigated in order to reach the expected result.

The aim of the research was to provide and improve the use of low-altitude low-cost civil UAVs as measurement instruments

* Corresponding author

through geomatics techniques, investigating in depth some fundamental aspects that have not been adequately addressed so far. For this reason, the thesis covered the following:

- the analyses of on-board and external sensors to evaluate their performance and their behaviour during the flights since this aspect is often forgotten or underestimated;
- the investigation of the impact of flight planning features for the photogrammetric orientation of a block of images since it is on the flight design that the final results of photogrammetric triangulation depend;
- finally, the proposal of a procedure for the registration of different photogrammetric blocks, that is a strategy to perform low-cost analyses.

The main idea is to analyse all the steps ranging from knowledge of the aerial platform to the acquisition of the data and their correct use since a complete knowledge of the whole process can help to better manage and take control of these aerial systems. Since a lot of people are using UAVs for different applications, the aim is to improve the understanding of the influence of different variables and to identify the most significant to be taken into account during the flights to better and more consciously use these systems.

2. NAVIGATION SENSORS ANALYSES

According to the UAV definition, it is fundamental to consider and analyse all the components that constitute the system both from an aerial (the UAV system) and a terrestrial (pilot, ground control station, etc.) perspective. The main feature of the unmanned systems is their capability to fly without a pilot on board; thus, their principal component is the navigational one that comprises positioning sensors and control systems. In relation to the specific application in which the UAVs are involved, it is fundamental to study the behaviour of these on-board sensors in order to correctly choose the most suitable platform. The aim of this part was to analyse the UAV components of the systems employed in the research to study their features and behaviour.

The main components of a UAV can be divided in three main categories: the aerial platform, which includes the airframe, the navigation system, the power system and the payload; the ground control station, which allows the human control from a remote emplacement; and the communication system, which supports the communication between the other two components. It is important to deeply analyse the performances of the navigation sensors in order to control the system precision and properly managed the missions. For this reason, different tests have been made in order to analyse the sensors (on-board and external) and to calibrate the entire system to reach a stable and reliable solution.

My attention was focused on multi-rotors systems since they can be more easily investigated and customized external sensors can also be installed on-board if needed. A methodology to test these sensors was presented. In particular, it is based on a reference data extracted from topographic measurements from total stations to validate the precision of the navigation sensors of investigated UAVs. Two different solutions, mainly based on the same kind of approach, were proposed:

- one for the positioning sensors validation (based on the use of a single prism and a total station);
- one for the angles estimation (based on the use of two prisms and two total stations).

Methodology for positioning sensors: As regards the positioning system, a retro-reflector composed by three small prisms was housed on-board. In this way, the UAV can be automatically tracked along the flight paths by a motorized total station (Figure 1) that can autonomously measure both distance and angles with accuracies of 2 mm and 1 sec, respectively, within an operative range of 1 Km.



Figure 1. The retro-reflector on-board and the track with the Total Station.

After the synchronization, to have comparable sets of data, the track extracted from the (on-board and external) positioning sensor can be compared with that one obtained from the data of the total station, consider as reference. The difference between the two set of data is used to evaluate the reliability of the positioning system considering the accuracy of the proposed methodology based on total station measurements and the differences between the two set of data.

Methodology for angles sensors: The data validation was performed as a comparison between the on-board sensors data and a reference solution acquired from the ground. The proposed strategy involves the use of two total stations on the field and two prisms mounted on the UAV. For this reason, a bar with two prisms was installed on board (Figure 2), it was a homemade solution that consists of the combination of three smaller prisms.



Figure 2. The UAV with the bar and the focus on the two prisms.

Before the flights, the new system was calibrated in the Topographic laboratory of the Politecnico di Torino and to track the flights, two total stations were used in the position tracking mode. One of the used instruments can be also synchronized with the GPS-Time by using an external receiver that can be placed on the instrument and update the total station time according to the GPS. Finally, the same sampling rate of 0.2 s was used for the two instruments.

During the flights, each total station can follow one prism because of the track mode of the instrument, and it is than possible to relate the two measurements.

2.1 On-board sensors evaluation

GNSS: In order to know the performance of the internal GNSS receiver, a reference data is required. For this reason, the methodology for positioning sensors previously described was

adopted. The two acquired tracks (internal receiver and total station) were compared adopting a local reference system. Table 1 shows the comparison results.

Table 1. Internal GPS accuracy evaluation.

Direction	Min value	Max value	Mean value	Std
	m	m	m	m
Horizontal	-3.310	5.340	0.414	0.875
Vertical	-15.342	19.332	1.66	2.175

The results demonstrate that the performance of the internal receiver is consistent with a low-cost single frequency GPS receiver in standalone positioning using EGNOS correction (Bulusu et al., 2000) (accuracy of few meters with the vertical component four times worse than the horizontal one).

IMU: Then the UAV attitude during the flight and the reliability of the data recorded from the internal sensors were evaluated by taking particular attention to the compass component. This is important to assess whether it is necessary to install an external IMU to have a precise compass component. In order to test the recorded attitude of the UAV, various flights were performed considering the proposed methodology; in particular, linear and cross planning were considered.

The result (Table 2) of the linear flight shows that, using the ArduCopter system, the angles can be estimated with precisions less than 1 gon, which is acceptable for our investigations. In the second case, the estimated angles are very close to the one observed with the TS, and we can affirm that the procedure is reliable.

Table 2. Statistics about the angles estimation.

Flight	Mean value	Std	Median value
Linear	- 0.547°	±0.867°	- 0.650°
Cross	- 0.022°	±0.910°	- 0.073°

2.2 Evaluation of external sensors

For the major part of the geomatic applications (photogrammetry, thermal analyses, radio-frequency measurements, etc.), centimetric positioning is required. For this reason, the introduction of an external GNSS receiver on board on the UAV was investigated. The use of an external IMU was also evaluated to assess if it is possible to improve accelerometers, magnetometers and gyroscopes data to enhance positioning and attitude information.

GNSS: In order to know the UAV position along the flights in an accurate manner, an external GNSS geodetic receiver was mounted on board. In particular, a Novatel OEM 615 GNSS card (Figure 3) was connected to an active antenna, which was installed on the cover of the UAV. The selected antenna model is an ANTCOM ID L1L2 1215 A2, which is able to receive GPS, GLONASS and Galileo constellation and the receiver is a dual-frequency (L1 = 1575.42 MHz and L2 = 1227.60 MHz) and multi-constellation (GPS and GLONASS) model.

The storage of the raw data has been realized by making a direct connection between the GNSS OEM and a dedicated ArduLog data logger. The GNSS raw data (pseudo-range and carrier phase), were recorded in a text file using an ASCII format.

The receiver can be programmed to acquire different sample rates of the data, and we set up two different cards, one at 1 Hz and the other one at 5 Hz.

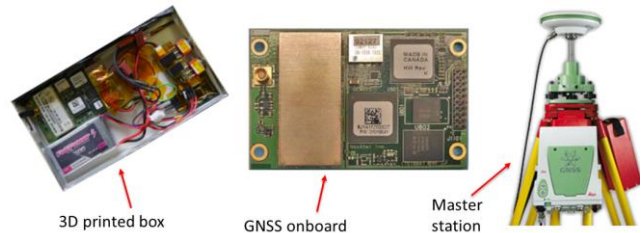


Figure 3. The OEM GNSS receiver and the master reference GNSS station.

The data recorded by the external receiver are processed with a PPK (Post Processed Kinematic) approach (Stempfhuber et al, 2011; Gao et al., 2004) to define the UAV positions respect to a master station on the ground. The relative kinematic positioning can be realized in relation to the master station, since a geodetic GNSS receiver was installed over a ground vertex with known coordinates and the positions for each epoch of the receiver on the UAV as the moving rover were determined.

Three different feature were evaluated: positioning accuracy, constellation configuration and kinematic data processing strategies. Table 3 and Table 4 show the obtained results for the firsts two tests.

Table 3. Evaluation of the positioning results of the external GNSS receiver.

Direction	Min value	Max value	Mean value	Std
	m	m	m	m
Horizontal	-0.124	0.130	0.010	0.040
Vertical	-0.182	0.213	0.032	0.092

Table 4. Mean precision of different GNSS solutions related to satellite constellations.

GPS	GLONASS	Std _x mean	Std _y mean	Std _z mean
		m	m	m
8	0	0.18	0.13	0.42
10	11	0.016	0.017	0.031

Tests demonstrate good performances of the external GNSS receiver.

The usage of the GLONASS constellation have a strong influence in the final solution. In fact, looking at the table, it is possible to observe that without the GLONASS data the estimated precision is about 40 cm, while it can be improved to 1-3 cm adopting that constellation.

So, the employed receiver can be used for high precision UAV tracking, and the strategies adopted for the acquisition and processing steps have been adequately fixed to reach the best results.

To process the kinematic data recorded from the OEM card, the RTKLib software (Wisniewski et al., 2013) was adopted. Tests showed that it is possible to reach the best results using a Kinematic-Continuous approach in order to continuously re-estimate the ambiguity, which avoids to have false ambiguity estimated values.

IMU: Some experiments have been conducted to evaluate if it is possible and useful to house an external IMU platform on-board on the UAV to have more precise angles.

We made some analyses using the low-cost sensor of Microstrain, the 3DM-GX3-35 model because of its low weight and size.

To evaluate the platform, tests were performed with the UAV with the engines off and placed on the table and also during a flight.

During the flight test, the recorded data in the three directions shows a significant noise for all the IMU components. The sensor betrays the UAV vibrations due to flight movement, and the magnetic component can have large interferences from the engines operation.

A further test was done trying to filter out this noise. In particular, through the Matlab Wavelet Analyzer, the signal were filtered with the Daubechies 3 Level 7.

However, after the filter it has remained a clear difference between the signal acquired in static and that recorded in dynamic. The noise can be reduced, but a lot of dispersion still remain.

Since next photogrammetric investigations show that precise attitude information is not really necessary for photogrammetric triangulations, this device was not installed on-board during our operative surveys.

2.3 Real case evaluation

The evaluated GNSS external receiver has been deeply investigated to evaluate the benefit of its use in the evaluation of the pattern of installed antennas for radio-astronomy purposes. This section shows the benefit in the precisely locating the position of the employed system in comparison to the use of the available on-board sensors for antenna pattern measurements.

To characterize the pattern of these installed antennas, the UAV has been equipped with a continuous-wave radio-frequency (RF) transmitter in order to operate as a far field test source to characterize and instrumentally calibrate the Antenna Under Test (AUT) (single elements or small subarrays) in their real environment, i.e. either on soil ground or with a metal ground plane, and a dipole antenna (Figure 4).

The ArduCopter was used, and it was equipped with the external GNSS receiver.



Figure 4. ArduCopter configuration for the SKA project.

The transmitter is a customized frequency synthesizer based on the Analog Devices PLL with integrated VCO ADF4351 and a frequency divider. The output frequency can be set in the range from 4.3125 MHz to 4400 MHz. Additionally, the output power is programmable from 0 dBm to 8 dBm in four steps. The transmitter is battery powered and completely shielded in a custom metal box with output RF connector.

The presence of an RF transmitter on-board causes interferences to the GNSS system. This problem has been studied and solved with additional hardware items (attenuators, filters). It is important to consider the interference possibility at each new test and when the transmitter and antennas sources change.

A dipole antenna is connected to the transmitter output. The antenna includes the balun, which employs the Mini Circuits RF transformer ADTL1-12 enclosed in a metal case. The dipole

is connected to the balanced port, and it can be easily replaced with others having different lengths in order to achieve impedance matching and a proper radiation pattern at the various operative frequencies.

The field radiated by the UAV is received by the AUT during the flight. The output power at the AUT port is measured through a spectrum analyser (e.g. Agilent E4402B), which is triggered by the Pulse Per Second (PPS) signal from a GPS receiver ublox EVK 6T (Dabove, 2014). A computer acquires both the trace of the analyser and the message from the GPS receiver (Hoffmann-Wellenhof, 2000 - 2008). Thus, a common time reference is used for all the data that are required for the post processing, i.e. the received power, the position of the UAV and its orientation (Virone et al., 2014). From these data, the AUT pattern is extracted.

The measurement survey has been performed in a dedicated airfield in Tetti Neirotti (TO) on a single polarized log periodic reference antenna PMM LP-02 to validate the whole system (see Virone et al., 2014). The antenna was a wideband radiator made up of many dipoles electrically connected to the feed line. Each element resonates at different frequencies within the overall antenna bandwidth (200 MHz-2.7GHz).

According to the Friis formula (Virone et al., 2014), the AUT pattern is extracted from the measured RF power (given by the spectrum analyser) by removing the contributions of the path loss, the constant gains and attenuations (e.g. cables and amplifiers), and the simulated contribution of the test source gain.

In addition, both the real UAV path and its orientation may be slightly different from the programmed ones, i.e. the UAV does not follow the required rectilinear path along North-South or East-West (y and x-axis, respectively, in the AUT-centred reference system). However, this fact is kept into account in the pattern extraction procedure, since the above mentioned contributions are computed according to both the real UAV position (DifferentialGNSS data) and orientation (IMU data).

The error of the position measured with the internal GPS receiver is considerably higher than the error produced by the DGNSS. Figure 5 shows the trajectories in the two cases (GPS and DGNSS) for this particular experiment: mean discrepancy is around 1 m for the horizontal component (Figure 5 left) and 3 m for the vertical component, with 5 m peak (Figure 5 right).

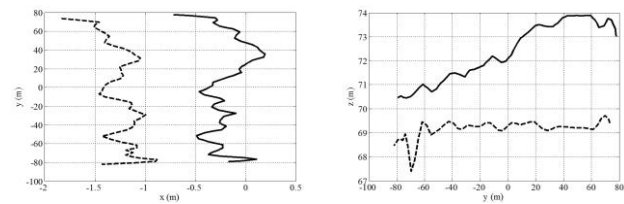


Figure 5. Trajectories of the UAV measured with on-board GPS (solid lines) and differential GNSS (dashed lines). (left) Top view (horizontal plane); (right) UAV height as a function of the y coordinate (North-South position).

There are two main consequences. Firstly, the two trajectories lead to different values of distance between AUT and UAV. Thus, the spatial attenuation of the radiated signal (path loss) is different in the two cases, as shown in Figure 6 left.

The average discrepancy is 0.5 dB with 1 dB peaks. In addition, the test-source gain has different values in the two cases. In fact, its value depends on the relative position of the AUT with respect to the UAV. Also, in this case, as shown in Figure 6 right, the average discrepancy is around 0.5 dB with 1 dB peaks.

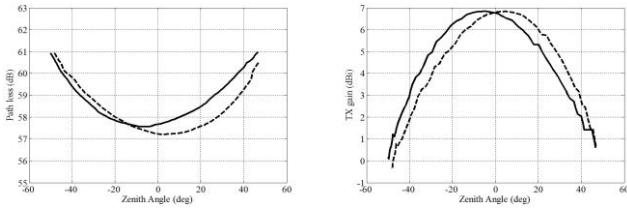


Figure 6. Path loss (left) and test-source gain (right) as a function of the zenith angle. Measured with on-board GPS (solid line) and differential GNSS (dashed lines).

Owing to the above mentioned errors, the resulting AUT patterns are much different. Figure 7 left shows the AUT pattern extracted using the position data provided by the UAV navigation board (GPS), whereas Figure 7 right shows the AUT pattern computed using the position data of the DGNSS receiver. Both the curves are compared to the simulated AUT pattern. Figure 7 left (GPS) shows a significant discrepancy between measurement and simulation, generally 1.5 dB, which also produces an evident distortion of the pattern. Such a discrepancy is consistent with the combined effect of the two errors introduced on the path loss and the test-source gain. In contrast, Figure 7 right (DGNSS) shows a better agreement. The discrepancy is generally within 0.3 dB, which demonstrates the higher position accuracy of the differential GNSS. This residual discrepancy can be mainly explained by uncertainties in a) the electromagnetic model of both AUT and test-source, b) the measured UAV orientation during the flight (IMU), and c) the AUT positioning on the measurement field.

For more sensible pattern measurements, as for the cross-polar components, whose amplitude levels are up to -30 dB lower than the co-polar component, the lower accuracy of the native UAV navigation board would be definitively unacceptable.

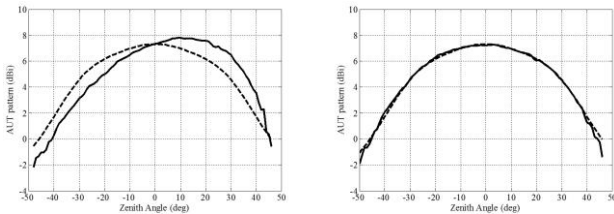


Figure 7. AUT pattern extracted using the position data of (left) the UAV navigation board (GPS), (right) the DGNSS unit. In both sub-plots: measurement (solid), simulation (dashed line).

The implemented system demonstrated good performances for characterizing Very High Frequency antennas and arrays. The cost effectiveness and the transportability are the main advantages of this system.

3. UAV FLIGHT PLAN SIMULATIONS

The aim of this part of the research is to evaluate the flight planning on the UAVs and to analyse the final block orientation according to different flight configurations.

Different features that can modify the flight will be investigated alone or in conjunction with other parameters.

This investigation is important to define some operative procedures that can be used in the production of photogrammetric 3D models both by expert users and also small photogrammetric companies that may have a schema of how to change certain parameters to reach the required result.

3.1 Proposed methodology

The evaluation of the flight parameters was investigated through a code implemented in Matlab. The simulation allows to better analyse the behaviour of the parameters without the interference of other external factors.

The idea is to use the collinearity equations to estimate the TPs (Tie Points) ground position and the precision with which they can be defined. The workflow of the code is shown in Figure 8.

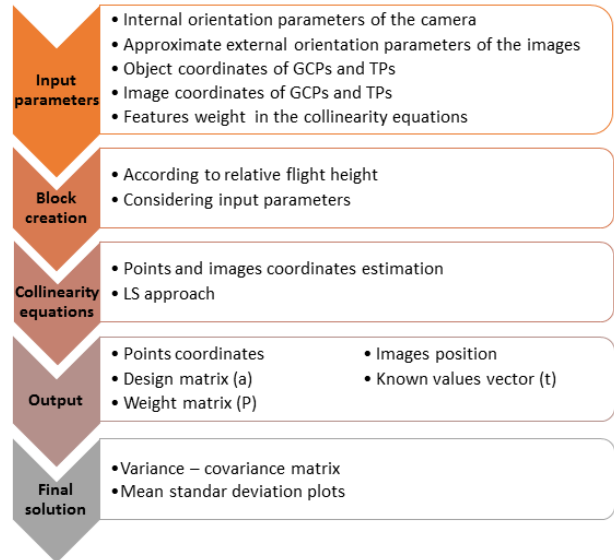


Figure 8. Simulation code workflow.

For the analyses of the influence of different flight plans, a synthetic model was created.

The features of the block are the following:

- it is a rectangle of dimensions 250 x 120 m;
- it is a not-flat area with points at altitudes up to 30 m;
- the relative altitude of the flight was considered at a height of 60 m from the ground and this parameter was taken into account for the image footprint estimations and the block configuration;
- fifteen well distributed GCPs were introduced considering a wheelbase of 5·B in the x-direction and 4·B in the y-direction (where B is the acquisition base between two consecutive images);
- one thousand TPs were used to perform the image matching. As explained below, their number is due to computational restrictions. These points are randomly distributed along the area in 3D coordinates to simulate a non-flat area;
- the interior parameters of the camera were introduced as known and fixed. This strategy was used in order to not introduce other variables into the simulation since the aim was to evaluate the results obtainable through different block configurations.

3.2 Results

The reference solution is composed of the parameters commonly available in literature with well distributed GCPs, with only nadir images in a one direction flight with 80% and 60% forward and side overlap, respectively. The solution employed constituted 1000 TPs, mainly due to computational issues, and they were well distributed in the three directions.

Different tests have been performed to analyse the behaviour of the block according to the changes in certain parameters in the flight plan. In particular, the following features have been investigated:

1. border strips;
 2. cross strips;
 3. oblique images;
 4. different overlaps between images;
 5. different precisions of the projection centre;
- changing each time also the GCPs distribution and analysing the interference between different parameters (Figure 9).

Case	Strips long. overlap	Strips side overlap	Direction	Images	n. GCP	n. TIE	n. img	Images position precision	Images attitude precision		
0a	80%	60%	single	only nadir	15	1000	126	2 m	10 gon	Reference	
0b	80%	60%	single	only nadir	15	2000	126	2 m	10 gon		
0c	80%	60%	single	only nadir	15	3000	126	2 m	10 gon		
1	80%	60%	with borders	only nadir	15	1000	144	2 m	10 gon	Border strips	
1a	80%	60%	with borders	only nadir	4 at edges	1000	144	2 m	10 gon		
2	80%	60%	cross	only nadir	15	1000	252	2 m	10 gon	Cross strips	
2a	80%	60%	cross	only nadir	4 at edges	1000	252	2 m	10 gon		
3	80%	60%	single	only oblique	15	1000	252	2 m	10 gon	Oblique images	
3a	80%	60%	single	nadir-oblique	15	1000	378	2 m	10 gon		
3b	80%	60%	single	nadir-oblique	4 at edges	1000	378	2 m	10 gon		
3c	80%	60%	single	nadir-oblique	0	1000	378	4 cm	0.1 gon		
3d	80%	60%	single	nadir-oblique	0	1000	378	4 cm	10 gon		
3e	80%	60%	single	cross-oblique	4 at edges	1000	504	2 m	10 gon		
3f	80%	60%	single	cross-oblique	0	1000	504	4 cm	0.1 gon		
3g	80%	60%	single	cross-oblique	0	1000	504	4 cm	10 gon		
4	90%	60%	single	only nadir	15	1000	252	2 m	10 gon		Overlaps
4a	90%	40%	single	only nadir	15	1000	180	2 m	10 gon		
4b	90%	20%	single	only nadir	15	1000	144	2 m	10 gon		
4c	80%	40%	single	only nadir	15	1000	90	2 m	10 gon		
4d	80%	20%	single	only nadir	15	1000	72	2 m	10 gon		
4e	70%	60%	single	only nadir	15	1000	98	2 m	10 gon		
4f	70%	40%	single	only nadir	15	1000	70	2 m	10 gon		
4g	70%	20%	single	only nadir	15	1000	56	2 m	10 gon		
4h	60%	60%	single	only nadir	15	1000	70	2 m	10 gon		
4i	60%	40%	single	only nadir	15	1000	50	2 m	10 gon		
4l	60%	20%	single	only nadir	15	1000	40	2 m	10 gon		
4m	60%	20%	cross	only nadir	15	1000	80	2 m	10 gon		
4n	60%	20%	cross	only nadir	4 at edges	1000	80	2 m	10 gon		
5	80%	60%	single	only nadir	15	1000	126	50 cm	1 gon	Projection centres	
5a	80%	60%	single	only nadir	0	1000	126	4 cm	0.1 gon		
5b	80%	60%	cross	only nadir	0	1000	252	4 cm	0.1 gon		
5c	80%	60%	single	only nadir	0	1000	126	4 cm	10 gon		
5d	80%	60%	cross	only nadir	0	1000	252	4 cm	10 gon		

Figure 9. Performed tests.

All the tests have been performed 500 times, changing each time the TP distribution to simulate an approach which is statistically robust. The presented results represent the mean obtained values.

The performed tests highlight different behaviour in relation to the use of different features in the flight planning. A graphical representation of the performed tests and the Z-component standard deviation is schematically reported in Figure 10.

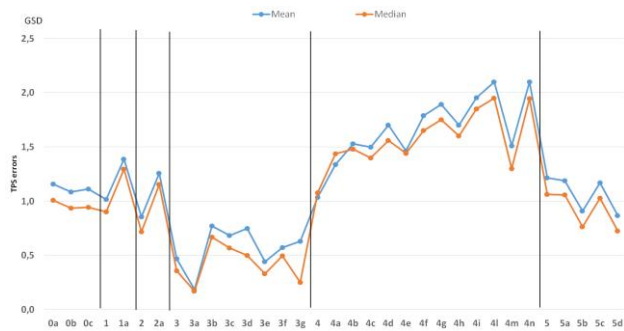


Figure 10. Mean and median standard deviations for the TPs Z component in all the simulated

To briefly summarize the obtained tests, it is possible to state that:

- the reference case study with different TP numbers leads to the concept that 1000-3000 TPs can lead to same results;
- the use of cross strips leads to a more constrained block and if less GCPs are used, the result is comparable to that obtained with the reference case, while border strips are not so convenient because they can constrain less the block;
- as expected, oblique images are a key solution, especially if vertical variations (urban or mountain areas) are present. Also in this case, the concomitant use of cross strips and oblique images leads to very good results also with only 4 GCPs at the edges;

- the investigations about the forward and side overlaps highlighted that less coverage can be applied (60% - 20%) if cross strips are introduced. However, the result is comparable to the reference one, both from a precision and an acquisition time point of view;

- as expected, the availability of a precise positioning system on-board lets us remove the GCPs, especially if cross strips are used. On the other hand, it was demonstrated that precise attitude information does not much influence the block orientation if a BBA was performed. For this reason, a precise GNSS receiver is enough (this strategy allows us also to save payload weight).

Furthermore, Figure 11 below shows the required time for each simulated test for the most significant steps of the survey and photogrammetric image orientation.

This simple graph can be useful in comparison to the previous one since it allows us to relate the benefit of an approach to the survey/processing time.

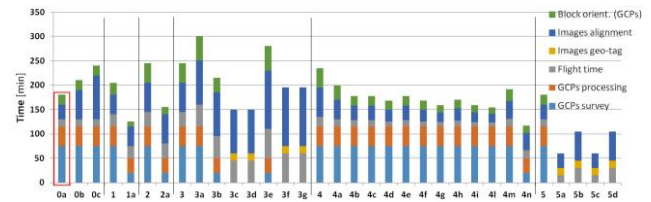


Figure 11. Time comparison for different steps of the survey and processing. The graph highlights each single step and the required time for each simulated case. The red rectangle indicates the reference case.

As expected, cross and oblique flights require more time, generally due to image acquisition and processing, but this is acceptable since they show an improvement in the final orientation of the block. Different overlaps require more or less the same time as the reference case, and also the figure 5.25 shows that the commonly used configuration (80% - 60%) is the best one. Obviously, the more significant gain in terms of time is given by the GNSS-assisted solution where the GCPs survey and processing are not required. This strategy remains desirable since it allows us to reduce the time and to obtain final results close to the reference case. For this reason, future work needs to be concentrated on the study of an RTK- solution and in the improvement in the navigational sensors.

3.3 Methodology validation

To validate the obtained results it is important to test the strategies in real cases. For this reason, a real case study will be presented to support the investigated parameters. In particular, more significant features will be investigated.

The case study was an aerial architectural acquisition of the Rocca San Silvestro. Flight data are summarized in Table 5.

Table 5. Rocca San Silvestro flight data.

Flight	H	Forward overlap	Side overlap	N. linear strips
Nadir	m	%	%	7
Nadir perpendicular	60	80	60	12
Oblique 45°	60	80	60	11
Oblique 135°	60	80	60	11

The image processing was performed through the Pix4D software. In particular, the following variations were conducted (inside the brackets the references of the previously analysed simulations are shown):

1. the two nadir blocks were processed separately (0a);
2. they were then merged together into a single project (single BBA) to consider a cross strips configuration (2);
3. the two oblique blocks were processed separately (3);
4. they were then merged together in a single project (single BBA) to form one single block (3);
5. cross and both oblique blocks were merged together to analyse the benefit of their simultaneous use (3e).

The RMSE results for the performed test are summarized in Figure 12.

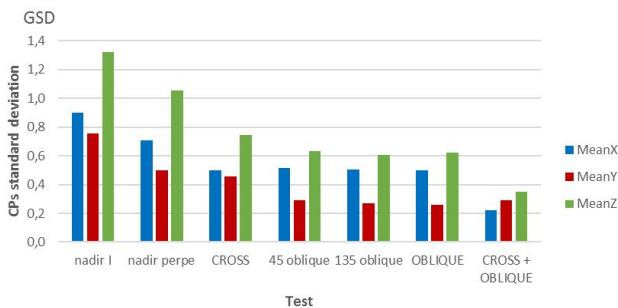


Figure 12. CPs mean RMSEs for the Rocca San Silvestro case study.

The figure shows that:

1. the use of a cross flight for nadir acquisitions can better constrain the final block orientation. In fact, an improvement can be appreciated, especially in the vertical component. This result is in agreement with the simulation test;
2. oblique images acquired in two different directions provide the same final result and it is better than the cross solution. Even if the two flights are processed together, the final orientation error is the same. This is probably due to the fact that the blocks are over the same area, but they acquire different parts of the scene. For this reason, the multiplicity of the points does not increase as in the case of crossed nadir strips and the final solution is the same as that achieved considering one single block;
3. the simultaneous use of both the nadir and both of the oblique flights (4 blocks) lead to a very constrained block in which also the vertical component had errors of less than half the GSD. In this case, using both nadir and oblique data, the multiplicity of points increases and this allows us to better constrain the orientation. This result is in agreement with the simulation test.

The performed tests confirm the behaviour analysed through the simulations and also the values of the validation solution agree with those obtained experimentally.

4. CO-REGISTRATION OF UAV MULTI-TEMPORAL DATASETS

In order to detect temporal changes in object space, the information (images) acquired over time need to be geometrically aligned. Different fields, like archaeology, disaster management and construction, require monitoring investigations and change detection analyses to observe, as soon as possible, the differences in time. Nowadays, UAVs may be considered efficient instruments for monitoring applications. This is due to the fact that these systems can perform repetitive

flights in a very easy and low-cost manner, they can fly at low altitude and they can provide high resolution and high quality data. UAVs allow for the easy selection of different flight parameters and can fly as often as possible when the weather conditions permit.

For this reason, they have often been analysed for multi-temporal investigations (Gulch, 2011; Vallet et al., 2012) and they can be employed in different scenarios, especially in dynamic scenes like the construction of buildings (El-Omari et al., 2011), damage identification in disaster management (Adams, 2004), digging works for geological purposes (Masini, 2015) and change detection applications (Matikainen et al., 2004; Champion, 2007). However, the topic of geometrically registering several multi-temporal epochs is still an open problem since it requires a priori knowledge of some positioning data in flight or on the ground. These data can be generated by knowing the UAV position with time with high precision (direct georeferencing (Rehak, 2013; Chiabrando et al., 2013) or by the use of a number of GCPs (Ground Control Points) on the ground. However, the use of GCPs is time consuming, costly (since it should be repeated before each new acquisition) and, sometimes, difficult to achieve. It also requires manual user work to incorporate the data derived in this manner into the processing, which can be time consuming and prone to gross errors. On the other hand, most UAVs are not equipped with an accurate GNSS receiver (since this item can be quite expensive) and even if some solutions with an RTK approach have been recently introduced (Gerke, 2016), the registration of multi-temporal epochs might need to be refined as well.

In this section a methodology to register multi-temporal high resolution datasets from UAVs is analysed.

The main idea is to constrain the orientation (Bundle Block Adjustment (BBA)) of the datasets to be congruent to the reference orientation. This can be achieved by introducing into the orientation of the datasets some anchor images selected from the reference epoch, with fixed internal (IO) and external (EO) parameters. This will spare the need for GCPs collection and will avoid their incorporation in the SfM (Structure from Motion (Dellaert et al., 2000; Westoby et al., 2012) elaboration. The presented co-registration methodology solves the relative transformation between datasets, but leaves the absolute accurate localization unknown. If an accurate positioning in the mapping frame is desired, some GCPs in the reference epoch will still be needed to adjust the block accordingly.

4.1 Proposed methodology

The main strategy of the proposed methodology for the co-registration of multitemporal UAV datasets is based on the use of some anchor images from an epoch selected as reference. These images are chosen in the unchanged part of the area and they are introduced in the processing of the following epochs to constrain their orientation to be consistent with the reference one. Different approaches have been evaluated to define if it is possible to perform a registration between multiple datasets without the use of GCPs, considering only an image-based approach:

- Geo-tag only: using only the GNSS information contained in the EXIF (Exchangeable Image File format) file (low precision).
- Reference Image Block Co-registration (RIBC): proposed registration based on the use of anchor images from a reference epoch. These images were chosen first in a manual way and then through a developed automatic approach.

• Reference GCP-based Co-registration (RGCP): based on the use of points (GCPs). It has been introduced to verify the accuracy of the RIBC solution. The proposed methodology (Figure 13) follows photogrammetric and Computer Vision algorithms to solve the multi-temporal registration problem. The current implementation of the procedure can be easily exploited through available commercial and open-source software tools and all the tests shown in this dissertation were achieved with the Pix4D (Pix4D, 2016) solution. The proposed methodology is based only on the use of images, considering one epoch as reference and aligning the others to the reference one.

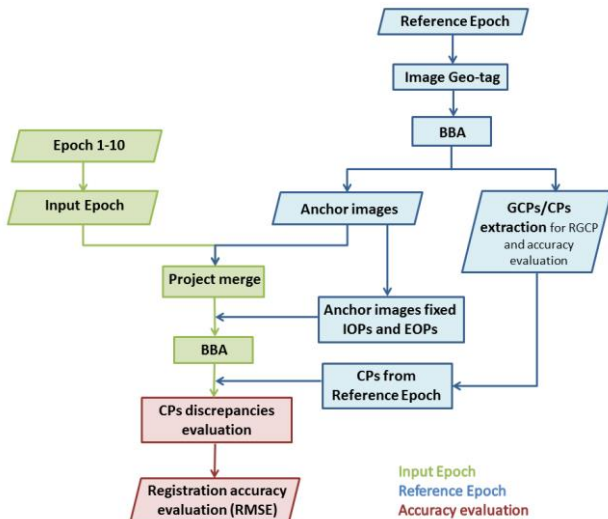


Figure 13. RIBC (Reference Image Block Co-registration) procedure (Aicardi et al., 2016c).

It follows these steps:

1. the first epoch is chosen as reference and the BBA is performed considering all the images at full resolution. The GNSS information contained in the Exif file is used to define starting orientation parameters to first align the block. If available, GCPs can be introduced to correctly orient the images and accurately georeference the model. A self-calibration is performed to evaluate the internal orientation (IO) parameters of the used camera;
2. a set of images (anchor images) is manually selected across the stable (unchanged) part of the area in order to be useful for the entire process. These images were chosen in the area external of the changing site, regarding the context and avoiding too much vegetation. Moreover, they need to be well distributed along the area around the changed part in order to have an optimal coverage and distribution. The selected images must be considered for the following processing with their internal and external orientation parameters;
3. the images from the subsequent block (input images) and the anchor images can be merged together into a single project to constitute one single block;
4. the external orientation parameters of the used anchor images are introduced into the project and are assigned a higher weight (as pseudo observations). In the bundle block adjustment, this strategy means that the EO parameters of these images are constraints and the other images should be aligned according to them;
5. the IO parameters (IOPs) are treated separately. The anchor images are introduced with fixed IOPs, while the camera parameters of the input block are estimated in the orientation phase (step 1). The reason why IO and EO parameters are fixed

is that they are highly correlated; freeing one of them would modify the final solution;

6. the image matching and orientation can be performed through the bundle block adjustment between the input epoch and the anchor images with fixed parameters without constrain about the different GSD of the epochs;

7. the final solution accuracy can be assessed considering some Check Points (CPs), if available, or with the RGCP approach proposed above.

To mathematically solve the image matching problem, two anchor images can provide enough observations, but at least 3 non-linear well distributed images should be used to have a more stable final solution.

In order to speed up the process and to decrease the manual input of the user, a methodology to select only the anchor images is also developed.

It is based on the matching of local interest features automatically extracted between the reference and the input epochs. The approach follows these steps:

1. to save time, a pre-selection of the images to match is initially performed with regards to the position information in the Exif file. With this strategy, each image of the reference epoch will not be matched with all the data of the input epoch, but only with the images approximately in the same area. The overlap between images is estimated considering their footprint, with the latter estimated through the following features:

- the approximate position registered by the GNSS receiver on-board;
- the flight height;
- the camera parameters, like the focal length and the sensor size.

2. to better extract features from the images, the Wallis filter (Wallis, 1976) is applied to the images to enhance their quality through an adaptive contrast filter. This can be very useful in the case of multi-temporal data to reduce the illumination differences and to balance the contrast and brightness between epochs;

3. feature extraction and matching algorithms are applied to select pairs of common points between epochs. It can be done through the following steps:

- features are extracted from images with the SIFT (Scale Invariant Feature Transform (Lowe, 2004)) operators;
- the extracted features are then matched between pairs of images to define corresponding pairs of keypoints;
- the presence of outliers is evaluated and removed through the use of the Lowe ratio test (Lowe, 2004). According to the original implementation of this algorithm, the ratio of distance from the closest neighbour to the distance of the second closest is considered and all the matches whose distance ratio is greater than 0.8 are rejected. From the experimental tests (presented by Lowe in (Lowe, 2004)) this method has been demonstrated to eliminate about 90% of false matches while discarding less than 5% of the correct matches;
- the extracted matches are then used to estimate the fundamental matrix (Hartley, 2003) between pairs of corresponding points (x' and x): $x'^T F x = 0$.
- To have statistically robust results, the RANSAC (RANdom SAMple Consensus (Fischler, 1981)) is adopted to remove outliers;
- since some outliers can still remain, the epipolar lines are computed. Outliers are excluded through a distance threshold based on the distance (d_c): the distance of each point from the epipolar line is estimated and the points whose distance is larger than the used threshold (2 pixels) are excluded.

This step is fundamental to the selection of a set of common points between pairs of images in the same (unchanged) area: no or few points represent changed and dynamic areas and, on the contrary, large sets of points between stereo-pairs are probably found in unchanged scenes;

4. this set of points can now be used to define an area on each image of the reference epoch. This can be achieved using the Alpha Shape algorithm (Akkiraju et al., 1995). Using an iterative procedure, for each set of points in the stereo-pairs, a polygon is designed and the final described area is the sum of the area described by each polygon created between the image of the reference epoch and all the matched input images. Also, in this case a distance-based threshold (d_a) is used to discard isolated points to avoid overestimation of the area;

5. considering the drawn area, the selection of anchor images is achieved by applying again a threshold (t_A): images are selected and then used as anchor only if the area is bigger than the defined threshold. With this approach, only the images in the unchanged part of the scene are selected and the others, describing the construction, are rejected.

The workflow of the methodology can be schematized as reported in Figure 14.

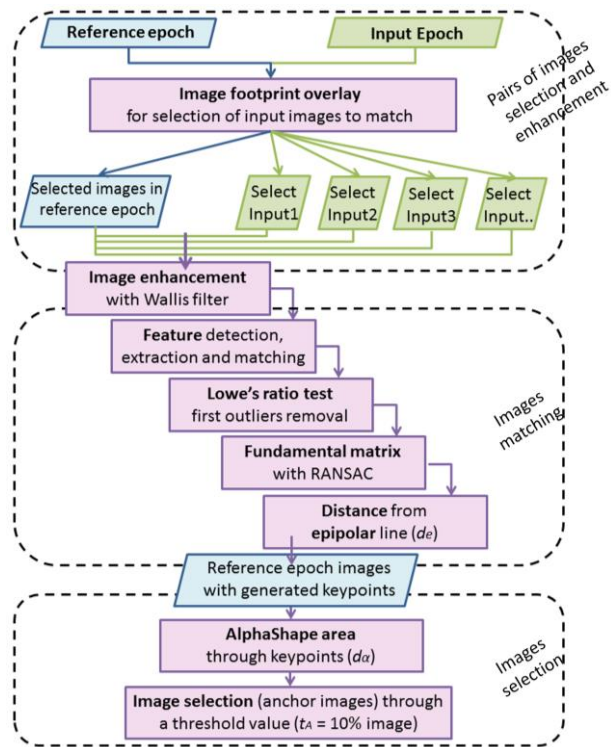


Figure 14. The steps of the automatic procedure for anchor image selection.

4.2 Results

The proposed methodology was firstly evaluated with the images of a construction site.

The data are composed of 10 multi-temporal flights acquired during the construction of the EFPL's SwissTech Convention Center in Lausanne, Switzerland, over a period of about 3 years. For the aerial acquisitions, a light weight UAV (eBee of Sensefly) was used. It houses a GNSS receiver and it can be controlled through the autopilot circuit board. The approximate position information was used to geo-tag the images at the time of exposure and to store the information in the Exif file. In this

specific case, its payload was composed of different RGB cameras to acquire the multi-temporal images.

The flights were performed with a photogrammetric approach (80% forward overlap and 60% side overlap) and the images were also taken along two orthogonal directions (as demonstrated in the simulation section, this strategy can greatly improve the final result). For the accuracy evaluation two approaches were adopted:

- construction of the synthetic reference solution: all the epochs were oriented with the RGCP approach and 15 GCPs extracted manually from the reference epoch were used to georeference the models;
- accuracy evaluation of RIBC: for each image-based registration, the accuracy was evaluated through the use of 11 CPs manually extracted from the reference epoch and the results were compared with the point-based solution (RGCP approach).

Figure 15 - Figure 16 summarize the results obtained by the three most significant tests: manual approach with 18 or 37 images and automatic procedure.

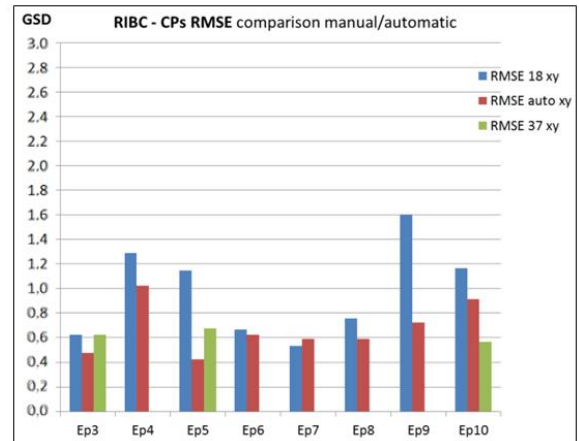


Figure 15. RIBC methodology, CPs' RMSExy evaluation for three approaches: manual with 18.

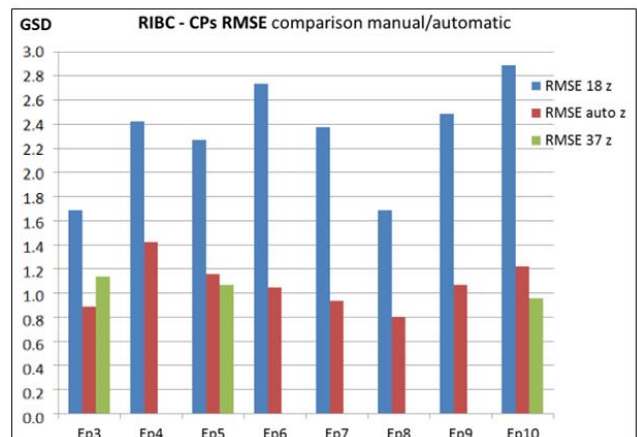


Figure 16. RIBC methodology, CPs' RMSEz evaluation for three approaches: manual with 18.

Comparing the results, it is possible to observe that, with the automatic approach, the horizontal component slightly decreases, while a large improvement is achieved in the vertical component with respect to the manual case with 18 anchor images. The mean difference in the vertical component is about 1.2 GSD and this demonstrates that the proposed procedure with the automatic selection of anchor images can provide

results similar to the common point-based approach. This is due to the fact that, if more images cover the same area, more common and repeated points can be defined and used for the orientation of the epochs. This can better constrain the relative orientation between reference and input epochs and exclude false positive common features. However, as for any automatic procedure, considering automatic selection can be a best practice to verify the selected anchor images distribution to avoid any uneven arrangement that might occur, for example, in the case of a vegetated area or images of poor quality.

4.3 Methodology validation

To further validate the proposed procedure, a second dataset in a completely different scenario was used. In this case, we used the images of an earthquake in Taiwan acquired by a DJI Phantom3. Two flights were performed with the same UAV platform and sensors to acquire information before the earthquake (177 images) and after the event (232 images). Since one building collapsed after the occurrence, we applied the registration procedure to monitor this change.

Since just two datasets were available, the first one (before the earthquake) was used as reference and the second (with the collapsed building) as input.

Also, in this case the automatic procedure was applied to select the anchor images and the images representing the collapsed building were successfully excluded.

After the anchor images selection from the reference epoch, the image-based registration procedure was applied to this dataset and 13 points manually selected from the reference epoch were used as control points to assess the final accuracy (Table 6).

Table 6. Taiwan dataset registration results.

[GSD]	Δx	Δy	Δz
Min	-1.8	-1.0	-2.5
Max	2.0	0.5	1.2
Mean	-0.2	0.0	-1.1
Std	1.2	0.4	1.0
RMSE	1.2	0.4	1.5

The results previously achieved with the construction dataset are here confirmed since the mean RMSE is about 1.5 GSD (GSD = 3.60 cm). This good result is due to the high image quality (acquired at a lower altitude) and the high number of images in the unchanged area that allows for the definition of a big and well distributed set of matched features around the collapsed building.

5. CONCLUSIONS

The aim of the research was to investigate sensors and flight planning in order to define general rules that can help the user in achieving the desired result.

To this aim, deep knowledge and analyses of the on-board available sensors are crucial to understand their behaviour and to test their performance. This need has been investigated with the development of a specific methodology to evaluate GNSS and IMU platforms and particular flights were adopted to analyse the performance of the sensors in comparison with well-established topographic techniques. The analysis strategy employed for the on-board navigation sensors (GNSS receiver and IMU) allowed us to assess the metrical position achievable through the low-cost devices installed on-board. On the other hand, it was demonstrated that, if a real time knowledge of the precise position of the UAVs during the flight is not required, it

is possible to use an external GNSS receiver. The used device was investigated to analyse its installation on-board, the procedures to correctly perform the flights and to fix the phase ambiguity of the GNSS data. The processing of the acquired data was also analyzed to obtain a precise knowledge of the system position along the flight. Considering these strategies, it is possible to reconstruct the UAV position with a centimetre level of detail which is the required level for precise geomatics analyses and for direct photogrammetry scenarios.

The benefit of the use of the investigated system was further demonstrated in a specific case study with regards to the use of UAVs for the measurement of the pattern of installed antennas in the radio-astronomy field. Tests demonstrated that a good knowledge (centimetre) of the UAV position along the flight can guarantee a more reliable pattern measurement. This was demonstrated with regards to a reference antenna specifically used for methodology validation.

The use of an external IMU platform was also investigated, but the used sensors suffered too much from vibrations and interference and it was not possible to assess any improvement in the angles definition. However, for photogrammetric applications, it was demonstrated during the second part of the thesis in the simulation section, that a good knowledge of angles does not improve the final images block orientation.

The second part of the research had dealt with the understanding of the impact of different flight parameters for the correct photogrammetric use of UAVs. Since the correct use of UAVs for photogrammetric purposes is quite complex, the relationship between accuracy on the ground and flight parameters are sometimes hard to define.

This study was conducted by means of the definition of different flight configurations and features (like cross and border stripes, precise positioning systems, different overlaps and oblique images) to understand how the change in one of these parameters may interfere with the final orientation of the block. Tests were carried out via simulation with a Matlab code. The choice to develop the image orientation through the collinearity equation has originated from the need to better understand and control all of the parameters. In fact, the main advantage with respect to the use of an available photogrammetric software package is that the implemented code allows for the complete control of the process. This is not really possible using software packages that, in most cases, return very little by way of detailed reports.

The results of the tests show that the use of cross stripes can guarantee an improvement in the block registration even if less ground control points are available.

Moreover, if a precise positioning system is available on-board, the ground true can be totally eliminated, and we obtain the same results as reported in the case of cross stripes and full GCPs configuration. Moreover, accurate image initial position can also suppress the block deformation with a few GCPs.

The most outstanding result is that obtained relative to the use of oblique images.

It is well known that the use of this kind of acquisition can improve the knowledge of the area since information not included in nadir images can now be made available.

Furthermore, it was demonstrated that the combined use of oblique and nadir images allows us to obtain a rigid block with fewer orientation problems with respect to the reference solution. In fact, this configuration has the best accuracy in comparison to all the others.

It was also demonstrated that the commonly used overlap (80% - 60%) is the best one unless cross stripes are applied. In fact,

reducing the percentage of forward and side overlap will inevitably aggravate the final achievable accuracy.

Finally, the use of boarder strips or a precise knowledge of the angles during the flight do not denote an improvement in the orientation of the photogrammetric blocks.

The knowledge of these behaviours is important to define general rules for each case study according to the expected final result in terms of accuracy of the block orientation.

The experimental results were finally further evaluated through real case studies in which the influence of the most significant features was evaluated. Also, the case studies confirmed the estimated results, which can thus be considered as a reference for future surveys.

Finally, the last part of the thesis was focused on the usage of the acquired photogrammetric data. In particular, a methodology for the co-registration of multi-temporal high resolution UAV blocks was presented.

The proposed method is built on the use of an image-based approach that was evaluated in comparison to a commonly used point-based strategy in a changing scenario. Tests demonstrated that the proposed methodology can be used in place of the ground control point-based registration, especially if a correct set of images is selected and considered for the block orientation. This was also validated to a second case study that confirmed the reliability of the methodology.

However, it should be mentioned that, since the method is image-based, the quality of the images is a key factor. For this reason, it is fundamental to correctly plan the flight (also considering the features evaluated in the simulation section) and to consider adequate flight velocity and camera settings to avoid motion blur effects or overexposed images which do not allow us to make a correct matching between the features of different images.

Concluding, it is possible to state that UAVs can be considered to be a reliable platform for measurements if the user knows how to manage the on-board sensors and the data. It is important for the scientific community to analyse the metrical use of the data and to define strategies that can be directly applied by commercial or industrial users to improve also the automation.

According to this direction, critical control of the final product should be encouraged.

The user needs to previously know the expected final result in terms of accuracy and product completeness and it also should have some instruments (software tools) to take control of processing parameters and features. However, this is currently not always possible since the reports of the software packages often suffer from a deficient of information and do not help the user to fully understand the performance at each step.

REFERENCES

Adams B.J., 2004. "Improved disaster management through post-earthquake building damage assessment using multi-temporal satellite imagery". In Proceedings of the ISPRS XXth Congress, Turkey, 12-23 July 2004, Vol. 35, pp. 12 - 23. Available online: <http://cartesia.es/geodoc/isprs2004/comm7/papers/121.pdf> (accessed on 23 June 2016).

Aicardi I., Chiabrando F., Grasso N., Lingua A.M., Noardo F., 2016. "UAV photogrammetry with oblique images: First analysis on data acquisition and processing". In: International

Archives of the Photogrammetry, Remote Sensing and Spatial Information Sciences, Vol. 41, pp. 835 - 842.

Aicardi I., Garbarino M., Lingua A., Lingua E., Marzano R., Piras M., 2016. "Monitoring post-fire forest recovery using multitemporal Digital Surface Models generated from different platforms". EARSel eProceedings, Vol. 15, pp. 1 - 8.

Aicardi I., Nex F., Gerke M., Lingua A. M., 2016. "An Image-Based Approach for the Co-Registration of Multi-Temporal UAV Image Datasets". In: Remote Sensing, Vol. 8(9), pp. 779 - 799.

Aicardi I., Nyapwere N., Nex F., Gerke M., Lingua A. M., Koeva M. N., Causeway H., 2016. "Co-registration of multitemporal UAV image datasets for monitoring applications: A new approach". In Proceedings of the ISPRS XXIII Congress, Prague, Czech Republic, pp. 12-19.

Akkiraju N., Edelsbrunner H., Facello M., Fu P., Mucke E.P., Varela C., 1995. "Alpha shapes: Definition and software". In Proceedings of the 1st International Computational Geometry Software Workshop, Minneapolis, MN, USA, 20 January 1995, Vol. 63, pp. 63 - 66.

Behling R., Roessner S., Segl K., Kleinschmit B., Kaufmann H., 2014. "Robust automated image co-registration of optical multi-sensor time series data: Database generation for multi-temporal landslide detection". In: Remote Sensing, Vol. 6, pp. 2572 - 2600, doi:10.3390/rs6032572.

Bulusu N., Heidemann J., Estrin D., 2000. "GPS-less low-cost outdoor localization for very small devices". In: IEEE personal communications, Vol. 7.5, pp. 28 - 34.

Champion N., 2007. "2D building change detection from high resolution aerial images and correlation digital surface models". In: International Archives of the Photogrammetry, Remote Sensing and Spatial Information Sciences, Vol. 36.

Chiabrando F., Lingua A.M., Piras M., 2013. "Direct photogrammetry using UAV: Tests and first results". In: International Archives of the Photogrammetry, Remote Sensing and Spatial Information Sciences, Vol. 1, pp. 81 - 86.

Dabove P., Manzano A.M., 2014. "GPS & GLONASS mass-market receivers: positioning performances and peculiarities". In: Sensors, Vol. 14, pp. 159 - 179.

Dellaert F., Seitz S.M., Thorpe C.E., Thrun S., 2000. "Structure from motion without correspondence". In Proceedings of the IEEE Conference on Computer Vision and Pattern Recognition, Hilton Head Island, SC, USA, 13-15 June 2000, Vol. 2, pp. 557 - 564.

ENAC, 2015. "ENAC Draft Regulation 'Remotely Piloted Aerial Vehicles'", 2nd Edition, published on March 19th 2015. [http://www.aeroclubcagliari.it/sites/default/files/last access 27/06/2016](http://www.aeroclubcagliari.it/sites/default/files/last%20access%2027/06/2016).

El-Omari S., Moselhi O., 2011. "Integrating automated data acquisition technologies for progress reporting of construction projects". In: Automation in Construction, Vol. 20, pp. 699 - 705, doi:10.1016/j.autcon.2010.12.001.

European Parliament, 2015. "Civil drones in the European Union". Briefing.

- Fischler M. A., Bolles R. C., 1981. "Random sample consensus: a paradigm for model fitting with applications to image analysis and automated cartography". *Communications of the ACM*, Vol. 24(6), pp. 381-395.
- Frueh C., Sammon R., Zakhor A., 2004. "Automated texture mapping of 3D city models with oblique aerial imagery". In: *3D Data Processing, Visualization and Transmission, 3DPVT Proceedings. 2nd International Symposium on IEEE*.
- Gao Y., Wojciechowski A., 2004. "High precision kinematic positioning using single dual-frequency GPS receiver". In: *The International Archives of the Photogrammetry, Remote Sensing and Spatial Information Sciences*.
- Gerke M., Nex F., Remondino F., Jacobsen K., Kremer J., Karel W., Ostrowski W., 2016. "Orientation of oblique airborne image sets-experiences from the ISPRS/EUROSDR benchmark on multi-platform photogrammetry". In: *International Archives of the Photogrammetry, Remote Sensing and Spatial Information Sciences*, Vol. 41, pp. 185 - 191.
- Gerke M., Przybilla H.-J., 2016. "Accuracy analysis of photogrammetric UAV image blocks: Influence of onboard RTK-GNSS and cross flight patterns". In: *PFG Photogrammetrie, Fernerkundung, Geoinformation Jahrgang*, Vol. 1, pp. 17 - 30.
- Gulch E., 2011. "Photogrammetric evaluation of multi-temporal fixed wing UAV imagery". In: *International Archives of the Photogrammetry, Remote Sensing and Spatial Information Sciences*, Vol. 38, pp. 265 - 270.
- Hartley R., Zisserman A., 2003. "Multiple view geometry in computer vision". Edited by Cambridge university press.
- Hoffmann-Wellenhof B., Lichtenegger H., Collins J., 2000. "GPS: Theory and Practice". 4th edition of Springer-Verlag Wien.
- Hoffmann-Wellenhof B., Lichtenegger H., Waskle E., 2008. "GNSS: Global Navigation Satellite System. GPS, GLONASS, Galileo and more". Springer- Verlag Wien.
- International Civil Aviation Organization, 2011. "Unmanned aircraft systems (UAS)". ICAO circular 328-AN/190.
- Lowe D.G., 2004. "Distinctive Image Features from Scale-Invariant Keypoints". In: *International Journal of Computer Vision*, Vol. 60, pp. 91 - 110, doi:10.1023/B:VISI.0000029664.99615.94.
- Masini N., Lasaponara R., 2015. "On the use of Multisensor and multitemporal data for monitoring risk degradation and looting in archaeological site". In *Proceeding of the EGU General Assembly Conference, Vienna, Austria, 12-17 April 2015*, Vol. 17.
- Matikainen L., Hyyppä J., Kaartinen H., 2004. "Automatic detection of changes from laser scanner and aerial image data for updating building maps". In: *International Archives of the Photogrammetry, Remote Sensing and Spatial Information Sciences*, Vol. 35, pp. 434 - 439.
- NASA, 2015. "A report overview of the civil UAV capability assessment".
- Pix4D, version 2.2. UAV mapping software; Pix4D SA: Lausanne, Switzerland, 2016. Available online: <https://pix4d.com/> (accessed on 21 March 2016).
- Ramsey C.L., Griffiths P.A., Stokes T.R., 2014. "Multi-rotor Unmanned Aerial Vehicles (UAVs) and high-resolution compact digital cameras: a promising new method for monitoring changes to surface karst resources". In: *Acta Carsologica*, Vol. 43.2/3, pp. 269.
- Rehak M., Mabillard R., Skaloud J., 2013. "A micro-UAV with the capability of direct georeferencing". In: *International Archives of the Photogrammetry, Remote Sensing and Spatial Information Sciences*, Vol. 40, pp. 317 - 323.
- Stempfhuber W., Buchholz M., 2011. "A precise, Low-cost rtk gnss system for uav Applications". In: *International Archives of the Photogrammetry, Remote Sensing and Spatial Information Sciences*, Zurich, Volume XXXVIII-1/C22. Available online: <http://www.int-arch-photogramm-remote-sens-spatialinf-sci.net/XXXVIII-1-C22/289/2011/isprsarchives-XXXVIII-1-C22-289-2011.pdf> (accessed on 28/04/2015).
- Vallet J., Panissod F., Strecha C., Tracol M., 2012. "Photogrammetric performance of an ultra-light weight swinglet UAV". In: *International Archives of the Photogrammetry, Remote Sensing and Spatial Information Sciences*, Vol. 38, pp. 253 - 258, doi:10.5194/isprsarchives-XXXVIII-1-C22-253-2011.
- Van Blyenburgh P., 2015. "RPAS Remotely Piloted Aircraft Systems - The Global Perspective 2015/2016. 13th Annual Edition". (url: [%5Curl%7Bhttp://uvs-info.com/index.php/yearbooks/yearbook-2015%7D](http://uvs-info.com/index.php/yearbooks/yearbook-2015%7D)).
- Virone G., Paonessa F., Peverini O. A., Addamo G., Orta R., Tascone R., Bolli P., 2014. "Antenna pattern measurements with a flying far-field source (Hexacopter)". *Proceedings of IEEE International Conference on Antenna Measurements and Applications, Antibes Juan-les-Pins, France, 2014, November 16-19, 1-2*.
- Wallis R., 1976. "An approach to the space variant restoration and enhancement of images". In *Proceedings of the Symposium on Current Mathematical Problems in Image Science, Monterey, CA, USA, 10-12 November 1976*, pp. 329 - 340.
- Westoby M. J., Brasington J., Glasser N. F., Hambrey M. J., Reynolds J. M., 2012. "Structure-from-Motion' photogrammetry: A low-cost, effective tool for geoscience applications". In: *Geomorphology*, Vol. 179, pp. 300 - 314.
- Wisniewski B., Bruniecki K., Moszynski M., 2013. "Evaluation of RTKLIB's Positioning Accuracy Using low-cost GNSS Receiver and ASG-EUPOS". In: *TransNav: International Journal on Marine Navigation and Safety of Sea Transportation*, Vol. 7(1), pp. 79 - 85. Available online: http://www.transnav.eu/Article_Evaluation_of_RTKLIB%27s_Positioning_Wi %C5%9Bniewski,25,412.html (accessed on 28/04/2015).
- Wong A., Clausi D.A., 2007. "ARRSI: Automatic registration of remotesensing images". In: *IEEE Transactions on Geoscience and Remote Sensing*, Vol. 45, pp. 1483 - 1493.

FROM SURVEY TO ANALYSIS FOR CULTURAL HERITAGE MANAGEMENT: A NEW PROPOSAL FOR DATABASE DESIGN IN BIM

N. Bruno

XXX ciclo di dottorato

Università degli Studi di Parma, Dipartimento di Ingegneria e Architettura, Parco Area delle Scienze 181A, 43124, Parma, Italy – nazarena.bruno@studenti.unipr.it

KEY WORDS: HBIM, Cultural Heritage, Survey, Metadata, 3D Modelling, Database design

ABSTRACT:

The need to safeguard and preserve Cultural Heritage (CH) is increasing and especially in Italy, where the amount of historical buildings is considerable, having efficient and standardized processes of CH management and conservation becomes strategic. At the time being, there are no tools capable of fulfilling all the specific functions required by Cultural Heritage documentation and, due to the complexity of historical assets, there are no solution as flexible and customizable as CH specific needs require. Nevertheless, BIM methodology can represent the most effective solution, on condition that proper methodologies, tools and functions are made available.

The thesis work, presented here, aims to give a concrete answer to the lack of specific tools tailored for Cultural Heritage documentation. It addresses the implementation of a BIM system aimed at maintenance, conservation and restoration of Cultural Heritage. BIM methodology is addressed from a geomatics perspective, giving on the one hand a contribution especially to survey and database implementation, and, on the other hand, interfacing with other disciplines actors, in order to collaborate and share objectives and strategies.

In particular, a specifically designed database was implemented, where all data about the historical building can be stored. A tailored database is necessary to organize historical data that generally are not standardized, have a complex structure and are fuzzy in their description.

The application was implemented with the specific aim of providing tools also for non- AEC experts: it gives user-friendly graphical interfaces to access the data and makes available tools for data entry, element modelling, attribute query and thematic mapping.

It can be integrated into the main commercial BIM software (at the moment the experimentation has been limited to Revit) or accessed via web. One of the main goals was not to be bounded to a specific software and to make the system usable on a larger scale.

Database design and system usability have been the most investigated topics, since to date there are still few studies concerning the organization of semantic data, system usability and data sharing. Nevertheless, all the aspects concerning the application of BIM process to historical assets (level of accuracy, compliance with the surveyed data, parameterization of complex elements, management of deformations and irregularities, integration of pre-existing databases) have been addressed, in order to define a complete methodology.

The Cathedral of Parma was chosen as case study to test the methodology, but the system was implemented to be flexible and customizable, in order to apply this methodology to a wide range of historical assets.

1. INTRODUCTION

In recent years, there has been an increasing diffusion of the BIM (Building Information Modelling) methodology, mainly thanks to the introduction of regulations and standards that impose or at least regulate its use. Italy, thanks to the recent publication of the new UNI 11337:2017 standard, is also moving towards a progressive adoption of the BIM in public contracts.

BIM methodology allows managing, in a coherent and coordinated way, all phases of a building lifecycle and is therefore not simply a design tool, but can also be applied to existing buildings.

The use of BIM for documentation and management of historical buildings would certainly have positive effects. In fact, as shown by literature, BIM greatly simplifies the management of the time factor in building documentation. It makes it possible to handle coherent and coordinated data relating to different time phases, to highlight and separate the different construction phases, as well as to keep track of all the performed or scheduled interventions. It also provides a single

access point for all the available data, constituting a sort of unique and searchable archive.

Especially in Italy, where the amount of historical buildings is considerable, having efficient and standardized processes of CH management and conservation becomes strategic.

BIM represents an effective tool for supporting scheduled maintenance and conservation activities, which are an increasing important instrument for safeguard and conservation of Cultural Heritage. Preventing the onset of risk and damage situations helps to limit the invasiveness of restoration interventions and avoid situations of danger for the asset.

Nevertheless, currently BIM is principally associated to new construction works and only in the last years its use is spreading to existing buildings too (Volk et al., 2014), while in the field of Cultural Heritage, the use of BIM is very limited and remains the prerogative of universities and research institutes (De Luca et al., 2011; Fassi et al., 2015; Dore et al., 2015).

The reasons for this disparity can be traced back to the difficulties involved in setting up a BIM of historic buildings. There are not specific regulations and, in general, there is not yet a shared awareness of the importance of BIM in Cultural

Heritage and, therefore, there is no commitment to act in this regard by providing *ad hoc* solutions for cultural assets.

Problems arise w.r.t. geometric modelling, especially of irregularities that do not fit well with the parametric modelling typical of BIM (Eastman et al., 2008; Garagnani et al., 2013). At the same time, information organization pays the lack of as flexible and customizable solution as required by the heterogeneous and difficult to standardize structure of historical data.

Another non-trivial aspect is the multi-temporality of information and the need to have a system usable for diachronic analyses. Historical data are, in fact, by their nature multi-temporal and, in addition, conservation is a continuous activity that requires constant updating of information and continuous collection and processing of different data.

Last but not least, an interdisciplinary approach is mandatory to well know the building and translate it correctly in a virtual model. The operators who work in Cultural Heritage field are not used to work with databases, information systems, 3D models etc., so a system tailored for CH management should be user-friendly and easy to use/learn even for non-experts (Fassi et al., 2015).

Nevertheless, BIM should represent the most natural and modern approach to historical assets management, providing many advantages such as documentation over time, management of different construction phases (Stefani et al., 2010), support for structural analysis (Dore et al., 2015; Crespi et al., 2015), unique database for all data about the building (Fai et al., 2011), support for ordinary maintenance programs (Fassi et al., 2015), support for Augmented Reality applications and web sharing (Fassi et al., 2015) and so on. In this context, the implementation of a BIM for historical building documentation can be a big challenge but, at the same time, a technological improvement that enables a better and deeper knowledge of these assets.

The thesis project led to the realization of a Historic BIM system for the Parma Cathedral aimed at restoration and maintenance of historic buildings. The implemented system has been conceived to give a concrete answer to the lack of tailored tools for Cultural Heritage documentation.

The application, thanks to a specific database, allows storing and querying the data necessary for the description of historical buildings. A tailored database is necessary to organize historical data that generally are not standardized, have a complex structure and are fuzzy in their description.

It can be integrated into the main commercial BIM software (at the moment the experimentation has been limited to Autodesk Revit (Autodesk, 2018)) or accessed via web.

This thesis addressed the BIM methodology from a geomatics perspective, giving a contribution especially to survey, modelling and database design.

Database design and system usability, in particular, have been the most investigated aspects. In fact, if the themes related to surveying and modelling are widely investigated in literature, there are still few studies concerning the organization of semantic data, system usability and data sharing.

To test the proposed methodology, the Cathedral of Parma was chosen as case study, but the system can be applied to other similar historical buildings.

2. METHODOLOGY

The first phase of the work involved the analysis of the regulatory requirements and specific needs that the building chosen as case study presents. Then, the acquisition of both geometric and semantic data, through instrumental survey and

documentary and normative analysis, were performed. On the basis of the data acquired, working in an integrated way between the need for modelling, documentation, accuracy, data manageability and system usability, the three-dimensional model has been created and the information system has been implemented.

The HBIM has been conceived as an information system on the architectural scale and as an integrated process of survey & data acquisition, 3D modelling and database design & data entry (Figure 1).

Especially in the cultural heritage field, the creation of a BIM is not a linear process, but an integrated and circular one. Survey, modelling and database design influence each other. For example, the accuracy with which the survey is performed and the achieved level of knowledge of the object influence the quality of the model (in terms of accuracy and adherence to reality) and of the database (in terms of organization of information and data stored).

For this reason, designing these components independently leads to inconsistencies and reduces the effectiveness of the global system.

For each of the three phases, the main features and problems have been identified, trying to give an original contribution to the solution of some outstanding issues.

Today there are different consolidated techniques available in each of these fields, but in order to analyse historical assets, not all the methodologies are suitable. In the work, all the three issues have been addressed, in order to define a complete methodology.

As far as the survey is concerned, in such complex contexts, geometric and spatial data are generally acquired through integrated surveys, increasing the available products and overcoming the specific limitations of each technique. Literature references are many (Castagnetti et al., 2017; Fassi et al., 2010; Remondino, 2011) and the acquisition techniques are well-established. On the contrary, no specific references are about the integration of these acquired data in a BIM environment, nor about their exploitation to certify the quality of the BIM model.

Likewise, 3D modelling techniques and commercial software that can be used to represent a building are well-known and discussed by literature (Achille et al., 2007; Guidi et al., 2009). As for the survey, even for modelling, it is not yet adequately defined how to certify and validate BIM model quality and accuracy, which are influenced by the quality of the data surveyed and the modelling operations carried out.

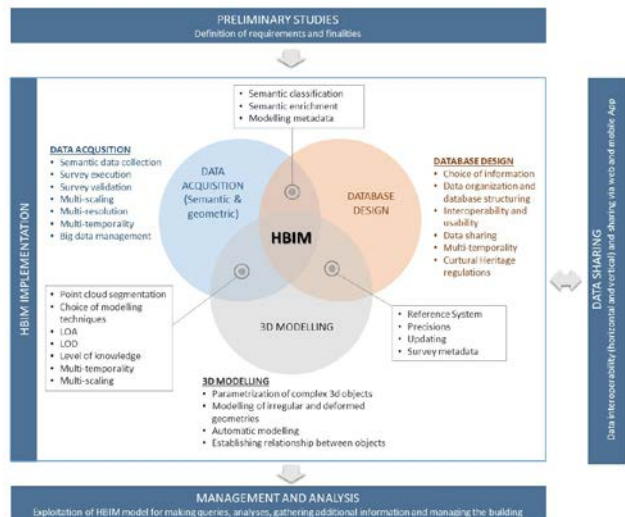


Figure 1_Methodology overview.

On the contrary, semantic data acquisition and their organization in a relational database are less investigated topics, with only a few literature references. The main focus was therefore on the database design phase and data usability, since these issues have still many open research fields and suffer from the difficulties of identifying a standard methodology adaptable to different historical contexts and at the same time able to ensure simple and dynamic access to information.

3. THE CASE STUDY: PARMA CATHEDRAL



Figure 2_Parma Cathedral example views.

The history of Parma Cathedral has still some unclear aspects, in particular with regard to its construction dates. It is now accepted opinion (Blasi et al., 2006) that its construction started in the second half of the XI century and was completed under the direction of Matilde of Canossa at the beginning of the XII century.

During its lifetime, the church has been subject to changes, additions, damages and repair works. The most important event that influenced the cathedral conformation was the strong 1117 earthquake, which caused the collapse of many parts.

Since that event, the history of works and restorations has been long and lasting. At present, the building suffers structural and material problems. Structural problems have always affected the cathedral, in particular the central nave and the crypt. They are principally due to the high thrusts of the vaults of the central nave and the weight of the dome, which cause a considerable out-of-plumb in the side walls and the subsidence of the structures under the dome.

Material decay affects instead principally stones and decorative elements in the façades. Externally, the cathedral is chiefly built of bricks, although, as evidenced by some plaster remains, it had to be entirely plastered. Lesenes and corners are instead made of stone, especially sandstone and limestone, which are very sensitive to atmospheric agents, and tend to delaminate and crumble.

As continuous restoration and maintenance works are required, its complexity, size and characteristics, the Cathedral offers a significant sample of challenges and issues to which refer and is a suitable case study to implement the methodology proposed.

4. THE INTEGRATED SURVEY

The survey has been designed in order to be integrated, multi-resolution and scalable in time. Integration allows indeed overcoming the specific limitations of each technique, having more complete results (Bianchi et al., 2016); multiresolution is useful to manage the huge amount of data that generally comes from such survey and to have, at the same time, a correct overview and an adequate level of detail; finally, scalability

ensures the progressive survey implementation in time and the supports for monitoring purposes, by comparing data acquired in different epochs.

The survey, even in complex and articulated contexts such as the one under investigation, from the point of view of execution, follows the methodology now consolidated, obviously declined on the specificity of the object under examination. In particular, with regard to Parma Cathedral, the main difficulties have been related to the cathedral volumetric features and to the surrounding context: occlusions, different levels of detail, façade height, narrow streets around the Cathedral made acquisition phases difficult.

From a methodological point of view, the thesis addressed, in addition, the interaction between survey and BIM: how the survey data and metadata can be entered into the database to document and validate the operations carried out (see paragraph 6.1).

As far as the outputs are concerned, restitution was planned for a nominal average scale of 1:50, reserving the 1:100 scale for less accessible areas and 1:20 for some peculiar details. In addition to the 3D model for HBIM implementation, particular attention was paid to material degradation representation. To this aim, the realization of orthophotos of the external façades was mandatory and the possibility to associate them to the 3D model has been foreseen.

4.1 Topographic survey

In order to refer the integrated survey to a stable reference network, identifiable station points have been marked all around and inside the Cathedral. As shown in Figure 3, twenty-two stations were materialized and surveyed.

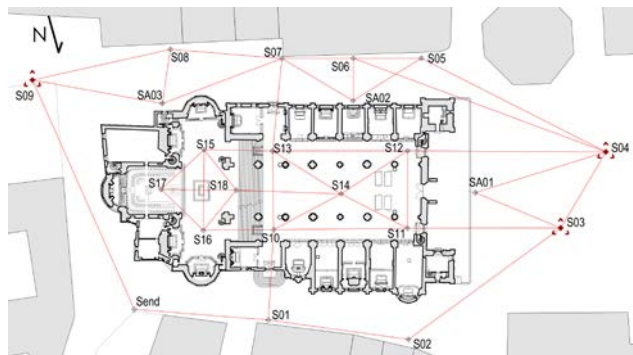


Figure 3_Topographical network of traverses.

The Topcon Image Station IS2 total station was used and the observations were adjusted through rigorous least squares minimization with the software Calge (Forlani et al., 1986). The adjustment provided a mean accuracy of ca. 2.1 mm, which can be considered acceptable for most modelling and monitoring activities if very high precisions are not required.

The topographical network was georeferenced with a GPS survey of three vertices (vertices S03, S04 and S09), placed in the two squares at the opposite corners of the cathedral (Piazza Duomo and Piazzale S. Giovanni). The GPS coordinates were obtained through 4 hours static session with respect to a station of the CORS (Continuous Operation Reference Station) network Netgeo about 9 km away and then transformed in a local Cartesian reference system with origin in the midpoint between the GPS stations.

4.2 Laser scanner survey

As said before, the terrestrial laser scanner (TLS) survey was made with a multi-resolution approach, so two different scan phases have been designed: a global survey and a detailed survey. The global survey aimed at generally document the cathedral, having a complete survey of its main volumes.

19 scans were performed in correspondence of the topographic network points. In the nave, in the transept and in the choir, the scans were acquired with an average resolution of 6÷7 mm on the object. In the presbytery (S15, S16, S17, S18), the resolution was instead equal to 2÷3 mm on the object, due to the high level of detail in the presbytery area.

The detailed survey has been designed as a local survey, in order to increase the resolution (average distance between the points equal or less than 5 mm) in the most complex and detailed areas. The methodology was tested in some areas, such as the loggias in the apses.

All the scans were acquired with the Leica Geosystem C10 scan station and were registered in Cyclone, using as reference the known coordinates dataset obtained from the topographic survey

The registration provided satisfying results, with an average residual of 2 mm and a standard deviation of 1 mm, in accordance with the instrument nominal precision.



Figure 4_The complete point cloud after registration.

4.3 Photogrammetric survey

In the Parma Cathedral survey, photogrammetry provides an essential integration to TLS. Image acquisition was far from simple, since the presence of many occlusions and the narrowness of the streets around the Cathedral that dictates oblique imaging in order to frame the upper part of the façades, with large variations in image scale from the base to the top of the façade. This in turn cause a progressive decrease of accuracy and resolution from the lower to the upper parts.

An Unmanned Aerial System (UAS) would provide a much better imaging geometry and would be beneficial for detection of the areas not visible from the ground level, with reduction of occlusions and for the roofs survey. However, at this time, it has not yet been possible for issues related to authorization to fly in the city centre.

Therefore, for the moment, only images from ground have been taken, suitable to model the building up to the level of the lower eave (side chapels and apses).

A Nikon D3x (resolution 6048x4032 pixel, pixel size 6 µm) with 35 mm optics has been used. The photogrammetric block

was designed to reach a precision adequate for 1:50 representation scale ($\sigma = 1$ cm).

The image sequence consisted of 326 images that were oriented automatically using Agisoft Photoscan. High accuracy image orientation with a generic pair pre-selection modality has been chosen. To define the reference system of the restitution and orient absolutely the image block, 15 well-distributed Ground Control Points (GCP) were selected on natural features (e.g. edges, corner, surface discontinuities, etc.) since, for the moment, the Cathedral Fabbriceria did not granted permission the installation of permanent targets to the Cathedral walls.

The use of natural points makes collimation more difficult and point identification less precise. This is true despite a GSD of the order of 3 mm, as the edges of architectural elements are always worn and corroded. For this reason, in order to improve the accuracy of the photogrammetric survey, using artificial targets is desirable. Therefore, in accordance with the drone survey campaign, the authorization for installation will be requested again.

The lack of targets on the walls of the Cathedral caused great difficulties also for the validation of the photogrammetric survey. Two different procedures have been applied: the analysis of the residuals on some check points located on natural features and a comparison between the photogrammetric DSM and the laser scanner point cloud.

- Check points validation: 33 natural points have been acquired by topographical measurements and used as check points. From the residual stats (Table 1), it is possible to note that the solution is apparently a little worse than the accuracy estimated in the block design phase (1 cm), with an RMS of 16.1 mm. On the contrary, the maximum error values are rather high. Given the difficulties of collimation mentioned above, it is possible that these high values are due to errors of collimation, either during the topographical survey or the image point identification.

	XYZ Error [mm]	X error [mm]	Y error [mm]	Z error [mm]
RMS	16.1	9.2	9.7	9.0
Mean	14.9	2.0	0.8	2.3
Std. dev.	6.2	8.9	9.7	8.7
Max val	26.8	17.4	23.9	16.4
Min val	0.7	-14.6	-15.6	-20.9

Table 1_Check points residuals.

- DSM comparison: the second validation procedure concerns the comparison between the DSM obtained from the photogrammetric survey and the laser scanner point cloud. The outcomes of this comparison are shown in Figure 5.

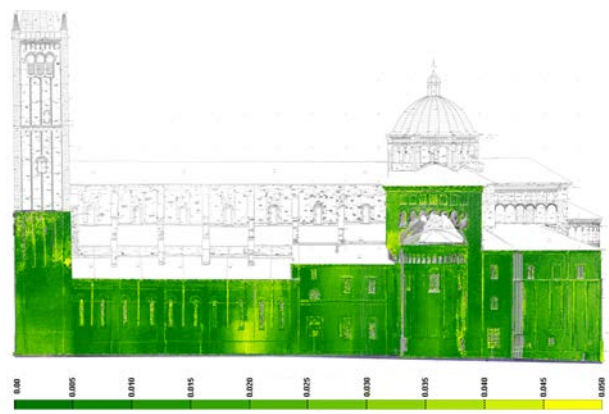


Figure 5_Map of displacement [m] between DSM and laser scanner point cloud.

The analysis of the discrepancies histogram shows that 71 % of the points distances are lower than 16 mm (1σ) and 94 % of the whole dataset is under 32 mm (2σ) of displacement. The results tend to confirm the pointwise indication gathered by the check point analysis.

At the end of the structure from motion procedure, with the same software package, the DSM of the exterior side of the Cathedral was obtained. In addition, the high-resolution orthophoto (GSD 3 mm) were produced (Figure 6).

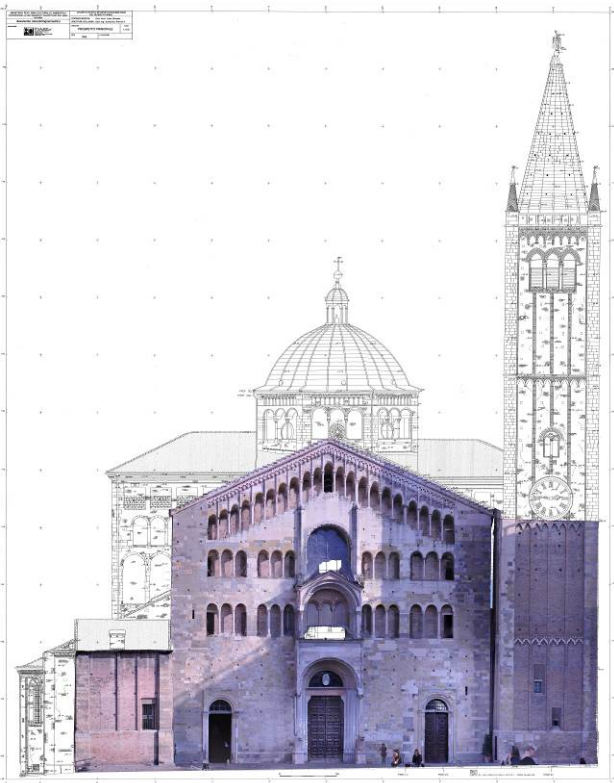


Figure 6_Orthophoto of the Cathedral main façade overlapped to the drawings of the photogrammetric survey made by FOART in 1989.

5. THE 3D MODELLING

Historical buildings are irregular and characterized by heterogeneous and complex shapes. For this reason, the modelling methodology is still an open question and copes with the difficulty to retrace the correct shape of the object (Barazzetti et al. 2015).

The advantages of parametric modelling (both generative and object oriented) are evident: it speeds up modelling phase allowing the user to replicate and modify object dimensions by changing the value of some parameters.

In CH field, one of the most crucial aspects in implementing an HBIM is the lack of libraries of historical architectural elements (Apollonio et al., 2012). Nevertheless, parametric object modelling is not flexible and imposes many constraints that limit the accuracy of the model and its conformity to surveyed data. Especially in the field of cultural assets, this causes many problems and limitations on the correctness of the modelling of objects.

Working on historical buildings, the attempts to create parametric models often is not sufficient and a model based on families of pre-modelled elements hardly fits the actual form of the object.

In modelling irregularities, there are several class of problem to take into account. First of all, the capabilities of the available

software. BIM tools are conceived for new construction and, generally, do not allow “irregularities” such as out of plumb of the walls, not perfect planarity, off axis lines etc. All these irregularities can be solved more easily with direct modelling tools, but this causes interoperability problems. In addition, creating a high accurate model results in very long modelling times and unmanageable size models.

Literature references on this topic are many (Tommasi et al., 2016; Dore et al., 2015; Bitelli et al., 2017, Barazzetti et al., 2015) but the modelling of irregularities is still an open issue. The representation scale and the purpose of the model are key factor to determine the adequate level of detail, even to avoid having totally unmanageable model unusable for requested analyses (Donato et al., 2017). The representation scale entails a defined tolerance and therefore, according to it, the admissible level of accuracy is defined.

Integration of different modelling techniques using mesh surfaces too could be a feasible solution, but cause interoperability problems (Tommasi et al., 2016). It is therefore author’s opinion that to correctly merge in a unique model elements modelled with different techniques and with different software the new direction of development must look at concrete interoperability; an interoperability that allows data exchange (without loss of information) and thematic data association.

5.1 The adopted strategies for irregular shape modelling

In this case study, a hybrid solution that combines parametric models, direct modelling into BIM environment and meshes has been proposed, trying to overcome interoperability problems using links to external references. In this way, the HBIM is conceived as an archive, an information collector and a unique access point to different data.

Mesh modelling was applied to decorative elements that were linked as external files to BIM elements modelled using simple shapes with comparable volume.

Parametric modelling was performed for repetitive and geometrizable elements, but some parameters were defined as instance parameters in order to edit them locally on the model to allow a better correspondence with the point cloud.

In all other cases, combined techniques were used. First of all, the direct modelling of the elements by extracting 2D profiles from the point cloud and modelling through functions such as extrusion, blending, revolution and Boolean operations.

In addition, on some sample elements (walls, vaults, semi-domes and floors), a test was performed in order to compare different modelling workflow and evaluate the better adherence to surveyed data. The test was realized in Revit environment and three different modelling strategies have been tested, in order to reach the highest level of accuracy, trying to preserve, as far as possible, the parametric feature of the objects.

Here, in particular, the test on a deformed wall is presented: non-linear development, out of plumb and deformations along the vertical development are considered.

The first tested methodology (A) (Figure 7) refers entirely to in-place modelling using only direct modelling tools. The point cloud representing the wall was sectioned with a horizontal plane at the base and at the top. The two closed profiles that define these two sections were then drawn. A blending operation allowed to create the wall starting from the base and top profiles.

The second implemented methodology (B) was to create a wall based on a surface, using the Revit function “Wall by face” that allows placing walls on non-horizontal faces of a mass instance or a generic model. Conversely from the previous case, here it is

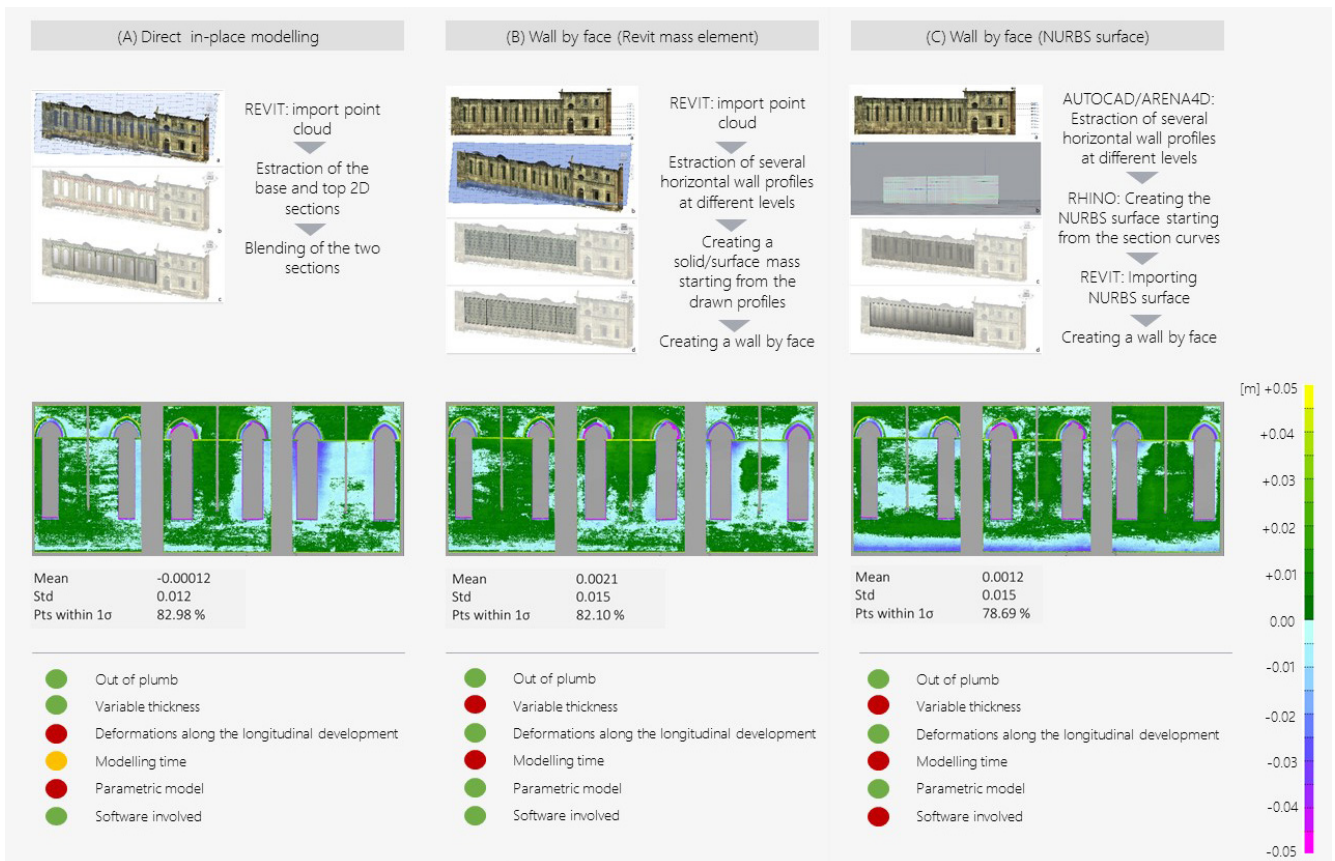


Figure 7_Summary and comparison of the three tested methodologies.

necessary to section the wall at different levels to reproduce more faithfully its conformation. Moreover, only one side of the wall (e.g. internal) is sectioned while the other will be modelled consequently. Based on the sections made, a surface or solid mass is created. On this surface, then, the parametric wall by face will be created.

The third approach (C) is similar to the second one, but it differs in the first step. As in the previous case, this workflow leads to the creation of a wall by face, but starts from a NURBS surface. Creating a NURBS surface from the point cloud, using modelling software such as Rhinoceros (Rhinoceros 2018), could ensure a higher accuracy and a better adherence to reality. Nevertheless, it requires the use of software different from Revit and could cause interoperability problems.

The comparison (Figure 7) showed that the results from a metric point of view are more or less comparable. Other factors, in particular the need to create parametric or unique elements, modelling times and efforts, must therefore be taken into account.

5.2 2D and 3D mapping

In historic buildings documentation, the surface mappings (referring at the same time to material, decay or damages) are an important requirement. They enrich the geometrical survey and give thematic information about the asset. Mappings are the basis for any restoration or conservation interventions that affect the façades of a building and are, therefore, one of the documents required by the superintendents when approving the projects. For this reason, considering a progressive use of the BIM for building conservation, it is mandatory to edit these documents directly into BIM.

Producing mappings in BIM environment is difficult. In fact, BIM software usually does not allow associating information to two-dimensional elements, such as polygons. A first response to this need is presented by (Chiabrando et al., 2017), producing 3D mapping directly on the building façade through specific adaptive components.

The methodology proposed here starts instead from orthophotos and is able to produce automatically the correspondent mapping on the 3D model.

A plug-in to Revit was implemented for:

- Associating the orthophoto to the element and displaying it in a floating window in Revit
- utilizing the orthophoto as a basic tool for 2D mapping
- Automatic 3D modelling of the correspondent elements starting from the 2D polygons.

This tool has been designed to facilitate the tasks of restorers, who usually work with two-dimensional mapping of materials, degradation or interventions to do/already done. With the tool presented here, the aim was to provide a new way of working on

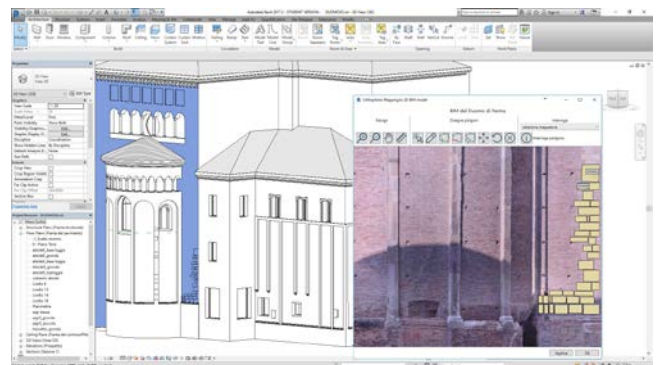


Figure 8_Example of mapping starting from orthophoto.

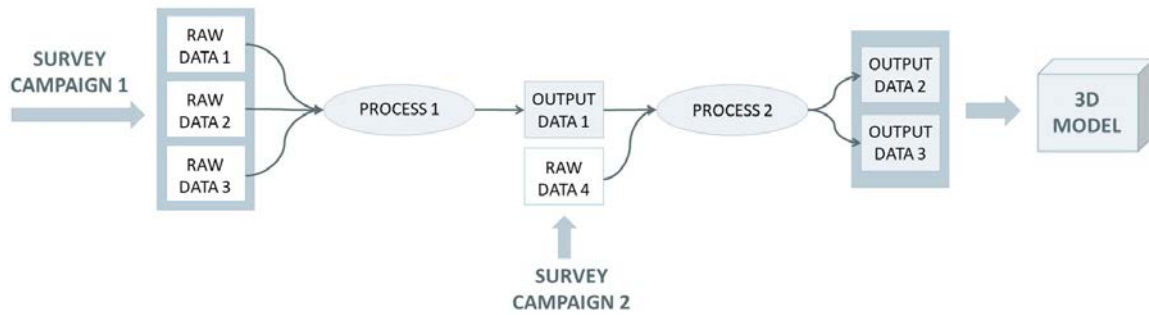


Figure 9_Schematic example of a survey process

2D drawings, directly in the BIM environment, with additional potentials that can be assimilated to GIS: the polygons drawn on the orthophoto are not simple hatched areas but vector polygons with attributes and with corresponding 3D element in the BIM model.

Moreover, each orthophoto is spatially related to the element to which it is attached.

In this way, by using the “Create Parts” function of Revit, which divides the wall surface into delimited portions, the wall is automatically divided into parts corresponding to the 2D polygons drawn on the orthophoto. This also allows the user to get mappings in the three dimensions.

6. SURVEY AND MODELLING METADATA

The final accuracy of the model is influenced by both the quality of the data surveyed and the modelling operations carried out. For this reason, since the information system is based on the 3D model, for a correct use of the data obtained from it, it is important to certify its accuracy and reliability. Metadata on survey and modelling methods, on the accuracy obtained and on the correspondence of the model to reality, are a first instrument for monitoring data quality and the basis for a rigorous and scientific analysis of the object under investigation.

6.1 Survey metadata

In complex surveying processes, documentation of the executed process becomes even more important to allow the entire chain to be reconstructed and the executed control/verification to be performed.

Therefore, a methodology to enter the quality of the survey in the database linked to the geometric model, and let the user to verify at any time the correctness of the product he is working on, has been set up.

A database section was specifically structured to host data and metadata related to the survey, which would allow its description and documentation, in order to provide the user with a tool to control and keep track of the operations carried out.

The survey has been conceived as the sum of Survey Data and Processes. The data may be either the raw data or the processes output. Processes document the type of elaborations, with the associated input and output data.

The structure of the database makes it possible to link data and processes in a sequential way, in order to reconstruct the entire sequence of raw data, processes and processed data, from the initial data produced by the instrument to the output data used for modelling (Figure 9). Both with regard to data and processes, it is possible to associate descriptive metadata and the link to specific external reference files.

The data entry is possible through specific graphical user interfaces.

6.2 Modelling metadata

As for the survey, even for modelling, it is not yet adequately defined how to certify and validate BIM model quality and accuracy.

To document the modelling process these data are required:

- A description of how the modelling has been done
- Data about the adherence of the model to the surveyed data (Level of Accuracy LOA)
- Data about the knowledge (geometric, structural and material) of the object (Level of Knowledge LK)

LOA refers to the five Levels of Accuracy (LOA10, LOA20, LOA30, LOA40, LOA50) as defined by the US Institute of Building Documentation (USIBD) and described in (USIBD 2016).

For the Level of Knowledge, instead, a specific reference standard that defines this parameter does not exist. Nevertheless, this concept can be compared with the *Level of Knowledge (LK)*, provided by the Italian “Technical Standards for Construction” (Italian NTC 2009). Four different levels

Level of Knowledge	Geometry (LKG)	Structure (LKS)	Material (LKM)
LK 0 Supposed	The geometry of the structure is not known and is supposed from analogies or images.	The structure and the construction technique of the element is not known and supposed from analogies.	Materials are not known and supposed from images or from view.
LK 1 Limited	The geometry of the structure is known from 2D surveys or original drawings.	Construction details are based on a simulated design carried out according to the construction practice.	Materials are known but their properties are not available neither from constructive designs nor from test certificates.
LK 2 Appropriate	The geometry of the structure is known from 3D incomplete survey integrated with other data.	Construction details are known from an in-situ analysis or are partially available from constructive designs.	Information on the mechanical properties of the materials is available on the basis of either the original design drawings or original test certificates, or appropriate in-situ tests.
LK 3 Accurate	The geometry of the structure is known from 3D complete and certified survey, with adequate accuracy to the representation scale.	Construction details are known from an accurate in-situ analysis or are available from original constructive designs.	Information on the mechanical properties of the materials is available on the basis of the original design drawings or certificates, or by in-situ accurate tests.

Figure 10_ Implemented Level Of Knowledge (LK) classification

(LK0 Supposed, LK1 limited, LK2 Appropriate, LK3 Accurate) were introduced, divided by geometry, materials and structures, as described in the figure (Figure 10)

A section of the database was then structured to describe the modelling process (modelling technique, author, date, etc.) and to insert values related to the model's adherence to the surveyed data: LOA and LK.

This information can be entered through a specific interface and is associated to each single object modelled, since the global quality of the model could be, and is in the most cases, different from the local quality of the single items.

7. THE HBIM IMPLEMENTED SYSTEM

A BIM process applied to Cultural Heritage must respect the peculiarities of historical assets, both in terms of its geometric description and association of information. This involves considerable problems and difficulties that are still open research topics (Donato et al., 2017; Fassi et al., 2015). As far as the management of the semantic data and the model enrichment are concerned, at the time being, there are no commercial tools capable of fulfilling all the specific functions required by Cultural Heritage documentation.

The thesis implements a HBIM system with the aim to be a concrete solution to the lack of suitable instruments for Cultural Heritage maintenance, conservation and restoration. The application is an information system at the architectural scale and has been designed in order to be as flexible and customizable as CH specific needs require. It is based on a BIM 3D model of the building and, thanks to the interaction with an external database specifically structured, allows users to properly archive and query the data required to describe the building. The application is standalone and has been structured to be integrated with major BIM software and with web applications as well.

7.1 Database design phase

In order to cope with the limitations imposed by the main BIM software, which generally do not allow to create hierarchical information or to manage many-to-many relationships, it was decided to implement an external and independent database and to interface it with the BIM software (in this case Revit). In addition, this choice has allowed not to be bound to a specific

software house and to create a flexible solution, adaptable to the needs of the case study and accessible through different desktop and web applications.

Database design was based on the analysis of the asset and on regulations relating to planned maintenance. The building was then classified into four semantic levels: Building, Functional Areas, Technological Elements and Technological Sub-Elements. The functional areas breakdown reflects the spatial organization of religious buildings (central nave, aisles, transept, choir etc.); the technological elements follow the guidelines for the drafting of plans for planned conservation (Della Torre, 2003) and are divided into vertical structures, horizontal structures, roofing etc.; the technological sub-elements were introduced to allow for a further breakdown of the main elements, in order to better detail the structure of the building.

At the building level, according to the DPCM 9 February 2011 and the Code of Cultural Heritage and Landscape, the building is identified uniquely through three fundamental parameters: denomination, toponymastics and cadastral data.

Since the primary goal of the implemented HBIM was to archive and manage all data about the building, document the interventions occurred and assist maintenance and conservation planning, the database implementation focused on information and data required for scheduled conservation. Therefore, the requirement-performance analysis and the methodology proposed by (Della Torre, 2003) have been adopted.

According to this approach, the quality of the built objects is expressed according to "performance" and/or conservative "problems", which, summarizing both the "requirement" for use and the "risk" for conservation, was more suitable for describing historical elements behaviour (Della Torre, 2003):

Therefore, to each technological element, data about:

- *Problems* that can affect the element
- the evaluation of *Damages* that affect the object
- the program of preventive *Actions*
- the consequent *Inspections*.

has been associated.

All this information contributes to the drafting of the technical manual and maintenance program of the conservation plan.

In addition to these data, to describe the actual state of the Parma Cathedral, the Fabbrica administration required data entry to document the degradation of external façades (resulting in decay and material mapping) and structural monitoring. In

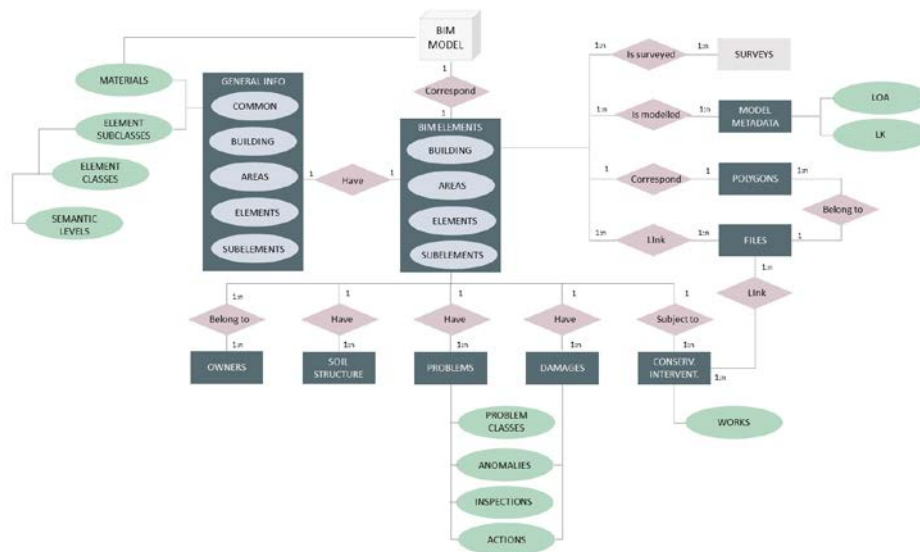


Figure 11_Entity- Relationship schema.

addition, the main documents concern: data about previous surveys, both textual and graphic data; archival data; photographic images (current and historical); historical analyses and publications about the Cathedral.

As shown in the entity-relationship schema (Figure 11), a unique atomic database entity was identified corresponding to a general BIM Element. This entity is the link between the database data and the three-dimensional model.

Despite the presence of four different semantic levels, it was decided to create a single database table as, conceptually, the four levels are the same. In fact, they all correspond to a graphic element and are BIM elements, even if with different levels of hierarchical grouping.

From the data association point of view, the structure has been designed in order to be as flexible as possible and implementable over time with different data. It was decided to organize the data into independent database tables. These tables can be associated to the element according to the needs. In this way, the user decides which data to associate with the element, making the system flexible. Additionally, it is always possible to add a new entity and associate it with the elements.

As far as the choice of the RDBMS is concerned, Microsoft SQL Server (Microsoft SQL, 2017) was used, since it can be perfectly integrated with the application structure based on Entity Framework technology, as will be explained below.

7.2 Technical features of the implemented application

The application implemented in the thesis has been developed to ensure easy usability and multi-platform implementation. The idea was to apply the same data model to different application usages (desktop and web interfaces), without changing the basic logical structure and preserving the same functions and rules.

It was possible thanks to the use of .NET Framework. .NET Framework provides a consistent object-oriented programming environment, minimizes software deployment and versioning conflicts (.NET Framework, 2017). In the present case study, the application has to be integrated with BIM software and, in particular, Autodesk Revit has been used to test this integration. Revit provides .NET compliant API, thus, for the development of application, it was chosen to operate within the .NET Framework, using the available libraries for interfaces creation, database implementation, integration with other software and on-line extension, ensuring consistency and interoperability.

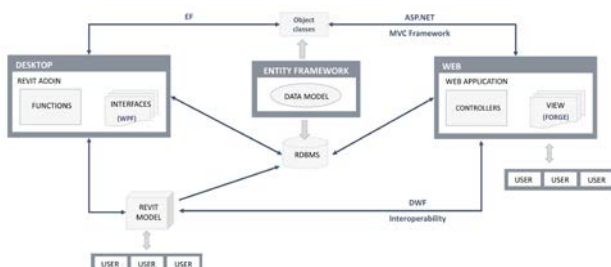


Figure 12_Architecture of the implemented application.

In particular, the Entity Framework (EF) technology was used to support the development of the whole application enabling the easy interaction with the underlying relational database. EF technology allows the developer to define in an abstract way the data model that governs the entire application. This model is compliant to the entity-relationship schema described previously. From this data model, EF automatically creates, on the one hand, the relational structure of the database, and, on the other, the object classes useful for programming the

application. Therefore, all information can be managed in a consistent and coordinated way, simultaneously at the database, desktop and web application levels. (Figure 12)

For desktop side development, to make the system use easier and more intuitive, graphical interfaces and data forms have been developed to help with the consultation and implementation of the database. Windows Presentation Foundation (WPF) was used to develop graphical interfaces and to build the desktop client application.

In parallel with the development of the desktop application, its web extension has also been implemented. ASP.NET technology was used in order to exploit the same data model and on the basis of this develop the graphical interface and controllers.

7.3 Integration with Autodesk Revit

The application dialogues with Revit as a plug-in and enrich its functionalities with additional features. The implemented features can be summarized as follows: Connect/create the database; Display data about an item through the graphical interfaces; Query the database and thematic mapping the 3d model; Associate orthophoto to elements, perform 2d mapping and 3D automatic modelling from 2D elements (paragraph 5.2) and Enter survey and model metadata (paragraph 6).

Each Revit project is associated to one database, which can be accessed every time the project is opened. The user can create/connect to the specific database associated to the Revit project, by clicking the “Connect / Create DB” button in the ribbon bar. This function allows Revit to connect to the database, if it already exists, or to create a new one if it does not exist.

The second implemented function (“Info” button) allows the user to get/set all the information about the elements of the model and access directly the database. In order to simplify the interaction with the database, graphical interfaces have been implemented that make operation as data entry, data retrieve, modify and delete, user-friendly and immediately comprehensible to the user.

The user is requested to select an item. The system gets the Id of the selected item and, if it has been already stored in the database, its information is displayed; on the contrary, a new element is created. In this way, the tool allows the user not only to look at and edit the data in the database but also to enter new entities. A dialog box with information opens when the user selects the item as shown in Figure 13.

The User Interface is quite simple and gives access to all the database information. As described above, the information is classified by semantic level of element and grouped by type in descriptive forms. Each form gives access to a specific part of database data. Through these GUI, the user can enter, edit or simply retrieve all data. The available forms allow to:

- Access to all the general and morphological data about the element,
- View the problems that the element presents and the related anomalies,
- See the current and past damages in order to plan the restoration and maintenance operations,
- Access the information about restoration/maintenance/survey works, including photos, textual and technical documents,
- View the original survey data and metadata about methodology, accuracy and execution techniques of the survey
- View or enter metadata about the model execution process

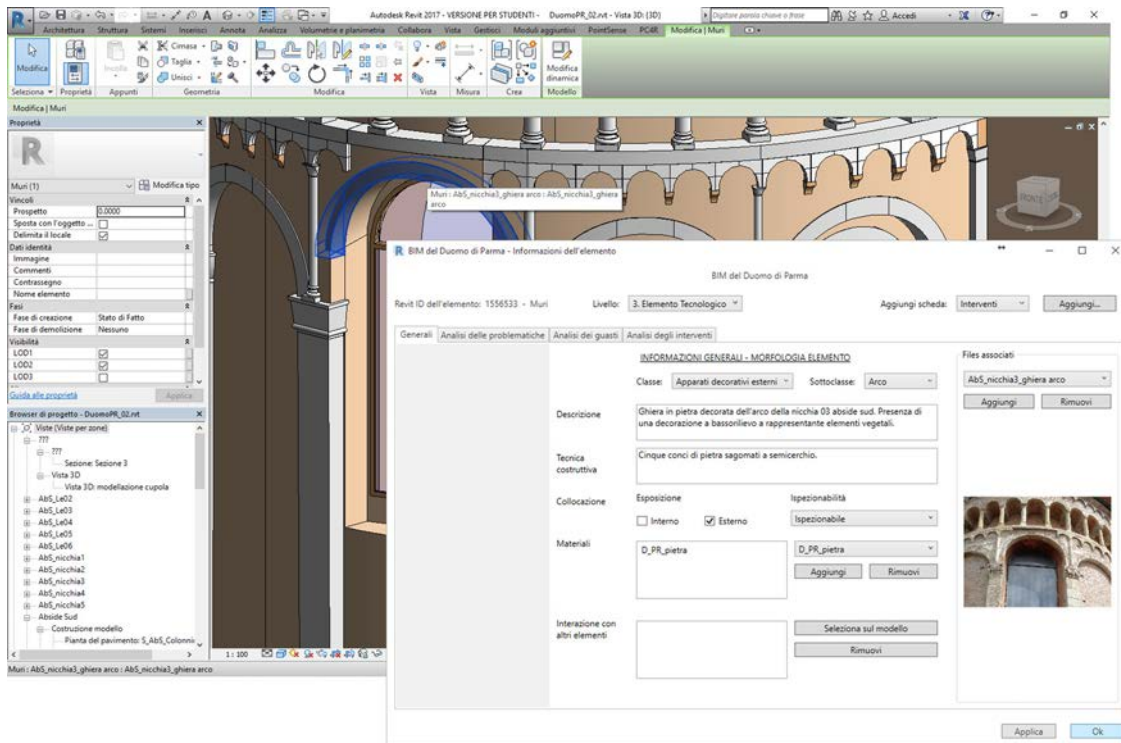


Figure 13_ Example of access to the data contained in the database directly in the Revit environment through a dedicated interface.

- link external files to the model, such as photos, orthophotos, text files, pdf, dwg etc.

In this way, all the information is connected in a consistent and coordinated way and is consultable through a single point of access.

In addition to the data entry function, in a database the query function is very important too. Directly querying a relational database implies the writing of queries (usually through SQL syntax) with different degrees of complexity, depending on analysis to perform, which does not fit the usability required by non-Information Technology specialists.

Thus, to match the user's needs, a graphical interface was implemented that allows querying the database both through text queries and a query builder, theming the Revit 3D model according to the attributes stored in the database and exporting the search results in Excel.

7.4 Data sharing and web application development

In order to allow a wider sharing of the developed application, its use via web has also been implemented. The web allows not to be bound to a specific software solution, guarantees an easy access to data even for non-experts and allows data portability even on site.

The web page (Figure 14) follows the schema developed for the desktop side. The upper part is occupied by tabs that give access to information organized in sheets.

The central part of the interface is constituted by the 3D model viewer. It is provided by Autodesk 3d Forge viewer (Autodesk Forge, 2017), which allows uploading and viewing the Revit model and its parameters directly via the web. By clicking on elements in the model the user can access to the same of the desktop side, operating directly on the database.

In this way, being the database shared between all the applications (desktop and web/mobile), all data are consistent and it is possible to access the information about the model everywhere and from any device.

8. CONCLUSIONS

In this work, the implementation of a BIM system aimed at maintenance, conservation and restoration of Cultural Heritage was presented. Its main goal was to give a concrete answer to the lack of specific tools required by Cultural Heritage documentation: organized and coordinated storage and management of historical data, easy analysis and query, time management, 3D modelling of irregular shapes, flexibility, user-friendliness, etc.

To address all these topics, the experience typical of geomatics in design and implementation of relational databases integrated into GIS software has been essential. In the HBIM the approach is comparable and only the scale of investigation changes, from the territorial to the architectural one.

The proposed solution, thanks to a freestanding database, allows, on the one hand, customizing data organization according to the asset specific needs; on the other hand, it gives more flexibility without being tied to a specific commercial solution.

The application was implemented with the specific aim of providing tools also for non-AEC experts: it gives user-friendly graphical interfaces to access the data and makes available tools for data entry, element modelling, attribute query and thematic mapping.

In addition, in any BIM process applied to existing building, the validation of the model is fundamental: geometric and semantic data have to be reliable and accurate enough to fulfil specific requirements and their reliability and accuracy should be properly documented by BIM authors. The model accuracy is affected by both the survey accuracy and the modelling accuracy, so survey and modelling phases should be certified. The thesis offered a contribution on this topic, by proposing prototype tools that allow inserting survey metadata. The system allows each modelled element to be associated to the survey products used for its modelling and also to trace backwards all the survey chain processes (up to the raw data), in order to

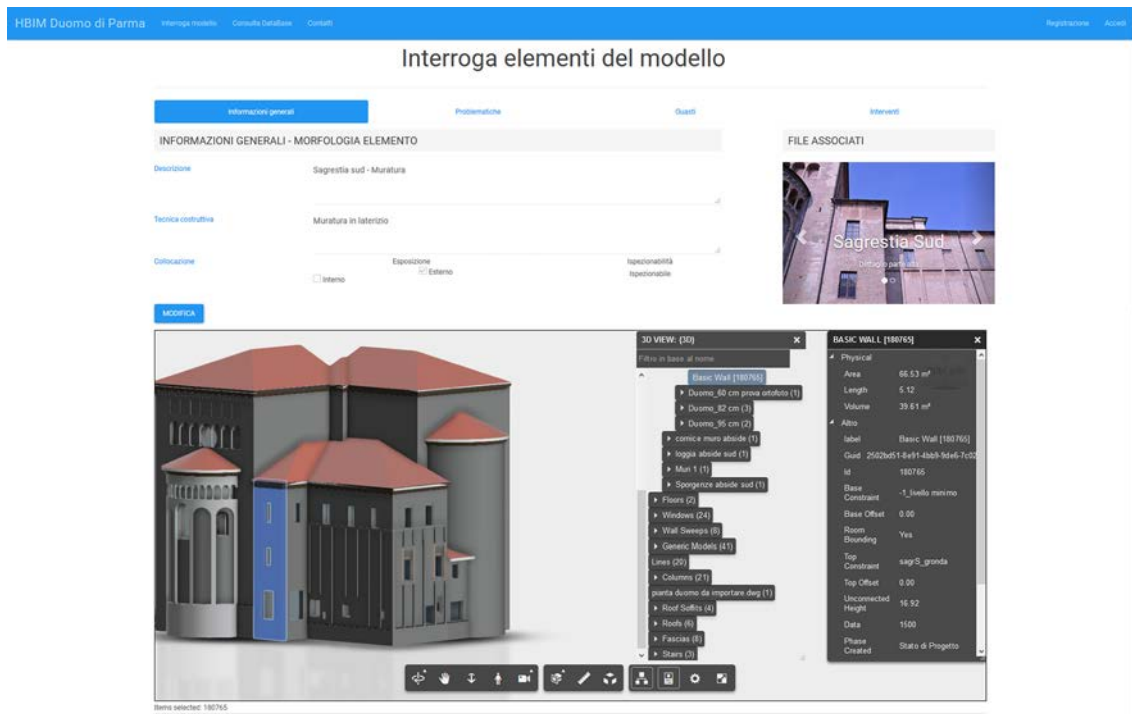


Figure 14_ Web page created for access to database data and to the 3D model.

evaluate the correctness and quality of the operations carried out.

The experimentation carried out in this research shows that the use of HBIM in the cultural heritage field is a good solution and a potential for more coordinated and efficient management and preservation. Nevertheless, a widespread application of HBIM system to cultural heritage buildings requires a large investment in terms of costs, training and processing times.

In particular, it is necessary to invest in technological development and scientific research to provide accurate and verifiable data, optimise and speed up surveying and modelling processes, overcome interoperability problems and create user-friendly systems.

On the other hand, it is necessary to have a common and shared normative references and standards for addressing processes and methodologies, in order to support the transition to BIM.

It is essential to invest in training, both to make people aware about the importance and opportunities that these tools can provide and to make BIM use effective.

Only in this way, it will be possible to create the effective and interdisciplinary dialogue between all the actors involved, which is fundamental when approaching a complex heritage such as the Cultural Heritage one.

ACKNOWLEDGE

The Fabbrica del Duomo di Parma assistance, in particular of Eng. Gualtiero Savazzini and Arch. Sauro Rossi, and the precious helpfulness of Stefano Volta are greatly acknowledged.

REFERENCES

NET_Framework <<https://docs.microsoft.com/en-us/dotnet/framework/get-started/overview>>, Last access 26/09/2017.

Achille, C., Brumana, R., Fassi, F. & Tuncer, H. (2007). Application of mixed technique for the 3D modelling of the

noble floor of the Real Villa in Monza. *International Archives of the Photogrammetry, Remote Sensing and Spatial Information Sciences*, 36(5/C53).

Apollonio, F., Gaiani, M. & Sun, Z. (2012). BIM-based modeling and data enrichment of classical architectural buildings. *Scires-It*, 2(2), pp. 41-62.

Autodesk Forge < <https://forge.autodesk.com/>>. Last access 26/09/2017

Autodesk Revit - <https://www.autodesk.it> - Accessed 04/2018.

Barazzetti, L., Banfi, F., Brumana, R. & Previtali, M. (2015). Creation of parametric BIM objects from point clouds using NURBS. *The Photogrammetric Record*, 30(152), pp. 339–362.

Bianchi, G., Bruno, N., Dall'Asta, E., Forlani, G., Re, C., Roncella, R., Santise, M., Vernizzi, C., & Zerbi, A. (2016). Integrated survey for architectural restoration: a methodological comparison of two case studies, *The International Archives of the Photogrammetry, Remote Sensing and Spatial Information Sciences*, XLI (B5), pp. 175-182.

Bitelli, G., Dellapasqua, M., Girelli, V.A., Sanchini, E. & Tini, M.A. (2017). 3D geomatics techniques for an integrated approach to Cultural Heritage knowledge: the case of San Michele in Acroboli's Church in Santarcangelo di Romagna. *The International Archives of the Photogrammetry, Remote Sensing and Spatial Information Sciences*, 42(5/W1), pp. 291-296.

Blasi, C. & Coisson, E. (Editors) (2006). *La fabbrica del Duomo di Parma. Stabilità, rilievi e modifiche nel tempo*. Grafiche Step, Parma.

- Bruno, N. (2018). From survey to analysis for Cultural Heritage management: a new proposal for database design in BIM. PhD Thesis, University of Parma, Italy <<http://hdl.handle.net/1889/3578>>.
- Castagnetti, C., Dubbini, M., Ricci, P.C., Rivola, R., Giannini, M. & Capra, A. (2017). Critical issues and key points from the survey to the creation of the historical building information model: the case of Santo Stefano Basilica. *International Archives of the Photogrammetry, Remote Sensing and Spatial Information Sciences*, 42 (5/W1), pp. 467-474.
- Chiabrando, F., Io Turco, M. & Rinaudo, F. (2017). Modeling of the decay in a HBIM starting from the 3D point clouds. A followed approach for cultural heritage knowledge. The *International Archives of the Photogrammetry, Remote Sensing and Spatial Information Sciences*, 42(2/W5), pp. 605-612.
- Crespi, P., Franchi, A., Ronca, P., Giordano, N., Scamardo, M., Gusmeroli, G. & Schiantarelli, G. (2015). From BIM to FEM: the analysis of an historical masonry building. In Mahdjoubi L., Brebbia C.A. & Laing R. (editors), *Building Information Modelling (BIM) in Design, Construction and Operations*, Witpress, pp. 581-592.
- De Luca, L., Bussayarat, C., Stefani, C., Véron, F. & Florenzano, M. (2011). A semantic-based platform for the digital analysis of architectural heritage Computers & Graphics. Volume 35, Issue 2, April 2011, Pages 227-241. Elsevier.
- Della Torre S. (editor), 2003. *La conservazione programmata del patrimonio storico architettonico, Linee guida per il piano di manutenzione e il consuntivo scientifico*. Edizioni Angelo Guerrini e Associati Spa, Milano.
- Donato, V., Biagini, C., Bertini, G. & Marsugli, F. (2017). Challenges and opportunities for the implementation of H-BIM with regards to historical infrastructures: a case study of the Ponte Giorgini in Castiglione della Pescaia (Grosseto – Italy). *International Archives of the Photogrammetry, Remote Sensing and Spatial Information Sciences*, 42 (5/W1), pp. 253-260.
- Dore, C., Murphy, M., McCarthy, S., Brechin, F., Casidy, C. & Dirix, E. (2015). Structural simulations and conservation analysis – historic building information model (HBIM). *International Archives of Photogrammetry, Remote Sensing and Spatial Information Sciences*, 40(5/W4), pp. 351–357.
- Eastman, C., Teicholz, P., Sacks, R. & Liston, K. (2008). *BIM Handbook – A Guide to Building Information Modeling for Owners, Managers, Designers, Engineers, and Contractors*, John Wiley & Sons, Inc.
- Fai, S., Graham, K., Duckworth, T., Wood, N. & Attar, R. (2011). Building Information Modelling and heritage documentation. Proceedings XXIII International CIPA Symposium, Prague, Czech Republic, September 12 - 16, 2011.
- Fassi, F., Achille, C., Fregonese, L. Monti, C. (2010). Multiple data source for survey and modelling of very complex architecture. *International Archives of Photogrammetry, Remote Sensing and Spatial Information Sciences*, 38(5), pp. 234–239.
- Fassi, F., Achille, C., Mandelli, A., Rechichi, F. & Parri, S. (2015). A new idea of BIM system for visualization, web sharing and using huge complex 3D models for facility management. The *International Archives of the Photogrammetry, Remote Sensing and Spatial Information Sciences*, 40(5/W4), pp. 359-366.
- Forlani G. & Mussio L., 1986. Test on Joint adjustment of geodetic and photogrammetric data. *International Archives of Photogrammetry and Remote Sensing*, vol. XXVI, part 3.1, Rovaniemi, 1986, 237-251. issn 0256-1840.
- Garagnani, S. & Manferdini, A.M. (2013). Parametric accuracy: Building Information Modeling process applied to the cultural heritage preservation. *International Archives of the Photogrammetry, Remote Sensing and Spatial Information Sciences*, 40(5/W1), pp. 87-92.
- Guidi, G., Remondino, F., Russo, M., Menna, F., Rizzi, A. & Ercoli, S. (2009). A multi-resolution methodology for the 3D modeling of large and complex archaeological areas. *International Journal of Architectural Computing*, 7(1), pp. 39–55.
- Italian NTC (2009), Circolare 2 febbraio 2009, n. 617 - Istruzioni per l'applicazione delle "Nuove norme tecniche per le costruzioni" di cui al D.M. 14 gennaio 2008 – Cap. 8, Costruzioni esistenti.
- Microsoft SQL <Server <https://www.microsoft.com/it-it/sql-server/sql-server-2016>>. Last access 26/09/2017.
- Remondino, F. (2011). Heritage recording and 3D modeling with photogrammetry and 3D scanning. *Remote Sensing*, 3(6), pp. 1104-1138.
- Rhinoceros - <https://www.rhino3d.com/it/> - Accessed 04/2018.
- Saygi, G. & Remondino, F. (2013). Management of Architectural Heritage Information in BIM and GIS: State-of-the-art and Future Perspectives. *International Journal of Heritage in the Digital Era*. 2 (4), pp. 695-713.
- Stefani, C., De Luca, L., Veron, P. & Florenzano, M. (2010). Time indeterminacy and spatio-temporal building transformations: an approach for architectural heritage understanding. *International Journal for Interactive Design and Manufacturing (IJIDeM)* 4(1), pp.61-74.
- Tommasi, C., Achille, C. & Fassi, F. (2016). From point cloud to BIM: a modelling challenge in the Cultural Heritage field. The *International Archives of the Photogrammetry, Remote Sensing and Spatial Information Sciences*, 41(B5), pp. 429-436.
- USIBD (2016). Level of Accuracy (LOA) Specification Guide.
- Volk, R., Stengel, J. & Schultmann, (2014). Building Information Modeling (BIM) for existing buildings – Literature review and future needs. *Automation in Construction* 38, pp. 109–127.

3D MODELLING BY LOW-COST RANGE CAMERAS: METHODS AND POTENTIALITIES

R. Ravanelli ^a

^a Geodesy and Geomatics Division, DICEA - University of Rome "La Sapienza", Rome, Italy
roberta.ravanelli@uniroma1.it

KEY WORDS: Close-range 3D modelling, Range cameras, Kinect v1, Kinect v2, Structure Sensor

ABSTRACT:

The aim of this work is to evaluate the potentialities of low-cost range cameras for geomatic applications and to provide useful indications for their practical use. The three most popular and/or promising low-cost range cameras, namely the Microsoft Kinect v1, the Microsoft Kinect v2 and the Occipital Structure Sensor, were firstly characterized from a geomatic point of view in order to assess the metric quality of the 3D geometry data retrieved by them. These investigations showed that such sensors present a depth precision and a depth accuracy in the range of some millimeters to few centimeters, depending both on the operational principle adopted by the single device (Structured Light or Time of Flight) and on the depth itself. On this basis, two different models were identified for precision and accuracy vs. depth: parabolic for the Structured Light (the Kinect v1 and the Structure Sensor) and linear for Time of Flight (the Kinect v2) sensors, respectively. Then the effectiveness of such accuracy models was demonstrated to be globally compliant with the found precision models for all the three sensors. Furthermore, the proposed calibration model was validated for the Structure Sensor. Finally, four case studies were carried out to test the use of range cameras for monitoring oscillatory motions (relevant for structural and/or industrial monitoring), for the 3D surveying of indoor environments, for the documentation of cultural heritage and for testing their integration with photogrammetry. The case studies confirmed the promising performances of the investigated range cameras.

1 INTRODUCTION

Nowadays, the demand of 3D models for documenting objects and environments is continually increasing in several disciplines such as robotics, medicine, cultural heritage, architecture. However, the traditional 3D modelling techniques (*i.e.* photogrammetry and laser scanners) can be very expensive and/or time consuming, as they often need qualified technicians and specific post-processing phases. Thus, it is important to find new instruments, able to provide low-cost 3D data quickly and in a user-friendly way, at least for some applications.

Range cameras seem one of the most promising tools to achieve this goal: they are active imaging sensors, low-cost and easy-to-use, able to natively measure the distances of several points at high frame rate (30 - 60 Hz). At every acquisition, they produce a depth map of the scene, an image in which each pixel contains its own distance from a specific reference, normally associated to the sensor itself. Starting from this depth map, range cameras capture a dense point cloud of the scanned scene.

Therefore, according to the definition given in (Boehler and Marbs, 2002), range cameras can be considered, to all intents and purposes, veritable 3D scanners. Furthermore, Simultaneous Localization And Mapping (SLAM) algorithms, such as KinectFusion (Izadi et al., 2011), (Newcombe et al., 2011), leverage the depth data and the high frame rate of such sensors, in order to fuse the depth maps captured from different view points as soon as they are acquired. In this way, the depth maps are merged into an overall 3D model easily and practically in real-time by continually estimating the pose of the moving sensor. In addition, range cameras are continually evolving and they will be soon integrated in consumer grade smart devices, becoming available to a wider audience and enabling their use together with other sensors (see, for example, (Benedetti et al., 2016), (Ravanelli et al., 2016)).

Thanks to all these features, nowadays this technology can play an important role in close-range 3D modelling: range cameras can be used as 3D scanners to easily collect dense point clouds practically in real-time. At the same time, though, range cam-

eras still remain a relatively new 3D measurement instrument, not yet exhaustively studied. Thus it is essential to assess the metric quality of the depth data retrieved by these sensors. This work is precisely included in this background: the aim is to evaluate the potentialities of range cameras for geomatic applications and to provide useful indications for their practical use (Ravanelli, 2017a).

In particular, specific models are proposed to represent random and systematic errors of depth measurements (dependent on the operational principle adopted by the single sensor and on the distance from the captured object) for the considered range cameras, thus describing their precision and accuracy, and proves the effectiveness of such models for the calibration of these sensors (Section 3). Furthermore, some investigations about the registration process of depth and color images are also described (Section 4). Finally, some case studies are presented in order to provide insights into the practical usage of range cameras in different disciplines (Section 5).

2 BASICS OF RANGE CAMERA FUNCTIONING

The depth sensor is the heart of the range camera technology. Although its function is equivalent for all the range cameras, it is worth noting that the underlying working principle can be different, depending on the technique adopted by the specific range camera. To generate the depth map, range cameras can use two different operational principles: it is possible to distinguish between the Time of Flight (ToF) range cameras and the Structured Light (SL) range cameras (Dal Mutto et al., 2012), (Grzegorzec et al., 2012), (Remondino and Stoppa, 2013).

ToF range cameras generate the depth map by measuring the time of flight taken by an emitted electromagnetic wave to travel from the sensor itself to the object and back. For this family of devices the depth sensor consists of a matrixial collection of emitters and receivers.

Differently, SL range cameras are active triangulation systems that emit a bidimensional light pattern directly on the surface of

the object to be measured and generate the depth map by evaluating the deformation (disparity) between the pattern emitted and the one back-projected by the object itself. In this case the depth sensor consists of a projector and a frequency-matched camera. SL range cameras differ from traditional structured light systems since, instead of projecting a visible stream of changing shapes or bands of light, they illuminate the scene to be with a near-infrared pattern.

3 ANALYSIS OF THE GEOMETRIC POTENTIAL OF LOW-COST RANGE CAMERAS

In this Section, the 3D modelling capabilities of the three most popular and/or promising low-cost range cameras, namely the Kinect v1, the Kinect v2 and the Structure Sensor, are investigated and compared in order to assess the metric quality (precision and accuracy) of the depth data retrieved by them. After a brief overview of the main features of the investigated sensors, the geomatic characterization of the three considered devices is described in details.

3.1 Sensor technical specifications

As is well known, the first Microsoft Kinect has opened the way to a new generation of range cameras, although it was primarily designed as motion sensing input peripheral for Xbox 360 game console. In fact, both the Kinect v1 and the Kinect v2 are webcamstyle, add-on devices which enable users to interact with the game console without using a traditional hand-held joystick. Players can indeed control play, action and movement of their on-screen characters only using body gestures, through a Natural User Interface (NUI). Gesture recognition is made possible by the devices depth sensor which provides a real time depth map. Hence, the Kinect depth sensor is, to all intents and purposes, a range camera.

On the other side, the Occipital Structure Sensor has been conceived from the beginning to be the first range camera for mobile devices: characterized by compact dimensions and an internal battery, it can be quickly and securely connected to an iOS device through a specific bracket accessory. It was launched on Kickstarter in September 2013, raising almost 1.3 millions of dollars in 45 days of campaign.

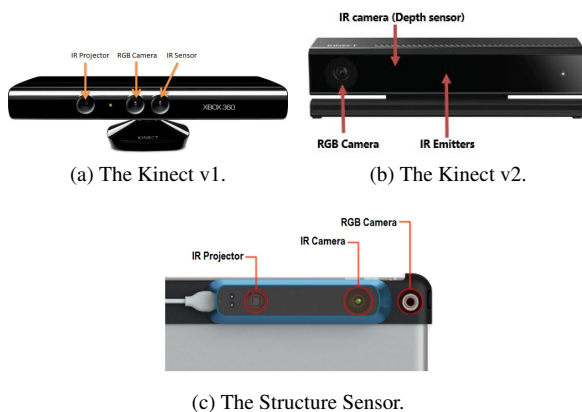


Figure 1: The internal components of the three investigated sensors.

Therefore, the technical specifications of the three investigated sensors are very different, although their principal hardware components (see Figure 1), namely the IR camera, the IR projector (for SL sensors: the Kinect v1 and the Structure Sensor) or the

IR emitters (for the ToF sensor, that is the Kinect v2) and the color camera, if present, fulfill the same function: the first two make up the depth sensor, that acquires the depth data, whereas the latter captures the texture information. Thus also the features of the data captured by them are diverse.

As regards the depth stream, the Kinect v1 supports three different resolutions: 640×480 pixels, 320×240 pixels, and 80×60 pixels, all at 30 frames per second (fps). The Kinect v2 sensor provides instead a 512×424 16-bit depth stream, again at the same 30 fps acquisition rate.

Furthermore, the Kinect v2 sensor uses an active infrared stream, lighting independent, characterized by a 512×424 resolution, at 30 frames per second; thanks to USB3 connection, the infrared stream can be used simultaneously with the colour stream.

For the Kinect v1, instead, this is not possible because of USB2 low bandwidth and infrared data (640×480 resolution - 30 fps) can be retrieved only disabling the colour stream.

Moreover, the Kinect v2 sensor presents a wider field of view (70°×60°), without needing a tilt motor, as it happens for Kinect v1 (57°×43°), where the motorized base can move the sensor bar 27° up and down.

In addition to the depth sensor, the bar of both the two Kinect sensors houses also the colour camera, an accelerometer and an array of four microphones (see Figure 1(a) and Figure 1(b)). The colour camera does not participate in the depth sensing process, but it has the purpose to collect the texture of the scene for applications like face tracking. The Kinect v1 colour camera is a 8-bit resolution VGA camera which supports different resolutions at different frame rates (Cathue, 2012): 640×480 pixels at 30 fps using RGB format; 1280×960 pixels at 12 fps using RGB format; 640×480 pixels at 15 fps using YUV format. Instead, the Kinect v2 colour camera is a full HD camera, with a resolution of 1920×1080 pixels returned at 30 fps in the YUY2 raw image format (the acquisition rate drops to 15 fps in case of low light). The microphones are needed for speech recognition. Finally the tri-axis accelerometer (a Kionix KXS9 for v1, a Kionix KXUD9 (Chipworks, 2013) for v2) is used to determine the orientation of the sensor (for Kinect v2 accelerometer APIs are no longer exposed in the official Microsoft SDK).

Concerning the Structure Sensor, it can stream depth data at two different depth resolutions: 320×240 pixels at both 30 fps and 60 fps and 640×480 pixels at 30 fps. As regards the infrared stream, the device provides two streams: one at 320×248 at 30 fps and one at 640×488 at 30 fps. However, the Structure Sensor does not have an own color camera, but it can retrieve the RGB data from the iOS device at which is connected. The depth streams at 30 fps can be aligned to the iOS device colour camera through the Structure SDK.

The technical specifications of the investigated sensors are summarized in Table 1.

	KINECT v1	KINECT v2	STRUCTURE SENSOR
Technology	Structured Light	Time of Flight	Structured Light
Official Depth Range	0.4–4 m	0.5–4.5 m	0.4–3.5 m
Depth Field of View (H×V)	57°×43°	70°×60°	58°×45°
Colour Stream	640×480 @ 30 fps 1280×960 @ 12 fps	1920×1080 @ 30 fps	n.a.
Depth Stream	80×60 @ 30 fps 320×240 @ 30 fps 640×480 @ 30 fps	512×424 @ 30 fps	320×240 @ 30 fps 320×240 @ 60 fps 640×480 @ 30 fps
Infrared Stream	640×480 @ 30 fps	512×424 @ 30 fps	320×248 @ 30 fps 640×488 @ 30 fps
Audio stream	4-mic array 16kHz	4-mic array 48kHz	n.a.
SDK Officially Supported OSs	Windows 7 Windows 8 Windows 8.1	Windows 8 Windows 8.1	iOs
Cost	150 \$	150 \$	379 \$

Table 1: Technical specifications of the investigated sensors.

3.2 Models for depth precision and depth accuracy

As mentioned, one Kinect v1, one Kinect v2 and one Structure Sensor were considered and characterized from a geomatic point of view. A specific test field was thus implemented in order to analyse the behaviours of the random and systematic errors of the depth measurements for the three investigated sensors.

In particular, the planar opaque surface of a cabinet (see Figure 2(b)) was acquired by each sensor at several known distances, taking care to place each device as parallel as possible to the target plane. For each distance, the Kinect v1, the Kinect v2 and the Structure Sensor were set together on top of the same tripod (see Figure 2(a)).

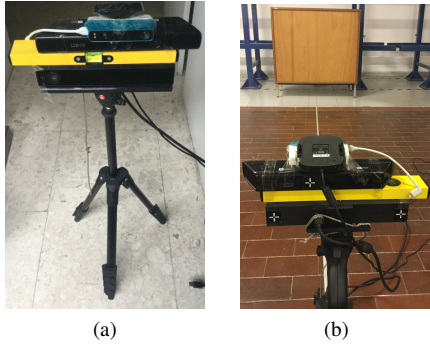


Figure 2: The experimental setup. (a) From top to bottom: the Structure Sensor, the Kinect v1, a spirit level and the Kinect v2 mounted on the tripod. (b) The tripod with the three sensors in front of the reference planar surface.

Moreover, in order to carefully measure the reference geometry with a total station, three targets were fixed onto the back side of the sensors. The parallelism between each sensor and the planar surface of the cabinet was achieved assuring that the horizontal distances of the three targets measured with the total station were equal (with an accuracy better than 1 mm) at each distance. In this way, the tripod was moved for a total of nine steps from 90 to 400 cm from the planar surface. Lower distances were not investigated since in that case the Kinect v2 depth maps were affected by a too strong backscattering signal severely impacting the measurements.

The procedure was identically repeated twice for each device, always considering the corresponding warm-up time (Chow et al., 2012), (Sarbolandi et al., 2015), (Lachat et al., 2015). For each position/step, 150 consecutive depth maps were acquired by each sensor, but, in order to exclusively investigate the area well within the reference planar surface, only the central 50×50 pixel window was considered.

3.2.1 Depth resolution analysis To evaluate the depth resolution of the three sensors, the depth histograms were computed considering a sample of 375000 observations (the depth of 50×50 pixels in the window for the 150 frames) for each distance from the reference surface (in our test case equivalent to the depth). Figure 6 shows the results obtained for the first test and clearly highlights two different behaviours, depending on the operational principle (SL or ToF) of the single sensor.

In particular, the resolution of the SL devices (Figure 3 and Figure 5) worsens following a parabolic trend (R^2 of 1.00 for both the Kinect v1 and the Structure Sensor) when the distance/depth from the target increases (d_R); on the other side, the Kinect v2 resolution shows a constant value of 1 mm for every distance (Figure 4).

Thus, the depth data acquired by the Kinect v2 are characterized

by a substantially continuous distribution with a resolution of a millimeter level, independently from the distance from the reference plane; on the contrary, for Kinect v1 and Structure Sensor the depth data present a discrete distribution, with a resolution dependent from the distance itself.

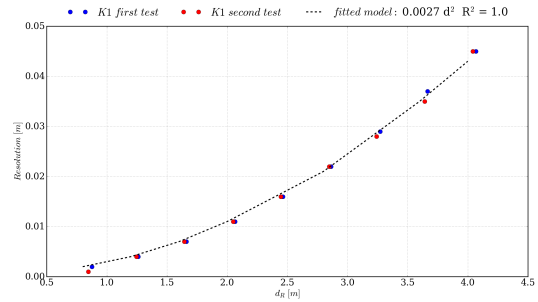


Figure 3: Kinect v1 resolution.

This behaviour can be explained considering that, for the SL range cameras, the resolution depends on the minimum measurable disparity $\Delta\delta$, so that, the resolution ΔZ_k at distance (or depth) Z_k results:

$$\Delta Z_k = \frac{Z_k^2}{fb} \Delta\delta \quad (1)$$

displaying a parabolic dependence over distance, as it is expected by a triangulation system.

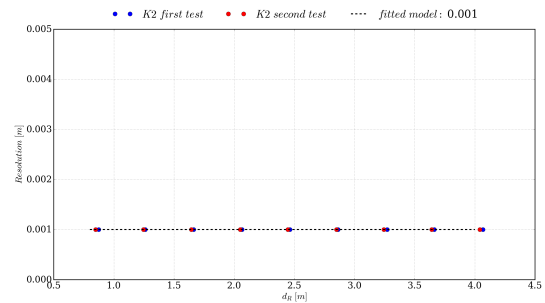


Figure 4: Kinect v2 resolution.

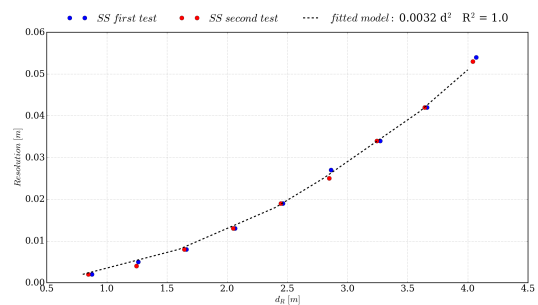


Figure 5: Structure Sensor resolution.

3.2.2 Depth precision analysis Considering the previous resolution analysis, the precision was evaluated through two different methods. For the Kinect v1 and the Structure Sensor, the half of the resolution was considered representative of their precision (Figure 7 and Figure 8). Differently for the Kinect v2, whose resolution is independent from the distance and equal to 1 mm, the global standard deviation was calculated over the sample of

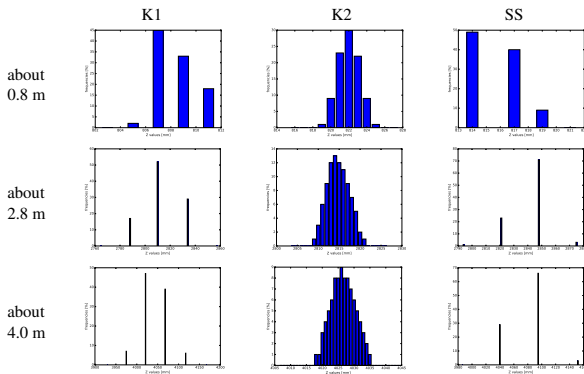


Figure 6: Distributions at different depths/distances of the 50×50 depth values over the 150 frames for the first test.

375000 depth observations for each distance from the reference surface.

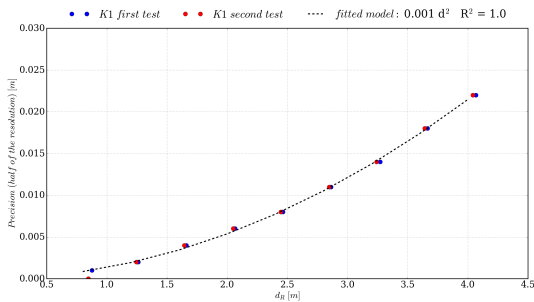


Figure 7: Kinect v1 precision vs. depth.

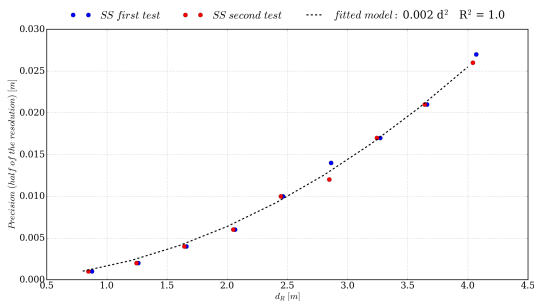


Figure 8: Structure Sensor precision vs. depth.

In details, the equation of the cabinet planar surface was least squares estimated for each distance and the dispersion around this plane in terms of standard deviation was considered as the precision (Figure 9); the obtained results clearly show that also for the Kinect v2 the depth precision is getting coarser as the distance from the target (d_R) increases. In particular, the precision varies linearly with the measured distance (R^2 of 0.96), as already reported by (Pagliari and Pinto, 2015). It is also evident (note that the scale along the vertical axis in Figure 9 is magnified 6 times with respect to the scales of the corresponding axes in Figure 7 and Figure 8) that Kinect v2 is the most precise sensor: the dispersion reaches the value of only 5 mm at 4 meters, clearly better than the 22 mm of Kinect v1 and 27 mm of Structure Sensor. In addition, to globally visualize the depth measurement noise, the depth standard deviation over the 150 frames of each pixel inside the analysed 50×50 window is shown in Figure 10 for the second test.

In general, the results show that SL depths are noisier than ToF ones; however, the latter are much more sensitive to the scanned object material: highly glossy surfaces and color differences may produce different depth estimates, as reported in (Gudmundsson et al., 2007).

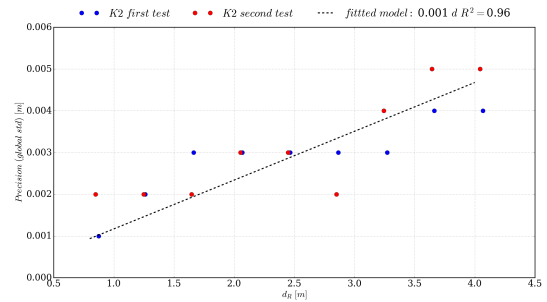


Figure 9: Kinect v2 precision vs. depth.

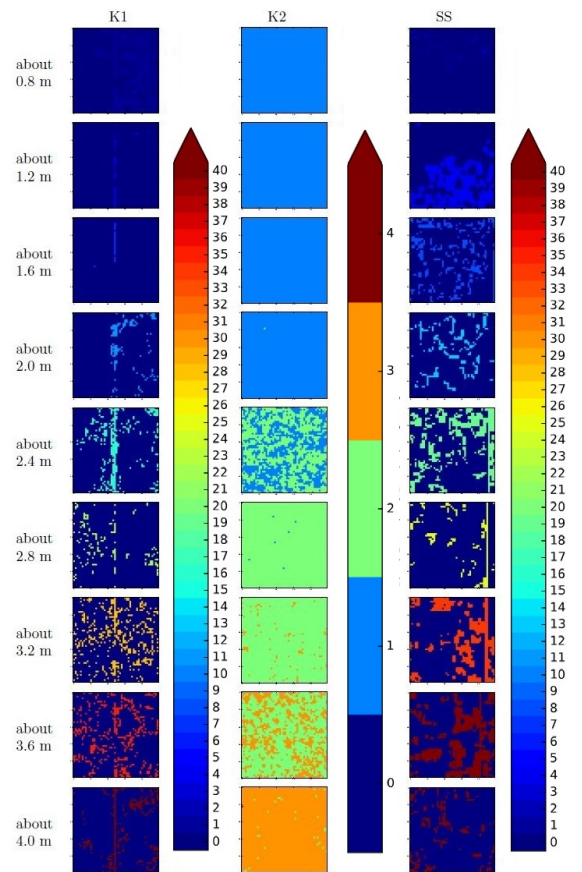


Figure 10: Depth standard deviation (expressed in mm) for each pixel of the 50×50 window over the 150 frames for the second test.

For each sensor, the statistical features (standard deviation for rows and columns and global standard deviation) are stable in the two tests, and also the cross correlation between the two tests at the same distance are very low (0.21 at the most), indicating that there are not stable patterns highlighting biases in the sensor behaviours, as also the figures show. Only in the case of the Kinect v1 and the Structure Sensor, some evident permanent features (vertical bands) remain (Pagliari et al., 2014). In the end, concerning the dependence of the depth random errors, that is precision, on the depth itself, the simple parabolic

(for the Kinect v1 and the Structure Sensor) and linear (for the Kinect v2) models (Figure 7, Figure 9 and Figure 8; Table 2) appear effective, at least under good reflective surface conditions.

3.2.3 Depth accuracy assessment The aim of the accuracy assessment is to compare the reference depth values with the same depth measured with the three sensors. This test is meant to show the geomatic potential of the investigated sensors in modelling a known surface (here represented by the cabinet planar surface) through a close-range survey.

Thus, for each depth/distance from the reference surface, the global mean was computed over the sample of 375000 depth observations. In this way it was possible to compute the differences between the observed values (d_O) and the reference depths (d_R) measured with the total station.

Due to its high precision of few millimeters, for the Kinect v2 the reference depths d_R were corrected in order to consider the possible residual inclination between the sensor and the reference plane surface. Only the inclination angle along the vertical direction was considered, since for the installation features it was the most critical to control, and their parameters ($Y = aZ + c$) were least squares estimated; then the effect of this vertical inclination was removed in the following comparison between the observed and reference depths. Moreover, the depth mean over the 150 frames of the depth map central pixel was used as observation for each distance from the reference plane surface.

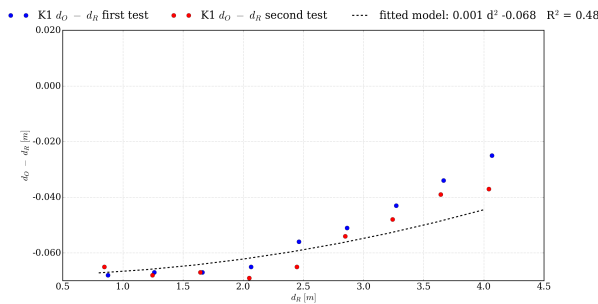


Figure 11: Kinect v1 accuracy vs. depth.

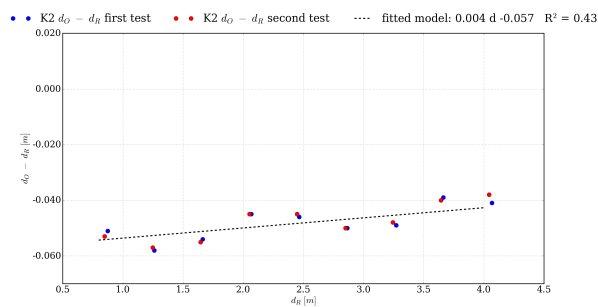


Figure 12: Kinect v2 accuracy vs. depth.

The results are reported in Figure 11, Figure 12 and Figure 13. A visible trend of the accuracy vs. the depth/distance is evident for all the sensors, pointing out the presence of systematic errors, which increase with the distance from the reference surface. In particular, the Kinect v2 is once again the best sensor, showing the lowest systematic error range: 0.019 m between the shortest and longest distance versus 0.044 m of the Kinect v1 and 0.078 m of the Structure Sensor. As previously done for the precision, these accuracy trends were modelled differently depending on the sensor operational principle (see Section 2): a linear model for

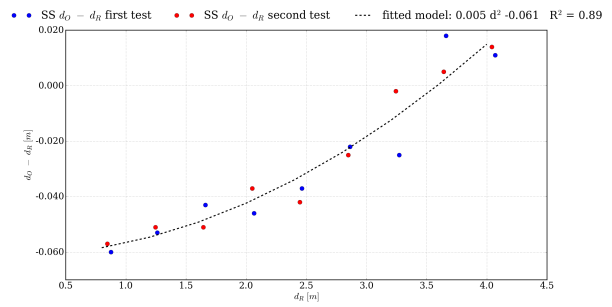


Figure 13: Structure Sensor accuracy vs. depth.

the Kinect v2 and a quadratic model (with the minimum constrained at $d_R = 0$) for the Kinect v1 and the Structure Sensor were chosen; the zero order parameter (error at $d_R = 0$) represents the contribution of more offsets, precisely the offset of the total station distancemeter and the internal offset relative to the nominal reference of the depth measurement with respect to each sensor body. Specifically, the weighted least squares were used to estimate the model parameters, with the weights based on the previously computed precisions. Even if the regression coefficient R^2 shows lower values than before, respectively of 0.48, 0.43 and 0.89 for the Kinect v1, the Kinect v2 and the Structure Sensor, the effectiveness of such accuracy models for calibration was tested by correcting the measured depths. In particular, it was checked if the residual errors after calibration were compliant and represented by the precision vs. depth models previously determined (Figure 7, Figure 9 and Figure 8; Table 2).

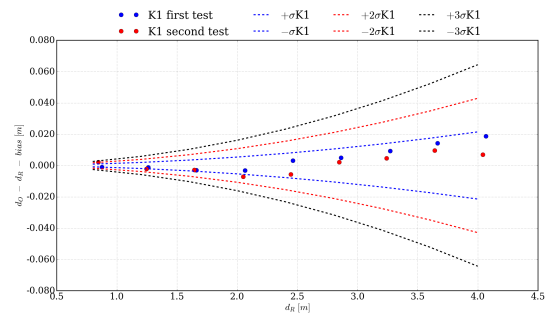


Figure 14: Kinect v1 residual errors.

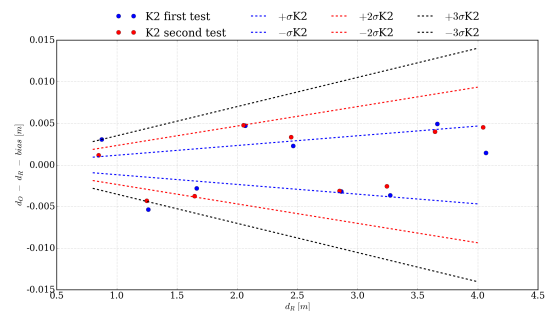


Figure 15: Kinect v2 residual errors.

All the residual errors are within the $(-3\sigma, +3\sigma)$ range for each sensor and each depth (with the exception of just one residual for Kinect v2), being sigma the precision derived from these models (Figure 14, Figure 15 and Figure 16), so that it is reasonable to conclude that the calibration has been effective by far. Therefore the estimated models of the accuracy vs. depth can be used to correct the measured depths in order to calibrate the sen-

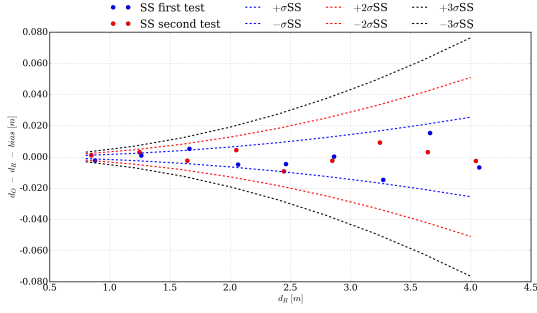


Figure 16: Structure Sensor residual errors.

sors, thus enabling their use in geomatic applications. Anyway, before effectively adopting them, a more accurate estimate of the constant representing the internal offset of the sensor is necessary, as described in the next section.

	Resolution [m]	Precision [m]	Accuracy [m]
Kinect v1	0.0027 d^2 ($R^2=1.0$)	0.0013 d^2 ($R^2=1.0$)	0.0015 $d^2 - 0.0681$ ($R^2=0.48$)
Kinect v2	0.001	0.0012 d ($R^2=0.96$)	0.0036 $d - 0.0572$ ($R^2=0.43$)
Structure Sensor	0.0032 d^2 ($R^2=1.0$)	0.0016 d^2 ($R^2=1.0$)	0.0048 $d^2 - 0.0615$ ($R^2=0.89$)

Table 2: Models for depth resolution, precision and accuracy (depth d in meters).

3.2.4 Validation of the proposed calibration models To validate the found calibration models, further tests were performed with the Structure Sensor. The aim was to compare the six known distances among the four external vertexes of a rectangular checkerboard grid, with the same distances measured with the sensor, before and after having applied the depth calibration model.

Specifically, nine validation tests were performed and the grid was captured by the Structure Sensor at various distances and with different orientations, both perpendicular and tilted. In particular, in test 3 (Figure 17) and test 4 the sensor was approximately perpendicular to the grid surface, which was acquired respectively at about 2 m and 4 m. In the first case the checkerboard occupied almost the whole width of the depth image, whereas in the latter it covered a smaller area. In the remaining tests the checkerboard was slightly or strongly inclined in relation to the sensor image plane (Figure 18), covering different parts of the depth map.

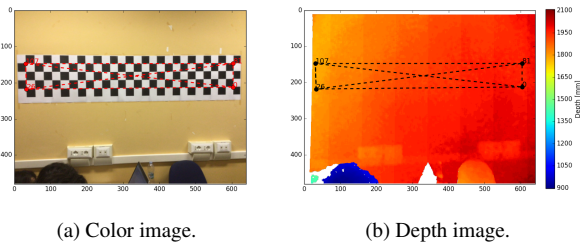


Figure 17: Test 3.

The 28×4 grid corners were automatically detected on the color image acquired by the iPad air 2 at which the range camera was connected, developing a specific iOS application. The depth image and the color image were thus co-registered using the aligned depth stream provided by the Structure SDK, in such a way that the 2D corners locations were the same on both images. Obviously the Structure Sensor was previously calibrated using the Occipital Calibrator App. In this way, it was possible to retrieve the 3D coordinates of the grid points and to compute the euclidean distances among them.

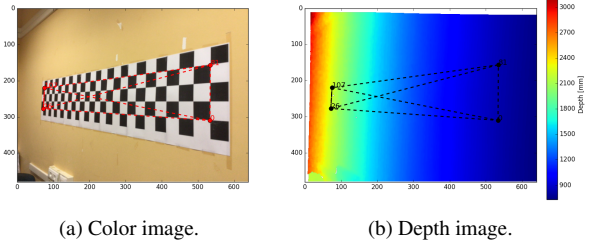


Figure 18: Test 6.

However, before applying the found accuracy vs. depth calibration model, the zero order parameter c was re-estimated since its role is essential to describe the systematic error err that affects the depth measurement:

$$err = 0.0048 Z_O^2 + c \quad (2)$$

In fact this kind error has to be removed from the depths observed Z_O by the sensor in order to properly calibrate the device:

$$Z_{CAL} = Z_O - err \quad (3)$$

More precisely, the c parameter was estimated in a single test, by calculating the value that minimizes the Root Mean Square Error (RMSE) of the differences between the six calibrated d_{CAL} and reference d_{REF} distances acquired:

$$RMSE = \sqrt{\frac{1}{6} \sum_{i=1}^6 (d_{CAL,i} - d_{REF,i})^2} \quad (4)$$

The found value for c is 31 mm, and it was then used in the nine validation tests to calibrate the Structure Sensor. Results are reported in Table 3: with the calibration, the overall RMSE, computed over the 9×6 distances, decreases from 27 to 16 mm. The proposed calibration model thus seems to improve effectively the accuracy of the Structure Sensor.

4 INVESTIGATIONS IN COLOR-DEPTH ALIGNMENT

To provide a complete description of an object, both the 3D geometry and the colour information are necessary. For range cameras these data are though captured from two different point of views. The alignment of color and depth images is therefore an important process in order to obtain a final 3D model characterized by high geometric accuracy and good quality texture.

In the following sections, two different investigations about this process are shortly described, respectively for the Kinect v1 and the Structure Sensor devices.

4.1 Kinect v1 RGB-IR shift

For the Kinect v1, the Microsoft SDK provides a specific object, the *CoordinateMapper*, able to map a color pixel into the corresponding position of the depth map. The point is that this mapper could be affected by errors and thus it is necessary to investigate its inner behaviour (Della Ventura, 2012-2013). In particular, the *MapColorFrameToDepthFrame* method, by knowing the format of both color and depth image, maps the information contained in

	d_{REF} [mm]	d_O [mm]	d_{CAL} [mm]	$d_O - d_{REF}$ [mm]	$d_{CAL} - d_{REF}$ [mm]
Test 1	1880	1878	1877	-2	-3
	1880	1881	1880	1	0
	221	222	225	1	4
	221	220	220	-1	-1
	1892	1895	1894	3	2
1893	1890	1889	-3	-4	
Test 2	1880	1938	1916	58	36
	1880	1961	1938	81	58
	221	222	224	1	3
	221	226	225	5	4
	1892	1971	1949	79	57
1893	1954	1931	61	38	
Test 3	1880	1851	1865	-29	-15
	1880	1852	1866	-28	-14
	221	219	221	-2	0
	221	217	219	-4	-2
	1892	1869	1882	-23	-10
1893	1860	1874	-33	-19	
Test 4	1880	1889	1876	9	-4
	1880	1897	1883	17	3
	221	225	224	4	3
	221	222	220	1	-1
	1892	1906	1892	14	0
1893	1907	1893	14	0	
Test 5	1880	1966	1876	-14	-4
	1880	1883	1893	3	13
	221	223	224	2	3
	221	220	222	-1	1
	1892	1878	1888	-14	-4
1893	1897	1906	4	13	
Test 6	1880	1893	1886	13	6
	1880	1887	1882	7	2
	221	224	231	3	10
	221	223	224	2	3
	1892	1902	1897	10	5
1893	1904	1898	11	5	
Test 7	1880	1932	1903	52	23
	1880	1898	1870	18	-10
	221	223	225	2	4
	221	224	222	3	1
	1892	1906	1878	14	-14
1893	1950	1921	57	28	
Test 8	1880	1914	1884	34	4
	1880	1925	1896	45	16
	221	221	223	0	2
	221	226	225	5	4
	1892	1931	1902	39	10
1893	1935	1905	42	12	
Test 9	1880	1895	1866	15	-14
	1880	1892	1862	12	-18
	221	222	224	1	3
	221	223	222	2	1
	1892	1910	1881	18	-11
1893	1902	1874	9	-19	
		MEAN	11	4	
		STD	24	16	
		RMSE	27	16	

Table 3: Validation results.

depthPixels into *depthPoints*. The former is an array of 640×480 elements where the depth information is stored, whereas the latter is an array long as the number of color image pixels, depending on the resolution (usually 1280×960).

In order to study the coordinate mapper, it was necessary to bypass it somehow, developing a specific application. The solution was found in the infrared image. In fact, one of the formats of the color stream is the infrared with 640×480 resolution (see Figure 19).

Since depth image and infrared image coincide, they are already aligned and, in order to retrieve the depth of a point on the IR image, it is sufficient to calculate its pixel index, i.e. $x + (y \cdot width)$, and to use it to access the correspondent element in *depthPixels* array, where the depth information is contained.

Notice that, to allow the automatic corner detection on the IR image, the emitter has to be disabled and afterwards activated again to allow to get depth information.

It was decided to refer directly to the image coordinates, in pixel

Distance [cm]	Test A		Test B	
	Δx pixel	Δy pixel	Δx pixel	Δy pixel
50	3.872	-6.318	3.842	-6.251
100	3.725	-6.458	3.628	-6.206
150	4.031	-6.600	4.150	-6.370
200	3.782	-6.609	3.689	-6.418
250	3.205	-6.656	3.393	-6.423
300	2.575	-6.770	missing	missing

Table 4: Test A, artificial light on and Test B, only sunlight.

units. For the IR image it was straightforward thanks to the unique correspondence of the images. On the other hand, to obtain comparable image coordinates for the color image, it was necessary to pass through the *depthPoints* array, which means through the mapper. In fact, *depthPoints* elements have the *.x* and *.y* properties which give back the image coordinates of the corresponding element (relatively to the pixel index) on the depth image.

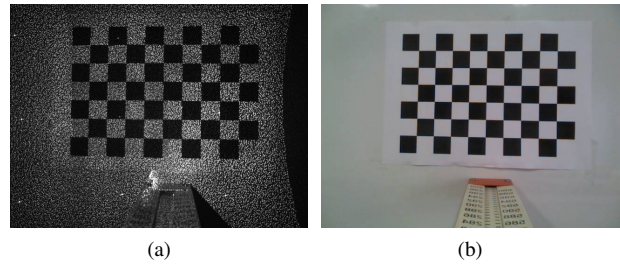


Figure 19: In (a) there is the IR image, while in (b) there is the same view but in the RGB format.

At this point, several tests were performed. First of all, it was necessary to check if the mapper applied on the infrared image gives the same result obtained by-passing it. Secondly, it was decided to verify that the mapper works well on both color image resolution. Also with a 640×480 color image the results were acceptable. Then, the possibility to oversample the infrared image was also evaluated in order to make the automatic collimation easier. Magnification factor of $\times 2$, $\times 4$, $\times 6$, and $\times 8$ were investigated and they all show the same results, unless of numeric approximation. Notice that it was necessary to divide the corners location by the resize factor to obtain the correct image coordinates.

All these tests showed an evident shift between image coordinates obtained with or without going through the mapper. According to the previous assumptions, it was therefore decided to study the shift when the distance from the target increases. Initially the sensor was located at the nominal distance of 50 cm from the target, and moved in 50 cm steps up to 300 cm. For each position, the collimation was performed first on the infrared image and afterwards on the color image, without moving the Kinect v1 device. Test A was performed with artificial light, while test B with only sunlight. All the other conditions were unchanged. A 6×9 checker board with 35.04 mm step was used. For every distance the Δx and Δy (RGB – IR) was calculated for every point, and then the average values were recorded. The results are shown in Table 4. A negative shift means that the IR-coordinate is bigger than the RGB-coordinate, and as a result there is a collimation error towards the left (*x*-direction) and towards up (*y*-direction) with respect to the color image. On the other hand, if the shift is positive, the collimation error on the color image is towards right and down respectively. From data in the Table 4 it is possible to see an almost constant negative shift of around 6 pixels in the *y*-direction and a positive shift of around 4 pixels in the *x*-direction.

4.2 Stereo calibration of the Structure Sensor

Since the Structure Sensor does not have its own colour camera, the 3D scanning apps leverage the iPad camera in order to retrieve the color information of the objects being scanned. Therefore, considering that the 3D geometry and the texture are captured from two different points of view, it is necessary to calibrate the precise alignment (reconstruct the geometric relationship) between the Structure Sensor and the iOS device camera in order to accurately overlap the 3D and colour data. The Occipital Calibrator app, the unique calibration app actually available on the Apple Store, can achieve this goal. It supplies already good calibration results, but its code is not open and it is designed specifically to work with the bracket accessory, which imposes a constraint for the baseline length and orientation. Furthermore it does not share the computed calibration parameters and requires the user to refine manually the calibration quality (only for the horizontal component), by touching and dragging the depth map over the colour image until they are perfectly superimposed.

For all of these reasons, it was decided to develop a specific calibration application, exploiting the capabilities of the OpenCV library (Nibi, 2014-2015). It implements a stereo vision calibration approach, allowing the user to automatically acquire, from different positions, several pairs of images of a chessboard grid, both with the Structure Sensor infrared camera and the iPad color camera.

In particular, the calibration grid was captured from different angles of view and in a range of distances that would have been used later for the depth map acquisition. Particular attention was paid in measuring the size of the grid squares providing the geometry scale. The grid corners, whose 2D positions on both the IR and color images are automatically detected by the OpenCV algorithms, act as ground control points: their positions are known both in object space and image space.

In this way the application is able to compute the interior and the distortion parameters of two cameras, together with the rotation matrix and the translation vector that relate the color image to the IR/depth image.

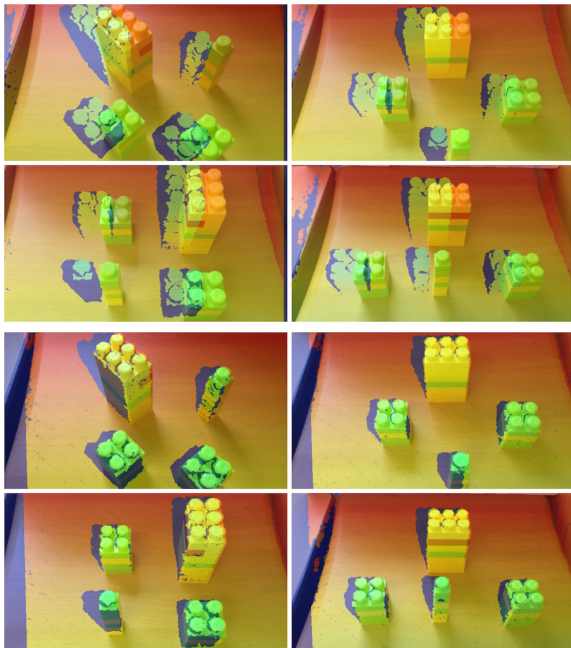


Figure 20: Calibration results on simple geometry objects.

The calibration accuracy was measured through the reprojection error, that is the sum of squared 2D distances between the ob-

served feature points (the 2D locations of the corners) detected in the calibration images and the corresponding world points projected (using the found values for camera parameters and the poses) into the same images. The reprojection error was always lower than one pixel (it is respectively 0.32, 0.32 and 0.34 for the IR interior parameters, the color interior parameters and the stereo parameters).

Finally, the computed calibration parameters were further tested to check if they were effectively able to register the depth and colour images captured by the Structure Sensor and the iPad camera. Results are reported in Figure 20 and show a good alignment between the two images, at least from a visual inspection.

5 CASE STUDIES

The specific knowledge of the geometric quality of range cameras, as investigated in Section 3 and Section 4, allows to correctly and efficiently use them in geomatic applications such as architectural surveys, documentation of cultural heritage, monitoring applications and many more.

In this Section, four examples of the practical use regarding two of the three range cameras previously characterized are presented in the form of case studies.

5.1 Performance of Kinect v2 for small amplitude oscillatory motion monitoring

In the first one, the performances of the Kinect v2 sensor for monitoring oscillatory motions characterized by small challenging amplitudes (0.02 m and 0.03 m) and different oscillation frequencies (in the range of 1.5–3 Hz) were evaluated (Benedetti et al., 2016). Specifically, displacements, velocities and accelerations of a vibrating table collected by the Microsoft Kinect v2 (30 Hz) were compared to those recorded by the Mikrotron EoSens (100 Hz) high-resolution camera which served as reference. Both the sensors were placed at a distance of about one meter from the table, with the optical axis of both cameras orthogonal to the target (Figure 21).

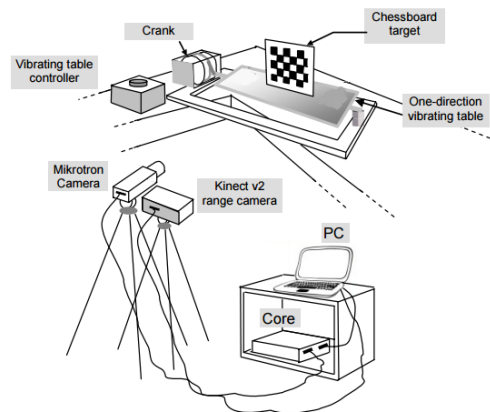


Figure 21: Vibrating table equipped with target and sensors.

The images acquired by the Mikrotron EoSens camera were post-processed using a Lagrangian Particle Tracking technique named Hybrid Lagrangian Particle Tracking (HLPT) (Shindler et al., 2012), which selects image features (in our case as the corners of a chessboard target, see Figure 21) and tracks them from frame to frame. Once the trajectories are reconstructed, displacements, velocities, and accelerations are computed via central differences. Displacement, velocity and acceleration components belonging to the same frame are arithmetically averaged to compute their

time history.

For what regards the Kinect v2, it acquired in real-time the displacement data, while the velocities and the accelerations were retrieved by differentiation.

The Fast Fourier Transform (FFT) was then employed to identify the four different oscillation frequencies of the vibrating table on displacement data. A part of the results is shown in Figure 22 and Figure 23.

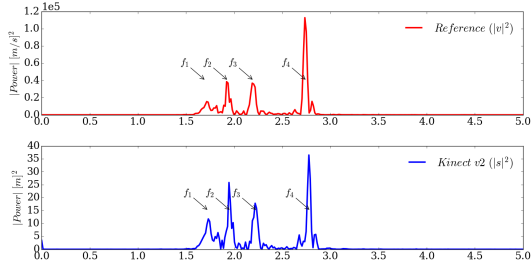


Figure 22: Power spectrum of the results related to the test with 0.02 m oscillation amplitude: velocities for the Mikrotron EoSens camera (red) and displacements for the Kinect v2 range camera (blue).

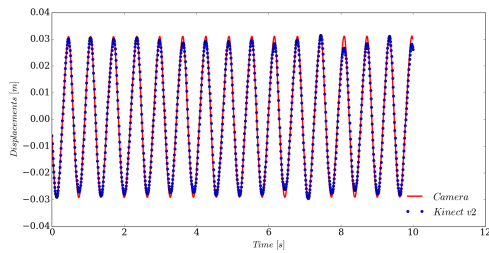


Figure 23: Displacements retrieved with the Kinect v2 sensor in comparison with the Mikrotron EoSens camera for the lowest frequency (f_1) and 0.03 m oscillation amplitude.

The similarity among the kinematic parameters of the Kinect v2 sensor and the reference data was thus evaluated in terms of RMSE, defined as:

$$RMSE = \sqrt{\frac{1}{N} \sum_{i=1}^N (kp_{K2,i} - kp_{ref,i})^2} \quad (5)$$

where N is the amount of data available within each test, kp_{K2} is the kinematic parameter monitored by the Kinect v2 sensor, kp_{ref} is the kinematic parameter detected with the Mikrotron camera. The accuracy (RMSE) of displacements was generally within 4 - 5% of the reference solution, with a generally increasing trend in function of the frequency.

Furthermore, the Kinect v2 performances were characterized by a rather stable noise across all the tests and a high stability (lower bias) on displacements. The results obtained are thus promising in the prospective of employing the Kinect v2 in the field of oscillatory motions monitoring, such as structural monitoring, industrial control system development, ground monitoring and so on.

5.2 Kinect v2 and RGB stereo cameras integration for point cloud enhancement: a first test

The second case study was performed to evaluate the integration feasibility of range camera technology with a classical stereo sys-

tem (Ravanelli et al., 2016).

For this purpose, a 3D model of a DUPLO bricks construction was reconstructed both with the Kinect v2 and through photogrammetry, by processing one stereo pair acquired with a Canon Eos 1200D DSLR camera. The two 3D models were then fused, obtaining the integrated model.

In particular, a specific software tool was developed to download the 3D data with the Microsoft SDK and the point cloud was reconstructed from the depth map (see Figure 24) acquired in a single frame, since the final aim was the near real-time integration. Regarding the stereo model, one stereo pair was acquired

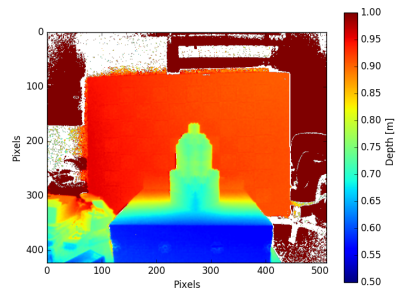


Figure 24: Depth map acquired by the Kinect v2 range camera.

with a proper stereo baseline (base-to-height ratio of about 0.3) and it was processed with the Agisoft PhotoScan™ photogrammetric software (Agisoft PhotoScan, 2017). The approximated model scale was estimated by imposing the values of the coordinates measured by the Kinect v2 to eight points collimated on both images (see Figure 25).

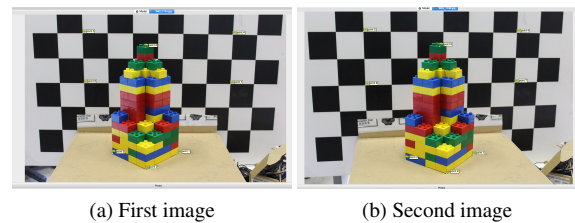


Figure 25: Acquired stereo pair.

The scale of the photogrammetric model was then retrieved from the coordinates measured by the Kinect v2. Finally, the fusion of the Kinect v2 and the photogrammetric models was performed through the CloudCompare (Girardeau-Montaut, 2016) 3D point cloud and mesh processing software. Since the two points clouds were already in the same reference system, the co-registration was only refined using the Iterative Closest Point (ICP) algorithm (Best and McKay, 1992).

To assess the metric quality of the results, both the integrated model and the models reconstructed with the single 3D modelling technique were compared with the reference model of the DUPLO bricks construction. Specifically, precision and accuracy were evaluated in terms of signed distances (positive inside and negative outside the reference mesh surface) of the 3D model points from the reference mesh.

The results are encouraging (see Table 5) and show that this integrated approach leads to higher metric accuracy of the final 3D model with respect to that obtained by only using a range camera and to a higher level of completeness respect to that obtained by exclusively processing a stereo image pair.

Model	Distance mean [m]	Distance std [m]	Completeness [-]
Photogrammetric	0.000	0.002	38%
Kinect v2	0.004	0.015	67%
Integrated	0.001	0.003	69%

Table 5: Distance statistics.

5.3 Near real-time indoor mapping with the Structure Sensor

The third case study analyzed the potentialities of the Structure Sensor for the surveying of indoor environments (Ravanelli, 2017b). The specific aim was to evaluate its accuracy in reconstructing near real-time planimetric maps of building interiors. Several 3D models of three different rooms were thus captured with the free Room Capture application, included by Occipital in the Structure SDK samples. The resulting 3D models were then processed to obtain a planimetric map (Figure 27) allowing to uniquely measure the principal quantities (sides, perimeter and area) of the scanned rooms. The aim was to compare them with the ones obtained through a traditional survey performed with a measuring tape.

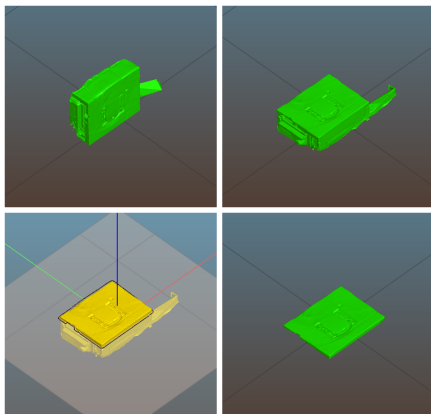
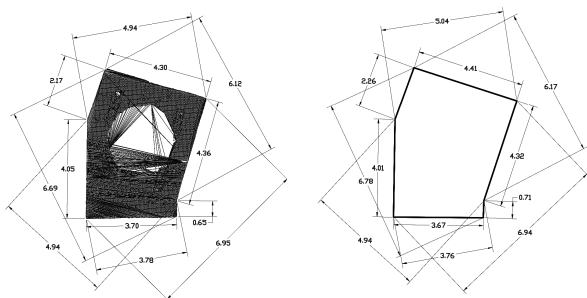


Figure 26: Cutting of the model.



(a) Structure Sensor: Perimeter = 19.29 m; Area = 23.19 m²
 (b) Reference: Perimeter = 19.37 m; Area = 23.36 m²

Figure 27: Planimetric maps of *Aula tesisti* room.

To evaluate the accuracy, for each room model, the differences between the lengths of the sides measured with the Structure Sensor and those obtained through the traditional survey were firstly computed. Successively, the mean and the standard deviation of the residuals were computed over all the sides. In this way, it was possible to calculate the RMSE for each model, representing its accuracy. The obtained results are reported in Figure 28 and in Table 6: the RMSE varies in the range of 3 - 10 cm, very low

	RMSE [m]		
	<i>Aula Piccola</i>	<i>Aula Tesisti</i>	<i>Aula Grande</i>
Model 1	0,03	0,06	0,05
Model 2	0,05	0,05	0,07
Model 3	0,03	0,07	0,05
Model 4	0,05	0,07	0,10
Model 5	0,04	–	–
Model 6	0,03	–	–
Model 7	0,03	–	–
Mean	0,04	0,06	0,06

Table 6: RMSE over the length of the sides for the obtained planimetric maps.

values if compared to the dimensions of the sides of the room. The achievable degree of accuracy is therefore better than 10 cm. Furthermore, results highlight a slight trend as a function of the dimensions of the rooms, generating better 3D models for smaller rooms. In conclusion, the obtained results show that the reconstructed planimetric layouts are characterized by a mean accuracy of 5 cm, 10 cm in the worst case, and thus they are suitable for collecting 2D maps at a scale 1:200 and several applications not demanding for centimetric accuracy.

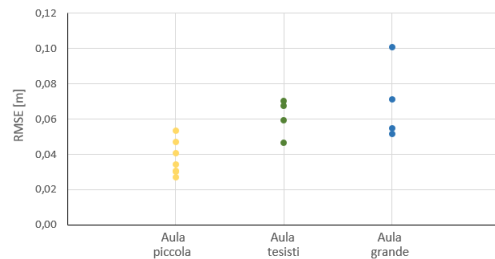


Figure 28: RMSE over the length of the sides for the obtained planimetric maps.

5.4 Archaeological applications: capturing small finds in 3D

Finally, in the last case study, the first applications of the Structure Sensor for scanning archaeological small finds were performed. In fact, cultural heritage documentation can be one of the natural field of application of range camera technology, where speed and ease of use are predominant with respect to accuracy. A general procedure was therefore identified in order to allow non expert users to reconstruct a 3D model of archaeological small finds with a range camera (Ravanelli et al., 2017). In particular, the Structure Sensor was used to scan several small finds coming from the excavations of the University of Rome "La Sapienza" directed by Prof. Lorenzo Nigro in the island of Motya, a Phoenician city in Western Sicily (Nigro, 2015). The Scanner app was selected among all the 3D scanning apps actually available for the Structure Sensor since it is free, very easy to use and furthermore its code is open, thus customizable according to the specific requirements of the application. The Structure Sensor was able to reconstruct the geometry of these objects with an accuracy level of few millimeters. Concerning the texture reconstruction, it is instead less accurate, since occasionally the colour is not perfectly aligned to the 3D geometry in some areas of the model, in particular for those captured at end of the scanning process. This behaviour can be explained with a not perfect outcome of the calibration and/or residual tracking errors. Finally the colouring approach used by the Scanner app (the only 3D scanning app tested so far) of Occipital tends to smooth the texture details. The 3D models so easily collected provide all the necessary information to completely describe the archaeological small finds. Furthermore they allow to take in depth a posteriori measurements, such as the volume computation and section visualization.

It is important to notice that all these measurements are expressed in metric units because, as mentioned above, the Structure Sensor generates 3D models that belong intrinsically to a metric space. In particular, with the CloudCompare software it is possible to cut the model in one and/or several slices through the Cross Section Tool (Figure 30) and then to measure the principal quantities (Figure 31).

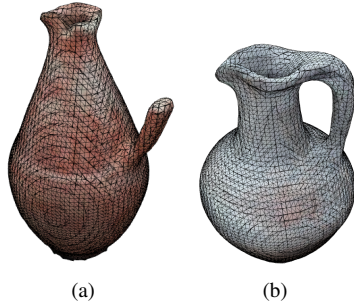


Figure 29: The wireframe visualization of the obtained 3D models for vase (a) T180/4 and vase (b) T181/2.

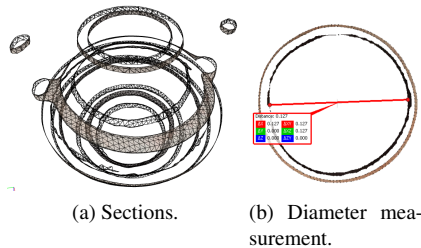


Figure 30: Elaboration performed on the model T177/2.

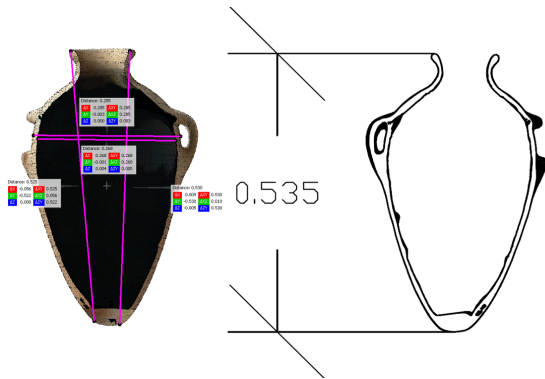


Figure 31: Vertical sections on model BL1536.

6 CONCLUSIONS

Range cameras are low-cost 3D scanners; thanks to their high frame rate they can easily collect dense point clouds in a short range (few meters) from the imaged objects. The aim of this thesis was to evaluate the potentialities of these sensors for geomatic applications and to provide useful indications for their practical use. The leading idea that guided this work is to supply a feasible and effective procedure for the calibration of range cameras, enabling their use for close-range 3D modelling of objects and environments.

Therefore, the three most popular and/or promising low-cost range cameras, namely the Microsoft Kinect v1, the Microsoft Kinect v2 and the Occipital Structure Sensor, were firstly characterized from a geomatic point of view in order to assess the metric quality

of the depth data retrieved by them. These investigations showed that such sensors present a depth precision and a depth accuracy depending both on the operational principle adopted by the single device (SL or ToF) and on the depth itself.

On this basis, two different models were identified for precision and accuracy vs. depth: parabolic for the SL (the Kinect v1 and the Structure Sensor) and linear for ToF (the Kinect v2) sensors, respectively. Then the effectiveness of such accuracy models for calibration was tested by correcting the measured depths through the estimated parameters. The residual errors were globally compliant with the found precision models for all of the sensors. Overall, the best performances, at an accuracy level of very few millimeters, were supplied by the Kinect v2 Time of Flight sensor. In fact, for the Kinect v2 the residuals are always below 5 mm, independently from the depth/distance, while for the Kinect v1 and the Structure Sensor they are within 19 mm and 15 mm respectively, thus leading to an accuracy level around 1 cm.

Furthermore, in order to validate the found calibration models, nine additional tests were performed with the Structure Sensor. First of all, the value of the constant representing the internal offset in the accuracy model was re-estimated. Then the six known distances among the four external vertexes of a rectangular checkerboard grid were measured through the sensor, before and after having applied the depth calibration model. With calibration, the overall RMSE, computed over the 9×6 distances, decreased from 27 to 16 mm. The proposed calibration model thus seems to improve effectively the accuracy of the Structure Sensor, at least for this limited number of tests.

Successively, some investigations about the registration process of depth and color images were also performed. Specifically, for the Kinect v1 some tests were carried out in order to evaluate the effect and the performances of the aligning/mapping algorithm (provided by the Microsoft SDK) between the two images. The goal was to investigate if the coordinates collimated on the RGB image were affected by the mapping algorithm, therefore leading to wrong depth values. As a result, an almost constant negative shift of around 6 pixels in the y direction and a positive shift of around 4 pixels in the x direction was observed at several distances from the captured object.

For the Structure Sensor, instead, a stereo calibration was carried out in order to reconstruct the geometrical relationship between the depth sensor and the color camera of the device at which it was connected. The estimated calibration parameters were effectively able to register the depth and color images captured by the Structure Sensor and the color camera.

Finally four case studies were analyzed in order to evaluate:

- the performances of the Kinect v2 sensor for monitoring oscillatory motions;
- the integration feasibility of Kinect v2 with a classical stereo system;
- the potentialities of the Structure Sensor for the 3D surveying of indoor environments;
- the potentialities of the Structure Sensor to document archaeological small finds.

The case studies show the promising performances of the investigated range cameras.

In conclusion, although the experimental results demonstrated that range cameras have the capability to give good and encouraging results, the performances of traditional 3D modelling techniques in terms of accuracy and precision are still superior and must be preferred when the accuracy requirements are restrictive. But for a very wide and continuously increasing range of applications, when the required accuracy can be at the level from few millimeters (very close-range) to few centimeters, then range cameras can be a valuable solution, especially when non expert

users are involved. Furthermore, the technology on which these sensors are based, driven also by the new generation of AR/VR reality kits (see for example (Occipital, 2016)), is continually evolving and certainly also their geometric performances will soon improve.

Finally, future work should be directed towards improving the calibrations results and studying the integration with other 3D modelling techniques. Summarizing, further developments could be devoted to:

- refine the precision and accuracy models for the Kinect v1 and the Kinect v2;
- develop similar functional and stochastic models for other low-cost range cameras as soon as they come on the market;
- analyze the effectiveness of the proposed calibration procedure in practical applications, where possible non-optimal reflection conditions may also arise
- apply the calibration models in the 3D modelling software.

ACKNOWLEDGEMENTS

The author wants to express her gratitude to her advisor Mattia Crespi and her co-advisor Andrea Nascetti.

REFERENCES

- Agisoft PhotoScan, 2017. <http://www.agisoft.com/>.
- Benedetti, E., Ravanelli, R., Moroni, M., Nascetti, A. and Crespi, M., 2016. Exploiting Performance of Different Low-Cost Sensors for Small Amplitude Oscillatory Motion Monitoring: Preliminary Comparisons in View of Possible Integration. *Journal of Sensors* 2016, pp. 10.
- Best, P. J. and McKay, N. D., 1992. A Method for Registration of 3-D Shapes. *IEEE Transactions on pattern analysis and machine intelligence* 14(2), pp. 239–256.
- Boehler, W. and Marbs, A., 2002. 3D scanning instruments. *Proceedings of the CIPA WG 6*, pp. 9–18.
- Cathue, D., 2012. *Programming with the Kinect for Windows Software Development Kit*. Microsoft Press.
- Chipworks, 2013. chipworks web page. <http://www.chipworks.com/en/technical-competitive-analysis/resources/blog/inside-the-xbox-one-kinect/>.
- Chow, J., Ang, K., Lichti, D. and Teskey, W., 2012. Performance Analysis of a Low-Cost Triangulation-Based 3d Camera: Microsoft Kinect System. *ISPRS-International Archives of the Photogrammetry, Remote Sensing and Spatial Information Sciences* 1, pp. 175–180.
- Dal Mutto, C., Zanuttigh, P. and Cortelazzo, G. M., 2012. *Time-of-Flight Cameras and Microsoft Kinect™*. Springer Science & Business Media.
- Della Ventura, L., 2012-2013. *Low cost range camera geomatics applications: an innovative calibration method for Microsoft Kinect*. M.S. Thesis, University of Rome "La Sapienza", Faculty of Civil and Industrial Engineering. Advisor: M. Crespi. Coauthors: R. Ravanelli, A. Nascetti.
- Girardeau-Montaut, D., 2016. *Cloud Compare3D Point Cloud and Mesh Processing Software - Version 2.7.0*. Open Source Project.
- Grzegorzek, M., Theobalt, C., Koch, R. and Kolb, A., 2012. *Time-of-Flight and Depth Imaging - Sensors, Algorithms, and Applications*. Springer.
- Gudmundsson, S. Á., Aanæs, H. and Larsen, R., 2007. Environmental effects on measurement uncertainties of time-of-flight cameras. In: *Signals, Circuits and Systems, 2007. ISSCS 2007. International Symposium on*, Vol. 1, IEEE, pp. 1–4.
- Izadi, S., Kim, D., Hilliges, O., Molyneaux, D., Newcombe, R., Kohli, P., Shotton, J., Hodges, S., Freeman, D., Davison, A. and Fitzgibbon, A., 2011. *Kinectfusion: Real-time 3d reconstruction and interaction using a moving depth camera*. *Proceedings of the 24th annual ACM symposium on User interface software and technology*.
- Lachat, E., Macher, H., Mittet, M., Landes, T. and Grussenmeyer, P., 2015. First experiences with Kinect v2 sensor for close range 3D modelling. *The International Archives of Photogrammetry, Remote Sensing and Spatial Information Sciences* 40(5), pp. 93.
- Newcombe, R., Izadi, S., Hilliges, O., Molyneaux, D., Kim, D., Davison, A., Kohli, P., Shotton, J., Hodges, S. and Fitzgibbon, A., 2011. *Kinectfusion: Real-time dense surface mapping and tracking*. *Proceedings of the 10th IEEE International Symposium on Mixed and Augmented Reality (ISMAR)*.
- Nibi, E., 2014-2015. *From computer vision to geomatics: high precision calibration and metric potentialities of the "Occipital Structure Sensor"*. M.S. Thesis, University of Rome "La Sapienza", Faculty of Civil and Industrial Engineering. Advisor: M. Crespi. Coauthors: R. Ravanelli, A. Nascetti.
- Nigro, L., 2015. *Il Nuovo Allestimento Del Museo Del Vicino Oriente, Egitto E Mediterraneo Della Sapienza*. *Vicino Oriente XIX* pp. 309 – 340.
- Occipital, 2016. *VR DEV KIT: our next generation of mobile 6-DoF positional tracking*. <http://structure.io/use/vr-positional-tracking>. Last edited: December 2016.
- Pagliari, D. and Pinto, L., 2015. Calibration of Kinect for Xbox One and Comparison between the Two Generations of Microsoft Sensors. *Sensors* 15(11), pp. 27569–27589.
- Pagliari, D., Menna, F., Roncella, R., Remondino, F. and Pinto, L., 2014. Kinect fusion improvement using depth camera calibration. *International Archives of the Photogrammetry, Remote Sensing and Spatial Information Sciences* 40(5), pp. 479–485.
- Ravanelli, R., 2017a. *3D modeling by low-cost range cameras: methods and potentialities*. PhD thesis, University of Rome "La Sapienza", Italy. Advisor: M. Crespi. Coauthor: A. Nascetti.
- Ravanelli, R., 2017b. *Building Information Modeling in near-real-time con range camera: analisi delle potenzialità dello Structure Sensor*. *Bollettino SIFET*.
- Ravanelli, R., Nascetti, A. and Crespi, M., 2016. *Kinect V2 And RGB Stereo Cameras Integration For Depth Map Enhancement*. *The International Archives of the Photogrammetry, Remote Sensing and Spatial Information Sciences* XLI-B5, pp. 699–702.
- Ravanelli, R., Di Rita, M., Nascetti, A., Crespi, M., Nigro, L., Montanari, D. and Spagnoli, F., 2017. *PENGUIN 3.0-Capturing small finds in 3D*. *Mediterranean Archaeology and Archaeometry* 17(2), pp. 49–56.
- Remondino, F. and Stoppa, D., 2013. *TOF Range-Imaging Cameras*. Springer.
- Sarbolandi, H., Lefloch, D. and Kolb, A., 2015. Kinect range sensing: Structured-light versus Time-of-Flight Kinect. *Computer Vision and Image Understanding* 139, pp. 1–20.
- Shindler, L., Moroni, M. and Cenedese, A., 2012. Using optical flow equation for particle identification and velocity prediction in particle tracking. *Applied Mathematics and Computation* 218, pp. 8684–8694.

UAV MONITORING TO SUPPORT PRECISION FARMING: A STUDY-CASE IN THE LAND OF THE CESANESE DEL PIGLIO

Andrea Rotondi

PhD., DICeM – Via G. Di Biasio, 43 – 03043 Cassino (FR); +39 333 7676774; ing.rotondi@yahoo.com
DICeM – Dipartimento di Ingegneria Civile e Meccanica
Università degli Studi di Cassino e del Lazio Meridionale

key words: UAV, Precision farming, RGB, NIR, multi-spectral image, sensor, ortho-image

ABSTRACT

New generation sensors (RGB, thermal, NIR and multispectral cameras) on unmanned aerial vehicles are continuously being developed for precision farming applications. The procedures for integrating data acquisitions from UAV and ground physico-chemical parameters are a major research topic aimed at improving agricultural production in order to obtain savings in terms of use fertilizers, pesticides and water resources. The adoption of techniques and technologies for precision farming and, in particular, for precision viticulture, is surely an opportunity for botanists, producers and entrepreneurs in the industry to optimize the use of inputs in the production process by modulating agronomic interventions in a targeted manner while reducing environmental and health pressure. This work presents a study and an experimentation linked to the determination of viticulture growth indexes by integrating the innovative techniques of digital photogrammetry from UAV platform, GPS satellite technique and traditional measures. Furthermore we demonstrate that the products from the processed raw-data represent good quality support to determine health state of the crop, and provide in addition a quantitative evaluation of the observed data. Through the use of such a technology it is possible to improve productivity between 15% and 17%, reducing the market price of the product and the costs of control and management. In particular, during the monitoring campaign lasting two years from 2015 to 2016, it was possible to observe that vine cultivation increased the growth index by about 12% following the corrections resulting from the critical interpretation of the results.

1. INTRODUCTION

The adoption of techniques and technologies for Precision farming allows one to modulate agronomic interventions in a targeted manner while reducing the pressure on the environment and health.

In addition food safety and environmental conservation are two of the greatest challenges in the contemporary era. In relation to the global population growth forecast of around 9 billion by 2050 (Nikos and Bruinsma 2012), FAO estimates that increases of food and food products will rise by 60% if compared to the 2007 average. However, the globally cultivated area will grow to a negligible extent. In addition, factors such as technological evolution, socio-political changes, increased environmental degradation, water shortage, increased energy needs and the presence of new parasites and diseases are some current trends, different from the past, that affect agricultural production .

Increasing the size and structure of farms, automation strategies and climatic changes also have to necessarily integrate technological innovation in a consolidated manner in the productive processes of modern agriculture. This is to address the challenges that will be faced in the coming decades, trying to make agriculture more productive and at the same time sustainable.

The need to improve productivity, competitiveness and environmental performance does not only concern the economy. With about 805 million people worldwide suffering from chronic malnutrition, most of which live in developing countries, Europe and the rest of the industrialized countries have the moral obligation to optimize agricultural production by boosting production in more sustainable way. Finally, the long-term challenges related to sustainable agriculture should be tackled by industrialized countries with a joint approach in order to support technological innovation, as well as a risk-based regulatory framework supported by scientific evidence,

continuity of basic and applied research and the development of skills in the agricultural field.

Recent investments and new funding priorities at Member State and EU level offer encouraging signals. The Horizon 2020 Framework Program is the largest EU research and innovation program, with around 80 billion euro available over the space of 7 years. New investments are being made in the Member States. For example, in the United Kingdom, the UK government is investing in a new Agri-Tech strategy aimed at making the UK the world's leading technology, innovation and sustainability of agriculture. Margins in the agricultural sector are reduced and additional costs threaten the survival of some small-scale activities. Finally, the long-term challenges of sustainable agriculture should be tackled with a joint approach by the Commission and the Member States to support technological innovation, a risk-based regulatory framework supported by scientific evidence, continuity of basic and applied research, and the development of skills in the agricultural field.

Within this framework UAV platforms equipped with low weight cameras and sensors offer flexible and low-cost tools for agricultural applications. Such systems, based on accurate measurements of the emitted and reflected energy, can monitor a wide range of crop parameters such as moisture content, surface temperature, photosynthesis activity and presence of weeds and parasites. This information is of growing importance to ensure the economic efficiency of agricultural production and harvest forecasts under a broader perspective of crop mitigation and adaptation to climate change and environmental sustainability.

2. PRECISION AGRICULTURE

The industrial agri-food system that has established itself over the last fifty years has led to indiscriminate exploitation, and irreversible deterioration, of natural resources faultly assumed to be unlimited and inexhaustible. The costs incurred in

environmental and social terms due to intensive agriculture have been enormous, especially in terms of pollution, loss of biodiversity, soil fertility reduction, marginal land abandonment, thus creating obvious sustainability issues. Nowadays a possible response to the negative trend just described may be due to the development of technologies and the implementation of the so-called Precision Agriculture (PA), whose birth dates back to the nineties in the United States, where it continues to have the widest spread and technical and technological evolution. The term precision farming is associated with many others similar meanings, such as precision agriculture, site-specific management and prescription farming. At the same time, several and still evolving are the definitions of the term in the literature. Among the most common, we find the following expression: "That kind of agriculture that increases the number of decisions (correct), which are associated with net benefits, per unit area and per unit of time". The definition contains some fundamental aspects and precisely Agriculture is of Accuracy when:

- minimizes costs;
- maximize productions;
- minimizes environmental impacts (or optimizes available environmental resources like water);
- it uses advanced technology to selectively intervene in crop and space.

In North America, where farms compete aggressively both in the domestic and world markets, "Precision Farming" has already had a major development. Synthetically, we can summarize the technologies that are used integrally in:

- Remote sensing with UAV platform;
- GNSS Systems;
- Geographic Information Systems (GIS).

Currently, the application of this integrated methodology is particularly indicated in the wine-growing sector.

2.1 PRECISION VITICULTURE

Precise farming applied to vineyards, Precision Viticulture (VP) involves the monitoring of physical, chemical and biological variations that provide the data needed to understand the real productivity of vineyards. The vast scientific research that is being done around the world aims to determine whether traditional sources of data acquisition (satellite and aerial photogrammetry) can support precision viticulture. Much of the research has focused attention on the ability to determine the general indexes obtained from the acquired images.

Cultivations and vegetation monitoring is highly dynamic, in particular that required by vineyard cultivation, which means that sensors on board of satellites in remote sensing are very limited due to the time needed to allow the next flight of the satellite on the same area. Moreover, the vineyards, which are not a crop with a homogeneous distribution in the area, are difficult to observe by using the satellites, as the chambers installed on them can not precisely distinguish the vegetation between the individual screws. This requires the use of photogrammetry from UAV platform using high resolution cameras.

Therefore, precision viticulture must necessarily be oriented to understanding the interactions between the vineyard and the environment in order to handle them to obtain quality grapes, which are the first requirement for excellent production. In viticulture, the management of agronomic practices such as fertilization, irrigation, pruning, processing, pesticide treatment

requires not only a deep knowledge of plant physiology, but also of the territory and the environment.

This is particularly true in the light of the new environmental scenarios due to climate change that viticulture must and will have to adapt in the future. The precision viticulture approach is therefore based on a continuous cyclical process that begins with observation of the vineyard performance and associated parameters, followed by the interpretation and evaluation of the collected data, until a targeted input management and / or selective grape harvest.

2.2 VIGOUR INDICES

In precision farming one often uses the spectral indices obtained as a simple algebraic combination of the measured spectral values at some specific wavelengths. They allow one either to synthesize the multispectral information in a single parameter related to the physiological and health status of the culture or to attenuate the disturbance of factors that similarly affect the different spectral bands (variations in lighting level, shading, effects due to the geometry of the vegetation, etc.). As the measurement techniques progressed, numerous spectral indices have been gradually introduced: among them the most used one is the Normalized Difference Vegetation Index (NDVI), defined by the ratio between the difference and the sum of reflectance in the near infrared and red:

$$NDVI = (NIR_{780} - RED_{680}) / (NIR_{780} + RED_{680})$$

This index is significantly related to the amount of plant biomass for unit surface (or Leaf Area Index, LAI), hence to the vigor of the crop. Its value varies from 0.1 to 0.3, corresponding to a bare or little grassy soil, until reaching an asymptotic saturation value around 0.8-0.9 for vegetation with LAI > 5.

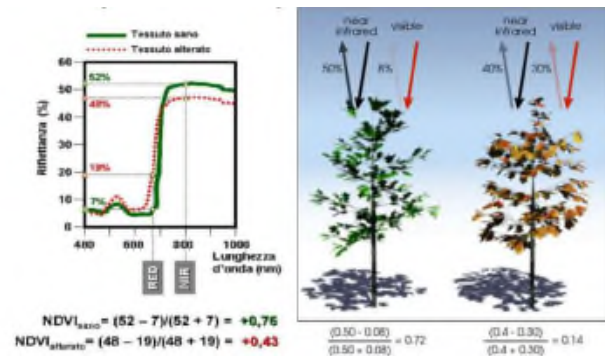


Figure 1. NDVI index

In the previous images the reflectance phenomena used to determine NDVI values are illustrated. It is also possible to use other spectral indices, among which the one that seems to give the best benefits to identify particularly vigorous plants is the NDRE (Normalized Difference Red Edge - Normalized Difference in the Red band):

$$NDRE = (NIR_{780} - RedEdge_{730}) / (NIR_{780} + RedEdge_{730})$$

where the values 780 and 680 nm are indicative of bands centered on values of slightly different wavelengths that allow one to compute the same NDVI index using several sensors. The NDRE index expresses the fact that the reflectance in the red band is, above all, influenced from the presence of chlorophyll and less biomass. The NDVI index has a linear

response in the early stages of plant development, when the present biomass is limited but, viceversa, when the plant is in an advanced stage growth indicates that NDVI tends to be saturated by the high biomass content. On the contrary the NDRE index has a linear trend at all stages of growth. In particular, the following graph shows how the NDVI considerably changes between crops healthy and stressed at different stages of growth. However, as the development of the plant increases, the NDVI is no longer an effective indicator to distinguish the stressed and healthy plants because the relationship that binds the index to the vegetative vigour tends to flatten. The graph shows how NDRE is the best indicator to identify stronger and healthier plants than weaker ones, even in the most advanced stages of growth; this is because, even with high levels of vigour, one has a linear relationship between x and y.

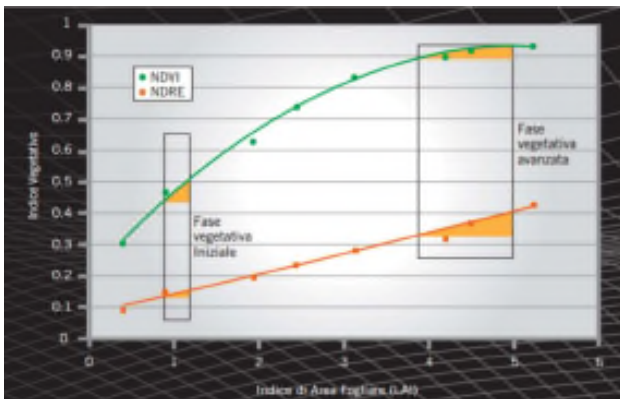


Figure 2. Graph of the NDVI / NDRE vigour indicators

As it can be seen from the previous graph, the NDVI index tends to become saturated in the presence of very vigorous plants, viceversa the NDRE index always grows linearly even with high LAI values.

3. METHODS

Since decades, the development and application of vegetation indices (VI) to monitor crop status has been in the focus of several research activities (Thenkabail et alii, 2000; Tucker 1979). Generally these VI are developed from multi-or hyper-spectral images of the field or remote sensing data (Gnyp et alii, 2014; Koppe et alii 2010; Li et alii 2008).

In these last five years the image acquisition with UAVs has exponentially increased (Colomina and Molina 2014; Zhang and Kovacs 2012). If the multi and hyper-spectral sensors are still expensive and image capture and analysis require a high expertise (Aasen et alii 2015; Kelcey and Lucieer 2012), it is nowadays possible to acquire geo-referenced RGB images with a very high spatial resolution by means of UAV platforms.

The RGB images from UAVs are very relevant for the research because this data source have many applications for precision farming (Ballesteros et alii, 2014; Lopez-Granados et alii, 2016). A well-established crop monitoring approach, which is also based on RGB images from UAV platforms, is the generation of multi-temporal Crop Surface Models (CSMs) for defining the plants height and the biomass estimations (Bending et alii, 2013; Hoffmeister et alii, 2015; Tilly et alii, 2014). In this context tests and investigations were conducted by Bending et alii (2015) to analyze and evaluate the potential of RGB -

based vigor indices proposed by Tucker (1979) and Hunt et alii (2005).

Bending et alii (2015) have also introduced a new, moderately performing, visible domain vegetation index, the RGBVI, which is applied in combination with the plant height from CSMs. Similar research are described by Tilly et alii (2015) and Bareth et alii (2015) and refer to the potential of the RGB vegetation indices. Both studies evaluated the RGBVI against the vegetation indices that were computed from hyper-spectral field spectrometer measurements.

Conversely the overall objective of this research is to further investigate the performance of the RGBVI from RGB images, NIR images, thermal and multi-spectral images captured with a low-cost UAV system. In this study the performance is not tested against field spectrometer measurements since this issue will be addressed in future research.

Therefore, four working packages are investigated below:

- Sensor 1: Carl Zeiss optics for RGB images
- Sensor 2: Canon S110 for NIR images
- Sensor 3: Flir thermal imaging
- Sensor 4: Tetracam ADC Micro for multi-spectral images.

The ground-controlled UAV carrier or GCS mode, Gimbal Control Station, requires reliable communications from the aircraft to the control station and vice versa. In this experience a Skyrobotic ES - SRF SF6 has been used, with the following hardware configuration:

- 6 engines TIGER MOTOR MN 3508 380kV;
- 6 propellers TIGER MOTOR 14X4,8 CF PROPELLER;
- Autopilot: SR4000 MAIN rev 1.4 SKYROBOTIC;
- Powerboard: SR4000 rev 1.4 SKYROBOTIC;
- gimbal stabilized two axes - SIRALAB ROBOTICS;
- frame (frame + landing gear) SKYROBOTIC CARBON;
- SKYROBOTIC LiPo10900mA 22.2V batteries;
- FTS (Flight Termination System) SKYROBOTIC with dedicated processor



Figure 3. UAV SR – SF6 Skyrobotic

The duration of each flight was 15 minutes on average, at an average speed of 2.5 m / sec with each type of sensor. In order to verify the acquisitions, during the measurement campaign, a

first download of country data and a quality check of the acquired images were made. This control became necessary because during the flight phase small wind bursts appeared. In particular, multispectral image captures were made at an altitude of about 52 meters, with a continuous acquisition rate of 1 second in order to ensure at least 60% overlap. The teflon tag image was acquired directly before the flight. The main purpose was to fix the coordinates of the GCPs (Ground Control Point) by means of white wooden panels of 50x50 cm in size and some of teflon tag taking into account all the problems arising from the atmospheric conditions and of the light conditions (such as the value of the incident angle of sunlight).

4. SITE STUDY

4.1 Topographic framework

The vineyard object of study is located in the territory of the municipality of Anagni, in the province of Frosinone. The farm, whose coordinates are shown in the table, is located near the Anagni highway (Fig. 2) of the A1 motorway, about 45 km in the south of Rome.

WGS84 coordinates	° ' "	
Latitude	41° 43'	13.64 "
Longitude	13° 06'	03.75 "

Table 1. WGS84 Coordinate of the site



Figure 4. Monitoring area

The site is part of the geological structure of the Alban Hills. This specific geographic position makes the chemical and physical composition of the soil to be volcanic (Vulcano Lazio, Latium Volcano), with the presence of red molten clay equal to almost 54% of the soil sample analyzed. The high amount of clay makes the soil poorly permeable with high water retention properties. From the chemical point of view, the soil contains potassium, calcium and minerals. The levels of nitrogen and phosphorus measured by property-commissioned analyzers are low. For what concerns the vineyards present in the farm, new cultivations were planted in 1962, following criteria that relate to ancient techniques. Weak or medium vigor rootstock have been implanted with high rigidity of the plant and with permanent filling of the interlayer to favor the development of the roots of vines at the expense of the grass roots. Such choices led to the limitation of the growing period of the shoots and the consequent elongation of the period of accumulation of sugars and noble compounds in berries. Among the vineyards, the predominant grape is the Cesane di Affile, a real viticultural and

oenological jewel of this land as well as the native red grape native of Lazio. In addition, other red berries of international diffusion and traditional cultivation on our hills, such as Cabernet Sauvignon, Cabernet Franc, Petit Verdot, Merlot and Syrah are also grown.

5. MONITORING ACTIVITIES

Cultivation growth index monitoring was performed through the elaboration of photogrammetric images from last generation drones equipped with photogrammetric sensors of the type:

- Thermal;
- RGB (visibile);
- NIR (Near Infrared);
- Multi-spectral.

Thanks to the experience gained on the site under review, acquisitions with such sensors were carried out during the months of June and September 2015 and 2016 for a total of 4 flights.

The surface of the site, amounting to 150,000.00 m² (15 ha), has made possible the use of UAVs with high flight range, in order to cover the entire plot of land.

5.1 Monitoring activities in 2015

During the first year of tracking, several flights were carried out at various points using different photogrammetric cameras installed on board of a single Aibotix X6 aircraft. Once the system was calibrated, processing of images captured during 2 flights made in June and July 2015 with different cameras for RGB images and for NIR images, produced the following orthophotos (Fig. 3 and 4).



Figure 5. Orthophoto RGB June 2015

From the orthophotos generated in RGB mode it is possible to uniquely determine the extension of the vineyard and the adjacent crops. The vineyard appears to be of intense green color unlike the grain crops that have on a yellow tint.



Figure 6. Orthophoto RGB July 2015

To determine the NDVI (Normalized Difference Vegetation Index) that can be calculated from the usable spectral information, further flights were performed with NIR image capture using a Canon PowerShot ELPH 110 Hs camera with distance focal length of 4.3 mm (Fig. 6).

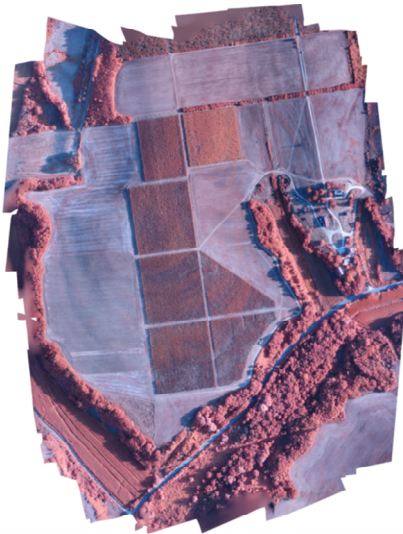


Figure 7. Orthophoto NIR

After having obtained the NDVI index maps for the months of June and July 2015, the average values of the NDVI index, identified by the pixels of the samples of the vineyards, have been those shown in the following table:

June 2015	July 2015
0,541	0,637

Table 2. NDVI index in 2015

5.2 Monitoring activities in 2016

Based on the monitoring activities in 2015, the 2016 measurements campaign was carried out by using new sensors installed on the above mentioned UAV platform as well as an RGB camera and a NIR camera, including a thermal sensor and another multi-spectral sensor. In addition, as the new sensors were not compatible with the previously used drone, the UAV was changed to a Skyrobotic SF-6 esacotter.

The work platform has been implemented with ground-based remote control thus making possible to tune the flight plan via mobile Internet connection. Thanks to this type of remote control, the flight of the drone has been completely monitored on the ground: sending corrections of the flight and route parameters, the UAV aircraft has followed the overlay scheme shown in Figure 8.

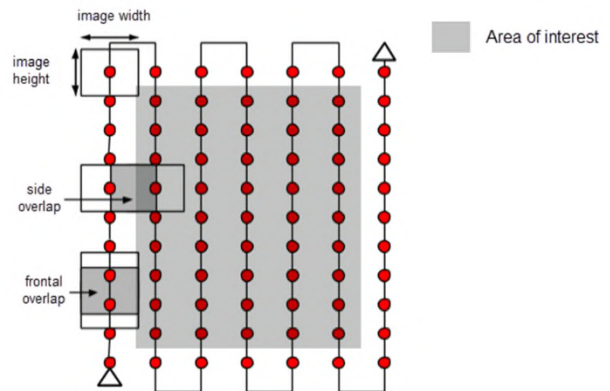


Figure 8. Overlapping scheme

The measurements were carried out on 27/07/2016 and 03/09/2016 from 12:00 to 13:00 in order to minimize the effect of shadows, so that the sun position is as vertical as possible. In both days atmospheric temperatures were greater than 30 ° C, with peaks of 35 ° C. Wind conditions were very favorable; only at the end of the last flight, when the UAV was installed on the multispectral sensor, the rise of a slight breeze forced the UAV driver to make small corrections of the flight plan. Therefore, image acquisition has taken place, and Figure 7 shows an excerpt of the orthophoto RGB.



Figure 9. Partial RGB orthophoto

The image shown in Figure 7 was acquired in RGB mode at a flight height of 58.00 meters. The ground reprojection error was 1.72 pixels. The high degree of coverage and the image quality

make it possible to clearly identify the targets that materialize the Ground Control Point (GCP) used as a topographic support network.

After flying in RGB mode, a first test was carried out, with a FLIR thermal sensor, in order to determine the temperature range of the vineyard. On the day of acquisition - 27/07/2016 - the outdoor temperature was extremely high, close to 40 ° C; hence some portions of the vineyard, especially those most exposed to sunlight, have an extremely high temperature gradient (Fig. 8). This very helpful information at the agronomic level has allowed the farmer to make timely irrigation in order to overcome the water shortage caused by the high temperature.

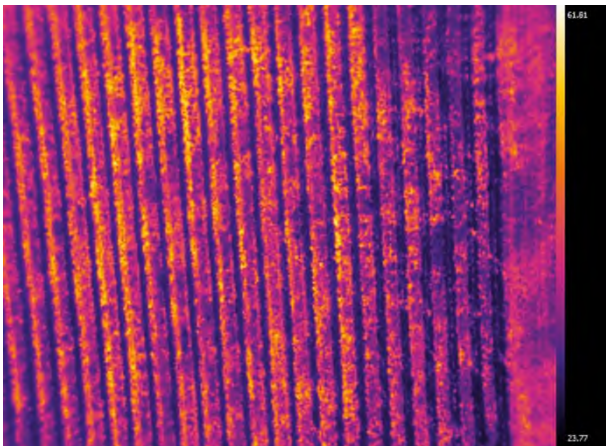


Figure 10. Acquisition by FLIR thermal camera

In a further flight a TETRACAM ADC Micro multispectral sensor was used, with a "rolling shutter" sensor that allows the image of Fig. 9 to show a extract of the obtained multispectral ortho-images.

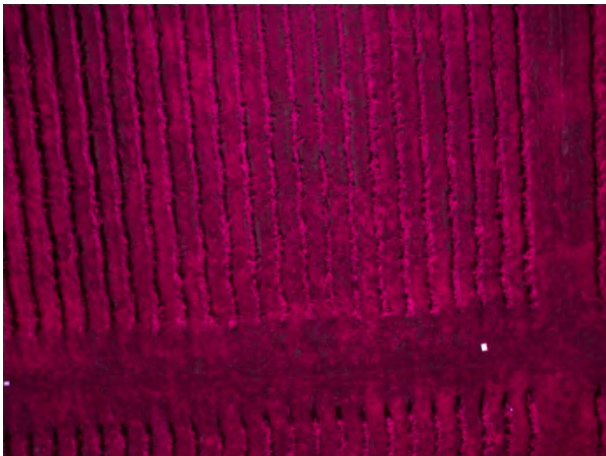


Figure 11. Multi-spectral orthophoto

After the acquisition phase, post-processing of the images allowed the NDVI index to be estimated for both measurement sessions in July and September. A summary of the values of the vigor indexes throughout the monitoring period is shown in the sequel:

July 2016	September 2016
0,715	0,995

Table 3. Index NDVI 2016

Monitoring	Values of the index NDVI
June 2015	0,541
July 2015	0,637
July 2016	0,715
September 2016	0,995

Table 4. Estimated NDVI values during the monitoring period

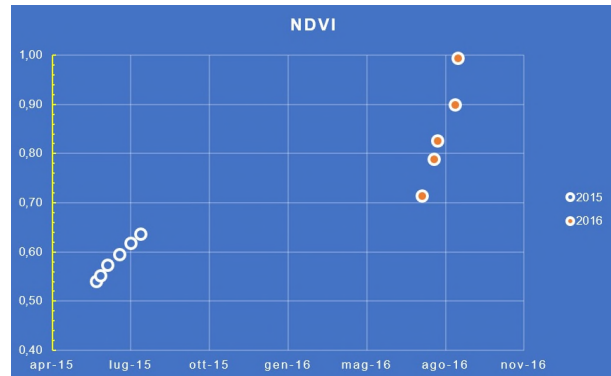


Figure 12. NDVI values 2015 - 2016

From a comparison of the obtained results it is possible to say that the NDVI value computed in July 2016 is about 12% greater than the one calculated in June 2015. This increase in the NDVI index is mainly due to the corrective inputs applied by the farmer following the monitoring carried out after June 2015.

5.3 Rolling shutter

From the reading the camera's technical data sheet, it was found that the capture of images is carried out in the "Picture taking line" mode - the frame displays by line, and for the different color bands it was possible to infer the spectral response graph. The following figure, Fig.11, which also shows the spectral response graph for the several color bands, shows that the maximum room responsiveness of the camera is in the green band and the red band, in the wavelengths contained in the spectrum of the visible.

Camera spectral response for red and green (blue is blocked for NIR Sensing):

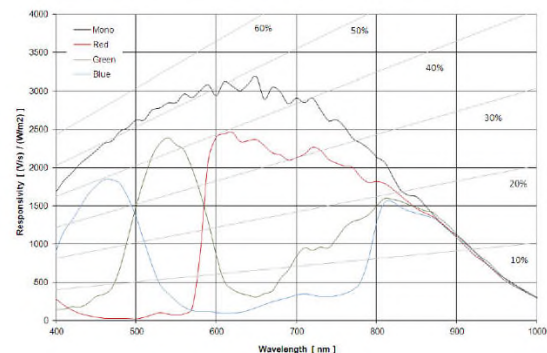


Figure 13. Spectral camera response for red and green

In few years the recent technological development has allowed one to obtain more advanced types of sensors equipped with an electronic mechanism known as "global shutter". For this kind of sensors all pixels contained in an image are captured at the same time. This means that the image will be "frozen", i.e. sharp without the blurred effect.

The following chart shows a representative diagram relative to the different image capture mode with global shutter sensors and rolling shutter sensors.

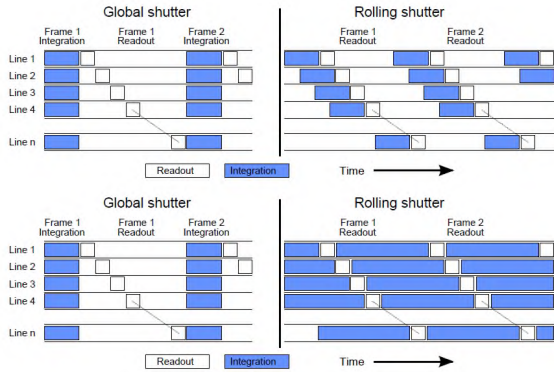


Figure 14. Different acquisition modes between global and rolling shutter

In the use of UAV platform rooms, the presence of a global shutter sensor has a great importance as the shutter is moving. It is easy to deduce the greater sharpness of the images, as well as the improved quality of the final processing.

The advantage of a "global shutter" room when it is used with the UAV platform is the ability to fly at an increasing speed without the risk of blurred and crisp images.

For example, in the Structure for Motion (SfM) field, cameras equipped with "global shutter" sensors, allows one to use only one image; viceversa for cameras equipped with rolling shutter sensor multiple images are needed. This yields an increase in the computational burden due to a larger number of parameters to be estimated. However, the use of rolling shutter sensors is not precluded and one can continue to use them by performing a calibration process to make the "line delay" known.

The research activity that has been carried out allowed us to realize that using a rolling shutter sensor during field acquisition, with non-optimal climatic conditions, requires a speed flight lower with respect to the one typical of flights with a global shutter.

Although the flights with a rolling shutter sensor were carried out at a speed of about 3 m/s, we still faced the problem of the low sharpness since the images were acquired by lines.

In the future, it will be advisable to perform step-by-step tests to reduce UAV flight speed to minimize this effect on the photogram.

5.4 Accuracy of the surveyed data

To be able to estimate the accuracy of processed data detected through the use of the Agisoft Photoscan software a subdivision in sub - sectors, taken as sample areas, of the whole area occupied by rows of vineyards, has been considered The attention has been concentrated on the plots n. 3 and n. 4.

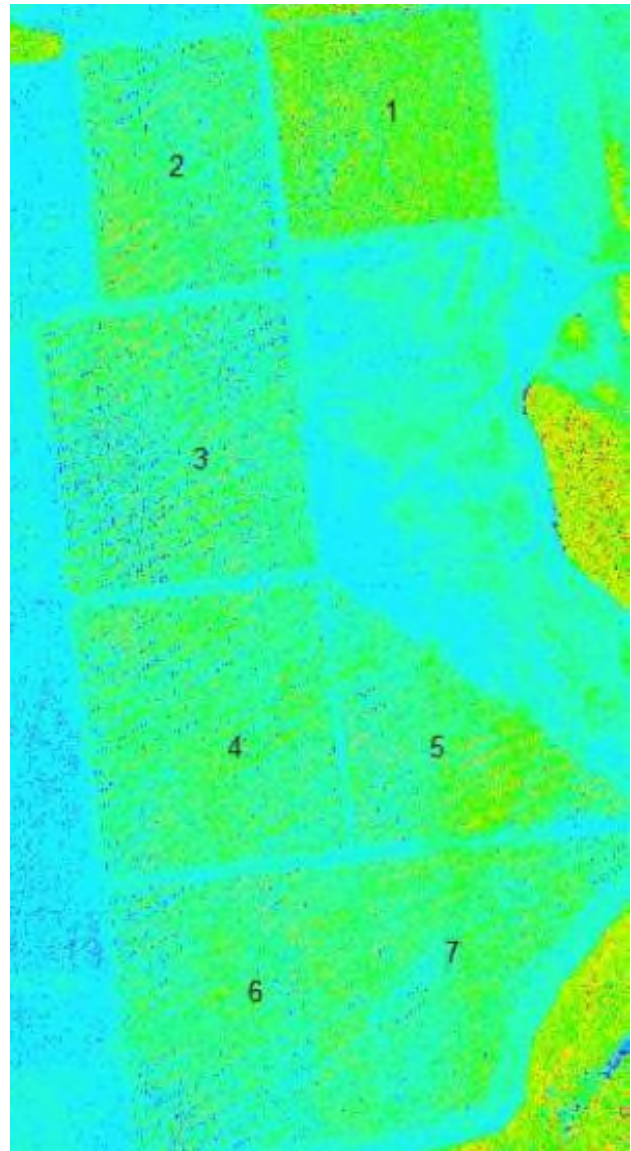


Figure 15. Study sectors

For each of them the precision data obtained have been deduced for the estimate of the NDVI index.

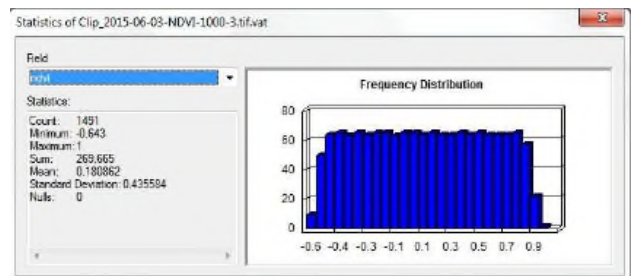


Figure 16. Sector 3 - Distribution frequency 03/06/2015

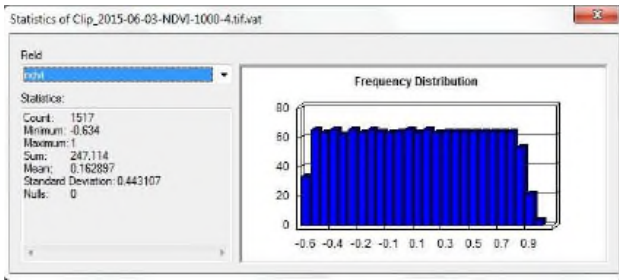


Figure 17. Sector 4 - Distribution frequency 03/06/2015

The values shown are representative of the individual sector. For the determination of the index NDVI of the vineyard we proceeded to a query of the individual sample pixels. It's interesting to note that the values of standard deviation obtained on two different sectors are similar. This allows us to state that the acquisitions are accurate, and that the determined NDVI index values are representative of the health status of the vineyard.

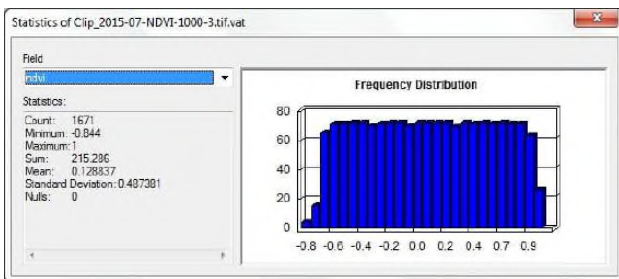


Figure 18. Sector 3 - Distribution frequency 10/07/2015

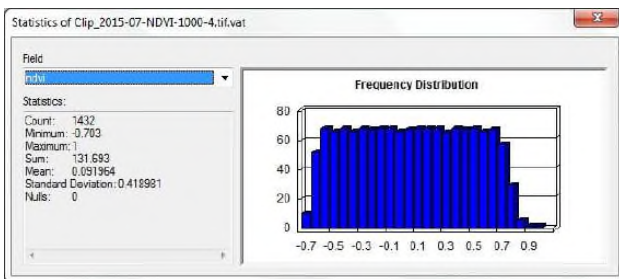


Figure 19. Sector 4 - Distribution frequency 10/07/2015

5.5 Analysis of the results

From the analysis of the results it can be concluded that the increase of the NDVI VOC index of about 12% estimated during the monitoring period from June 2015 to September 2016 is indicative of the response of the vineyards to different climatic conditions and in accordance with the corrective remedies provided to the producer following the monitoring activities. This response is also correlated with the type of soil, strong clay matrix, thus characterized by a significant water retention.

In fact, from a meteorological point of view, rainfalls in the year 2015, more abundant than the year 2016, resulted in greater leaf production at a disadvantage of the quantity and quality of berries. Moreover the soil with a strong clay component, retaining rainwater by swelling, tends to decrease the amount of sugars present within the berries. The growth of the vineyard improved during the year 2016, characterized by a modest

rainfall. In fact, a high rainfall is responsible for the formation of pests and mushrooms in the vines, and so that no antiparasitic and anticritogamic treatment was practiced in 2016; Moreover, the less water content retained by soil clay has allowed the higher sugar content of the acines, thus improving the alcoholic potential of the grape used for vinification (Fig. 13).



Figure 20. Vineyard ripening

6. CONCLUSIONS AND REMARKS

The growth index estimated by the NDVI parameter (Normalized Vegetation Index) represents a satisfactory description of the state of health of the vineyard and of its critical issues, although more reliable values of this indicator can be obtained through ground measurements for monitoring the physical and chemical characteristics of soil and culture that were not performed in this first phase.

Nowadays the real need to develop the growing farming sector is mainly dictated by the need to improve production, achieving savings in terms of fertilizer and pesticide use, with a consequent reduction in environmental pollution and increased security for communities.

Through the use of combined information (data processed by photogrammetry by UAV and ground spectrometric measurements) the producer can uniquely determine which sector of his field presents real-time resolutions, such as the administration of major or minor quantities of fertilizers and / or higher irrigation cycles.

Among the critical issues of this brand-new surveying methodology there are the flight autonomy of the UAV aircraft and the ability to install on board low-cost sensors rather than high-performance sensors. To avoid the risk of blurry and unclear images, it is advisable to use cameras/sensors equipped with electronic mechanisms known as a "global shutter" that allows the aircraft to move at increased speeds without the risk of blurring.

A further constraint found during the measurement campaigns was the limited number of spectral bands provided by the multispectral cameras which did not allow estimation of some vegetation parameters such as moisture content.

For this reason, it would be desirable in the future to acquire data with hyper-spectral sensors.

In addition the proposed approach based on UAV platform and high-resolution sensors provides a precision tool for botanists, oenologists, producers and professionals in the field of precision agriculture. This disseminates the knowledge of photogrammetric measurement techniques able to analytically

determine the geometry of vineyards and to monitor species of vines subjected, at present, to multiple grafts in order to make them more resistant to disease and to improve quality and productivity.

The market today is becoming more competitive and demanding. This is particularly true in a country like Italy where high quality wine production standards justify the adoption of management practices that simultaneously increase both the quality and the quantity of the crop.

Given the first results obtained in this study, more extensive and intensive field monitoring sessions will be able to be used to determine in the future how many samples of vines measured by the proposed methodology can become representative of the health status of vineyards and how they can be linked to the conditions of the ground.

In this sense the proposed approach can be an effective example of precision viticulture that seeks to consider a wider range of observations through the development of hardware and software platform, integrating multi sensor systems for the collection of information beyond the visible (thermal cameras, oblique cameras, etc.), the implementation of algorithms pre-selection / data processing, the verification of application methods, operational and critical issues of the carriers as well as the development of spectrometers on the ground for the control of chemical - physical parameters of the soil and root system.

Finally the know-how gained from these first tests allows us to suggest that in the future the emergence of UAVs from geomatics technical digital photogrammetry can provide prescription maps for viticulture and provide recommendations to improve the efficiency of management in terms of quality, productivity and sustainability.

7. ACKNOWLEDGMENTS

The authors would like to thank the owner of the agricultural land Farm Coletti - Accounts for the availability of the site and the companies Geores srl, Via Marittima snc - Frosinone (FR); Gagliardini Brothers - operators SAPR ref. ENAC 5369, Via Enrico Mattei n. 21 - Montecassiano (MC) and Fly Engineering, Via Sandro Pertini - Tolentino (MC) for the availability of UAV platforms and the support.

8. BIBLIOGRAPHY

Aasen A., Burkart A., Bolten A., Bareth G., (2015), Generating 3D hyperspectral information with lightweight UAV snapshot cameras for vegetation monitoring: From camera calibration to quality assurance. *ISPRS Journal of Photogrammetry and Remote Sensing*, 108, pp.245-259. doi: 10.1016/j.isprsjprs.2015.08.002

Adamczyk J., Osberger A., (2015), Red-edge vegetation indices for detecting and assessing disturbances in Norway spruce dominated mountain forests. *International Journal of Applied Earth Observation and Geoinformation*, 37, pp. 90-99

Atzberger, C., 2013: *Advances in Remote Sensing of Agriculture: Context Description, Existing Operational Monitoring Systems and Major Information Needs*. *Remote Sensing*, 5(2), pp.949–981. doi: 10.3390/rs5020949

Aicardi I., Lingua A., Noardo F., Maschio P., *Criticità e soluzioni per il rilevamento in ambito ambientale con piattaforme UAV*. Politecnico di Torino, DIATI.

Angelov P. “Sense and Avoid in UAS” *Research and Applications*. Wiley (2012)

Bareth, G., Bolten, A. Hollberg, J., Aasen, H., Burkhart, A., and Schellberg, J., 2015: Feasibility study of using non-calibrated UAV-based RGB imagery for grassland monitoring: case study at the Rengen Long-term Grassland Experiment (RGE), Germany. *DGPF Annual Conference'15*. – Cologne, Germany: 55-62. http://www.dgpf.de/src/tagung/jt2015/proceedings/papers/07_DGPF2015_Bareth_et_al.pdf

Ballavita D., Tolomei L., Mazzitelli A. – *Realizzazione di cartografia di dettaglio di area franosa attraverso l’uso di UAV planante Sensefly e software innovativo APS per generare ortofoto, DSM e DTM*. Atti 16a Conferenza Nazionale ASITA – Fiera di Vicenza 6-9 Novembre 2012

Barazzetti L., Remondino F., Scaioni M., Brumana R. (2002), “Fully automatic UAV image based sensor orientation”, *International Society for Photogrammetry and Remote Sensing (ISPRS)*, vol. XXXVIII;

Bareth G., Bolten A., Gnyp M. L., Reusch S., Jasper J. (2016), Comparison of uncalibrated RGBVI with spectrometer – based NDVI derived from UAV sensing system on field scale. *The International Archives of the Photogrammetry, Remote Sensing and Spatial Information Sciences*, doi:10.5194/isprsarchives-XLI-B8-837-843; XXIII ISPRS Congress, 12-19 July 2016, Praga , Repubblica Ceca

Bending J., Bolten A., Bareth G. (2012), Introducing a low – cost mini – UAV for thermal – and multispectral – imaging. *The International Archives of the Photogrammetry, Remote Sensing and Spatial Information Sciences Volume XXXIX-B1-345; XXII ISPRS Congress , 25 August-01 September 2102, Melbourne, Australia*

Dandois J.P., Olano M., Ellis E.C. (2015), Optimal Altitude, Overlap, and Weather Conditions for Computer Vision UAV Estimates of Forest Structure, *Remote Sensing* 7, 13895-13920.

D’Urso M.G., Marino C.L. (2016), An application of close – up photogrammetry in viticulture. . *The International Archives of the Photogrammetry, Remote Sensing and Spatial Information Sciences*, doi:10.5194/isprsarchives XLI – B8,1243-1250- 2016 XXIII ISPRS Congress, 12-19 July 2016, Praga , Repubblica Ceca

Eisenbeiß H., *UAV Photogrammetry*. ISBN 978-3-906467-86-3 – Zurich 2009

Eisenbeiß H. (2009), “UAV Photogrammetry”, Ph.D. thesis, Institute of Geodesy and Photogrammetry, ETH Zürich. Zurich, Switzerland

Fahlstrom P., “Introduction to UAV Systems”, 4th Edition ISBN 978-1-119-97866-4

Floris A., Clementel F., Colle G., Gubert F., Bertoldi L., De Lorenzi G., *Stima di volumi legnosi forestali con dati fotogrammetrici telerilevati da UAV su piccole superfici: un caso studio in Trentino*. Atti 16a Conferenza Nazionale ASITA – Fiera di Vicenza 6-9 Novembre 2012

- Gini R. (2010), Processing of high resolution and multispectral aerial images for forest DSM production and tree classification. Master thesis, DIIAR, Politecnico di Milano, Italy.
- Gini R., Passoni D., Pinto L., Sona G., Aerial images from an UAV system: 3D modeling and tree species classification in a park area. *Int. Arch. Photogramm. Remote Sens. Spatial Inf. Sci.*, Vol. XXXIX-B1, 361-366, XXII ISPRS Congress, Melbourne, Australia
- Gini R., Passoni D., Pagliari D., Pinto L., Sona G. – Rilievi multispettrali da UAV per la modellizzazione di edifici e del territorio: esperienze condotte al Politecnico di Milano. DICA – Sez. Geodesia e Geomatica
- Guo T., Kujitai T., Watanabe T. (2012), Mapping crop status from an unmanned aerial vehicle for precision agriculture applications. . The International Archives of the Photogrammetry, Remote Sensing and Spatial Information Sciences, ISPRS Archives XXXIX-B1-485.
- Herwitz S.R. , Johnson S.F., Higgins R.G., Leung J.G., Dunagan S.E. (2002), “Precision agriculture as a commercial application for solar – powered Unmanned Aerial Vehicles”, AIAA Technical Conference and Workshop on Unmanned Aerospace Vehicles, Systems, Technologies and Operations. Portsmouth, Great Britain
- Lo Brutto M., Sistemi UAV per rilievi in ambito archeologico. Giornata di Studio “Potenzialità e prospettive del rilievo fotogrammetrico aereo di prossimità con l’ utilizzo di droni: applicazioni nel campo ambientale e dei beni culturali”. Palermo (PA), 22/11/2013.
- Marenchino D. , PhD Tesi– Tecniche innovative di rilievo UAV e fotogrammetria.
- Minarik R., Langhammer J. (2016), Use of a multispectral UAV photogrammetry for detection and tracking of forest disturbance dynamics. The International Archives of the Photogrammetry, Remote Sensing and Spatial Information Sciences doi:10.5194/isprsarchives, XLI-B8-711-718; XXIII ISPRS Congress, 12-19 July 2016, Praga , Repubblica Ceca
- Patil P., Dutta D., Biradar C., Singh M. (2015), Quantification of the terrestrial phytomass and carbon in the mountainous forest ecosystem using remote sensing and in-situ observations. ISPRS Archives XL-7-W3-483.
- Perry E.M., Fitzgerald G.J., Poole N., Craig S., Whitlock A. (2012), NDVI from active optical sensors as a measure of canopy cover and biomass. ISPRS Archives XXXIX-B8-317
- Remondino F., Nex F., Sarazzi D. - Piattaforme UAV per applicazione geomatiche.
- Sarazzi D., Julitta F., Quartieri A., D’Argenio A., Acquisizione ed elaborazione fotogrammetrica di immagini da micro e mini UAV. 5° Workshop tematico – Telerilevamento e le Nuove Scienze della Terra. 23/24 Giugno 2011 S. Giovanni in Monte con il patrocinio di ENEA.
- Sona G., Passoni D., Pinto L., Pagliari D., Masseroni D., Ortuani B., Facchi A. (2016), UAV multispectral survey to map soil and crop for precision farming application. The International Archives of the Photogrammetry, Remote Sensing and Spatial Information Sciences , doi:10.5194/isprsarchives-XLI-B1-1023-1029; XXIII ISPRS Congress, 12-19 July 2016, Praga, Repubblica Ceca
- Tavakoli H., Mohtasebi S.S., Alimardani R., Gebbers R. (2014), Evaluation of different sensing approaches concerning to nondestructive estimation of leaf area index (LAI) for winter wheat. *International Journal on Smart Sensing and Intelligent Systems* vol. 7, n. 1, March 2014
- Turner D., Lucieer A., Watson C. Development of an Unmanned Aerial Vehicle (UAV) for hyper resolution vineyard mapping based on visible, multispectral and thermal imagery
- Tsouvaltsidis C., Zaid Al Salem N., Benari G., Vrekalic D., Quine B. (2015), Remote spectral imaging using a low cost UAV system. The International Archives of the Photogrammetry, Remote Sensing and Spatial Information Sciences; doi:10.5194/isprsarchives, XL-1-W4-25-31, International Conference on Unmanned aerial Vehicles in Geomatics, 30 August-02 September 2105, Toronto , Canada
- Turner D., Lucieer A., Watson C., Development of an Unmanned Aerial Vehicle (UAV) for hyper resolution vineyard mapping based on visible, multispectral, and thermal imagery.
- Valavanis K.P. (University of South Florida, Tampa, Florida, USA) ed. Springer, *Advances in Unmanned Aerial Vehicles*. ISBN 978-1-4020-6113-4.
- Zhang C. (2008), “An UAV–based photogrammetric mapping system for road condition assessment”, The International Archives of the Photogrammetry, Remote Sensing and Spatial Information Sciences, vol. XXXVII, part B5. Beijing, China.

SURVEYING AND THREE-DIMENSIONAL MODELING FOR PRESERVATION AND STRUCTURAL ANALYSIS OF CULTURAL HERITAGE

Ilenia Selvaggi

Dept. of Civil, Chemical, Environmental and Material Engineering (DICAM), University of Bologna,
Viale Risorgimento 2, Bologna, Italy – ilenia.selvaggi2@unibo.it

KEY WORDS: Terrestrial Laser Scanning, Close Range Photogrammetry, historical buildings, Cultural Heritage, geometrical modeling, numerical modeling, comparison data, finite element analysis, structural analysis.

ABSTRACT

The present paper aims at exploring the potential contribution of Geomatics to Structural Engineering, by investigating the capabilities and advantages of Terrestrial Laser Scanning TLS and Close Range Photogrammetry CRP. In this perspective, the research has been carried out in three notable case studies, of which two belong to the Italian Cultural Heritage. The first one has been the San Felice sul Panaro Fortress, a historical building damaged by the Emilia Earthquake, on May 2012. It is composed by a square plan with a tower in each corner with the most important, the Mastio tower, with a height of about 32 m. As a second case, the complex of Aquileia was chosen for its distinguishing octagonal shape, which is suitable for geometric comparisons and analyses. Finally, the study focused on San Luzi Church with its bell tower of about 60 m high. The three case studies are definitely different each other, for geometrical and historical elements. Therefore, the transformation of the point cloud obtained from Geomatics techniques into a Finite Element Model FEM –which is the required starting point for a structural analysis- must follow different approaches, in order to obtain adequate and detailed voxel models. With the aim of evaluating the proper definitions of the FE models, both static and dynamic analyses were carried out. The outcomes of the presented research demonstrates how the capabilities of Geomatics to produce comprehensive and detailed description of the geometry of buildings can be exploited also for structural analysis, especially for heritage buildings for which focused analyses ensure their preservation.

1. INTRODUCTION

In the field of Cultural Heritage, the possibility to integrate point cloud acquisition using Terrestrial Laser Scanner (TLS) with Close Range Photogrammetry (CRP) using Structure from Motion approach (SfM) allows to preserve the history and memories of historic buildings, archaeological sites and cultural landscapes. In fact, the opportunities to collect accurate and detailed three-dimensional datasets, using both image- and range-based techniques, allows to obtain a deep investigation as input for multidisciplinary analysis (Guarnieri et al., 2006; Remondino and Menna, 2008; Russo and Manferdini, 2014).

The necessity for preservation and documentation of ancient buildings is increasing, such as the rapid development of new techniques and technologies in the last years. In fact, during the last decade several improvements in the digital technologies offers news methods and different approaches for surveying with TLS and CRP (Bitelli et al., 2017). Through TLS and CRP, the geometry of a building can be described in a complete and very detailed point cloud dataset. However, it is not possible to follow standard procedures, but the campaign of acquisition data depends on the context, the kind of architecture to be surveyed, the goals to be achieved etc. (Aicardi et al., 2016).

Several works demonstrated how Cultural Heritage can greatly benefit from three-dimensional modeling applied to object or historical site analysis, documentation, preservation and restoration (Callieri et al., 2011; Grussenmeyer et al., 2008; Manferdini and Galassi, 2013; Remondino, 2011). A complete three-dimensional survey allows to obtain a complete and detailed three-dimensional model and the deep knowledge of a building is the initial step for different studies, such as modeling, monitoring, structural behavior (Dellepiane et al., 2013; Fritsch et al 2011).

Focused on historical buildings, they are mainly composed by masonry and the structural behavior is strictly related to the geometric characteristics of the walls. With a deep knowledge of ancient buildings, problems concerning the structural damage can be examined, monitored and limited, increasing the service life of the historical heritage (Guimarães et al., 2014). An interesting approach is presented in Barazzetti et al. (2015) and Guarnieri et al. (2017) where the authors describe the use of Building Information Modeling (BIM) derived from point clouds for the structural simulation based on FEM.

In this context, Geomatics can provide an important support in the structural field, by transforming initial dataset into FE models (Bitelli et al., 2016; Castellazzi et al., 2016). The opportunity to generate FE model very detailed, without the loss of important details, allows to have an accurate and detailed modeling of the object, corresponding to the real configuration.

1.1 Research aim

The main aim of this research was to analyse the connection between the Geomatics and the structural analysis. Starting from the point cloud dataset, different analyses have been performed considering three case studies.

The first one concerned the San Felice sul Panaro Fortress (MO), an important building damaged by the 2012 earthquake in Emilia. The analyses focused on the transformation of the complex point cloud into a polygonal model with continuous surfaces. Hence, a structural analysis with a semi-automatic approach has been carried out.

The elements composing the Basilica of Aquileia (UD), with particular attention to the Baptistery, have been analysed in the second case study. Two different models have been realized: a geometrical model generated starting from traditional tools and historic documentations, and a numerical polygonal model derived from point cloud dataset. The

comparison between these output models have been performed to highlight the advantages of using point cloud data.

Finally, problems related to the noise and to the definition of a correct polygonal model have been faced. The study has been focused on the San Luzi church, in Switzerland.

2. SAN FELICE SUL PANARO FORTRESS

The San Felice sul Panaro Fortress is a monumental historical building located near the city of Modena (Italy). In 2012, the Fortress was hit by the Emilia earthquake with two magnitude peaks on 20 May (MW = 5.86) and on 29 May (MW = 5.66). Several studies aimed to preserve its integrity have been carried out (Scognamiglio et al., 2012). After the earthquake, the Fortress presented many cracks, and parts partially collapsed. The roofs of the Fortress, after the earthquake, are partially collapsed (Figure 1). The Mastio and the North tower were damaged in the external and internal part.



Figure 1. From left, view of the North front before the earthquake, after the earthquake and currently

Irregular plans and elevations of the Fortress denote a high seismic vulnerability. Perimeter walls connect the towers without continuity causing torsional and bending effects. Furthermore, the different height between the perimeter walls and the towers determines a different dynamic response of the structures. The seismic behavior of the Fortress derives from its geometry and from the type and quality of its materials. The entire Fortress is composed by masonry and mortar, with a minimum thickness of 30 cm to a maximum of 250 cm, in the basement of Mastio tower (Ferrari L. and Goldoni G., 2014). Being masonry, the thickness of the walls decreases from the bottom to the top. The horizontal elements are characterized by vaults and, in the roofs, by wood with principal and secondary frame.

The Mastio tower, with an overall height of about 32 m, a wooden roof and variable wall thickness thinner in the highest part, is the most characteristic part of the Fortress. For this reason, an analysis focused on the Mastio as isolated building has been carried out. With its square plan characterised by a tower in each corner, the San Felice sul Panaro Fortress was an interesting topic for the analysis and management of damaged data.

2.1 Data acquisition

After the earthquake, the municipality did an accurate survey of the damaged building by using geomatic techniques, mainly laser scanning and photogrammetry, obtaining different products like point clouds, orthophotos and 3D visualization. A morphological and structural survey for the San Felice sul Panaro Fortress was planned by request of the municipality in order to generate a functional representation of the actual state of the building. The survey was performed by ABACUS s.a.s., using a FARO Focus 3D x 330 laser scanner and a total station Trimble S6. 163 point clouds have been acquired by different scanning positions. These scans were aligned to the topographic network using reference targets with a millimeter-level precision.



Figure 2. Initial point cloud with more than 40 million of point

2.2 Data processing

Following a first decimation, the point clouds were merged into a unique dataset containing more than 40 million points (Figure 2). This dataset is a comprehensive three-dimensional point cloud for the whole building, exterior and interior. Each point of the cloud is conveniently referred to a reference system with X, Y, Z coordinates. In order to obtain a point cloud with a regular density Poisson-disk distribution was applied (Bridson, 2007). The point cloud was then transformed in a polygonal model using Triangular Irregular Network (TIN) (Corsini et al., 2012). The resulting mesh consists of about 4.8 million triangles. This model describes all of the surfaces surveyed by the laser scanner, but some parts (Figure 3) resulted non-continuous due to the presence of furniture as well as rubble and debris. These disturbing elements increased the complexity of the survey; the special conditions of the building must be considered.

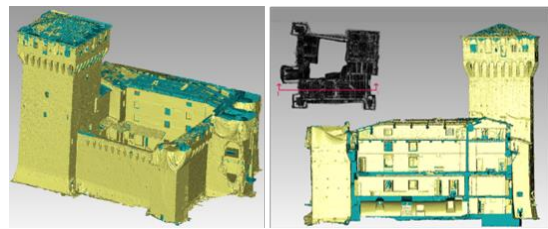


Figure 3. Isometric view (left) and transversal section (right) of the polygonal model. The green part is the non-continuous surfaces (missing parts, cut elements etc.), as opposed to the yellow part

2.2.1 The Mastio tower

From the point cloud of the Fortress, a subset of 0.8 million points related to the Mastio has been extracted and analysed, as seen Figure 4a. As represented in Figure 4b, the survey finely describes every single feature of the structure. The point cloud has a very heterogeneous density, primarily related to the distance between the single scan positions and the object acquired. The first polygonal model consists of about 1.670 million triangles (Figure 4b). After decimation and cleaning, the TIN model consists of about 1.120 millions of triangles (Figure 4c).

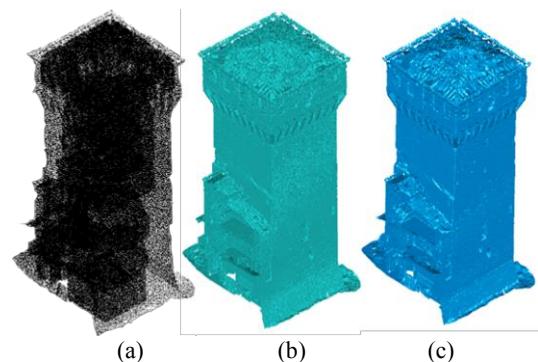


Figure 4. 3D models of Mastio Tower. Point cloud dataset (a); initial polygonal model (b); final TIN model (c)

2.3 FEM analysis

The resulting TIN model fully describes the surface enveloping the Fortress inside and outside, without volume.

In order to create a volume model, an overlap between polygonal model and slices with a constant step of 25 cm has been done. By inspecting every single slice in GIS software points not belonging to the Fortress, inevitably acquired during the scanning, have been cleaned. For more details see the CLOUD2FEM procedure described in Castellazzi et al. (2015). The proposed workflow aimed to minimize manual intervention in terms of time.

Based on the geometry properties and the characteristics of the building (Bitelli et al., 2016), a fine description of the Fortress was done by slicing the complex building height with a $\Delta z = 25$ cm. Therefore, 121 digital slices have been stacked (Figure 5), obtained from horizontal planes, and the distance of the Δ value depends on the desired resolution for the Finite Element model. The dimension of each pixel composing the slices was set as 25 x 25 cm: in this way, the third dimension was the distance between each slice, and the result was a three-dimensional voxel model. By using a unique local or global reference system, final datasets were stackable. Each pixel grid, obtained from the corresponding slice, contributes to the realization of the voxel model.

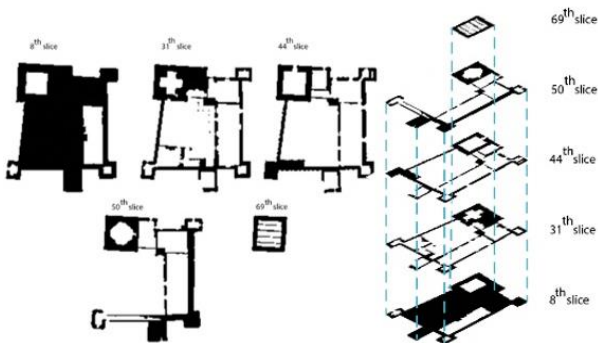


Figure 5. Example of digitalized slices of the Fortress (left), and their stacking (right)

Through the voxel three-dimensional model, it was possible to analyse the structure with static or dynamic analysis. The following figures show the modal shape.

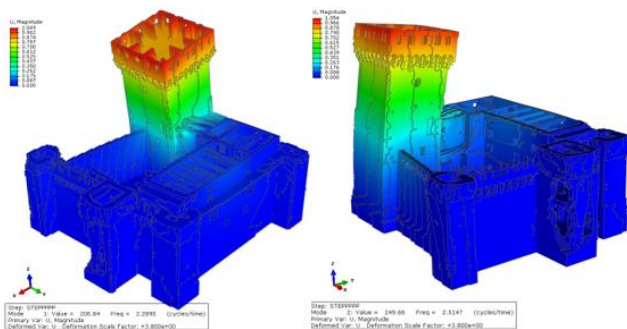


Figure 6. In the Mode 1 (left) the Mastio is along the Y axis; in the Mode 2 (right) the Mastio is along X axis

Considering the results of dynamic analysis, and according to the vibration modes for the entire Fortress, the Mastio tower is the most stressed part. For this reason, it was studied also as an isolated element.

2.3.1 Mastio tower

The horizontal slices with a step of 20 cm has been overlapped to the polygonal model, in order to simplify the structure from a 3D model to a stack of 2D elements (Figure 7).

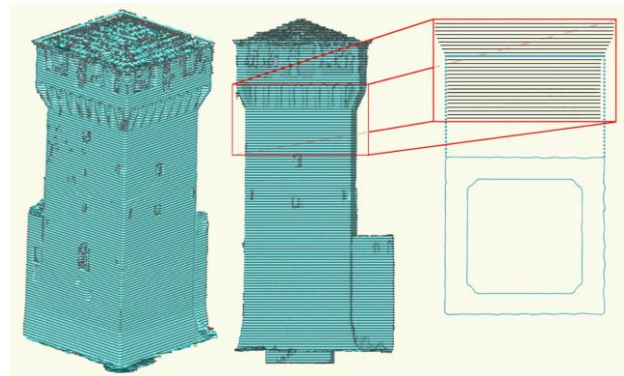


Figure 7. The two-dimensional slices are overlapped to the three-dimensional polygonal mode, for the whole height of the tower. In detail, a two-dimensional slice is shown (right)

The Mastio FEM obtained by using the proposed procedure was verified by means of the comparison with a reference finite element model obtained by a CAD procedure based on the same dataset (Figure 8) (Orlando A., 2014). A linear natural frequency analysis (eigenvalue analysis) was performed for the comparison. The mode shapes resulted very similar; they slightly diverge in terms of local displacement of the top part. The comparison in terms of frequency is shown in Table 1.

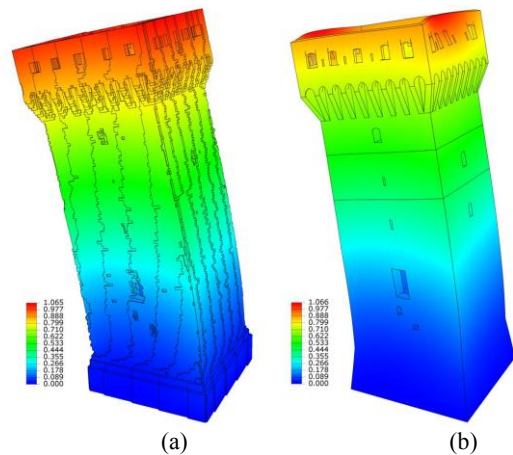


Figure 8. Bending mode shape with displacement magnitude: Voxel frequency = 1.9131 Hz (a); CAD Frequency = 1.9137 (b)

Mode No.	Voxel Frequency (Hz)	CAD Frequency (Hz)	Error (%)	Mode Description
1	1.9131	1.9137	0.031%	1st bending mode (E-W)
2	1.9276	1.9289	0.067%	1st bending mode (N-S)
3	4.5437	4.4253	2.675%	torsional mode
4	8.1623	8.0055	1.959%	axial mode

Table 1. Comparison between the voxel-based model and the CAD-based model

2.4 Considerations

The test performed on the San Felice sul Panaro Fortress showed that point clouds data can be effectively used for FE analyses. This is possible after transforming the polygonal model deriving from the geomatic survey in a voxel model suitable for the structural analysis. For this purpose CLOUD2FEM procedure has been successfully proved. The presented procedure is a rapid solution for generating a FE model of a complex structure, especially in the field of Cultural Heritage.

3. BAPTISTERY OF AQUILEIA

Aquileia is a small city near Udine, in Friuli-Venezia Giulia region (Italy). The entire structure including the Basilica of Aquileia dates back to the fourth century and the actual configuration is the result of transformations and different reconstructions during the centuries.



Figure 9. Geographic location of the case study: Basilica of Aquileia overview (aerial imagery AGEA, 2011)

After the destruction of the first bishopric, the Basilica was rebuilt four times, overlapping the new building to the previous ruins (Bratož, 2007). Nowadays the Baptistery, subject of this research, is composing only by the lower floor. The documents concerning the archaeological excavation from S. Tavano (1972; 1996) and the analysis on the structure of the walls by O. Brandt (Brandt, 2007) describe the historical evolution of this building.

The Baptistery is characterized by a square plan outside with a dimension of about 15 m, and by an octagonal plan inside with a dimension of each side of about 6,5 m. The building reaches a height of almost 11 m and the walls are composed by masonry stones with good texture. The original roof is missing and replaced by steel beams and coverage curtains.

The complex of Aquileia has been chosen for its characteristics octagonal shape, suitable for geometric comparisons and analyses. Furthermore, it has undergone various changes and reconstructions, and the study of the old data in different periods is an interesting topic.



Figure 10. View of the Baptistery from the North East side (left) and South West side (right)

3.1 Data acquisition

The acquisition has been performed in collaboration with the University of Udine, Department Polytechnic of Engineering and Architecture. Different instruments have been involved for the survey of the inside and the outside of the Baptistery (Figure 11)

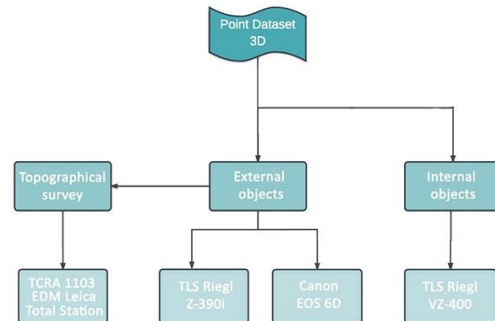


Figure 11. Instruments used for the survey

The exterior has been acquired by the laser scanning with the TLS system Riegl Z390i (Figure 12) integrated with a Nikon D200 calibrated camera. Eight scans were acquired from eight different stations, previously defined through a preparatory project.



Figure 12. Acquisition of the external and internal part using TLS

In order to proceed with the registration of the scans, 15 cylindrical ($\phi 10$ cm) reflective targets and 55 disk targets ($\phi 5$ cm) have been placed. A topographical survey of all the placed targets have been performed: the survey has been carried out with a Leica reflectorless TCRA 1103 EDM total station.

Once processed all the values of the topographical survey, the solution for the topographical network has been obtained, with a coordinate value (x, y, z) for each point. The adjusted values were then assigned to the targets recognized in RiSCAN software, in order to proceed with the registration of the point clouds.

The internal acquisition of the Baptistery was performed with the TLS system Riegl VZ400 in 18 different scan positions.

The integration of the data coming from a photogrammetric survey allowed to reduce the missing data that affected the high parts of the external walls. A full frame Canon EOS 6D camera was fixed on an extensible tripod. The maximum height of the tripod is 14 m, it is equipped with devices for the remote control of the camera and real-time visualization of the images. Pictures from four different heights were acquired, following the strategy of orthogonal and converging directions, for a total of 77 photos.

For the generation of the geometrical three-dimensional model, plans and sections derived from existing documents of the Baptistery have been used. In particular a ground floor plan

dating back to the 1906 (Lanckoronski, 1906) has been considered as reference.

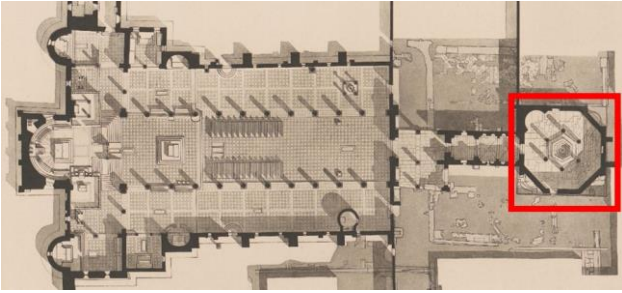


Figure 13. Lanckoronski plan. Red line identifies the Baptistery

3.2 3D processing and modeling

All the scans derived from the TLS and topographical survey were aligned and merged, and a dataset composed by more than 30 million of points have been obtained (Figure 14).

Concerning the CRP survey, the acquired photos have been processed using *Photoscan Pro* package, masking elements (vegetation, sky, buildings etc.) not useful for the three-dimensional model purposes (Figure 15). In order to get a good alignment and to scale the point cloud, the markers obtained from the topographic survey have been used. A residual error less than 1 pixel has been achieved.

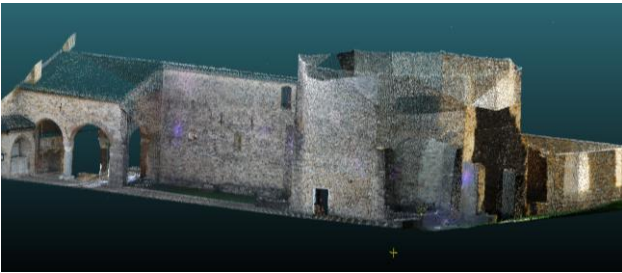


Figure 14. Perspective view of the North side of the point cloud dataset of TLS

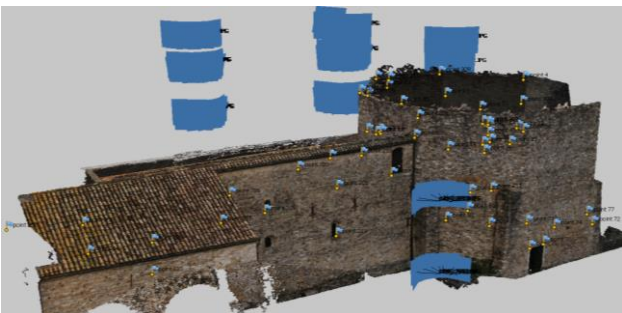


Figure 15. Dense point cloud with the position of photogrammetric acquisition (blue) and markers points, from the South front

The final point cloud obtained integrating the TLS and the CRP data consists of more than 40 millions of points (Figure 16). Once merged the point cloud datasets, noises, outliers and isolated points were eliminated, and a resampling performed to avoid portions with high difference in the point density. Considering that the point clouds were characterized by a high level of detail, the resampling operation did not compromise the data quality.



Figure 16. Complete point cloud dataset

Using the software package *Geomagic*, the point cloud has been downsampled to a spatial resolution of 1 cm. A triangular irregular network (TIN) has been generated from the point cloud dataset for regularization, i.e. removal of outliers, filling the holes and reconstruction of the surfaces parts occluded by obstructing objects during the scan of the internal parts of the building. Composed by more than 46 million of triangles, the resulting TIN fully described the surface of the complex of the Basilica of Aquileia (Figure 17).

The following analysis involved only the Baptistery; therefore it was necessary to separate all the elements belonging to the close buildings, as the Church of Pagans. All those unnecessary parts have been deleted, like the modern glass and the coverage curtains, the baptismal font with the internal columns and all the furniture.

The final model concerning only the Baptistery is composed by more than 3 millions of triangles. (Figure 18)

Referring to the “historical” model, the Lanckoronski plan has been scaled according to the actual sizes of the Baptistery. Due to the lack of information, the geometrical model has been obtained considering a constant thickness of the external walls. Furthermore, the value of the height was set equal to the current one. This historical model has been generated by means of the central symmetry using *Rhinoceros* software (Figure 19).

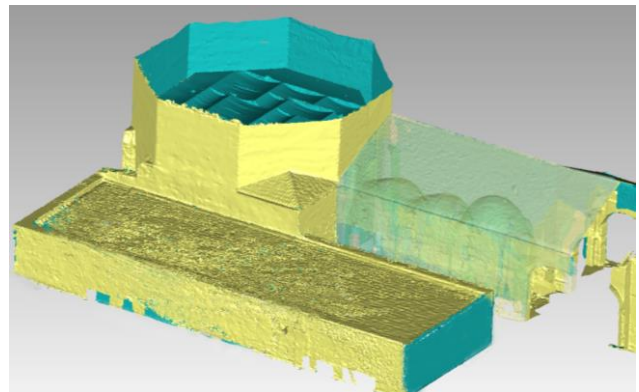


Figure 17. View of the model from the South side. The transparency is set for the Church of Pagans, where it is possible to observe the complete dataset also in its internal parts, with the vaults and the dome.

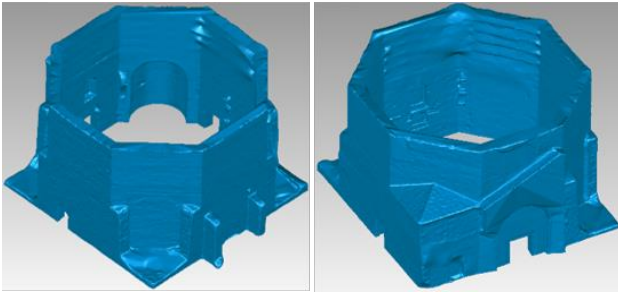


Figure 18. The final three-dimensional model of the Baptistery

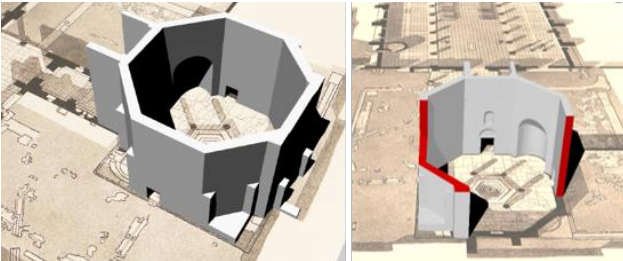


Figure 19. The geometrical model obtained by historical data: complete model on the left and sectioned model on the right (red identifies the sectioned parts).

3.2.1 FE modeling

The three-dimensional model has been analysed with different approaches, in order to transform the initial dataset into a FE model. Although this is not strictly a work of structural field, some analysis has been carried out in order to evaluate static and dynamic behavior of the structure. For the transformation of the polygonal model into a FE model, different approaches have been used, distinguishable into semi-automatic.

For the semi-automatic approach, Serantoni (2017) procedure has been applied. The automatic approach started from the raw point cloud dataset, and a *Matlab* code identified horizontal planes with a step of 30 cm and a thickness equal to 2 cm.

For the structural assessment and for transforming the input dataset in a FE model, three common aspects were defined: the characteristic of the material the boundary conditions and the forces acting on the Baptistery.

Within *Abaqus* software, the parameters have been set up according to the legislative framework (NTC 2008).

Type of masonry	f_m (N/cm ²)	τ_0 (N/cm ²)	E (N/mm ²)	G (N/mm ²)	w (kN/m ³)
Stones with good texture	192,6	4,15	1740	580	21

Table 2. Reference values of the mechanical parameters, considering the confidence factor equal to 1,35 and the level of knowledge equal to 1; f_m is the average compressive resistance of masonry, τ_0 is the average shear strength of masonry, E is the average value of the modulus of normal elasticity, G is the average value of the modulus of shear elasticity, w is the average weight of the masonry

Concerning boundary conditions (constraints), the foundations are not well defined but, from the historical documents, the walls continue for almost one meter underground. For this reason, constraints on the ground floor have been insert. The continuity with the “Church of Pagans” was simulated through the introduction of appropriate constraints, in order to obtain the function of direct connection between the two buildings.

Finally, the connection with the “Mosaic Hall” was not considered since this element was built recently, it has its own supports and it does not contribute to the structural behavior of the Baptistery.

Regarding the load acting on the building, only the gravity force has been considered.

3.3 Geometrical comparison

The Lanckoronski section has been employed in order to evaluate the differences and the changes with the actual conformation of the Baptistery. With the overlap between the old cross section and the actual one generated from the numerical model of the complete dataset, some discrepancies result evident.

In the actual configuration, the Baptistery is higher, and the distance between the perimetral walls is less than in the historical model. According to these differences, the baptismal font, placed in the center of the plan of the building, is translated; furthermore, it has been drawn slightly higher (Figure 20).

Concerning the Church of Pagans, the height of the two vaults is coincident. The dome has the same height, but is narrower than the actual one.

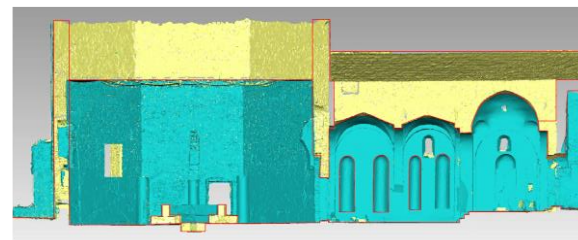


Figure 20. Cross section obtained from the complete three-dimensional polygonal model

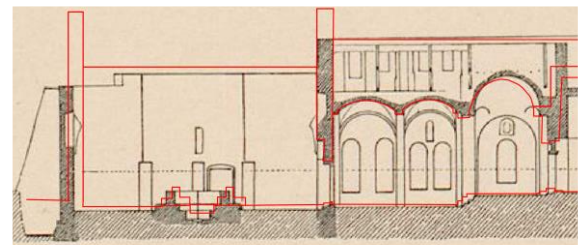


Figure 21. Cross section of the complex of Aquileia with the overlap of the section derived from the polygonal model (red lines)

The comparison between the numerical model (point cloud dataset or polygonal model) with the geometrical (reconstructed) one, was performed in order to evaluate the accuracy obtained from three-dimensional surveys. For this reason, starting from the polygonal surfaces concerning only the Baptistery, three horizontal sections have been selected at three different heights: 0,50 m, 5,00 m, and 10,75 m (Figure 22). In order to analyse the area of the masonry at different layers, the sections have been converted into binary images, composed by pixels: pixels with value equal to 0 represented the filled area (masonry) while digital number equal to 255 represented the empty space. Elements are classified directly through *eCognition Developer* software, in which the implemented procedure compares two input data each time. The binary images have been compared to assess the accuracy, the

decrease, increase and no-change between sections (Selvaggi et al., 2018). This procedure has been applied between the first section and the third one (Figure 22, Table 3).

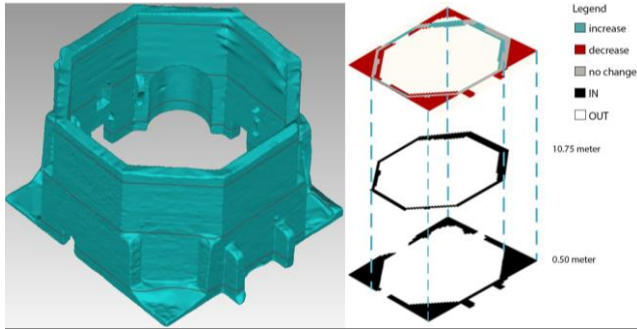


Figure 22. The polygonal model of the Baptistery with the overlap of the three horizontal section in different layers (left) and comparison analysis (right)

Moreover, it was possible to identify discrepancies between the masonry in the current model.

Red parts highlight the elements that are not present in the upper section (decrease); otherwise, green areas show the increase of the masonry compared to the lower sections. No changes are represented by grey colour concerning the masonry, and by white areas in terms of empty spaces.

The resulting discrepancies confirmed that the geometrical model is not able to perfectly reproduce the walls in their height and thickness; in fact, some red parts have been detected inside the octagonal perimeter of the current model. Red and green areas in correspondence of the outside demonstrate non-orthogonal walls. On the other hand, for the historical model the 2D comparison shows how the walls are characterized by a symmetrical geometry (Figure 22).

	Area (m ²)
Decrease	98.5
Increase	26.6
No change	577

Table 3. Values from the comparison analysis between the first and the third horizontal section

From the three-dimensional comparison performed overlapping the two models, significant differences have been identified in the corners, in the apse and in its vaults (southeast side); in some zones, the discrepancies reached almost 0.9 m as indicated by the red colour in Figure 23.

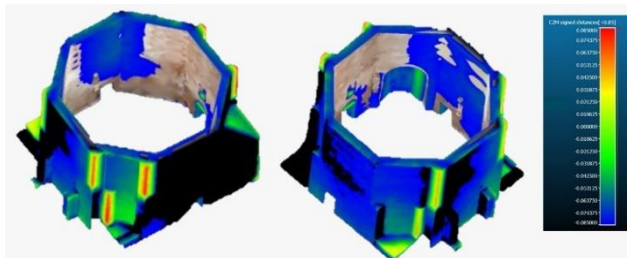


Figure 23. Results of the comparison between three-dimensional models: southwest view (left) and northeast view (right)

Min. dist.	Max. dist	Avg. dist	Sigma	Max.error
0	0.091	0.103	0.277	0.085

Table 4. Statistical values (m) of the overlap between the models

3.4 FE analysis

The outputs of the semi-automatic and automatic procedures were two voxel models, with different characteristics (Ramiya et al., 2016; Truong-Hong, L.; Laefer, 2013).

Concerning the model derived from the semi-automatic approach, a size equal to 20 cm has been set for the voxels, whereas for the other model a dimension of 50 cm allowed to have a speedy output in terms of time.

Several tests have been performed with different approaches in Selvaggi (2017), and two of these are reported in this work.

The geometrical characteristics of the two voxel models and the results obtained from the structural analysis have been compared and analysed.

The model derived from automatic approach (identified as A in the Table 5) is characterized by a lower mass and a lower number of voxels than the semi-automatic one (B model), while the volume is larger.

The results of the structural analysis concerning the semi-automatic model are shown in Figure 24; the static behavior of the Baptistery and the first bending mode along y and x direction are reported.

Despite the geometrical characteristics (Table 5) are very different from each other, the first four modes (Table 6) show how the computed error in percentage is low in terms of frequency (Hertz). In particular, for the fundamental modes, Mode 1 and Mode 2, is respectively less than 0.1% and less than 2.90%.

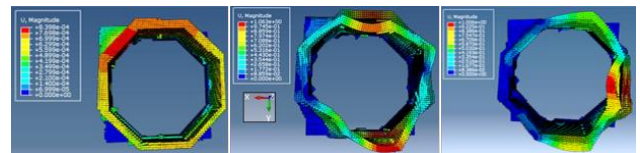


Figure 24. From left: static analysis, first bending mode along Y, first bending mode along X of the model generated with semi-automatic approach, with the overlap between deformed and undeformed shape.

Model	Mass (tons)	Volume (m ³)	Voxel (n.)
A	593.88	1247.14	5751
B	1201.25	606.01	66018

Table 5. Comparison between geometric characteristics of two examined models, the automatic model (A) and the semi-automatic model (B)

Mode No.	Mode description	Frequency (Hz) A	Frequency (Hz) B	Frequency (%)
1	1 st bending mode (along X)	6.8492	6.8763	0.396
2	1 st bending mode (along Y)	8.4455	8.2004	-2.90
3	axial mode	6.9558	6.1105	-12.15
4	torsional mode	8.9137	8.4984	-4.66

Table 6. Natural frequencies of the main mode shapes of the Baptistery. Comparison between the voxel-based models and deviation in percentage

3.5 Considerations

The integration between image- and range-based survey techniques, applied to a complex architectural case study as the Baptistery of Aquileia, allowed to obtain an accurate dataset necessary for a deep investigation in different disciplines. In particular, the historical data permitted to evaluate the evolution and the changes through the centuries, comparing the initial configuration of the Baptistery with the current one. The comparison has been performed in 2D, through horizontal sections, and in 3D, with evaluations of models in terms of volume. A different analysis concerning 3D models involved the transformation from initial dataset (point cloud data or polygonal model) into voxel models. Structural analysis is an example of the possibility to handle complete information deriving from the initial dataset.

4. SAN LUZI BELL TOWER

The San Luzi church is located in Zuoz (Switzerland) in the Upper Engadin. Its bell tower is about 60 m high and is equipped with four bells. It is characterized by ten floor plan, and the internal spaces are very narrow, as it is possible to see from Figure 25.

The historic bell tower of the San Luzi church showed high vibrations during the ringing of the bells. A finite element model (FEM) of the bell tower and the church was needed in order to come up with an appropriate solution. Workers in San Luzi noticed high tower vibrations when ringing the bells in 2003. One year later, measurements showed that the maximum vibration is 16 mm/s whereas the maximum acceptable value is only 3 mm/s. The two larger bells were then equipped with cranked yokes in order to distance the pendulum frequencies from the tower's natural frequency. The large vibrations caused by the bells 1 and 2 could be removed successfully. Bell 3 (see Figure 1.2) still showed too high impacts during measurements in 2009 though. The pendulum frequency was lowered as well. However, in 2011, it was found that this had negative instead of positive effects. In the following year, a 16-month monitoring was started, measuring accelerations of the bell tower, temperature, wind speed and wind direction. The fundamental frequency of the tower was determined and found to be varying following temperature and wind changes. The high vibrations caused by bell 3 cannot be removed through shifting the frequency because of limited technical possibilities. Solutions with a tuned mass damper are now considered. Therefore, a finite element model (FEM) of the bell tower was needed.

For the campaign of acquisition inside the bell tower, the following safety precautions have been taken:

- Risk of fall: When working at heights like on the bell tower, both humans and instruments had to be secured and prevented from falling. When working above level A, climbing equipment has been used.
- Bells: The bells were turned off during the measurements in the bell tower.



Figure 25. From left: San Luzi Church with Bell tower; cross section of the tower with its floors; view of inside from A and B floors

4.1 Data acquisition

The survey has been performed by the Institute of Geosensors and Engineering Geodesy (GEEG) of ETH Zurich, using two total stations and a laser scanner (Baumann M.; Hadorn P., 2015). The registration and the georeferencing of the scans, as well as the first cleaning of the points, have been done in the FARO software SCENE. Laser scan targets (checkerboard targets) were placed inside and outside of the bell tower, the church and the crypt. A network and all checkerboard targets were surveyed by a total station.

The network includes stations, tape targets, prisms, a far object and the cadastral points (see the Dorf network in Figure 26).



Figure 26. Network Dorf: all measurements of the ground (left) and inside the bell tower of the C-floor on the map and on the side view of the tower



Figure 27. Laser scans position

The total station measurements were carried out in two parts, the measurements outside and inside the bell tower. As many points as possible are installed visible both from inside and outside the tower (e.g. prism 1004, see Figure 28).



Figure 28. Bell tower inside. From left: View from the A-floor to the Z floor; prism number 1004; scan between the A and Z floor

The bell tower, the church and the crypt were scanned with the FARO Focus 3D S120 such that at least 3 checkerboard targets were visible on each scan (see laser scanner location in Figure 27). After the registration, cleaning and georeferencing, a total point cloud composed by almost 25 million of points has been obtained (Figure 29). Of these, more than 9 million concerns the bell tower and have been considered for the FE modeling.

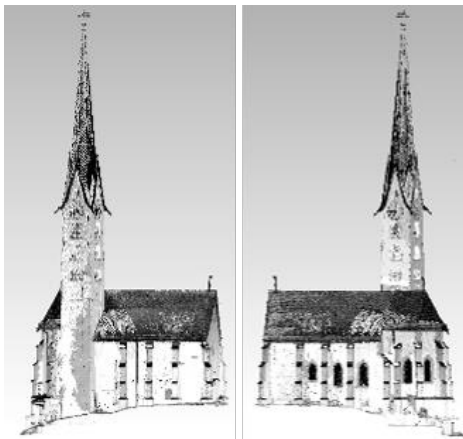


Figure 29. Point cloud dataset from North front (left) and South front (right)

4.2 Data processing

The initial dataset of the tower was composed by more than 9 million of points. The point cloud was thinned out uniformly with a distance of 0.15 m, and with optimizing for uniformly distributed data. Furthermore, the roof has been deleted; in this way, a final dataset composed by 2.291.570 millions of points has been obtained. Since some parts of the building had significantly less data than the rest, meshes could not be generated there. Some parts without meshes have been reconstructed with fitting planes.

The final model was a triangulated irregular network (TIN) with a few remaining holes that could not be reconstructed. The first polygonal model was composed by more than 2 million of triangles. The mesh generation was complete, but many holes resulted in the building, especially inside due to the narrow spaces, and (in the upper part) the thickness of the walls is larger than the width of the interior spaces.

As shown in Figure 30, the polygonal model is very noisy. The blue parts represent the continuous surfaces, the yellow parts are the cut or non-continuous surfaces; the green lines are the holes (Attene et al., 2013). For obtaining a continuous and correct model it has been necessary a few hours.

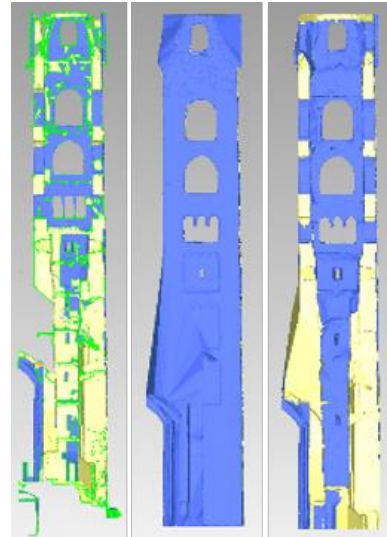


Figure 30. From left: noisy polygonal model of inside, final polygonal model and its cross section

4.3 FE model

The FE model is generated from the registered and merged point cloud, representing the entire surface of the object, following the Serantoni (2017) approach, after obtaining a correct definition of the model. The first attempt failed, because of the internal spaces of the bell tower, very tight. For this reason, the Alpha shape function did not distinguish between external surface and internal one (Figure 31a). With some precautions, as an offset of the external wall in the interspace, and an Alpha shape with an alpha radius of 0.2, a properly defined voxel model has been generated (Figure 31b). The final voxel model has been characterized by 29997 voxels, with the dimension of each voxel equal to 25 cm.

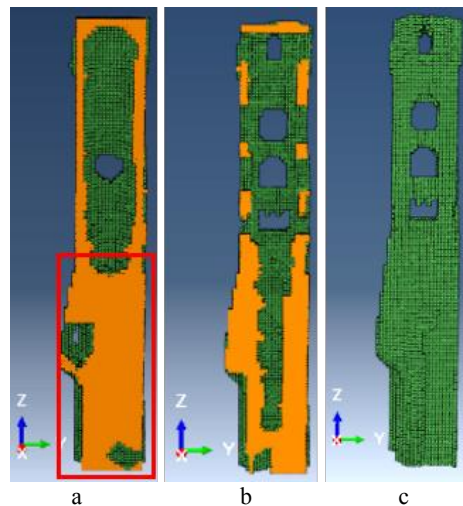
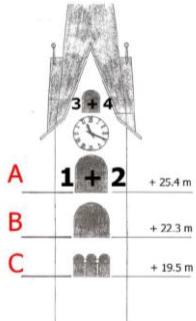


Figure 31. By using of a high alpha radius (value=1), almost all the openings have been closed (a). Nevertheless, some internal parts (red) remain open. Furthermore, in the bottom part of the tower, all the inside space has been incorrectly closed, without considering the interspacing between the surfaces. Cross section (b) along Y with all the internal parts correctly defined. The voxel model is defined with an alpha radius of 0.2 (complete model c).

Although there is not a survey or some indication about the materials composing the tower, the structural analysis has been done, only in order to verify if the final voxel model was correct. The only data available are the weights of the four bells, shown in the following table.



Bell	kg
1	1700
2	648
3	400
4	260

Figure 32. Location and characteristics of the bells

The parameters of the masonry have been chosen according with a masonry stones with good textures; instead for the floors, a calculation of the own weight (with an hypothetical section) for each beam has been done, and then these values have been multiplied for the effective clear span of the floor. The final values have been applied where there are the supports of the beams, as concentrated forces on the masonry. Furthermore, the weight of the bells has been applied as concentrated forces on the masonry as the half of the forces equal and contraries. Restraints were considered in the ground, and translation along the direction of the Church next to the tower has been avoided. Of course, this is an approximation of the real structural analysis. In fact, only a first initial test has to be considered, because the dimensions of beams are all supposed, and consequently the loads could be higher or lower (this depends on the chosen sections, if they are oversized or undersized). The results deriving from static and dynamic analysis in terms of natural frequencies have been reported in Table 7.

Mode n.	Mode description	Max displacement	Frequency
1	1 st bending mode (along X)	1.006	1.5797
2	1 st bending mode (along Y)	1.003	1.3621
3	Axial mode	1.023	5.5365
4	Torsional mode	1.315	4.4618

Table 7. Natural frequencies analysis of the main mode shapes of the bell tower

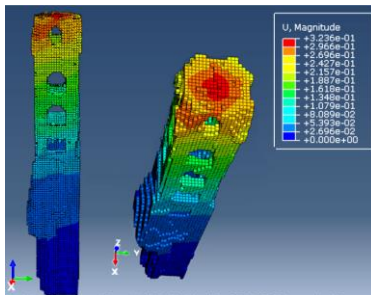


Figure 33. Static analysis (left) and 1st bending mode (along X)

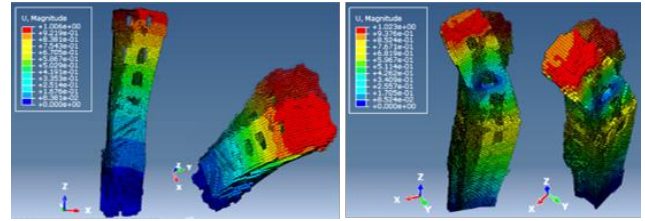


Figure 34. 1st bending mode along X (left) and Y (right)

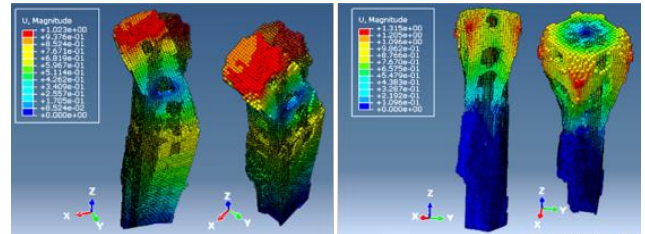


Figure 35. Axial model (left) and torsional mode (right)

4.4 Considerations

Starting from the acquisition data, the three-dimensional polygonal model of the bell tower has been generated. This is a very particular case study because of different elements. Firstly, the roofs could be acquired only from the outside. This causes a problem with the normals of the surfaces and therefore, it is difficult to connect the roof correctly with the rest of the tower. Secondly, the software does not recognize correctly which side of a surface is the inside and which is the outside, and this leads to further errors. A third problem are the missing parts. Some areas of the church were not scanned and could not be reconstructed easily, because of some parts of the building were not accessible or visible. For these reasons, lot of time has been required for the final polygonal model. Definitely, the final voxel model is an approximation of the tower, because of the internal structural elements have been inserted as concentrated loads. Nevertheless, a final structural analysis allowed to understand the behavior of the tower. In this context, as a future study, it would be useful to obtain a combined FE model, consisting of voxel elements and shell or beam elements.

5. CONCLUSIONS

The potentialities of Geomatics have been underlined, and the different analysis performed highlighted how the dense and accurate point cloud data, obtained by means of TLS and CRP techniques, allowed to have a comprehensive description of the case study. If the aim of the modeling is, for example, the reconstruction for architectural and structural purposes, the approach cannot be limited only to a geometrical modeling. For these reason, the research represents also an attempt to gather all available input data, in order to transform the initial point cloud into a FE model, suitable for structural analyses, by avoiding to loss important data. The aim is, furthermore, the obtaining of a complete model, and not an oversimplified one. In order to transform the initial point cloud into a Finite Element model, suitable for structural analysis, different methods have been studied. All the proposed procedures guaranteed the generation of a filled model, exploitable as input for structural analyses. In order to validate and show the capabilities of the proposed techniques, different case studies have been presented and discussed.

The study of the first approach, the Cloud2FEM procedure, was applied to a damaged building, with some parts collapsed. The

creation of horizontal sections, overlapped to the polygonal model, allowed to control each part of the structure, avoiding the loss or damaged or collapsed parts.

For the second case study, a complete analysis has been made because, the study started from the acquisition data, and it offered lots of analyses and comparisons. Concerning the structural analyses, two procedures generated a speedy solution for obtaining a voxel model, without compromising results.

The third and last case study has been the San Luzi bell tower, and the problems related to the polygonal model, characterized by discontinuities, holes etc. In order to obtain a correct geometrical model for the transformation in a FE model, lot of time was necessary. The results of the static analysis and the natural frequencies analysis denoted a correct definition of the voxel model.

In general, the current research permitted to relate the point cloud input data, into a detailed FE model, by connecting the Geomatics with the Structural Engineering

Through the different methods, a voxel model has been obtained. The output data is the same, because all the voxel models have the same physical characteristics, and a voxel is composed by corners where it is possible to define the loads bearing. The differences are in terms of computing time, geometrics characteristics, and number and dimensions of the voxels, from which depend the final results.

So, in the present work:

- the development of a part of programming code in order to obtain a final voxel model have been performed;
- the definition of geometric modeling has been carried out, for a comparison with the numerical modeling, in term of loss of level of detail;
- the historical reconstruction, carried out through old data has been performed, and comparison with real (current) model showed differences in terms of area and deviation;
- the FE models deriving from Geomatics acquisitions were obtained, and compared in terms of displacements and frequency.

Others key aspects and contributions of the current research were:

- integration data of different instruments, in order to obtain a complete dataset, suitable for several analyses;
- the issues related to dataset with different characteristics (e.g. in terms of density);
- the transformation of a very complex dataset (in terms of points and triangles) in a model, through the reduction and sampling of elements without the loss of important parts.

The connection of Geomatics with other areas (preservation, structural analysis, art history, material properties etc.) suggest a new multidisciplinary approach, able to combine different data sources providing a comprehensive geometric set of data in the perspective of Cultural Heritage management and preservation. The combination of TLS and CRP techniques produces the best results for Cultural Heritage documentation purposes.

ACKNOWLEDGEMENTS

The author would like to thank her PhD Supervisor Prof. Gabriele Bitelli, and Co-Supervisors Prof. Luca Vittuari and Prof. Andreas Wieser, Eugenio Serantoni and ETH University of Zurich - IGP Institute of Photogrammetry and Geodesy – Department of Civil, Environmental and Geomatic Engineering.

REFERENCES

- Aicardi, I., Chiabrando, F., Grasso, N., Lingua, A.M., Noardo, F., Spanó, A., 2016. UAV photogrammetry with oblique images: First analysis on data acquisition and processing. *Int. Arch. Photogramm. Remote Sens. Spat. Inf. Sci.*, 835–842. doi: 10.5194/isprsarchives-XLI-B1-835-2016
- Attene, M., Campen, M., Kobbelt, L., 2013. Polygon mesh repairing. *ACM Computing Surveys* 45, 1–33 . doi: 10.1145/2431211.2431214
- Barazzetti, L., Banfi, F., Brumana, R., Gusmeroli, G., Oreni, D., Previtali, M., Roncoroni, F., Schiantarelli, G., 2015. Bim from laser clouds and finite element analysis: Combining structural analysis and geometric complexity. *Int. Arch. Photogramm. Remote Sens. Spat. Inf. Sci.*, 345–350. doi: 10.5194/isprsarchives-XL-5-W4-345-2015
- Baumann M.; Hadorn P., 2015. Geometrical Modeling of a Historic Bell Tower, *Master Thesis*, ETH-IGP Zurich
- Bitelli, G., Balletti, C., Brumana, R., Barazzetti, L., D’Urso, M.G., Rinaudo, F., Tucci, G., 2017. Metric Documentation of Cultural Heritage: Research Directions From the Italian Gamher Project. *ISPRS - Int. Arch. Photogramm. Remote Sens. Spat. Inf. Sci.* XLII-2/W5, 83–90. doi: 10.5194/isprs-archives-XLII-2-W5-83-2017
- Bitelli, G., Castellazzi, G., D’altri, A.M., De Miranda, S., Lambertini, A., Selvaggi, I., 2016. Automated voxel model from point clouds for structural analysis of cultural heritage, in: *Int. Arch. Photogramm. Remote Sens. Spatial Inf. Sci.*, XLI-B5, 191-197, doi: 10.5194/isprs-archives-XLI-B5-191-2016
- Brandt, O., 2007. Il battistero “cromaziano” 60–72.
- Bratož, R., 2007. La basilica di Aquileia nelle fonti letterarie dal IV al VII secolo 15, 19–66.
- Bridson, R., 2007. Fast Poisson disk sampling in arbitrary dimensions, in: *ACM SIGGRAPH 2007*, p.1-22 doi: 10.1145/1278780.1278807
- Callieri, M., Chica, A., Dellepiane, M., Besora, I., Corsini, M., Moyés, J., Ranzuglia, G., Scopigno, R., Brunet, P., 2011. Multiscale acquisition and presentation of very large artifacts. *Journal on Computing and Cultural Heritage*. 3, 1–20. doi: 10.1145/1957825.1957827
- Castellazzi, G., D’Altri, A.M., Bitelli, G., Selvaggi, I., Lambertini, A., 2015. From laser scanning to finite element analysis of complex buildings by using a semi-automatic procedure. *Sensors (Switzerland)*.15, 18360-18380 doi: 10.3390/s150818360
- Castellazzi, G., D’Altri, A.M., De Miranda, S., Ubertini, F., Bitelli, G., Lambertini, A., Selvaggi, I., Tralli, A., 2016. A mesh generation method for historical monumental buildings: An innovative approach, in: *ECCOMAS Congress 2016 - Proceedings of the 7th European Congress on Computational Methods in Applied Sciences and Engineering*. doi: 10.7712/100016.1823.11948
- Corsini, M., Cignoni, P., Scopigno, R., 2012. Efficient and flexible sampling with blue noise properties of triangular meshes. *IEEE Trans. Vis. Comput. Graph.* 18, 914–924. doi: 10.1109/TVCG.2012.34
- Dellepiane, M., Dell’Unto, N., Callieri, M., Lindgren, S., Scopigno, R., 2013. Archeological excavation monitoring using dense stereo matching techniques. *Journal of Cultural Heritage*. 14, 201–210. doi: 10.1016/j.culher.2012.01.011

- Ferrari, L., Goldoni, G., 2014. Behind the sign. Inside and Outside the San Felice sul Panaro Fortress restoration work *Master thesis*, University of Parma
- Fritsch, D.; Khosravani, A. M.; Cefalu, A.; Wenzel, K., 2011. Multi-Sensors and Multiray Reconstruction for Digital Preservation. *Photogrammetry Week* 2011.
- Grussenmeyer, P., Alby, E., Landes, T., Koehl, M., Guillemin, S., Hullo, J.F., Assali, P., Smigiel, E., 2012. Recording approach of heritage sites based on merging point clouds from high resolution photogrammetry and terrestrial laser scanning. *Int. Arch. Photogramm. Remote Sens. Spat. Inf. Sci.* XXXIX-B5, 553–558. doi: 10.5194/isprsarchives-XXXIX-B5-553-2012
- Grussenmeyer, P., Landes, T., Voegtle, T., Ringle, K., 2008. Comparison methods of terrestrial laser scanning photogrammetry and tachometry data for recording of cultural heritage buildings. *Int. Arch. Photogramm. Remote Sens. Spat. Inf. Sci.* Vol. XXXVI, 213–218.
- Guarnieri, A., Fissore, F., Masiero, A., Vettore, A., 2017. From Tls Survey To 3D Solid Modeling for Documentation of Built Heritage: the Case Study of Porta Savonarola in Padua. ISPRS - *Int. Arch. Photogramm. Remote Sens. Spat. Inf. Sci.* XLII-2/W5, 303–308. doi: 10.5194/isprs-archives-XLII-2-W5-303-2017
- Guarnieri, A., Remondino, F., Vettore, A. (2006). Digital Photogrammetry and Tls Data Fusion Applied To Cultural Heritage 3D Modeling. *Digital Photogrammetry and Tls Data Fusion Applied To Cultural Heritage 3D Modeling*, 36(5), 1–6. doi: 10.1.1.72.3963
- Guimarães, T.C., Sánchez-Aparicio, L.J., Riveiro, B., González-Aguilera, D., Ramos, L.F., 2014. The combination of geomatic approaches and operational modal analysis to improve calibration of finite element models : A case of study in Saint Torcato Church (Guimarães, Portugal). *Construction and Building Materials* 70, 118–129. doi: 10.1016/j.conbuildmat.2014.07.106
- Lanckoronki, K.G., 1906. Der Dom von Aquileia, *Verlag von Gerlach & Wiedling*, Wien.
- Manferdini, A.M., Galassi, M., 2013. Assessments for 3d reconstructions of cultural heritage using digital technologies. ISPRS - *Int. Arch. Photogramm. Remote Sens. Spat. Inf. Sci.* XL-5/W1, 167–174. doi: 10.5194/isprsarchives-XL-5-W1-167-2013
- NTC 2008, Norme Tecniche per le Costruzioni, D.M. 14/01/08, 2008.
- Orlando A., 2014. Estense Fortress at San Felice sul Panaro: Modeling and Seismic Assessment, *Master Thesis*, University of Genoa.
- Ramiya, A.M., Nidamanuri, R.R., Ramakrishnan, K., 2016. A supervoxel-based spectro-spatial approach for 3D urban point cloud labelling. *Int. Journal of Remote Sensing* 37, 4172–4200. doi: 10.1080/01431161.2016.1211348
- Remondino, F., 2011. 3D recording for cultural heritage, In: Remote Sensing for Archaeological Heritage Management, D. Cowley (ed.), *Proc. EAC Symposium*, pp. 107-116.
- Remondino, F., Menna, F., 2008. Image-based surface measurement for close-range heritage documentation. *Int. Arch. Photogramm. Remote Sens. Spat. Inf. Sci.* XXXVII, 199–206.
- Russo, M., Manferdini, A.M., 2014. Integration of image and range-based techniques for surveying complex architectures. *Int. Arch. Photogramm. Remote Sens. Spat. Inf. Sci.* II-5, 305–312. doi: 10.5194/isprsannals-II-5-305-2014
- Scognamiglio, L., Margheriti, L., Mele, F.M., Tinti, E., Bono, A., De Gori, P., Lauciani, V., Lucente, F.P., Mandiello, A.G., Marcocci, C., Mazza, S., Pintore, S., Quintiliani, M., 2012. The 2012 Pianura Padana Emiliana seismic sequence: Locations, moment tensors and magnitudes. *Ann. Geophys.* 55, 549–559. doi: 10.4401/ag-6159
- Selvaggi, I.; Dellapasqua, M.; Franci, F.; Spangher, A.; Visintini, D.; Bitelli, G., 2018. 3D comparison towards a comprehensive analysis of a building in Cultural Heritage. *Int. Arch. Photogramm. Remote Sens. Spat. Inf. Sci.*, TC II, Symposium 2018 (accepted)
- Selvaggi, I., 2017. Surveying and three-dimensional modeling for preservation and structural analysis of cultural heritage, *PhD Thesis*. University of Bologna, Italy.
- Serantoni, E., Selvaggi, I., Wieser, A., 2017. Areal deformation analysis of a visco-plastic structure using point cloud data. Lienhart, W. *Ingenieurvermessung 17*, Beiträge zum 18. Int. Ingenieurvermessungskurs 403–413.
- Tavano S., 1996. Aquileia e Grado. Storia, arte, cultura. *Lint Editoriale*, p.486
- Tavano S., 1972. Aquileia cristiana in Antichità altoadriatiche. Ed. *Società istriana di archeologia e storia patria*, p.425-432
- Truong-Hong, L.; Laefer, D., 2013. Validating Computational Models from Laser Scanning Data for Historic Facades. *J. Test. Eval.* 41, 481–496.



Associazione **U**niversitari di **T**opografia **e** **C**artografia

Sezione Tematica 3 GIS e Remote Sensing

*

*Thematic Section 3
GIS and Remote Sensing*

REMOTE SENSING TECHNIQUES FOR MAPPING AGROFORESTRY PARAMETERS: APPLICATIONS FOR INDIVIDUAL TREE CROWN DETECTION

O. R. Belfiore^{1*}

¹ Department of Sciences and Technologies, University of Naples "Parthenope", Naples, Italy -oscarrosario.belfiore@uniparthenope.it

KEY WORDS: WorldView-2; Digital Aerial imagery; Orthorectification process; Pan-sharpening; Individual Tree Crown detection; Local Maxima Filter.

ABSTRACT:

In the last years, various Remote Sensing (RS) techniques and instruments were developed and utilized for purposes of management and monitoring of the natural and semi-natural resources. In details, with the growing introduction of the sensors, with high spatial and spectral resolution, the remote sensing techniques and the Geographic Information System (GIS), play a key role to provide more and detailed information, required for the precision agriculture tasks, and supporting, where possible, the decision-making process. The principal aim of this study, performed during the Ph.D. research, is to develop a chain process, based on different steps, to obtain by remotely sensed data, detailed information about location and detection of the olive tree crowns. The Individual Tree Crown (ITC) detection process was investigated. This semi-automatic process was tested applying the Local Maxima Filter (LMF) on the Digital Aerial image and WorldView-2 (WV-2) previously orthorectified and pansharpened. The results indicate that the image data characteristics play a key role to detect tree by remotely sensed data. In consideration of the spectral information, for both datasets, the results show a higher accuracy achieved with the NDVI, highlighting the spectral characteristics of the vegetation.

1. INTRODUCTION

In the last years, the availability of the very high-resolution satellite images (VHRSI) has increased. Commercial satellites like Pléiades (eoPortal Directory), QuickBird, GeoEye-1 and WorldView constellation (DigitalGlobe), provide very high resolution optical images (cell size < 1m), increasing the opportunity to detect and locate automatically terrain features for several remote sensing applications (González et al., 2007).

One of these applications is related to the Individual Tree Crown (ITC) detection and delineation by remotely sensed data.

According to Ke and Quackenbush (2011), the first research for this purpose was introduced at the mid-1980s, using digital aerial imagery to achieve detailed forest inventory information.

Subsequently, more studies were executed to detect and delineate the individual tree crown, considering several vegetation types, by remotely sensed data (Heenkenda et al., 2015). A wide variety of algorithms was developed to identify single trees (Ke and Quackenbush, 2008) and can be grouped into two general categories: individual tree crown detection and individual tree crown delineation. These categories are similar. However, the individual tree crown detection process is performed before the tree delineation. In this way, a greatly accuracy for the subsequent individual tree crown delineation process can be reached (Ke and Quackenbush, 2011). A review of methods for identification of individual tree in optical images is reported by Ardila Lopez (2012), describing four main approaches as: Local Maxima, Valley following, Tree modeling and image templates, Segmentation methods. However, the most intensively studied technique is Local Maxima (LM) detection. This detection technique assumes that each tree crown is corresponding to a peak intensity in the image. In other words, the pixel with the maximum brightness, can be related at the probable position of each tree in the image (Pouliot et al., 2002). Nevertheless, the LM approach was tested mainly to detect individual trees in a forest inventory, particularly for the coniferous forest (Gougeon and Leckie, 2006). This approach is less accurate if applied to detect tree in orchards, which are characterized with a less density than forestry. In fact, most variability as shadow, bright

soil background, grass and so on can be found in the optical image concerning orchards (Masson, 2005). However, in literature there are more examples, where automatic tree detection is performed to locate tree in the orchards (e.g., Santoro et al., 2013; Ozdarici-Ok, 2015; Caruso et al., 2014; González et al., 2007; Karantza and Argialas, 2004; Bazi et al., 2009; Díaz-Varela et al., 2015; Daliakopoulos et al., 2009; Ceylan et al., 2009). In this study, a semi-automatic process to detect individual olive tree was proposed, using the Local Maxima Filtering (LMF) on the WorldView-2 (WV-2) and Digital Aerial data. This paper is organized as follows. Section 2 and 3, illustrate, respectively, the details of the study area and of the remotely sensed and field data. The methodology of the semi-automatic process is described in the Section 4. The statistical analysis performed to quantify the accuracy of the tree detection process is reported in the Section 5. Final considerations are summarized in the Section 6.

2. STUDY AREA

This investigation was conducted in the Vesuvian Area (Campania Region), southern Italy. This area is particularly interesting because of both anthropological and natural aspects. In fact, a great part of it is included in Vesuvius National Park, founded in June 5, 1995, that houses 610 vegetable species and 229 vertebrates and invertebrates ones (Picariello et al., 2000). The area also presents one of the higher urban density in Europe and conserves the archaeological remains of Pompei, the ancient town that was destroyed by Vesuvius eruption in 79 d. C. The study site is located in the municipality of Torre del Greco (province of Napoli) in Campania Region. In this Vesuvian area, thanks to the high productivity of the volcanic soils (Shoji and Takahashi, 2002), horticulture, orchards, vineyard and greenhouse floriculture are the main agricultural productions. The analyses were conducted in a young and high dense olive grove, located at the foot of a lava dome (Colle di Sant'Alfonso) (centre coordinates: E = 449890.07 m; N = 4514314.38 m) (Figure 1). In this orchard, with an extension of 0.74 ha, 317 trees were planted

* Corresponding author

in 2009 with a square pattern planting (4m x 4m), and trained as a single trunk with the crown at about 1-m height.

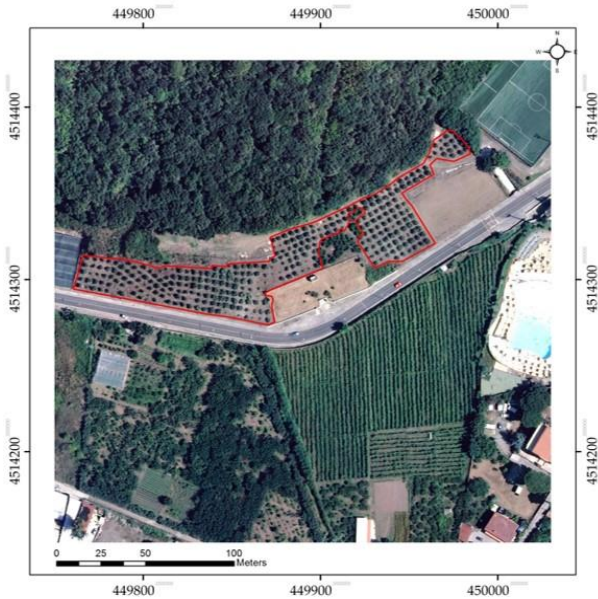


Figure 1. Olive grove and its location in the selected study area. (Coordinate system: UTM/WGS84 -33 N -zone T)

3. DATASETS

3.1 Remotely sensed data

For the purpose of this study WorldView-2 (WV-2) and digital Aerial imagery were used. Launched in October 2009 by DigitalGlobe, WV-2 satellite is placed at an altitude of 770 km; its orbit has an inclination of 97°.2 and a period of 100 min. The revisited frequency is 1.1 days at 1 m GSD and 3.7 days at 20° off-nadir at 52 cm GSD. The swath width, at nadir, is 16.4 km (DigitalGlobe). This satellite is part of the DigitalGlobe's constellation that now includes also WorldView-3 and WorldView-4 (Belfiore et al., 2016), (Kruse and Perry, 2013), (DigitalGlobe). The WV-2 satellite acquires panchromatic and multispectral images with two different push-broom scanners. The first have a spatial resolution of 0.46 meter at nadir, while the eight multispectral bands have a spatial resolution of 1.85 m, (they can be respectively resampled to 0.50 or 0.40 and 2 or 1.6 m for commercial scope). Radiometric resolution for both panchromatic and multispectral images is 11 bits (DigitalGlobe). Well corrected and georeferenced WV-2 images are used for many purposes, such as map creation and updating, high resolution coloured orthophotos production (Belfiore and Parente, 2015), vegetation mapping (Wolf, 2010), coastline identification (Maglione et al., 2014), object-based classification (Aguilar et al., 2014), (Figorito et al., 2012) and so on. In fact, the higher spatial resolution as well as availability of 8 bands make WV-2 very powerful source of information. In this study WV-2 imagery, concerning the study area was considered. Dataset was acquired on 2015/04/22 and supplied by the provider as Ortho Ready Standard product (ORS2A), that means already rectified using average terrain elevation of the scene (low accuracy) (DigitalGlobe). With aim to increase the planimetric accuracy, the WV-2 dataset was orthorectified using the OrthoEngine tool (Version 2015), implemented in PCI Geomatica software packages (PCI Geomatics). In details, a combination of 3D Rational Polynomial Function (3D RPFs) and 2D Polynomial Function (2D PFs) were applied (Belfiore and Parente, 2016). GCPs and CPs planimetric coordinates in UTM-WGS84 were derived from orthophotos of Campania Region with 0.20 m

resolution (nominal scale: 1: 5,000), while elevations were obtained by DEM, supplied by local government administration (Provincia di Napoli), with a horizontal resolution of 1 meter and a vertical accuracy of 0.16 meters (RMSE). In the first step, for the 3D RPFs application, 75 GCPs-15 CPs were considered. In the second step, 2D PFs, on the orthorectified image resulting from the first step, 1th order PFs using 15 GCPs and 15 CPs were performed. This approach permits to achieve low residuals, comparable with WV-2 cell size as well as to avoid other geometrical distortions associabile to PFs higher order (i.e. twist with 2th order). 3D RPFs and 2D PFs algorithms combination permitted to obtain the good results (RMSE_{GCPs}= 0.993 m - RMSE_{CPs}= 1.324 m). To increase the ITC detection process performance, nine pan-sharpening methods were tested (Table 1), to obtain a new image with the spatial resolution of the Panchromatic band and the spectral details of the Multispectral data.

Category	Methods	Reference
Simple methods	Multiplicative	Klonus and Ehlers, 2009
	Simple mean	ESRI, 2012
Component substitution methods	Intensity-Hue-Saturation	Carper et al., 1990
	Fast-IHS	Basile et al., 2010
	Principal Component Analysis	Chavez et al., 1991
	Gram-Schmidt	Laben and Brower, 2000
Modulation-based methods	Brovey	Vrabel, 2000
	Weighted Brovey	Parente and Santamaria, 2014; Belfiore et al. 2016
	Synthetic Variable Ratio of Zhang	Zhang, 2008

Table 1. Tested Pan-sharpening methods

According to the approach present in literature (Parente and Santamaria, 2013) (Belfiore et al 2015) the WV-2 Relative Spectral Radiance Response (RSRR) was considered to compute specific weight for each multispectral band. The values of these weights, showed in Table 2, are calculated considering the contribution of each eight multispectral bands in percentage to panchromatic one.

Coastal	Blue	Green	Yellow	Red	Red Edge	NIR1
0.009	0.130	0.211	0.142	0.234	0.161	0.113

Table 1. WV-2 multispectral band weights.

As can be seen in Figure 2, panchromatic curve does not have fully intersection with multispectral band ones, particularly for the NIR2 band. In fact, the weight of this band is equal 0. Therefore, for this reason the NIR2 band is excluded from the nine pan-sharpening.

Figure 2. Relative Spectral Radiance Response of WV-2 sensors (DigitalGlobe).

To evaluate the performance obtained from these methods Visual Quality Assessment (VQA) and Quantitative Quality Assessment (QQA) were performed. Considering both evaluation processes, the results confirm the higher performance of the SVR method of Zhang. In fact, this fusion algorithm permits to achieve similar colors to the primary ones, and preserves the spatial details of the panchromatic band, so this fusion algorithm enhances the detection of small objects like the olive trees.

The latter is the digital aerial imagery, supplied by local government administration (Campania Region), collected on August 2014, characterized by a cell size of 0.20 m for the visible and infrared multispectral bands, whereas the radiometric resolution is 8 bit. For both datasets, a subset is selected. The clipped area (Figure 3) extends 280 m x 280 m (UTM/WGS84 plane coordinates – 33 T zone: E1 = 449750 m; N1 = 4514428 m; E2 = 450030 m; N2 = 4514148 m).



(a)



(b)

Figure 3. Image subsets of (a) Pan-sharpened WV-2 data and (b) Digital Aerial including olive trees.

3.2 Field and Reference data

Ground truth survey was conducted on December 2014, in order to verify the position of each tree. Previously, this spatial information was mapped with a visual interpretation of aerial photographs and WV-2 images. Furthermore, the Average Crown Diameter (ACD_i) was calculated of each tree, measuring with a tape measure the major (D_i) and the minor diameter (d_i) of the crown projected to the ground. The ACD_i , using the geometric mean, was estimated for each crown (equation 1), and at orchard scale (ACD_{tot}), (equation 2).

$$ACD_i = \sqrt{D_i \cdot d_i} \tag{1}$$

$$ACD_{tot} = \frac{\sum_{i=1}^n \sqrt{D_i \cdot d_i}}{n} \tag{2}$$

where,

n is the total number of trees in the olive grove.

The descriptive statistics from the field data are shown in Table 3.

Min	Max	St. Dev.	ACD_{tot}	ACR_{tot}
0.9	4.5	0.5	2.7	1.3

Table 3. Descriptive statistics (in meters) of the tree crown diameter obtained by field measurements.

4. METHODOLOGY

4.1 Individual Tree Crown detection process

According to Pouliot et al. (2005), to optimize the ITC detection, image pre-processing phase is required. In this way, the user can select the best spectral band and enhances the image data to maximize the tree detection process. In this study, the ITC detection process consists in different steps shown in the Figure (4). Each step is detailed in the following subsection.

Figure 4. Flowchart of the ITC detection process.

4.2 Grey-Level Input Data (GLID)

According to Li et al., (2008), in the first step of the pre-processing chain, different illumination images were considered, with aim to improve the accuracy of the ITC process. So, in this phase, the Grey Level Input Data (GLID) were selected to be used in the ITC detection process. Particularly, for both datasets (Table 4, 5) the following data were considered: the original spectral bands, vegetation indices, Intensity (I) component image, and PC1 band, obtained respectively by IHS color space and PCA transformation.

GLID	Description
VIS-NIR and PAN	WV-2 spectral band
NDVI	(Normalized Difference Vegetation Index), (Rouse <i>et al.</i> , 1973)
LCI	(Leaf Chlorophyll Index), (Datt, 1999)
CCCI	(Canopy Chlorophyll Content Index), (El-Shikha <i>et al.</i> , 2008)
Maccioni	(Maccioni, 2001), (Index DataBase)
I	(Intensity component – IHS color space transformation),(Lillesand <i>et al.</i> , 2004)
PC1	(PCA transform), (Campbell <i>et al.</i> , 2011)

Table 4. GLID selected for the ITC detection (WV-2 dataset).

GLID	Description
VIS-NIR	Digital Aerial spectral bands
NDVI	(Normalized Difference Vegetation Index), (Rouse <i>et al.</i> , 1973)
I	(Intensity component – IHS color space transformation), (Lillesand <i>et al.</i> , 2004)
PC1	(First Principal Component – PCA transform), (Campbell <i>et al.</i> , 2011)

Table 5. GLID selected for the ITC detection (Aerial dataset).

4.3 Vegetation extraction

Following the GLID selection, for both datasets a vegetation mask was generated, with the aim to remove from the test site no-vegetated area as soil, road, build and other man-made objects. Thresholding, or commonly, binarization is a fundamental step to separate tree crown pixel from the background, before ITC detection process (Pitkänen, 2001). To obtain the vegetation mask, the binarization was performed on the NDVI grey-level. Firstly, using the ArcMap Raster calculator

tool the NDVI was computed, using the classical formula introduced by Rouse et al., (1973). The NDVI raster file was classified in two classes (vegetation and no-vegetation) using Maximum Likelihood algorithm (D’Allestro and Parente, 2015). According to Brivio et al., (2006) for both thematic classes, the size of the training sites is determinate considering about 5 percent of the pixel of the full scene. The threshold values of the histogram of the NDVI image are shown in the subsequent tables:

NDVI Threshold	WV-2 data	Aerial data
	0.24	0.11

Table 6. NDVI thresholds derived to produce the vegetation mask.

Subsequently, to estimate the accuracy of the thematic classification an error matrix is computed. Also called confusion matrix or contingency table (Brivio et al., 2006), the error matrix is a square array that permits to quantify the commission and omission errors using opportune accuracy measures as: Producer’s Accuracy (PA), User’s Accuracy (UA) and Overall Accuracy (OA) (Story and Congalton, 1986), (Congalton and Green, 2008), (Morisette and Khorram, 2000). In this study, to compute the error matrix, for both datasets appropriately test sites (pixel test) were identified for the considered thematic classes. The results of the accuracy assessment are reported in the following tables.

Accuracy measures (%)	vegetation class	no-vegetation class
PA	95.74	99.26
UA	99.30	95.49
OA	97.42	

Table 7. Thematic accuracy of the NDVI classification (WV-2 data).

Accuracy measures (%)	vegetation class	no-vegetation class
PA	99.28	97.68
UA	97.67	99.29
OA	98.47	

Table 8. Thematic accuracy of the NDVI classification (Aerial data).

4.4 Gaussian image smoothing

For each input data, Gaussian smoothing filter was applied. According to Gebreslasie et al., (2011) this low-pass filter reduces the noise level in the input image, enhances the tree peaks detection and theoretically minimizes the commission error in the ITC detection process. The formula of the Gaussian smoothing filter is:

$$G_{i,j} = \frac{1}{2\pi\sigma^2} e^{-\frac{i^2+j^2}{2\sigma^2}} \tag{3}$$

where,

- i is the distance on the horizontal axis from the origin in pixel,
- j is the distance on the vertical axis from the origin in pixel,
- σ is the standard deviation of the Gaussian distribution.

The value of the smoothing factor (σ) and the kernel size play a key role to optimize the ITC detection process (Novotný et al., 2011), (Pitkänen, 2001). In this study, the Gaussian-smoothing filter was performed using the Grid Filter module, implemented in the SAGA GIS tools package, available in the QGIS software. Particularly, circle kernel was selected. Considering the spatial resolution of WV-2 and Aerial data, a conversion of the field measurements (Table 3) to obtain the kernel size was performed (Table 9). Finally, tested σ values are 1 and 2, considering the

Local Maxima Smoothing Relation (LMSR) as reported in (Pouliot et al., 2005). Adopted from Culvenor (2000), this relation permits to identify the optimum Gaussian smoothing factor considering the number of local maxima detected (Pouliot and King, 2005).

ACR _{tot} (in meters)	Kernel radius (in pixel)	Dataset
1.3	3	WV-2 data
	7	Aerial data

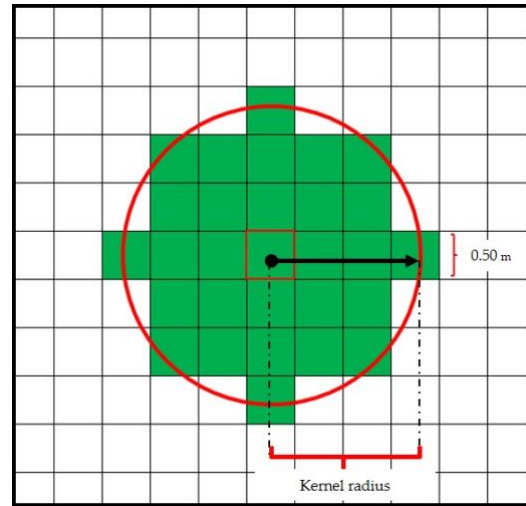
Table 9. Field measurement conversion to Gaussian kernel size in pixel.

4.5 Local Maxima Filter

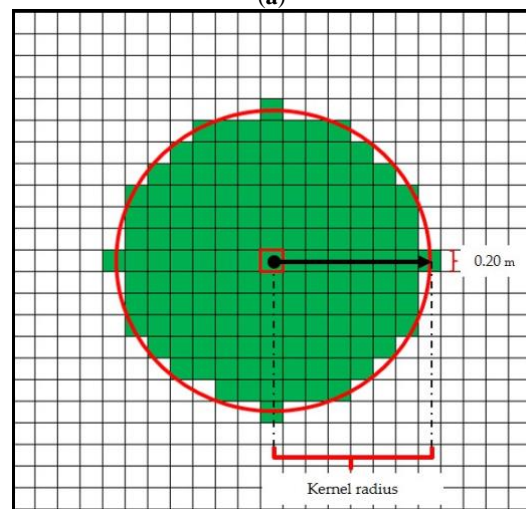
Before the LM detection, for each Smoothed Images (SI) the binary vegetation mask, previously described, was applied with the aim to remove no-vegetation area. Subsequently, the LMF was applied. It permits to detect the individual tree position considering that top of each tree crowns produces a local maximum value in the histogram of the optical image (Figure 5). In details, considering that the local maximum is located probably at the center of the tree crown, applying the Local Maxima Filter, with a specific moving kernel, on the image, the Tree Top (TT) positions can be detected (Ardila Lopez, 2012).

Figure 5. Three-dimensional view of the brightness profile identified for a tree peak in the NDVI GLID (Aerial dataset).

In this study, the TT detection was achieved using the Focal statistics tool, implemented in the ArcMap software. This spatial analyst tool permits to perform a neighborhood operation, where the value for each output cell is a function of the values of all input cells, considering a specified neighborhood around that location. The function executed on the input data is a statistic (as majority, maximum, mean, median, minimum, minority, range, standard deviation, and sum). Clearly, in this study, to detect tree peaks the maximum value was computed, while the neighborhood size was selected using a circle kernel as well as done for the image smoothing process (Table 9) (Figure 6).



(a)



(b)

Figure 6. Circle Kernel design for (a) WV-2 data and (b) Aerial data.

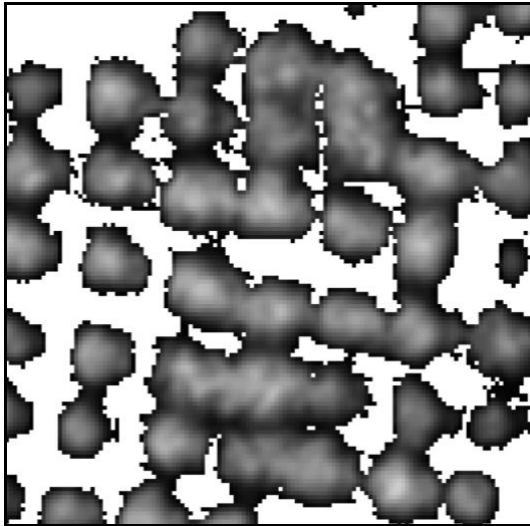
Subsequently, the maximum values detected within each neighborhood were extracted. In details, to find the hypothetical TT the Conditional Boolean operator (Con) was applied. Implemented in the Raster Calculator tool, it permits to find those pixels with higher values comparing SI and LMF output raster. The syntax of the function is:

$$TT_i = \text{Con}(SI_i = LMF_i, 1, 0) \quad (4)$$

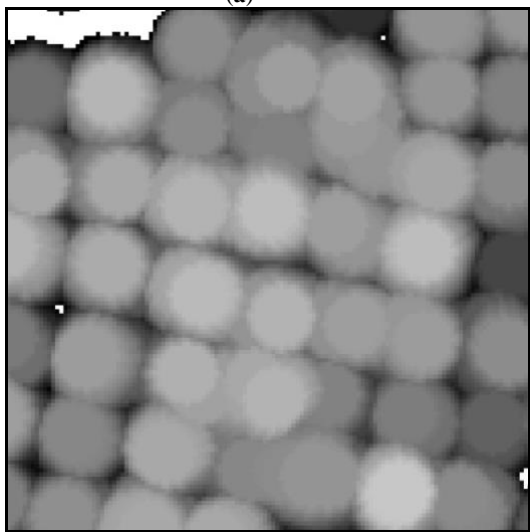
where,

TT_i is the i th Tree Tops output raster data,
 SI_i is the i th Smoothed Image obtained by the Gaussian Filter,
 LMF_i is the i th LMF output raster derived by Focal Statistic tool,

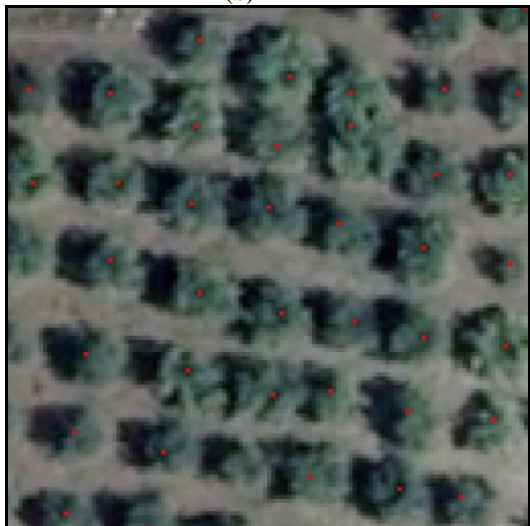
1 is the value assigned to each pixel with the maximum value,
 0 is the value assigned to the other pixels.



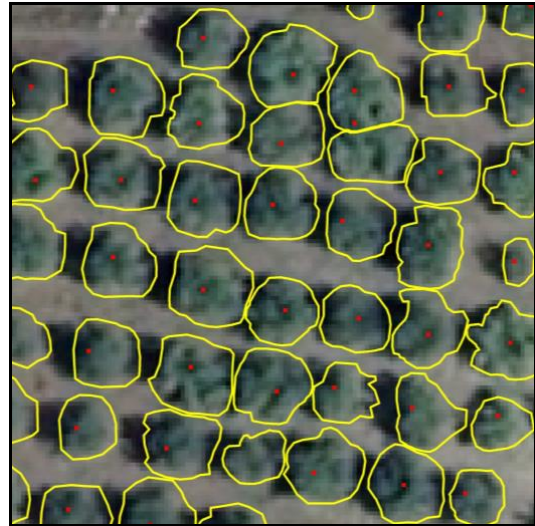
(a)



(b)



(c)



(d)

Figure 7. Example of (a) smoothed and masked NDVI image, (b) LMF output raster, (c) TT output raster (in red) overlaid on the digital aerial data RGB composition (d) and reference data (in yellow).

5. RESULTS AND DISCUSSION

5.1 Detection accuracy tests

According to Ke and Quackenbush, (2011), to perform a detailed accuracy tests, the correspondence of the detected and reference trees must be evaluated. Therefore, in this study to estimate the accuracy of the ITC detection process, for both aerial and WV-2 images, reference data were generated by visual photointerpretation and on-screen digitizing (Figure 3.7). This procedure was validated with field survey campaigns, as described in previous section, to confirm tree locations and estimate the crown diameter. Lamar et al., (2005) assert that, for ITC detection process the accuracy tests can be performed using the plot level assessment and individual tree level assessment. The Plot Level Accuracy (PLA) permits to estimate the aggregate proportion of rightly detected trees (Ke and Quackenbush, 2011), comparing the total number of automatically detected trees with the total number of manually detected trees, reported in the reference data (Lamar et al., 2005). The PLA is estimated using the following formula:

$$PLA = \frac{d}{n} \quad (5)$$

where,

d is the total number of detected tree using the ITC process,
n is the total number of reference tree crown.

For the individual tree level assessment, the Accuracy Index (AI) was applied. Introduced by Pouliot et al., (2002), this index provides the overall accuracy of the ITC detection process, considering the omission and commission errors.

The formula of the AI is:

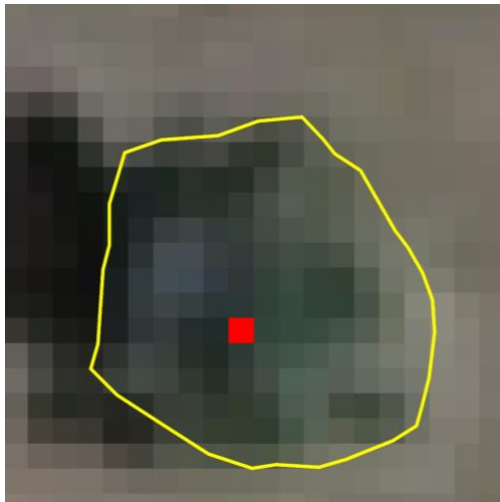
$$AI(\%) = \left[\frac{(n - (o + c))}{n} \right] \cdot 100 \quad (6)$$

where,

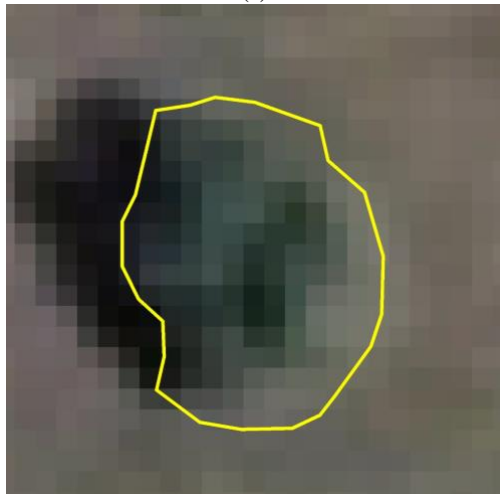
n is the total number of reference tree crown,
o is the total number of omission error,
c is the total number of the commission error.

In details, the omission error refers all those tree crown reference data, where tree top was undetected (Missed-M) (Figure 8.(b)). Instead, the commission error refers all those tree tops detected

out of the boundary of the tree crown reference data (Figure 8.(c)) or when the tree top was detected as multiple tree, in the single tree reference data (Figure 8.(d)) (False Positive-FP).



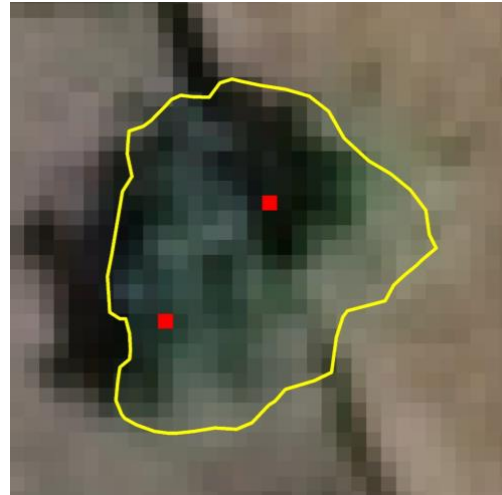
(a)



(b)



(c)



(d)

Figure 8. Example of (a) tree correctly detected, (b) tree missed (omission error), (c) tree erroneously identified and (d) tree detected as multiple tree crowns (commission error).

Finally, with the aim to achieve a clearer overview and a more accurate quantitative analysis of the results, the specific proportion values of trees detected as Correct (C), Missed (M) (omission error) and False Positive (FP) (commission error), were estimated, as reported in the (Wulder et al., 2000), (Wulder et al., 2004). The equations used are:

$$\text{Correct}(\%) = \frac{\text{Correct}}{n} \cdot 100 \quad (7)$$

$$\text{Missed}(\%) = \frac{\text{Missed}}{n} \cdot 100 \quad (8)$$

$$\text{False Positive}(\%) = \frac{\text{False Positive}}{n} \cdot 100 \quad (9)$$

where,

n is the total number of reference tree crown.

The results of the accuracy tests are reported in the following tables.

Smoothing factor	WV-2 GLID	C (%)	FP (%)	M (%)	AI (%)	PLA (%)
(σ) = 1	Coastal	2.9	107.3	97.1	-104.5	110.2
	Blue	1.0	101.3	99.0	-100.3	102.2
	Green	1.3	104.1	98.7	-102.9	105.4
	Yellow	2.5	95.9	97.5	-93.3	98.4
	Red	1.0	97.1	99.0	-96.2	98.1
	Red Edge	4.8	79.9	95.2	-75.2	84.7
	NIR1	18.8	59.6	81.2	-40.8	78.3
	Panchromatic	2.2	93.9	97.8	-91.7	96.2
	NDVI	61.5	1.9	38.5	59.6	63.4
	LCI	54.5	7.3	45.5	47.1	61.8
	CCCI	43.6	22.9	56.4	20.7	66.6
	Maccioni	45.9	18.8	54.1	27.1	64.6
	I	2.9	100.0	97.1	-97.1	102.9
	PC1	2.9	95.5	97.1	-92.7	98.4

Table 10. Accuracy of the ITC detection process for the WV-2 dataset - (σ)=1.

Smoothing factor	WV-2 GLID	C (%)	FP (%)	M (%)	AI (%)	PLA (%)
(σ) = 2	Coastal	2.2	93.6	97.8	-91.4	95.9
	Blue	1.0	98.1	99.0	-97.1	99.0
	Green	0.6	91.1	99.4	-90.4	91.7
	Yellow	2.2	89.5	97.8	-87.3	91.7
	Red	0.3	89.5	99.7	-89.2	89.8
	Red Edge	1.9	70.7	98.1	-68.8	72.6
	NIR1	19.4	36.6	80.3	-16.9	56.1
	Panchromatic	0.6	85.0	99.4	-84.4	85.7
	NDVI	54.5	1.6	45.5	52.9	56.1
	LCI	47.1	6.7	52.9	40.4	53.8
	CCCI	41.1	17.8	58.9	23.2	58.9
	Maccioni	43.3	15.6	56.7	27.7	58.9
	I	1.3	86.9	98.7	-85.7	88.2
	PC1	1.0	86.3	99.0	-85.4	87.3

Table 11. Accuracy of the ITC detection process for the WV-2 dataset - (σ)=2.

Smoothing factor	Aerial GLID	C (%)	FP (%)	M (%)	AI (%)	PLA (%)
(σ) = 1	Blue	75.1	49.8	24.9	25.2	124.9
	Green	76.7	47.3	23.3	29.3	124.0
	Red	70.7	57.1	29.3	13.6	127.8
	NIR	96.2	6.0	3.8	90.2	102.2
	NDVI	95.3	2.2	4.7	93.1	97.5
	I	79.2	40.1	20.8	39.1	119.2
	PC1	76.3	46.4	23.7	30.0	122.7

Table 12. Accuracy of the ITC detection process for the WV-2 dataset - (σ)=2.

Smoothing factor	Aerial GLID	C (%)	FP (%)	M (%)	AI (%)	PLA (%)
(σ) = 2	Blue	66.9	57.4	33.1	9.5	124.3
	Green	66.6	50.8	33.4	15.8	117.4
	Red	64.0	65.6	36.0	-1.6	129.7
	NIR	95.9	1.9	4.1	94.0	97.8
	NDVI	93.1	0.9	6.9	92.1	94.0
	I	71.3	43.5	28.7	27.8	114.8
	PC1	69.1	48.6	30.9	20.5	117.7

Table 13. Accuracy of the ITC detection process for the Aerial dataset - (σ)=2.

Smoothing factor	WV-2 GLID	AI (%)
(σ) = 1	NDVI	59.6
	LCI	47.1
	Maccioni	27.1
	CCCI	20.7
	NIR1	-40.8
	Red Edge	-75.2
	Panchromatic	-91.7
	PC1	-92.7
	Yellow	-93.3
	Red	-96.2
	I	-97.1
	Blue	-100.3
	Green	-102.9
	Coastal	-104.5

Table 14. WV-2 GLID accuracy performance ranked by AI (%) - (σ)=1.

Smoothing factor	WV-2 GLID	AI (%)
(σ) = 2	NDVI	52.9
	LCI	40.4
	Maccioni	27.7
	CCCI	23.2
	NIR1	-16.9
	Red Edge	-68.8
	Panchromatic	-84.4
	PC1	-85.4
	I	-85.7
	Yellow	-87.3
	Red	-89.2
	Green	-90.4
	Coastal	-91.4
	Blue	-97.1

Table 15. WV-2 GLID accuracy performance ranked by AI (%) - (σ)=2.

Smoothing factor	Aerial GLID	AI (%)
(σ) = 1	NDVI	93.1
	NIR	90.2
	I	39.1
	PC1	30.0
	Green	29.3
	Blue	25.2
	Red	13.6

Table 16. Aerial GLID accuracy performance ranked by AI (%) - (σ)=1.

Smoothing factor	Aerial GLID	AI (%)
$(\sigma) = 2$	NIR	94.0
	NDVI	92.1
	I	27.8
	PC1	20.5
	Green	15.8
	Blue	9.5
	Red	-1.6

Table 17. Aerial GLID accuracy performance ranked by AI (%) - $(\sigma)=2$.

For The WV-2 dataset, with a smoothing factor equal to 1 (Tables 10, 14), the better performance of the ITC detection process was obtained by the vegetation indices GLID. In details, using the NDVI data, a good level of overall accuracy (AI = 60 %) and a low value of the commission error was achieved (FP = 2%). For the other considered GLID, as single WV-2 spectral band, I and PC1, high value of commission and omission error was recorded. Similar results were obtained also considering a higher value of the Gaussian smoothed factor ($\sigma = 2$), (Tables 11, 15). In this case, with NDVI data the overall accuracy achieves a value equal to 53%, but more spectral information was lost. In fact, for each considered GLID, many trees were not detected. For the Aerial datasets, with a smoothing factor equal to 1 (Tables 12, 16), the better performance of the ITC detection was achieved by NDVI and NIR GLID, thanks to the spectral characteristics of the vegetation. Particularly, using the NDVI data, the tree detection process achieves an AI = 93% and low values for the omission (M = 4.7%) and commission (FP = 2.2 %) error. Similar results were achieved with the NIR band (AI = 90%). However, an overestimation of the detected trees was recorded (FP= 6%) (PLA = 102.2 %). This also happens for the other spectral bands of the visible, I image and PC1. In fact, the average values for the missed and false positive trees are respectively equal to 24% and 48%. Using a higher Gaussian smoothing factor ($\sigma = 2$) (Tables 13, 17), the better performance is carried out by the NIR band (AI of 94%). Comparable results were achieved also with the NDVI (AI = 92%). However, a higher value of the Gaussian smoothing factor determines a loss of spectral information. In fact, also for the other considered GLID, a higher omission error was recorded.

5.2 Positional accuracy tests

As reported in literature, the positional accuracy can be assessed comparing the coordinates of sample points on a map with the coordinates of the same points obtained from a ground survey or other reference data (Congalton and Green, 2008). This approach can be used to quantify the planimetric accuracy of the tree detected using the LMF (Khalid et al., 2014), (Santoro et al., 2013). In this study, the centroids of each reference data were extracted, and its (x, y) coordinates were compared with the same coordinates of each TT correctly detected by the LMF (Figure 9). Subsequently, to quantify the discrepancies between reference tree location and TT position, as accuracy measure, the RMSE is considered. Based on the results achieved from the detection accuracy tests, the positional accuracy tests were performed considering those GLID characterized by acceptable values of trees correctly detected (C %) (Tables 10, 11, 12, 13). In consideration of the results obtained with the detection accuracy tests, for the WV-2 dataset the vegetation indices GLID are chosen, while for the Aerial datasets NDVI and NIR GLID are selected. The results of the positional accuracy tests are reported in the following tables.

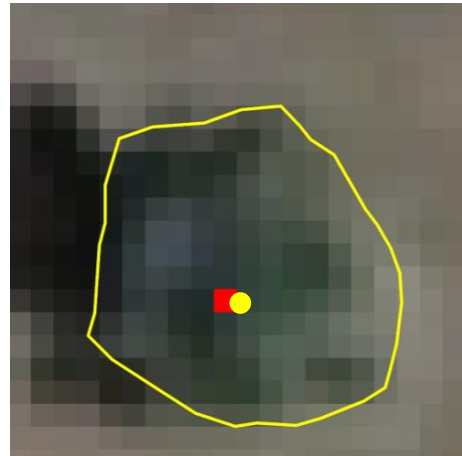


Figure 9. Example of tree crown reference data (yellow boundary), centroid (yellow dot) and TT point (red square) considered in the positional accuracy tests.

Smoothing factor	WV-2 GLID	RMSE (m)
$(\sigma) = 1$	NDVI	0.70
	LCI	0.87
	Maccioni	1.00
	CCCI	1.00
$(\sigma) = 2$	NDVI	0.69
	LCI	0.81
	Maccioni	0.98
	CCCI	1.05

Table 18. Positional accuracy (in meters) obtained for the WV-2 GLID.

Smoothing factor	Aerial GLID	RMSE
$(\sigma) = 1$	NDVI	0.46
	NIR	0.90
$(\sigma) = 2$	NDVI	0.32
	NIR	0.84

Table 19. Positional accuracy (in meters) obtained for the Aerial GLID.

As for the detection accuracy, also for the positional accuracy, the tests were performed considering the effect of the different values of the smoothing factor. For The WV-2 dataset, with a smoothing factor equal to 1, the better positional accuracy was obtained with NDVI and LCI GLID (RMSE < 1 m) (Table 18). In details, the NDVI data permit to obtain an acceptable positional accuracy (RMSE = 0.70 m), considering that the cell size of the WV-2 pan-sharpened images is of 0.50 m. Similar results were obtained also with a higher value of the Gaussian smoothed factor ($\sigma = 2$), (Table 18). Therefore, the influence of the smoothing factor can be defined negligible. In fact, with σ equal 2, a slightly better performance was reached for the NDVI, LCI and Maccioni GLID, while for the CCCI GLID a slight worse accuracy was obtained. For the Aerial datasets, the same trend was confirmed, especially for the NIR GLID (Table 19). In fact, with σ equal 2, a negligible improvement of the positional accuracy was recorded. However, the better performance was achieved by the NDVI GLID. In fact, increasing the smoothing factor ($\sigma = 2$), a better positional accuracy was reached (RMSE = 0.32) (Table 19), and thus comparable with the GSD of the Aerial data (0.20 m). In conclusion, the results obtained shown that, the spectral information of the considered GLID play a fundamental role in the ITC detection process. In fact, for both datasets and both accuracy tests, the better accuracy was

recorded using vegetation indices as input data of the detection process, especially with the NDVI. In fact, as reported in literature (Pouliot et al., 2002), using the vegetation indices in the ITC detection process, permit to enhance the tree peak detection and simultaneously minimize the brightness of the no-tree peaks and soil background pixels. In consideration of the results achieved in both accuracy tests, maybe, in part, explain that the spatial resolution of the digital aerial image (0.2 m), permit to obtain a higher accuracy to detect young olive trees than WV-2 images. In fact, the performance of the ITC detection process is directly related to image scale. In other words, high spatial resolution image is required to allow an acceptable number of pixels to discriminate the tree crown from the soil background (Daley et al., 1998). In addition, the lower accuracy, of the detection process, achieved with the WV-2 data, can be influenced also considering the high tree density (number of trees/ha). In fact, as reported in (Masson, 2005), one of the main problems in the ITC detection process is the high tree density, where the adjacent tree crown, appear like a continuous canopy. Regarding the positional accuracy tests, instead the performances are not much influenced by the spatial resolution. In fact, for both datasets were obtained a planimetric accuracy comparable at the cell size of the input data. However, as reported in (Khalid et al., 2013), other factors can be influenced the planimetric accuracy of the individual tree crown position, detected by the LMF method as image acquisition time (Masson, 2005), Sun illumination (Ke and Quackenbush, 2009), Sun elevation angle (Ozdarici-Ok, 2015) and so on.

6. CONCLUSIONS

In this study, the Individual Tree Crown (ITC) detection process was investigated. This semi-automatic process was tested on young olive trees, applying the Local Maxima Filter (LMF) on the Digital Aerial image and WorldView-2 (WV-2) previously orthorectified and pansharpened. The results indicate that the image data characteristics play a key role to detect tree by remotely sensed data. In consideration of the spectral information, for both datasets, the results show a higher accuracy achieved with the NDVI, highlighting the spectral characteristics of the vegetation. In fact, with the other considered input data, many trees were not detected, so providing a lower accuracy. Another factor affecting tree detection was the spatial resolution of the considered images. In fact, the relationship between tree spacing/tree crown size and the spatial resolution determines different level of accuracy. In details, with the Digital Aerial images (cell size=0.20 m) a higher accuracy was reached, than the WV-2 images, even if pan-sharpened (cell size=0.50 m). In fact, with the WV-2 data, the small trees were not detected, and more false positive trees were identified. Furthermore, the high tree density (428 trees/ha) and relative narrow tree spacing (4x4 m) determine that the olive tree crown appears like a continuous canopy. In fact, the soil background was not visible, because the trees, with large crown, are closed together. Concerning the positional accuracy test confirms the reliability of the LMF method, to detect individual tree crown location. In fact, the investigated approach permits to achieve a planimetric accuracy slightly greater than the pixel size, as well as reported in literature (Santoro et al., 2013). With the aim to increase the accuracy of the ITC detection process, other studies suggest that other factors affect the individual tree detection. Among them: sensor view angle, topography, sun elevation and shadow (Santoro et al., 2013), (Hirschmugl et al., 2007), (Wulder et al., 2004), value of the Gaussian smoothing factor (Pouliot et al., 2002), the binarization process to mask no-vegetation area (Pitkänen, 2001), kernel setting parameters (Wulder et al., 2000),

and so on. Finally, all these factors could be the focus of further lines of investigation, maybe considering other tree species as well as different multispectral sensor data.

ACKNOWLEDGEMENTS

This paper brings together the results of studies conducted during the author's Ph.D research. The author would like to thank Prof. Claudio Parente from University of Naples "Parthenope", and Prof. Manuel Ángel Aguilar Torres from the University of Almería, Spain, for their suggestions and scientific comments.

REFERENCES

- Aguilar, M. A.; Bianconi, F.; Aguilar, F. J.; Fernández, I. 2014. Object-based greenhouse classification from GeoEye-1 and WorldView-2 stereo imagery. *Remote Sensing*, 6(5), 3554-3582.
- Ardila Lopez, J. P. 2012. Object-based methods for mapping and monitoring of urban trees with multitemporal image analysis. Ph. D. dissertation, University of Twente Faculty of Geo-Information and Earth Observation (ITC), Twente, Netherlands, 2012.
- Basile Giannini, M., Maglione, P., Parente, C. 2010. Application of IHS Pan-Sharpener techniques to IKONOS images. In *Proceedings of the IEEE GOLD Conference*. 2010, Livorno, Italy, 29-30 April 2010.
- Bazi, Y., Al-Sharari, H., Melgani, F. 2009. An automatic method for counting olive trees in very high spatial remote sensing images. In: *Geoscience and Remote Sensing Symposium, 2009 IEEE International, IGARSS 2009*. IEEE, 2009, Cape Town, South Africa, 12-17 July 2009, pp. II-125-II-128.
- Belfiore, O. R., Meneghini, C., Parente, C., Santamaria, R. 2015. Comparison of Methods for IKONOS Images Pan-sharpening Using Synthetic Sensors. *Research Journal of Applied Sciences, Engineering and Technology*, 11(10), 1084-1090.
- Belfiore, O. R., Parente, C. 2016. Comparison of Different Algorithms to Orthorectify WorldView-2 Satellite Imagery. *Algorithms*, 9(4), 67.
- Belfiore, O. R.; Meneghini, C.; Parente, C.; Santamaria, R. 2016. Application of different Pan-sharpening methods on WorldView-3 images. *ARNP – JEAS*, 11(1), 490-496, ISSN 1819-6608.
- Belfiore, O. R.; Parente, C. 2015. Orthorectification and pansharpening of worldview-2 satellite imagery to produce high resolution coloured ortho-photos. *Modern Applied Science*, 9(9), 122-130.
- Brivio, P. A., Lechi, G., L Zilioli, E. 2006. *Principi e metodi di telerilevamento*. Torino, Italy, CittàStudi Edizioni.
- Campbell, J. B.; Wynne, R. H. 2011. *Introduction to Remote Sensing - Fifth Edition*, 5th ed., Guilford Press, New York, 2011.
- Carper, W. 1990. J. The use of Intensity-Hue-Saturation transformations for merging SPOT panchromatic and multispectral image data. *Photogrammetric Engineering and Remote Sensing*, 56(4), 459-467.
- Caruso, T., Rühl, J., Sciortino, R., Marra, F. P., La Scalia, G. 2014. Automatic detection and agronomic characterization of olive groves using high-resolution imagery and LIDAR data. In *SPIE Remote Sensing*. International Society for Optics and Photonics, 2014, pp 92391F-92391F.
- Ceylan, N., Unal, E., Masson, J. 2009. A Case Study of Developing An Olive Tree Database For Turkey. *Photogrammetric Engineering & Remote Sensing*, 75(12), 1397-1405.
- Chavez, P., Sides, S. C., Anderson, J. A. 1991. Comparison of three different methods to merge multiresolution and multispectral data- Landsat TM and SPOT panchromatic.

- Photogrammetric Engineering and Remote Sensing*, 57(3), 295-303.
- Congalton, R. G., Green, K. 2008. Assessing the accuracy of remotely sensed data: principles and practices. 2th edition, CRC press, Boca Raton, FL, USA.
- Culvenor, D. S. 2000. Development of a tree delineation algorithm for application to high spatial resolution digital imagery of Australian native forest. Ph. D dissertation, University of Melbourne, Department of Forestry, Melbourne, Australia, 2000.
- D'Allestro, P., Parente, C. 2015. GIS application for NDVI calculation using Landsat 8 OLI images. *International Journal of Applied Engineering Research*, 10(21), 42099-42102.
- Daley, N. M., Burnett, C. N., Wulder, C. N., Niemann, K. O., Goodenough, D. G. 1998. Comparison of fixed-size and variable-sized windows for the estimation of tree crown position. In: *Geoscience and Remote Sensing Symposium Proceedings, 1998. IGARSS'98. 1998 IEEE International*, Seattle, Washington, USA, 6-10 July 1998, pp. 1323-1326.
- Daliakopoulos, I. N., Grillakis, E. G., Koutroulis, A. G., Tsanis, I. K. 2009. Tree crown detection on multispectral VHR satellite imagery. *Photogrammetric Engineering & Remote Sensing*, 75(10), 1201-1211.
- Datt, B. 1999. Remote sensing of water content in Eucalyptus leaves. *Australian Journal of Botany*, 47(6), 909-923
- Díaz-Varela, R. A., de la Rosa, R., León, L., Zarco-Tejada, P. J. 2015. High-resolution airborne UAV imagery to assess olive tree crown parameters using 3D photo reconstruction: application in breeding trials. *Remote Sensing*, 7(4), 4213-4232.
- DigitalGlobe. Available online: <https://www.digitalglobe.com/resources/satellite-information> (15 March 2018).
- DigitalGlobe. Available online: <https://geomatics.planet.com/upload/digitalglobe/DigitalGlobe%20Core%20Imagery%20Products%20Guide.pdf> (15 March 2018).
- DigitalGlobe: Available online: https://mdacorporation.com/docs/default-source/product-spec-sheets/geospatial-services/dg_worldview2_ds_prod.pdf?sfvrsn=4 (15 March 2018)
- El-Shikha, D. M., Barnes, E. M., Clarke, T. R., Hunsaker, D. J., Haberland, J. A., Pinter Jr, P. J., Thompson, T. L. 2008. Remote sensing of cotton nitrogen status using the canopy chlorophyll content index (CCCI). *Transactions of the ASAE (American Society of Agricultural Engineers)*, 51(1), 73-82.
- eoPortal Directory – Satellite Mission Database. Available online: <https://directory.eoportal.org/web/eoportal/satellite-missions>. (15 March 2018).
- ESRI ARCMAP - Fundamentals of panchromatic sharpening. Available online: http://desktop.arcgis.com/en/arcmap/latest/manage-data/raster-and-images/fundamentals-of-panchromatic-sharpening.htm#ESRI_SECTION1_BB6652C8F5FB43E3BF678C5F8BE68552. (15 March 2018).
- Figorito, B.; Tarantino, E.; Balacco, G.; Fratino, U. 2012. An object-based method for mapping ephemeral river areas from WorldView-2 satellite data. In *SPIE Remote Sensing, International Society for Optics and Photonics*, 2012, pp. 85310B-85310B.
- Gebreslasie, M. T., Ahmed, F. B., Van Aardt, J. A., Blakeway, F. 2011. Individual tree detection based on variable and fixed window size local maxima filtering applied to IKONOS imagery for even-aged Eucalyptus plantation forests. *International Journal of Remote Sensing*, 32(15), 4141-4154.
- González, J., Galindo, C., Arevalo, V., Ambrosio, G. 2007. Applying image analysis and probabilistic techniques for counting olive trees in high-resolution satellite images. In: *International Conference on Advanced Concepts for Intelligent Vision Systems*. Springer, Berlin, Heidelberg, Germany, August 2007, pp. 920-931.
- Gougeon, F. A., Leckie, D. G. The individual tree crown approach applied to Ikonos images of a coniferous plantation area. *Photogrammetric Engineering & Remote Sensing*, 72(11), 1287-1297.
- Heenkenda, M. K., Joyce, K. E., Maier, S. W. 2015. Mangrove tree crown delineation from high-resolution imagery. *Photogrammetric Engineering & Remote Sensing*, 81(6), 471-479.
- Hirschmugl, M., Ofner, M., Raggam, J., Schardt, M. 2007. Single tree detection in very high resolution remote sensing data. *Remote Sensing of Environment*, 110(4), 533-544.
- Karantzalos, K. G., Argialas, D. P. 2004. Towards automatic olive tree extraction from satellite imagery. In: *Geo-Imagery Bridging Continents. XXth ISPRS Congress*, Istanbul, Turkey, 12-23 July 2004, pp. 12-23.
- Ke, Y., Quackenbush, L. J. 2008. Comparison of individual tree crown detection and delineation methods. In: *Proceedings of 2008 ASPRS Annual Conference*. Portland, Oregon, USA, 2 May 2008.
- Ke, Y., Quackenbush, L. J. 2009. Individual tree crown detection and delineation from high spatial resolution imagery using active contour and hill-climbing methods. In: *Proceedings of 2009 ASPRS Annual Conference*, American Society of Photogrammetry and Remote Sensing, Baltimore, Maryland, USA, 9-13 March 2009, pp. 9-13.
- Ke, Y., Quackenbush, L. J. 2011. A review of methods for automatic individual tree-crown detection and delineation from passive remote sensing. *International Journal of Remote Sensing*, 32(7), 4725-4747.
- Ke, Y., Quackenbush, L. J. 2011. A review of methods for automatic individual tree-crown detection and delineation from passive remote sensing. *International Journal of Remote Sensing*, 32(17), 4725-4747.
- Khalid, N., Hamid, J. A., Latif, Z. A. 2014. Accuracy assessment of tree crown detection using local maxima and multi-resolution segmentation. In: *IOP Conference Series: Earth and Environmental Science*, IOP Publishing 2014, 8th International Symposium of the Digital Earth (ISDE8), 26–29 August 2013, Kuching, Sarawak, Malaysia.
- Klonus, S.; Ehlers, M. 2009. Performance of evaluation methods in image fusion. In: *Information Fusion, 2009. FUSION'09. 12th International Conference on. IEEE*, 2009, pp. 1409-1416.
- Kruse, F. A.; Perry, S. L. 2013. Mineral mapping using simulated Worldview-3 short-wave-infrared imagery. *Remote Sensing*, 5(6), 2688-2703.
- Laben, C. A., Brower, B. V. 2000. Process for enhancing the spatial resolution of multispectral imagery using pan-sharpening. U.S. Patent No. 6,011,875. 4 January 2000.
- Lamar, W. R., McGraw, J. B., Warner, T. A. 2005. Multitemporal censusing of a population of eastern hemlock (*Tsuga canadensis* L.) from remotely sensed imagery using an automated segmentation and reconciliation procedure. *Remote Sensing of Environment*, 94(1), 133-143.

- Li, Z., Hayward, R., Zhang, J., Liu, Y. 2008. Individual tree crown delineation techniques for vegetation management in power line corridor. In *Computing: Techniques and Applications, DICTA'08*. Digital Image, IEEE. Canberra, Australia, 1-3 December, 2008.
- Lillesand, T., Kiefer, R. W., Chipman, J. W. 2004. *Remote Sensing and Image Interpretation*, 7th ed, JohnWiley and Sons, New York, 2004.
- Maglione, P.; Parente, C.; Vallario, A. 2014. Coastline extraction using high resolution WorldView-2 satellite imagery. *European Journal of Remote Sensing*, 47, 685-699. DOI: 10.5721/EuJRS20144739.
- Maccioni, A., Agati, G., Mazzinghi, P. 2001. New vegetation indices for remote measurement of chlorophylls based on leaf directional reflectance spectra. *Journal of Photochemistry and Photobiology B: Biology*, 61(1), 52-61.
- Masson, J. 2005. Use of very high resolution airborne and spaceborne imagery: a key role in the management of olive, nuts and vineyard schemes in the frame of the common agricultural policy of the European union. In: *Proceedings of Information and Technology for Sustainable Fruit and Vegetable Production, FRUTIC 05*. Montpellier, France, 12-16 September 2005, pp. 709-718.
- Novotný, J., Hanuš, J., Lukeš, P., Kaplan, V. 2011. Individual tree crowns delineation using Local Maxima approach and seeded region growing technique. In: *Proceedings of Symposium GIS Ostrava*. Ostrava, Czech Republic, 23-26 January 2011, pp. 27-39.
- Ozdarici-Ok, A. 2015. Automatic detection and delineation of citrus trees from VHR satellite imagery. *International Journal of Remote Sensing*, 36(17), 4275-4296.
- Parente, C., Santamaria, R. 2013. Increasing geometric resolution of data supplied by Quickbird multispectral sensors. *Sensors & Transducers*, 156(9), 111.
- Parente, C., Santamaria, R. 2014. Synthetic sensor of landsat 7 ETM+ imagery to compare and evaluate pan-sharpening methods. *Sensors & Transducers*, 177(8), 294.
- PCI Geomatics. Available online: http://www.pcigeomatics.com/pdf/Geomatica_v103_OrthoEngin_e_Tutorial_Worldview_1_and_2_v1.2.pdf (15 March 2018).
- Picariello, O.; Di Fusco, N.; Fraissinet M. 2000. *Elementi di biodiversità del Parco Nazionale del Vesuvio*, 1th eds., Ente Parco Nazionale del Vesuvio: Napoli, Italy, 2000, pp. XVI - 269. Available online: http://www.vesuviopark.it/pnv/comunicazione/libri/biodive_media.pdf (15 March 2018).
- Pitkänen, J. 2001. Individual tree detection in digital aerial images by combining locally adaptive binarization and local maxima methods. *Canadian Journal of forest research*, 31(5), 832-844.
- Pouliot, D. A., King, D. J., Bell, F. W., Pitt, D. G. 2002. Automated tree crown detection and delineation in high-resolution digital camera imagery of coniferous forest regeneration. *Remote Sensing of Environment*, 82(2), 322-334
- Pouliot, D. A., King, D. J., Bell, F. W., Pitt, D. G. 2002. Automated tree crown detection and delineation in high-resolution digital camera imagery of coniferous forest regeneration. *Remote Sensing of Environment*, 82(29), 322-334.
- Pouliot, D. A., King, D. J., Pitt, D. G. 2005. Development and evaluation of an automated tree detection delineation algorithm for monitoring regenerating coniferous forests. *Canadian Journal of Forest Research*, 35(10), 2332-2345.
- Pouliot, D., King, D. 2005. Approaches for optimal automated individual tree crown detection in regenerating coniferous forests. *Canadian Journal of Remote Sensing*, 31(3), 255-267
- Rouse, J. W., Jr.; Haas, R. H.; Schell, J. A.; Deering, D. W. 1973. Monitoring vegetation systems in the Great Plains with ERTS. In: *Third Earth Resources Technology Satellite-1 Symposium- Volume I: Technical Presentations*. NASA SP-351, compiled and edited by Stanley C. Freden, Enrico P. Mercanti, Margaret A. Becker, 1994 pages, published by NASA, Washington, D.C., 1974, pp.309-317.
- Santoro, F., Tarantino, E., Figorito, B., Gualano, S., D'Onghia, A. M. 2013. A tree counting algorithm for precision agriculture tasks. *International Journal of Digital Earth*, 6(1), 94-102.
- Shoji, S., Takahashi, T. 2012. Environmental and agricultural significance of volcanic ash soils. *Global Environmental Research-English Edition*, 6(2), 113-135.
- Story, M., Congalton, R. 1986. Accuracy assessment: A user's perspective. *Photogrammetric Engineering and Remote Sensing*, 52(3), 397-399.
- Vrabel, J. 2000. Multispectral imagery advanced band sharpening study. *Photogrammetric Engineering and Remote Sensing*, 66(1), 73-80.
- Wolf, A. 2010. Using WorldView 2 Vis-NIR MSI imagery to support land mapping and feature extraction using normalized difference index ratios. *DigitalGlobe 8-Band Research Challenge*. 1-13. Available online: http://www.harrisgeospatial.com/portals/0/pdfs/envi/8_bands_An tonio_Wolf.pdf (15 March 2018).
- Wulder, M. A., White, J. C., Niemann, K. O., Nelson, T. 2004. Comparison of airborne and satellite high spatial resolution data for the identification of individual trees with local maxima filtering. *International Journal of Remote Sensing*, 25(11), 2225-2232.
- Wulder, M., Niemann, K.O., Goodenough, D. G. 2000. Local maximum filtering for the extraction of tree locations and basal area from high spatial resolution imagery. *Remote Sensing of environment*, 73(1), 103-114.
- Zhang, Y. 2008. System and method for image fusion. U.S. Patent No. 7, 340, 099. 4 Mar. 2008.

NEW TRENDS FOR DSMS GENERATION FROM OPTICAL AND SAR SATELLITE IMAGERY: DEFINITION AND IMPLEMENTATION OF AN INNOVATIVE STRATEGY

M. Di Rita¹

¹ Geodesy and Geomatics Division, DICEA, University of Rome “La Sapienza”, Italy
martina.dirita@uniroma1.it

KEY WORDS: High-resolution optical and SAR satellite imagery, DSMS generation, object space Semi-Global Matching, Ground quasi-Epipolar images, free and open source software

ABSTRACT:

The topic of this research was the definition and implementation of an innovative strategy for DSMS generation from satellite imagery, exploiting efficient algorithms from computer vision without losing a rigorous photogrammetric approach. In this respect, a crucial point is the epipolar resampling for satellite images, which it is not straightforward, due to their multiple projection centers. A proper strategy both for optical and SAR imagery has been designed and an open source software, named Digital Automatic Terrain Extractor (DATE), developed and implemented in C++ programming language. DATE is able to perform a complete photogrammetric and radargrammetric processing chain, starting from the raw satellite images and their RPCs. The Ground quasi-Epipolar Images (GrEI) are the core of this original strategy for DSMS generation, able to return efficient and reliable solutions. The workflow first provides a ground projection for the raw satellite images, then, to bring the ground images in the quasi-epipolar geometry, a preliminary rotation is estimated for both images, in order to align them in the disparity prevailing direction. A refinement of the images relative position is subsequently performed. These orthorectified and aligned images act as GrEI and can undergo a dense image matching procedure. In order to evaluate the proposed strategy, both optical and SAR satellite datasets have been analysed. Results for a test site located in Northern Italy are here reported. The accuracy evaluation has been carried out comparing the extracted DSMS to a LiDAR-derived DSM, achieving good results both in accuracy and efficiency.

1. INTRODUCTION

A relevant application of remote sensing is the generation of Digital Surface Models (DSMs), which are growing more and more in relevance: the precise and repeated representation of the Earth's visible surface is of increasingly importance nowadays, being a core support for a wide variety of applications in many engineering, Earth sciences, safety and security fields, just to name a few.

Several approaches for DSMS generation exist (see 2.1). In this thesis the two stereo approaches are considered: the photogrammetric (from optical imagery) and the radargrammetric (or StereoSAR, from SAR imagery) ones. The fundamental goal of photogrammetry is to rigorously establish the geometric relationship between an object and its images, in order to derive information about its geometry from the images themselves, basing on stereoscopy; radargrammetry exploits similar geometric relationships using SAR imagery.

Over the years, following the increase in resolution for satellite imagery and the growing interest in the potential use of DSMS, many research groups around the world developed new methodologies and strategies for the DSM generation from satellite imagery, relying on different approaches. Some of these have been implemented in software, just very few are released as free and open source.

The topic of this research was the definition and implementation of a new and innovative strategy to generate DSMS from satellite imagery, exploiting efficient algorithms for feature and dense matching from computer vision without losing a rigorous photogrammetric approach.

The main challenge was to overcome the issues related to the epipolarity resampling for satellite images, which it is not straightforward, due to their multiple projection centers.

The idea was to find a proper approach applicable both to optical and SAR imagery, in order to obtain a general, reliable, effective, efficient and totally automatic solution. The Ground quasi-Epipolar Images (GrEI) generation is the core of this original strategy.

2. FROM SATELLITE IMAGES TO DSM

2.1 The Standard Procedure

The generation of DSMS is going through a period of renaissance due substantially to the new satellite sensors, able to provide sub-meter spatial resolutions, and to breakthroughs in keypoints detection and matching, and dense image matching algorithms, able to make fast and accurate the 3D reconstruction.

Hereafter, just the standard fundamental concepts related to DSM generation are very shortly summarized, in order to let a better understanding about the idea proposed in this work.

There are different methodologies to extract a DSM, characterised by different levels of accuracy, cost, time and ability to acquire more or less extensive areas. The choice of the method depends on the requirements of the tasks to be accomplished:

- the traditional integrated survey with GPS (centimeter accuracy, high time and cost, small areas of application)
- the terrestrial, aerial or satellite photogrammetry (accuracy from centimeters to meters, medium time and cost, medium and large areas of application)
- LiDAR technology (centimeters accuracy, short time but high cost, medium and large areas of application)

- InSAR and StereoSAR from satellite imagery (few meters accuracy, medium time and cost, medium and large areas of application)

As already said, in this thesis the focus is on the methodologies based on a stereoscopic approach: photogrammetry (from optical images) and radargrammetry (or StereoSAR, from SAR images) ones. Both of them use stereoscopic pairs acquired from different incidence angles.

The main steps to be followed to generate a DSM, with a stereoscopic approach, from two (or more) optical and SAR satellite images, are orientation and dense image matching (28).

Orientation is the operation used to recover the geometric relationship between the object space and the image space. Interior, relative and absolute orientations are the steps used to derive 3D coordinates information of objects from imagery. Two different types of orientation models are usually adopted for satellite imagery: the *physical sensor models* (also called rigorous models) and the *generalised sensor models* (also called Rational Polynomial Functions (RPFs)). Over the years, a huge literature has been produced on this topic (for example: (16), (9), (23), (4), (7)).

After the orientation step, dense image matching is performed. The matching process refers to the automatic technique for correspondence establishment between pixels representing the same detail in two or more images. Many different approaches to image matching have been developed in recent years within photogrammetry and computer vision. In every matching algorithm, though, three fundamental aspects have to be taken into account: the definition of a primitive model (that is the entity to be searched across different images), the search strategy and the similarity measure (the criterion to judge that the searched entity has been actually found in different images). According to the types of primitives to be matched, we can distinguish three basic families of matching methodologies: Intensity based matching or Area Based Matching (ABM), Feature Based Matching (FBM) and pixel-wise dense matching. Once the primitive model is defined, in the context of stereoscopic DSMs generation using both optical and SAR imagery, there are three main strategies able to limit the search area:

- geometric constraint
- region growing algorithms
- epipolar geometry

The geometric constraint is a strategy that allows to restrict the space of all possible matching solution making use of a-priori information about elevation.

The region growing (propagation of image matching) is the process of matching new points using an a-priori knowledge related to the preceding matched corresponding points.

The epipolar geometry is the space where epipolar images are generated. Epipolar images are normalised images where homologous points are located along the same row, which reduces the search space and ambiguity for image matching, and provides a global observation condition for stereoscopic feature extraction ((34), (47), (49), (21), (35), (24), (33), (51), (29), (25)). The epipolar geometry (that in the event of satellite images it is more properly called quasi-epipolar or pseudo-epipolar geometry) is the geometrical constraint selected, analysed and used for the DSM generation strategy identified and developed within this work.

Exploiting the image matching results, the elevation is computed, determining the corresponding 3D point on the ground using on reverse the mentioned orientation model.

2.2 The Innovative Procedure

This Section describes the workflow defined on the basis of the theory above illustrated, and implemented in C++ language in a Free and Open Source Software (FOSS), aimed at DSMs generation from optical and SAR satellite imagery.

The developed tool, named Digital Automatic Terrain Extractor (DATE), is conceived as an OSSIM plug-in¹. DATE is a totally automatic console application whose development started in summer 2014 in the framework of 2014 Google Summer of Code, within a project entitled "Photogrammetric image processing: DSM generation tool for OSSIM" (12), and went on for three years. The implemented tool is based on a hybrid procedure, whereby photogrammetric and computer vision algorithms are mixed in order to take the best of both. The synergy between computer vision and photogrammetry has taken hold over a decade ago and it has already returned outstanding results (36). As outlined, the main goal was to develop a fully automatic, effective, efficient and reliable tool for DSM generation from satellite imagery, paying special attention in finding a solution for the epipolar resampling for images acquired by optical and SAR satellite sensors: this is performed in the object space thanks to the images ground projection (see Section 2.2.1), and it is based on a roto-translation transformation model for GrEI generation (see Section 2.2.2) and on a coarse-to-fine pyramidal scheme.

The strategy is based on two well-known assumptions. First of all, assuming to have two or more satellite images acquired over the same area, if we know exactly the orientation for each image and we know perfectly the morphology of the area (DSM), all these images orthorectified using this DSM produce equal orthoimages in the same reference frame, apart from local occlusions and radiometric differences. Secondly, it is well-known that satellite pushbroom sensors acquire different images on the same orbit (including stereopairs and triplets) with smooth changes of attitude over time: these changes can be modelled with low-degree polynomial functions (usually up to third degree), so that the images can be reprojected in a quasi-epipolar geometry ((44), (37), (10)), without making use of the rigorous epipolar geometry, that is not straightforward with imagery acquired by pushbroom sensors, differently from standard imagery with one projection center only. Moreover, it is important to underline that potential orientation errors can be previously corrected with ground information (GCPs), so that orthorectification errors are mainly due to DSM inaccuracy.

Therefore, the leading idea is that the orthoimages generated using an a-priori (known, but generally coarse) DSM are affected by local pixel disparities lined up in a prevailing direction. For instance, in the simplest case of an along-track stereopair, this direction is still along the projection of the orbit on the ground, that is approximately North-South, considering the nominal keplerian elements of the orbits of the optical and SAR Earth observation satellites. These orthorectified images are the GrEI. The idea is to iteratively refine the a-priori DSM until the disparities are reduced as much as possible, theoretically to zero: the obtained DSM at each iteration is just the input for the following one. Of course, DSM errors can cause also transversal parallaxes with respect to the mentioned prevailing direction,

¹OSSIM is a FOSS4G that belongs to the wide OSGeo family and shows up as a set of libraries and applications for image, maps and terrain data processing, photogrammetric and remote sensing applications.

hindering the quasi-epipolarity condition and the DSM iterative refinement. Therefore, it is important to keep the transversal parallax errors well below the imagery resolution at each iteration; this is achieved adopting a coarse-to-fine pyramidal scheme. Following the good results of previous works (such as (50), (19), (41)), a classical coarse-to-fine pyramidal scheme (Figure1) is adopted to take advantage of an iterative solution based on multi-resolution imagery approach: intermediate DSMs at multiple resolutions are obtained, and matches at low-resolution serve as approximations to restrict the search space. Raw satellite images

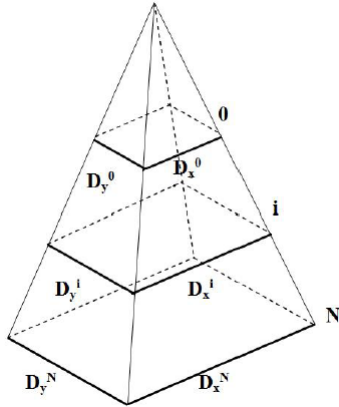


Figure 1. Image pyramidal approach

resolution is initially reduced by a downsampling factor that usually ranges between 20 and 10, then these sampled images are projected in a ground geometry using an a-priori (freely available) DSM, in order to generate orthorectified images with a transversal parallax error below the initial reduced resolution. These orthorectified images, after some proper transformations (see Section 2.2.2), can act as GrEI and can undergo a dense image matching procedure at the chosen reduced resolution, obtaining the final DSM corresponding to the first pyramidal level; this DSM is the input for the next pyramidal level, acting as the new a-priori DSM. The procedure is iteratively applied, increasing the resolution when passing from a pyramidal level to the next one, until the desired final resolution is achieved. In this way, a large parallax error is avoided (or however contained well below the current resolution) and the quasi-epipolar geometry is more easily achieved at each pyramidal level. It is quite evident that in this way, at lower resolution it is possible to detect larger structures (low frequency) whereas at higher resolutions small details are progressively added to the already obtained DSM. The advantage of the pyramidal approach is the high success rate in matching in the lower-resolution images at the top of the pyramid, thanks to their reduced size and implicit smoothing. In propagating through the pyramid, matching continues until the highest desired resolution is reached.

Summing up, the workflow implemented at each pyramidal level consists of the following steps:

- images ground projection
- GrEI generation
- dense image matching and disparity map generation
- DSM generation

Each processing step is hereafter described in order to analyse its peculiarities and its importance within the whole workflow.

2.2.1 Images ground projection As already outlined, the first step implemented is the image ground projection: raw satellite images are projected in a ground geometry, thanks to RPCs provided by the vendors along with the images, using a coarse DSM (e.g. SRTM, ASTER GDEM, AW3D30) or other freely available DSMs for the area of interest (Figure2).

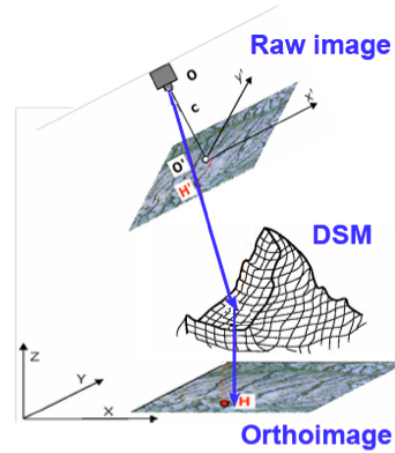


Figure 2. Image ground projection

Compared to classical approaches, here the quasi-epipolarity is achieved in the object space, producing an easier procedure for DSM generation. In some previous works, such as (20), a constant height plane is used for images projection, but in general it is better to know the elevation range of the area the scenes covered, in order to improve the accuracy of the generated epipolar lines.

Thanks to its modular structure, DATE is easily upgradable to upcoming sensors, since it is sufficient to format in a standardised way the images metadata files, in order to be able to manage images from new satellites. It might happen that satellite images (e.g. many of the SAR images) are not supplied with RPCs. In this case they can be generated. In this respect, for the TerraSAR-X imagery used for the tests, not equipped by vendors with RPCs, SISAR, a software developed at the Geodesy and Geomatics Division, University of Rome “La Sapienza” (6), has been exploited. It is able, among the other things, to generate RPCs starting from the rigorous sensor model, exploiting a terrain-independent approach. The procedure to generate the RPCs implemented within SISAR includes three main steps illustrated in (6).

If the orientations of all the images were fully consistent, so that also all the images relative orientation would not display global transversal parallax errors at the considered resolution, the orthorectified images generated in this way could be considered as GrEI at each pyramidal level, and they would satisfy the quasi-epipolar condition. It is, however, always needed an additional check for the estimation of a possible additional transformation to align the images for the actual GrEI generation. Furthermore, the scan direction as well has to be taken into account, in order to correctly rotate the images and achieve the quasi-epipolar geometry.

2.2.2 Ground quasi-Epipolar Imagery (GrEI) generation

In order to carry out the dense matching, it is necessary to align the ground images in the quasi-epipolar geometry. At first, a preliminary approximate rotation is estimated for both images, in

order to take into account the scan direction and orientate them in the disparity prevailing direction. This is performed according to forward and inverse RPF, on a square image grid 10×10 . Consider the point P_1 on the grid in Figure3 in the master image, and project it by inverse RPF (image-to-ground transformation) at two heights h_{max} and h_{min} (respectively the maximum and minimum heights of the analysed area), giving respectively P'_1 and P_3 . Then P_3 is forward projected onto the slave image giving P_2 ; P_2 is then inverse projected at h_{max} giving P'_2 .

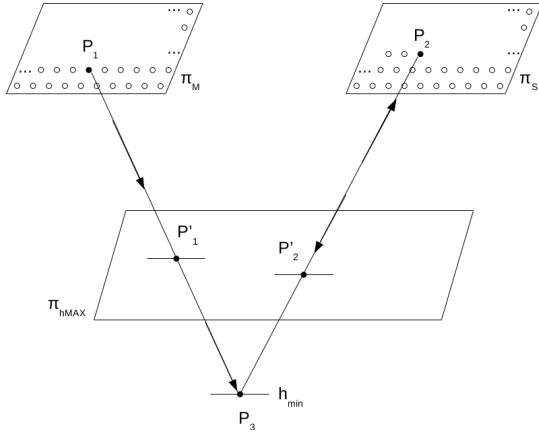


Figure 3. Procedure for P'_1 and P'_2 identification

The points P'_1 and P'_2 , both at height h_{max} , are considered for the computation of the rotation angle that takes into account the orientation of the satellite scan direction. As a matter of fact, the vector $P'_1 - P'_2$ define the quasi-epipolar direction in object space (as a matter of fact its direction is basically constant throughout the image), and thus the α angle (azimuth with respect to the North) to be applied to the images to let them act as GrEI (Figure4).

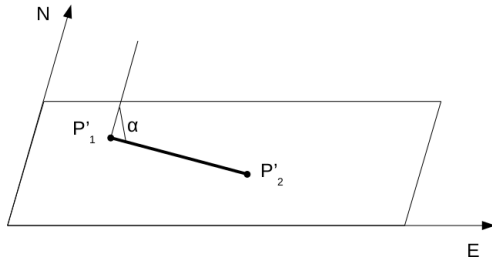


Figure 4. Procedure for α angle identification

The applied azimuth is the mean of those obtained over the grid points. This approach works both with along and across track data, and no additional information is needed apart from RPCs. Then, as a second step, a refinement of the images relative position is performed. This is done by estimating, thanks to a set of well-identified TPs and according to the equation (1), a residual rotation and a translation to be applied to the slave image, in order to correct possible residual roto-translations between master and slave images due to RPCs inaccuracy:

$$\begin{cases} x' = \cos\theta(x + D) + \sin\theta(y) \\ y' = -\sin\theta(x + D) + \cos\theta(y) + Ty' \end{cases} \quad (1)$$

Orthoimages are aligned in the disparity prevailing direction and, applying the model in equation 1, a potential shift (mean rotation and transversal parallax), caused by systematic error in the image relative orientation based on metadata RPCs, is removed. As a matter of fact, the model takes into account that each TPs can

have a whatever disparity value on the x coordinates, in order to return null y mean transversal parallax. The model is clearly non-linear, and it should be linearised as follows in order to be solved with a least squares approach. Under the hypothesis of small rotation angle ($\theta \simeq 0$), the following expressions are obtained:

$$\begin{cases} x' = (x + D) + \theta(y) \\ y' = -\theta(x + D) + y + Ty' \end{cases} \quad (2)$$

By linearising with respect to the disparity D using the median disparity as approximated value $\tilde{D} = D_{med}$, the equations become:

$$\begin{cases} x' = x + (\tilde{D} + \delta D) + \theta(y) \\ y' = -\theta x - \theta\tilde{D} - \theta\delta D + y + Ty' \end{cases} \quad (3)$$

As $\theta\delta D$ is a second-order term, it is possible to simplify and order the other terms as follows:

$$\begin{cases} x' = (x + \tilde{D}) + \delta D + \theta(y) \\ y' = y - \theta(x + \tilde{D}) + Ty' \end{cases} \quad (4)$$

The model can be written in a matrix form considering a set of n TPs:

$$y = \begin{bmatrix} x'_1 \\ y'_1 \\ \vdots \\ \vdots \\ x'_n \\ y'_n \end{bmatrix} \quad \mathbf{A} = \begin{bmatrix} y_1 & 0 & 1 & \dots & 0 \\ -(x_1 + \tilde{D}_1) & 1 & 0 & \dots & 0 \\ \vdots & \vdots & \vdots & \ddots & \vdots \\ \vdots & \vdots & \vdots & \ddots & \vdots \\ y_n & 0 & 0 & \dots & 1 \\ -(x_n + \tilde{D}_n) & 1 & 0 & \dots & 0 \end{bmatrix}$$

$$x = \begin{bmatrix} \theta \\ Ty' \\ \delta D_1 \\ \vdots \\ \delta D_n \end{bmatrix} \quad b = \begin{bmatrix} x_1 + \tilde{D}_1 \\ y_1 \\ \vdots \\ \vdots \\ x_n + \tilde{D}_n \\ y_n \end{bmatrix}$$

where x'_i, y'_i are TPs master coordinates; x_i, y_i are TPs slave coordinates; D_i is the disparity value in each point; \tilde{D}_i is the approximated value of disparity D , chosen as the median disparity D_{med} ; θ is the mean rotation angle; Ty' is the y mean transversal parallax; δD_i is the correction to the approximated value of disparity D in each point.

In particular, the TPs are homogeneously identified and matched on the orthoimages, exploiting Scale-Invariant Feature Transform (SIFT)-oriented OpenCV library algorithms and an OpenCV class, named Grid Adapted Feature Detector, adapting a detector to divide the source image into a grid and detect points in each cell (Figure5).

After the TPs identification phase, a specifically designed filter is employed to select only the most reliable TPs: first the 2% of the most reliable points is selected based on the higher feature descriptor values (representing a keypoint invariant description used to describe the similarity level between the matched points), computed with the Brief Descriptor Extractor OpenCV algorithm. Then a parallax threshold is set up in the y -direction in order to discard, among the remaining TPs, the points with the highest parallax values. At the end, a 3-sigma test is performed



Figure 5. TPs distribution for a GeoEye-1 stereopair tile before filtering (globally 500 TPs were automatically selected)

in order to remove residual outliers. As shown in Figure 6, after this thorough filtering chain, only the most reliable TPs are kept. The TPs identification step with a SIFT-oriented algorithm is performed also in SAR imagery: as a matter of fact, as stated in (43), this is a robust alternative for point feature based registration of SAR images (mainly for radargrammetric than interferometric applications), as subpixel registration consistency is generally achieved thanks to the algorithm robustness in the face of occlusion, clutter and noise (27).

2.2.3 Dense image matching and disparity map generation

To generate high resolution DSMs, in the last years methods first developed in computer vision, based on epipolar imagery and dense stereo matching ((42), (22), (26), (15)), have been more and more exploited (39). For a long time, local correlation-based matching methods dominated photogrammetry. Due to the size of the correlation window, resulting surface models have a lower spatial resolution than the input images, fine structures are lost and object boundaries are smoothed. In contrast, global methods allow pixel-wise matching, which is guided by a global smoothness constraint. The resulting DSMs have the same resolution as the input images, but global methods typically show a high processing time (48). The Semi-Global Matching (SGM) algorithm by Hirschmüller (22), performing matching of corresponding pixels along the epipolar lines, provides a very good trade-off between accuracy and processing speed. Moreover, the search range can be limited thanks to the initial projection using the a-priori DSM, which allows to shrink the dense matching search range, and lower the time needed for the process.

In order to compute a disparity map for the stereopair at each pyramidal level the SGM algorithm is used, as implemented in the OpenCV library. This is actually the Semi-Global Block Matching (SGBM) algorithm, that differs from the original one for considering only 5 search directions for cost aggregation instead of 8 (even if it is possible to run the full variant of the algorithm, yet consuming a lot of memory), for matching not individual pixels but blocks of pixels (even if, changing the default parameters, it is possible to reduce the blocks to single pixels) and for having implemented a simpler Birchfield-Tomasi sub-pixel metric (3) instead of a Mutual Information (MI) cost function (46).

It must be recalled that, for how it is implemented, the OpenCV SGBM code only allows the use of 8-bit images, instead of the 11-, 12- or 16-bit satellite imagery. This could lead to a compression of the range of radiometric values. Nevertheless, the majority of satellite images indeed presents a non uniform and mostly compressed radiometric distribution. The idea is to use the OpenCV SGBM having preliminarily reduced the bit depth,

considering a 95th percentile and successively scaling the image radiometry between 0 and 255. For the majority of the satellite images this leads to a negligible loss of radiometric information. As a matter of fact, for example, in the case of an 11-bit image such as GeoEye, the 95% of values is in the range 70-370 (Figure 7). So, in this case, starting from the 2048 nominal values, just about 300 of them are used, that is a value much more close to an 8-bit than to an 11-bit image. At the moment, this approximation is considered acceptable, given the SGBM high performances in terms of efficiency.

Note that, using the GrEI, the disparity maps obtained at each pyramidal level are in the same reference frame of the a-priori DSM, and the local pixel disparity values are proportional to the height correction that will be applied to the a-priori DSM (see Section 2.2.5).

In Figure 8, an example of a disparity map computed from Pléiades imagery on the Trento test site, is reported. Some unmatched areas are visible, due to occlusions and shadows: as a matter of fact, in general, DSMs which are automatically generated with stereo satellite image matching procedures, tend to have many null locations, called voids or holes, since occlusions especially in urban scenes result in some deficiencies in the stereo matching phase (2). In Section 2.2.5 is explained how these holes are handled.

2.2.4 SAR disparity map masking and fusion In the case of SAR imagery, an additional masking and merging step is carried out. As a matter of fact, when dealing with SAR imagery, it is quite common to have available both an ascending and a descending stack of multiple images for an analysed area, that implies having two different points of view generating dissimilar layover and foreshortening regions, geometric distortions typical for SAR images (30). Then, with the aim to improve the final DSM, the idea is to not consider one stack's distorted areas and masking them out, considering for that distorted region only what is acquired with the other stack, and vice versa, in order to globally eliminate layover and foreshortening regions, without compromising DSM completeness.

The method is based on the generation of a SAR simulated image for each acquired image, by means of image metadata and of an available (even coarse) DSM covering the area of interest (45). To this purpose, a specific DATE functionality has been developed, in order to generate simulated images to be applied as masks for filtering layover and foreshortening areas of each stack. A SAR image can be simulated combining topographic data (DSM) with a set of platform/sensor parameters which describe the scene acquisition geometry. The simulation process is

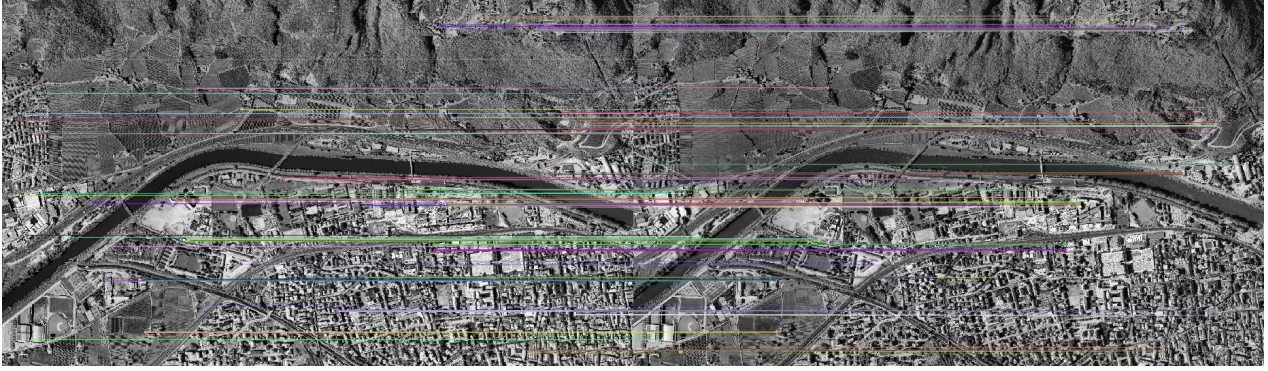


Figure 6. TPs distribution for a GeoEye-1 stereopair tile after the filtering phase (globally 128 TPs were automatically finally accepted)

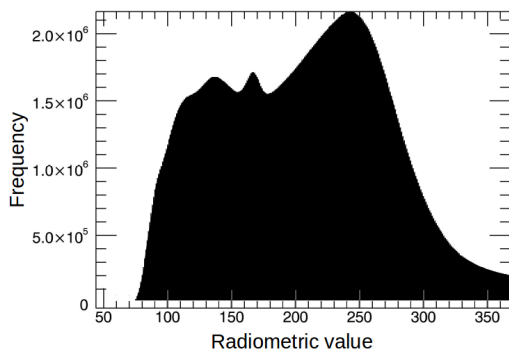


Figure 7. Radiometric histogram for GeoEye imagery



Figure 8. Disparity map from Pléiades imagery

very similar to the SAR orthorectification process based on the two radar equations, i.e. zero-Doppler and slant range constraint (31). The aforementioned equations are applied with an inverse projection approach, i.e. from ground coordinates to image coordinates in slant range (assuming a homogeneous land cover). As shown in Figure9, the starting step is the creation of a regular grid in ground coordinates, where a unique radiometric value is assigned to each raster image cell. The elevation information of each cell is retrieved from the available DSM, and then projected, through the SAR model, in the slant range plane. The radiometric value assigned to each simulated image cell is the sum of ground cells which are projected into the same slant range image coordinates. It can be highlighted that, therefore, in the simulated SAR image, the radiometric value is lower in dark zones where there is no a sum effect, while in correspondence of white spikes, where the well-known SAR deformations occurs, it is higher: as a matter of fact, areas characterized by layover and foreshortening

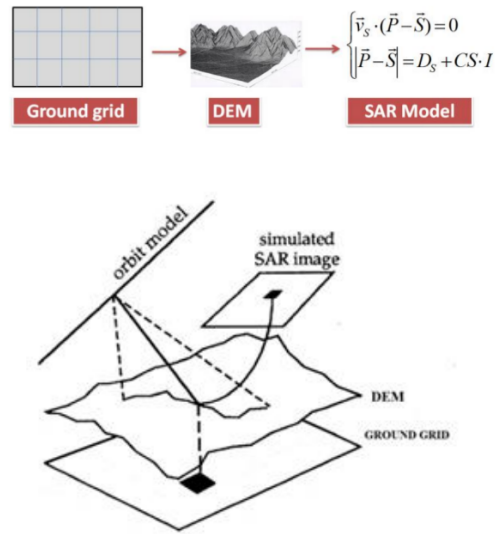


Figure 9. SAR simulation model

lead to many ground cells being projected in the same simulated cell, producing high radiometric values. Each simulated image can therefore be considered as a weighting mask. A global mask is generated for each stack, as a sum of the contribution of each image of the stack. The disparity maps are then merged according to these ascending and descending masks, and the final pixel values are obtained with a weighted computation of the contribution of each disparity map, according to Equation 5 (14). In such a way, a global, more accurate, and complete DSM is generated exploiting all the information available from the stack.

$$h_{i,j} = \frac{(\alpha\sigma_{asc} + \beta d_{asc})^{-1}}{(\alpha\sigma_{asc} + \beta d_{asc})^{-1} + (\alpha\sigma_{desc} + \beta d_{desc})^{-1}} \mu_{asc} + \frac{(\alpha\sigma_{desc} + \beta d_{desc})^{-1}}{(\alpha\sigma_{asc} + \beta d_{asc})^{-1} + (\alpha\sigma_{desc} + \beta d_{desc})^{-1}} \mu_{desc} \quad (5)$$

where $h_{i,j}$ = pixel merged height value
 σ_{asc} = height standard deviation for the asc. stack
 σ_{desc} = height standard deviation for the desc. stack
 μ_{asc} = height median value for the asc. stack
 μ_{desc} = height median value for the desc. stack
 d_{asc} = mask of the asc. stack
 d_{desc} = mask of the desc. stack
 α = weight for standard deviation contribution

β = weight for mask contribution

Disparity maps merging could be done also for optical images, particularly to exploit multi-view data from tri-stereo acquisitions, useful to minimise areas that cannot be reconstructed due to occlusions, e.g. in urban areas where a lower convergence angle is of advantage (see Figure10), or to eliminate outliers. The merging procedure implemented for the optical dataset is described in Section 3.2.1.

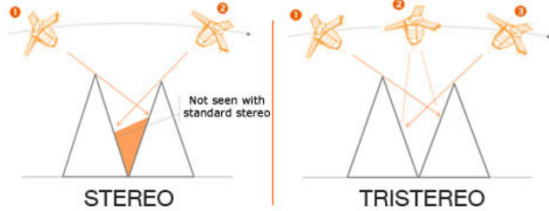


Figure 10. Benefit of a tri-stereo acquisition

2.2.5 DSM generation Generally, to obtain a DSM from stereo image pairs, homologous points are firstly automatically matched on the images; then these points are mapped by forward intersection, according to the images orientation model, into the object space and the DSM is retrieved from these points by triangulation and interpolation.

Since the disparities are computed in the object space, this step can here be avoided, it is now sufficient to sum them to the coarse DSM used as a reference for the initial projection, to obtain the final DSM. But first, the obtained local pixel disparity values have to be converted into height corrections with respect to the used a-priori DSM, through an efficient procedure based on the computation of a disparity-to-height conversion factor (C_{factor}), exploiting RPCs-based orientation model (Figure11).

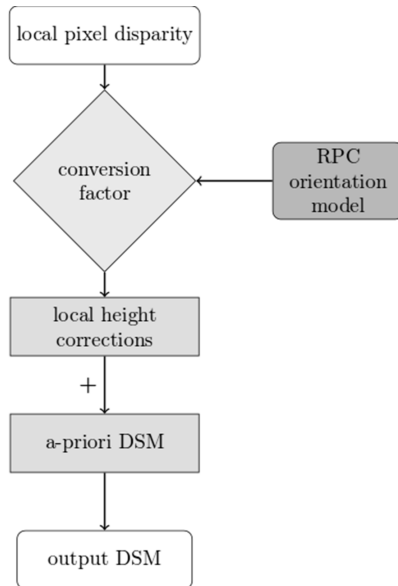


Figure 11. General workflow from pixel disparity to generated DSM

In particular, a constant C_{factor} is computed starting from the metadata RPCs, exploiting the procedure for the preliminary α rotation angle computation, aimed at the images alignment in the disparity prevailing direction for epipolar geometry achievement

(see Section 2.2.2). As a matter of fact, the C_{factor} is obtained dividing the magnitude of the vector $P_1 - P_2$ (see Figure4) to the height variation ($h_{max} - h_{min}$): the final C_{factor} used to transform pixel disparities to height corrections is just the mean of the values obtained over the 10×10 above mentioned grid:

$$C_{factor} = \frac{1}{100} \sum_{k=1,100} \frac{\sqrt{(\Delta E_k)^2 + (\Delta N_k)^2}}{\Delta h_k} \quad (6)$$

where C_{factor} is the disparity-to-height conversion factor; ΔE_k is the difference in the object space (at h_{max}) in East coordinates between two given points; ΔN_k is the difference in the object space (at h_{max}) in North coordinates between two given points and Δh_k is the height difference considered ($h_{max} - h_{min}$). It has been checked that the height variation set ($h_{max} - h_{min}$), has no appreciable influence on the final C_{factor} value nor on the preliminary rotation angle computation. As a matter of fact, both using a small height variation (e.g. 50 m) or the height variation of the entire analysed tile (in this case about 2000 m), retrievable from the coarse DSM, the final C_{factor} value does not change significantly.

The obtained height corrections are then summed up to the height of the a-priori DSM at each pyramidal level iteration. At the moment, in the no-matched areas, such as the black ones in Figure8, the SRTM value is left unchanged without summing up any height correction.

As last step of the deployed workflow, the geocoded DSM is saved in a standard geotiff format, exploiting OSSIM file handling functionalities.

3. RESULTS ASSESSMENT AND ANALYSIS

3.1 DSM assessment methodology

As well the software used for the DSM assessment has been specifically developed; it is written in Python Programming Language and it is based on some well-known libraries such as NumPy, SciPy, Matplotlib, GDAL.

The statistics used for the DSMs assessment, are those usually adopted for the assessment of the global DSMs (as SRTM, ASTER, TANDEM-X DSMs) ((40), (18)). The height accuracy (or vertical accuracy) is estimated in a 2.5D approach by the Root Mean Square Error (RMSE) of the DSMs. RMSE is the square root of the average of the squared differences between the height values of the DSM under evaluation, and the height values from another source (reference DSM) with higher accuracy (in this case a DSM from a LiDAR survey is used):

$$RMSE = \sqrt{\frac{1}{n} \sum_{i=1}^n (Z_{DSM,i} - Z_{REF,i})^2} \quad (7)$$

where n is the number of points being checked, $Z_{DSM,i}$ and $Z_{REF,i}$ are, respectively, the height values of the model and of the reference DSM. Together with the RMSE, the bias, the standard deviation and the Linear Error 95 (LE95) are calculated.

3.2 Results assessment

This innovative procedure, has been tested with Pléiades-HR and GeoEye-1 high-resolution satellite optical imagery and with SAR imagery acquired by TerraSAR-X platform. To show and analyse

DATE behaviour and performance, DSMs in areas with different land use/land cover and morphology as well as for the whole image footprint, have been generated and evaluated for the optical satellite data. All the three datasets are related to the same test site, which is the area of Trento. Located in the Northeast part of Italy, the test site lies in a valley at an average altitude around 200 m, surrounded by very steep slopes and Alps peaks up to 2000 m. It includes urban areas with residential, industrial and commercial buildings with different sizes and heights, agricultural and forested areas, offering, therefore, a very heterogeneous landscape in terms of morphological complexity, land use, and land cover (1).

In order to assess the obtained results, a 2.5D comparison, following the theory illustrated in the previous subsection, with respect to a reference DSM, is performed. The reference dataset used in this work to assess the generated DSMs, is a LiDAR DSM with grid posting 1.0 x 1.0 m and a mean elevation accuracy of 0.25 m, freely available on the website of “Provincia Autonoma di Trento” (<http://www.territorio.provincia.tn.it>).

3.2.1 Results for the optical dataset The analysed optical data set consists of three along-track Pléiades-HR and two along-track GeoEye-1 optical images.

The images composing the Pléiades-HR triplet, hereafter called image 01, image 02, and image 03, were acquired in August 2012 in North-South scan direction. The average incidence angles of the three images are, respectively, 13°, -13°, and -19° in along-track direction with respect to the nadir, and close to 0° in across-track direction. Thanks to the fast scanning, the illumination conditions are almost constant during the acquisitions. The data include metadata files together with their original RPCs. The dataset covers an area of about 392 km². The native mean GSD varies between 0.72 and 0.78 m depending on the viewing direction, even if the images are oversampled and supplied to the user with a 0.50 m GSD. The three images will be analysed by pairs, testing all possible combinations, this is:

- pair 1, composed by images 01 and 03
- pair 2, composed by images 01 and 02
- pair 3, composed by images 02 and 03

The GeoEye-1 stereopair has been acquired in September 2011 and shows 100% overlap; it is provided as GeoStereo product, that is, the images are projected to a constant base elevation. The available bands are the panchromatic one and four multispectral bands (blue, green, red, and near-infrared). The images cover an area of 100 km² with a GSD equal to 0.50 m. For each image the metadata RPCs were provided too.

The DSMs have been generated with a cell grid at 1.0 x 1.0 m, since it has been seen, through some experimental tests, that increasing further the resolution in the pyramidal scheme no valuable information, only noise, is added to the final extracted DSM. In order to evaluate the optimal DSM resolution in relation to the raw image resolution, it is important to consider that the inputs of the SGBM are the GrEI. GrEI are generated starting from the full resolution raw images, and, to correctly choose the DSM final resolution, the maximum information transferable during this re-projection process should be taken into account (8). In this sense, all the radiometric information content of the full resolution imagery is exploited reaching 1 m resolution.

In particular, the entire tile, an urban, a mainly flat (even if in this scene it is difficult to find a wide flat area) and a mountainous

areas are analysed. The urban tile is characterised by small adjacent buildings and narrow streets, whereas the mountainous one by very steep slopes.

As far as concerns the Pléiades-HR stereopairs, the statistic parameters trend is the same for each pair: higher standard deviation values for the whole, the urban and the mountain tile, lower values for the flat tile. In Table 1 the results for each Pléiades DSM for the different areas analysed are reported, together with the statistics for the merged DSM. As a matter of fact, a merging procedure has been applied in order to exploit the redundant information from the tri-stereo acquisition. The 3 generated DSMs have been merged, giving them a different weight percentage on the basis of the images intersection angles: a smaller intersection angle implies a weaker acquisition geometry (and thus a lower reliability in terms of reconstruction accuracy), whereas a larger one entails a stronger geometry (and a higher reliability in terms of reconstruction accuracy). On the contrary, pairs with small intersection angles can give a significant contribution to the DSM completeness, since occlusions are reduced, especially in the urban area. In general, a better accuracy is achieved in the flat area,

Analysed area	RMSE	St.dev.	Bias	LE95
	(m)	(m)	(m)	(m)
Whole tile pair 1	4.35	4.35	0.03	15.16
Whole tile pair 2	4.25	4.23	0.37	14.70
Whole tile pair 3	5.63	4.34	-3.60	13.83
Whole tile merged DSM	4.10	4.09	-0.27	14.01
Urban tile pair 1	4.80	4.78	0.48	15.85
Urban tile pair 2	4.83	4.77	0.77	15.87
Urban tile pair 3	4.89	4.28	-2.36	13.20
Urban tile merged DSM	4.35	4.34	0.30	12.76
Flat tile pair 1	1.76	1.65	0.63	6.46
Flat tile pair 2	1.85	1.57	0.98	6.14
Flat tile pair 3	4.42	2.57	-3.60	6.28
Flat tile merged DSM	1.50	1.47	0.26	5.15
Mountain tile pair 1	4.82	4.77	-0.69	14.57
Mountain tile pair 2	4.70	4.70	-0.17	14.29
Mountain tile pair 3	5.16	4.33	-2.81	11.91
Mountain tile merged DSM	4.29	4.25	-0.54	12.24

Table 1. DSMs assessment for Pléiades dataset

whereas the mountain and the urban areas behave pretty much in the same way. Moreover, it is evident that DSM from pair 3 shows always a very high bias with respect to the other 2 pairs. Furthermore, it is quite clear that with the merging procedure an improvement both in the statistical parameters and in the completeness level (see Table 2) of the final DSM is achieved. With respect to the 3 DSMs, the Pléiades pair 3 shows the higher degree of completeness (> 99%), while for the other 2 DSMs it varies between 91% and 94%: this is due to the fact that pair 3 offers the lowest intersection angle and hence the dense matching performs much better. The merged DSM shows a completeness percentage slightly greater than DSM from pair 3.

Analysed DSM	Completeness (%)
Pair 1 DSM	91.34
Pair 2 DSM	94.17
Pair 3 DSM	99.03
Merged DSM	99.35

Table 2. Completeness level (entire tile)

In Table 3 the results for the GeoEye-1 DSM for the different areas are reported. In order to limit bias, RPCs have been corrected

based on a translation estimated on 45 GCPs. It can be seen that the mountain tile produces higher RMSE values than the others and the flat one the lowest. The standard deviation is around 4 m, apart in the flat tile where it is less than 2 m. Note that the bias is positive when the reference LiDAR height is above the extracted DSM.

	RMSE (m)	st.dev. (m)	bias (m)	LE95 (m)
Whole tile	4.89	4.29	-2.07	15.31
Urban tile	4.90	4.78	-1.05	15.62
Flat tile	1.74	1.70	-0.40	6.29
Mountain tile	5.74	4.81	-3.13	14.52

Table 3. DSMs assessment for GeoEye-1 dataset

A final remark concerns the a-priori DSM used for DATE processing; as mentioned, SRTM was used, so that the question arises if the iterative processing was really able to enhance the a-priori known morphology, adding details and increasing the accuracy. This was certainly the case since the SRTM accuracy over the whole area is around 10 m, and in the urban tile it is around 6 m, values close to those presented in (17) for very similar situations in a very close (approximately 50 km far away) location.

Some investigations to evaluate Pléiades-HR and GeoEye-1 datasets on Trento test site have been carried out in recent years ((1), (5), (38)): the results here obtained outperform by about 10-20% those presented in these works, and this confirms the quality of the developed workflow. However, it is necessary to underline that DATE shows high performances also in terms of efficiency: as a matter of fact, as illustrated in (13), it is about 3 times faster than other well-known commercial software packages.

3.2.2 Results for the SAR dataset Here the results obtained with two stacks (one ascending and one descending) of three TerraSAR-X images each, acquired over Trento test site in January 2011, all with a right look side (Table 4), are discussed.

Sensor	Acquisition date	Incidence angle [°]	Orbit	Look side
TD-X	21/01/2011	54	Asc	Right
TS-X	22/01/2011	31	Asc	Right
TD-X	16/01/2011	44	Asc	Right
TS-X	19/01/2011	24	Desc	Right
TS-X	14/01/2011	39	Desc	Right
TS-X	20/01/2011	50	Desc	Right

Table 4. TerraSAR-X imagery specifications

In order to be able to process the TerraSAR-X images with DATE, RPCs have been generated with SISAR (10). A 3D grid of $10 \times 10 \times 12$, to discretize the volume to be investigated, is used. To be sure that no significant error is introduced with the RPCs use with respect to the zero Doppler SAR model, an assessment using the TPs supplied by the vendors and available in the metadata files, is carried out for each image. A standard deviation in the order of 10^{-3} pixel is obtained; this means that, for all the images, the zero Doppler model is very well preserved by the generated RPCs.

Overall, 6 pairs were analysed, 3 from the ascending stack and 3 from the descending one, using all the possible images combination and always adopting as master the image with the lower incidence angle. The results obtained from the ascending stack are reported in Table 5 and those from the descending stack in Table 6.

	RMSE [m]	st.dev. [m]	bias [m]	LE95 [m]
DSM 31°-44°	7.48	6.52	3.67	17.97
DSM 31°-54°	7.12	6.24	3.42	17.45
DSM 44°-54°	6.66	6.16	2.52	17.31

Table 5. DSMs assessment for TerraSAR-X ascending dataset

	RMSE [m]	st.dev. [m]	bias [m]	LE95 [m]
DSM 24°-39°	6.21	6.21	-0.11	18.39
DSM 24°-50°	5.84	5.84	0.25	16.75
DSM 39°-50°	5.85	5.80	0.76	16.61

Table 6. DSMs assessment for TerraSAR-X descending dataset

It is evident that the results obtained with the descending stack are quite better than the statistical parameters achieved with the ascending one, both in terms of bias and standard deviation. Besides, a high bias for the DSMs generated from the ascending stack is present. This bias is not compliant with the absolute geolocation accuracy of the zero Doppler SAR model (11); these anomalous results have to be investigated in the future. Note that the bias is positive when the reference LiDAR height is above the extracted DSM.

The statistical results achieved through the merging procedure illustrated in Section 2.2.4 are presented in Table 7. The final DSM has been generated with a cell grid at 8.0×8.0 m resolution.

	RMSE [m]	st.dev. [m]	bias [m]	LE95 [m]
Final DSM	6.13	5.85	1.85	16.61

Table 7. Merged DSM assessment for TerraSAR-X dataset

The height discrepancies histogram of the merged DSM is reported in Figure12 and the error map is shown in Figure13.

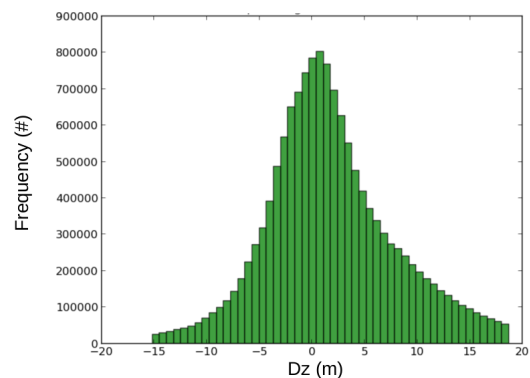


Figure 12. DSM height discrepancies histogram for TerraSAR-X imagery

4. CONCLUSIONS AND FUTURE INVESTIGATIONS

4.1 Conclusions

In this thesis an original procedure for DSM generation from optical and SAR satellite imagery has been defined. In particular, an innovative strategy in order to obtain the quasi-epipolar imagery from the raw satellite images has been identified and illustrated. As a matter of fact, a crucial point is the epipolar resampling for

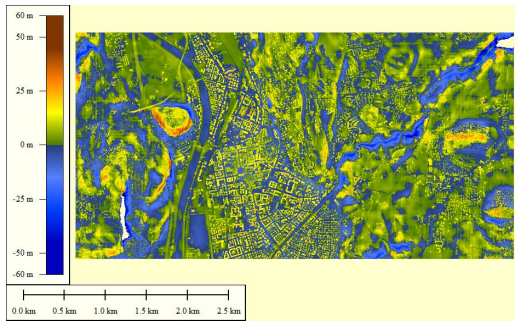


Figure 13. Error map of the merged DSM obtained from TerraSAR-X imagery

satellite images, which it is not straightforward, due their multiple projection centers.

The strategy for the epipolar resampling for satellite imagery relies on a preliminary ground projection using an a-priori DSM (such as SRTM, a coarse and freely available global DSM), thanks to which the search space for the successive dense matching is significantly restricted. Then, an approximate rotation is computed through RPCs, in order to align the images in the disparity prevailing direction. Afterwards, a roto-translation is estimated, thanks to a set of well-identified Tie Points, and applied, to refine the images relative orientation and to achieve the epipolar geometry: these orthorectified images can act as GrEI and can undergo a dense image matching procedure. Furthermore, in order to be able to keep the transversal parallax errors well below the imagery resolution, a coarse-to-fine pyramidal scheme is adopted: this allows to iteratively refine the a-priori DSM until the desired final resolution is achieved. The final DSM at each pyramidal level is the input for the next pyramidal level, acting as the a-priori DSM. In this way, at lower resolution it is possible to detect larger structures, whereas at higher resolution small details are progressively added to the already obtained DSM.

Relying on this strategy for epipolarity resampling, an effective, efficient, reliable, automatic and open source software (freely available at the URL of the GitHub repository https://github.com/martidi/opencv_dsm/tree/imageStack), named DATE, for DSM generation from optical and SAR satellite imagery, has been developed and implemented in C++ programming language. DATE is able to perform a complete photogrammetric and radargrammetric processing chain, starting from the raw satellite images and their RPCs. The tool exploits some algorithms coming from computer vision. Some functions of the free and open source library OpenCV have been adapted and used. Specifically, as far as concerns the automatic TPs identification for GrEI generation, algorithms for feature points detector and descriptors have been used. Furthermore, the SGM as implemented in OpenCV library has been adopted for disparity maps generation. This hybrid procedure does not undermine the rigorous photogrammetric approach; photogrammetry and computer vision are mixed in order to take the best of both, exploiting their capabilities in a synergistic way. Indeed, in the last years, algorithms first developed in computer vision are increasingly used in photogrammetric applications.

In order to evaluate the proposed strategy, both optical and SAR satellite datasets have been assessed over the same Trento test site, located in Northern Italy. The accuracy evaluation has been carried out comparing the DSMs extracted to a more accurate reference DSM obtained with LiDAR technology. In particular, three along-track Pléiades-HR and two along-track GeoEye-1

optical images have been analysed, along with two SAR stacks (one ascending and one descending) of three TerraSAR-X images each. For the TerraSAR-X imagery, not provided with RPCs by vendors, RPCs have been generated according to a terrain-independent scenario.

For the optical dataset, overall RMSE values less than 6 m are achieved, with some differences showed according to the prevailing land cover: as a matter of fact, for the flat tile the RMSE even reaches 1.5 m (depending on the analysed pair), whereas for the urban tile it even reaches 4.3 m. For Pléiades-HR and GeoEye-1 imagery the statistic parameters trend is the same, even if the GeoEye-1 dataset performs a bit worse than Pléiades-HR: this is probably due to the merging procedure applied to Pléiades DSMs that improves the overall results. It is quite clear that with the merging procedure an improvement both in the statistical parameters and in the completeness level of the final DSM is achieved. In general, by visual inspection, the terrain profile obtained appears well modelled, both for GeoEye-1 and Pléiades-HR derived DSMs, even if with quite different level of completeness. Moreover, these results, in terms of RMSE, are better by about 10-20% compared to those obtained by other authors in previous works on the same test site. Furthermore, DATE shows high performances also in terms of computational efficiency.

As far as concerns the SAR dataset, results from the ascending and the descending stacks have been analysed: quite better results, with RMSE even less than 6 m and almost no bias, are achieved with the descending stack, while the ascending stack shows a RMSE of about 7.5 m and a high bias, not compliant with the absolute geolocation accuracy of the zero-Doppler SAR model. Instead, exploiting all the available DSMs in the merged DSM, global accuracy around 6 m is achieved, with a much higher completeness.

These results are compliant with the accuracy required in several applications such as canopy volume and density estimation, urban volumes computation, emergency mapping, etc. Furthermore, as far as some active and passive high resolution data are freely available (e.g. the Sentinel constellation), a massive processing of such data, exploiting DATE capabilities, could contribute to the generation of an open source DSM, allowing, in the meantime, thanks to the revisiting time of the satellite, to produce also multitemporal analysis able to detect ground changes.

4.2 Future Investigations

As future works, in order to process at the same time a large number of stereopairs, also acquired by various satellites in different period of time, it could be worthwhile, at the dense matching step, to generate a fused cost volume by merging the single cost volumes obtained for each pair, so to get just one disparity map, instead of n disparity map to be fused.

Moreover, a regularization process for building reconstruction improvement, based on feature extraction, could be useful in order to properly shape all the buildings visible on the images.

Besides, a procedure to automatically generate bias-corrected RPCs, in order to check for potential bias removal, could be implemented.

REFERENCES

G. Aguiaro, D. Poli, F. Remondino. Testfield Trento: Geometric Evaluation of Very High Resolution Satellite Imagery. *International Archives of the Photogrammetry, Remote Sensing and Spatial Information Sciences*, 34(B1):191-196, 2012.

- Z.G. Bafghi, J. Tian, P. d'Angelo, P. Reinartz. A new algorithm for void filling in a DSM from stereo satellite images in urban areas. *ISPRS Annals of the Photogrammetry, Remote Sensing and Spatial Information Sciences*, 3(1):55-61, 2016.
- S. Birchfield, C. Tomasi. A pixel dissimilarity measure that is insensitive to image sampling. *IEEE Transactions on Pattern Analysis and Machine Intelligence*, 20(4):401-406, 1998.
- M.A. Brovelli, M. Crespi, F. Fratarcangeli, F. Giannone, E. Reolini. Accuracy assessment of high resolution satellite imagery orientation by leave-one-out method. *ISPRS Journal of Photogrammetry & Remote Sensing*, 63:427-440, 2008.
- P. Capaldo, M. Crespi, F. Fratarcangeli, A. Nascetti, F. Pieralice, G. Agugiaro, D. Poli, F. Remondino. DSM generation from optical and SAR high resolution satellite imagery: Methodology, problems and potentialities. *International Geoscience and Remote Sensing Symposium*, pp. 6936-6939, 2012.
- P. Capaldo, M. Crespi, F. Fratarcangeli, A. Nascetti, F. Pieralice. High-resolution SAR radargrammetry: a first application with COSMO-SkyMed SpotLight imagery. *IEEE Geoscience and Remote Sensing Letters*, 8(6):1100-1104, 2011.
- P. Capaldo, M. Crespi, F. Fratarcangeli, A. Nascetti, F. Pieralice. A radargrammetric orientation model and a RPCs generation tool for COSMO-SkyMed and TerraSAR-X high resolution SAR. *Italian Journal of Remote Sensing*, 44(1):55-67, 2012.
- M. Crespi, L. De Vendictis. A Procedure for High Resolution Satellite Imagery Quality Assessment. *Sensors*, 9:3289-3313, 2009.
- M. Crespi, F. Fratarcangeli, F. Giannone, F. Pieralice. High resolution satellite image orientation models. *Geospatial Technology for Earth Observation, Springer US*, pp. 63-104, 2009.
- M. Crespi, F. Fratarcangeli, F. Giannone, F. Pieralice. A new rigorous model for high-resolution satellite imagery orientation: application to EROS A and QuickBird. *International Journal of Remote Sensing*, 33(8):2321-2354, 2012.
- P. Capaldo, F. Fratarcangeli, A. Nascetti, A. Mazzoni, M. Porfiri, M. Crespi. Centimeter range measurement using amplitude data of TerraSAR-X imagery. *The International Archives of the Photogrammetry, Remote Sensing and Spatial Information Sciences*, 40(7):55-61, 2014.
- M. Di Rita. Photogrammetric image processing: DSM generation tool for OSSIM. <https://trac.osgeo.org/ossim/wiki/GsocDSMGenerationToolForOSSIM>, GSoc weekly reports, 2014.
- M. Di Rita, A. Nascetti, M. Crespi. Open source tool for DSMs generation from high resolution optical satellite imagery: development and testing of an OSSIM plug-in. *International Journal of Remote Sensing*, 2017, doi: 10.1080/01431161.2017.1288305.
- M. Di Rita, A. Nascetti, F. Fratarcangeli, M. Crespi. Upgrade of FOSS DATE plug-in: implementation of a new radargrammetric DSM generation capability. *International Archives of Photogrammetry, Remote Sensing and Spatial Information Sciences*, 41(B7):821-825, 2016.
- P. d'Angelo, M. Lehner, T. Krauss, D. Hoja, P. Reinartz. Towards automated DEM generation from high resolution stereo satellite images. *The International Archives of the Photogrammetry, Remote Sensing and Spatial Information Sciences*, 37(B4):1137-1142, 2008.
- C. S. Fraser, H. B. Hanley. Bias-compensated RPCs for sensor orientation of high-resolution satellite imagery. *Photogrammetric Engineering Remote Sensing*, 71(8):909-915, 2005.
- F. Fratarcangeli, G. Murchio, M. Di Rita, A. Nascetti, P. Capaldo. Digital surface models from ZiYuan-3 triplet: performance evaluation and accuracy assessment. *International Journal of Remote Sensing*, 37(15):3505-3531, 2016.
- D.B. Gesch, M.J. Oimoen, G.A. Evans. Accuracy Assessment of the U.S. Geological Survey National Elevation Dataset, and Comparison with Other Large-Area Elevation Datasets - SRTM and ASTER. *U.S. Geological Survey Open-File Report*, 1008:10, 2014.
- A. Gruen, Z. Li, H. Eisenbeiss. 3D precision processing of high-resolution satellite imagery. *ASPRS Annual Conference, Baltimore, USA*, on CD-ROM, 2005.
- N. Haala, D. Stallmann, C. Statter. On the use of multispectral and stereo data from airborne scanning systems for DTM generation and land use classification. *International Archives of Photogrammetry and Remote Sensing*, 32(B4):204-210, 1998.
- T. Heuchel. Experience in applying matching techniques using images from digital cameras. *Photogrammetric Week Wichmann, Verlag*, 05:181-188, 2005.
- H. Hirschmüller. Stereo Processing by Semi-Global Matching and Mutual Information. *IEEE Transactions on Pattern Analysis and Machine Intelligence*, 30(2):328-341, 2008.
- K. Jacobsen. Satellite image orientation. *The International Archives of the Photogrammetry, Remote Sensing and Spatial Information Sciences*, 37(B1):703-710, 2008.
- T. Kim. A study on the epipolarity of linear pushbroom images. *Photogrammetric Engineering & Remote Sensing*, 66(8):961-966, 2000.
- J.W. Koh, H.S. Yang. Unified piecewise epipolar resampling method for pushbroom satellite images. *EURASIP Journal on Image and Video Processing*, 11:1-14, 2016.
- T. Krauss, P. Reinartz, M. Lehner, M. Schroeder, U. Stilla. DEM generation from very high resolution stereo satellite data in urban areas using dynamic programming. *The International Archives of the Photogrammetry, Remote Sensing and Spatial Information Sciences*, 36(1/W3), 2005.
- D. Lowe. Distinctive image features from scale-invariant keypoints. *International Journal of Computer Vision*, 20:91-110, 2004.
- S. Lu, S. Huang, Z. Pan, H. Deng, D. Stanley, Y. Xin. High performance computing for DSM extraction from ZY-3 tristereo imagery. *ISPRS Annals of the Photogrammetry, Remote Sensing and Spatial Information Sciences*, 1(1):113-120, 2016.
- M. Morgan, K. Kim, S. Jeong, A. Habib. Epipolar resampling of space-borne linear array scanner scenes using parallel projection. *Photogrammetric Engineering & Remote Sensing*, 72(11):1255-1263, 2006.
- A. Nascetti. High resolution radargrammetry: development and implementation of an innovative image matching strategy, 2013. Doctoral dissertation Advisor: Crespi M.
- A. Nascetti, G. Colosimo. An open source Opticks plug-in for high resolution SAR imagery orthorectification and stereo measurements. *International Journal of Remote Sensing*, 37(15):3532-3546, 2016.

- P.D. Noerdlinger. Atmospheric refraction effects in Earth remote sensing. *ISPRS Journal of Photogrammetry and Remote Sensing*, 54(5-6):360-373, 1999.
- J. Oh, W.H. Lee, C.K. Toth, D.A. Grejner-Brzezinska, C. Lee. A piecewise approach to epipolar resampling of pushbroom satellite images based on RPC. *Photogrammetric Engineering & Remote Sensing*, 76(12):1353-1363, 2010.
- Y. Ohta, T. Kanade. Stereo by intra- and inter-scanline search using dynamic programming. *IEEE Trans. Pattern Anal. Mach. Intell.*, 7(2):139-154, 1985.
- T. Ono, Y. Honmachi, S. Ku. Epipolar resampling of high resolution satellite imagery. *Proceedings of ISPRS WG I/1, I/3 and IV/4, Joint Workshop on Sensors and Mapping from Space*, 7 pages (on CD-ROM), 1999.
- M. Pierrot-Deseilligny, I. Cléry. APERO, an Open Source Bundle Adjustment Software for Automatic Calibration and Orientation of a Set of Images. *International Archives of Photogrammetry, Remote Sensing and Spatial Information Sciences*, 38(5/W 16), 2011.
- D. Poli. Modelling of spaceborne linear array sensors, 2005. Doctoral dissertation, Swiss Federal Institute of Technology Zurich, Switzerland.
- D. Poli, F. Remondino, E. Angiuli, G. Agugiaro. Evaluation of Pléiades-1A Triplet on Trento testfield. *International Archives of Photogrammetry, Remote Sensing and Spatial Information Sciences*, 15-1(W1):287-292, 2013.
- P. Reinartz, P. D'Angelo, T. Krauss, H. Chaabouni-Chouayakh. DSM generation and filtering from high resolution optical stereo satellite data. *Remote Sensing for Science, Education, and Natural and Cultural Heritage*, pp.527-535, 2010.
- E. Rodriguez, C.S. Morris, E. Belz. A Global Assessment of the SRTM Performance. *Photogrammetric Engineering and Remote Sensing*, 72(3):249-260, 2006.
- L. Rong, F. Dazhao, J. Song, Z. Huiqin. Theory and algorithms of DSM generation from multi-line-array images matching. *The International Archives of the Photogrammetry, Remote Sensing and Spatial Information Sciences*, 37(B4):337-342, 2008.
- D. Scharstein, R. Szeliski. A taxonomy and evaluation of dense two-frame stereo correspondence algorithms. *International Journal of Computer Vision*, 47(1-3):7-42, 2002.
- P. Schwind, S. Suri, P. Reinartz, A. Siebert. Applicability of the SIFT operator to geometric SAR image registration. *International Journal of Remote Sensing*, 31(8):1959-1980, 2010.
- T. Toutin. Geometric processing of remote sensing images: Models, algorithms and methods. *International Journal of Remote Sensing*, 25(10):1893-1924, 2004.
- M. Vassileva, A. Nascetti, F.G. Tonolo, P. Boccardo. Unsupervised flood extent detection from SAR imagery applying shadow filtering from SAR simulated image. *IEEE International Geoscience and Remote Sensing Symposium (IGARSS)*, pp.2707-2710, 2015.
- P. Viola, W.M. Wells III. Alignment by maximization of mutual information. *International Journal of Computer Vision*, 24:137-154, 1997.
- M. Wang, F. Hu, J. Li. Epipolar arrangement of satellite imagery by projection trajectory simplification. *The Photogrammetric Record*, 25(132):422-436, 2010.
- J. Wohlfeil, H. Hirschmüller, B. Piltz, A. Börner, M. Suppa. Fully automated generation of accurate digital surface models with sub-meter resolution from satellite imagery. *The International Archives of the Photogrammetry, Remote Sensing and Spatial Information Sciences*, 39(B1):75-80, 2012.
- P. R. Wolf, B.A. Dewitt. Elements of photogrammetry, with applications in GIS. *McGraw-Hill, New York*, 608 pages, 2000.
- C. Zhang, C. Fraser. Generation of digital surface model from high resolution satellite imagery. *The International Archives of the Photogrammetry, Remote Sensing and Spatial Information Sciences*, 37(B1):785-790, 2008.
- D. Zhao, X.X. Yuan, J. X. Liu. Epipolar line generation from IKONOS imagery based on rational function model. *The International Archives of the Photogrammetry, Remote Sensing and Spatial Information Sciences*, 37(B4):1293-1297, 2008.

ACKNOWLEDGEMENTS

The Pléiades triplet was made available by e-Geos S.p.A. in the frame of a collaboration agreement: the author is indebted to e-Geos S.p.A. for this.

Furthermore, the author thank David Burken, David Hicks and Oscar Kramer for providing, as Google Summer of Code mentors, informatics support and all the necessary information to understand the wide OSSIM architecture.

BEYOND THE MAP. NUMERICAL AND COMPARATIVE ANALYSIS FOR THE STUDY OF HISTORICAL CARTOGRAPHY

C. Gottardi ¹.*

¹ Laboratorio di Fotogrammetria, Sistema dei Laboratori, Università Iuav di Venezia, Santa Croce 191, 30135, Venice, Italy - cgottardi@iuav.it

KEY WORDS: Historical Maps, Cartographic Heritage, Nautical Charts, Portolans, Oval Projections, Strain Cartographic Analysis

ABSTRACT:

This research focused on the study and application of analytical methods for the enhancement and the actualization of historical cartography. The aim was the development of a methodological procedure for studying cartographic data, distinguishing the investigation method according to the type of data, either numerical or graphical. Due to the passing of time and the lack of conservation, some maps usually can't be found if not on written sources or treaties. In this cases it is possible to take advantage of a numerical analysis in order to understand the graphic description missing, which used to be a part of the text.

The research was divided in two different case studies. The first is a comparative numerical analysis of a portolan dated between 1160 and 1200, the *Liber de Existencia Riveriarum et Forma Maris Nostri Mediterranei*: through the comparison of measurements of distance and direction, a GIS system was set for the metrical and geographical analysis of data, solving in this way the problems connected to the lack of a nautical chart. The second is an analysis of oval projections from the XVI century: starting from the graphic content of the renaissance maps, the projecting system and the semantic content were studied. Thanks to the method of the strain analysis it was possible to examine the metric parameters of the deformation of the cartographic projection.

1. INTRODUCTION

1.1 The historical cartographic heritage: the state of art

In the last years, thanks to an increasing sensitization toward the preservation of historical heritage, different methods and technologies were tested in order to preserve historical cartography and valorise its metrical, semantic and symbolic content, in a digital environment (Ceregato *et al.*, 2014).

The study of cartographical data is strictly connected to the issues concerning the digital acquisition without damaging the support, the geometric transformations for the georeferencing and the methods that can be used for data analysis. This thesis focused on this last point studying methods for digital data processing, with the aim of enriching the knowledge of metric and historical information of cartographic documents.

One of the main issues is the progressive deterioration of the support, due to its composition: just like for the treaties and ancient sources, historical maps need to be protected in order to be able to preserve both the support and its content. Their digitization is a solution for the conservation of the documents, providing an identical copy and permits multidisciplinary analysis without damaging the original support (Gatta, 2010).

The digitization of historical heritage has always been an issue in the field of Geomatics and Cartography. In the past years many methods have been developed for the digitization of the three-dimensional surface of the support and the representation of a bidimensional high definition image of it. In particular, some studies proposed the laser scanning and photogrammetric methods as useful techniques for acquisition of three-dimensional data (Balletti *et al.*, 2016; Ballarin *et al.*, 2015; Adami *et al.*, 2007). Once is digitally acquired, the content of the maps can be compared and georeferenced to modern cartography in order to support historical and spatial analysis (Balletti, 2000;

Guerra, 1999). The complete understanding of a cartographical document ends with a study on deformations and management of data in a digital environment. These studies can be pursued with different techniques and software: the strain analysis described here, already tested before (Balletti *et al.*, 2015; Livieratos, 2006; Boutoura *et al.*, 1986), is proposed as an alternative to the Tissot's Indicatrici for the study of metrical deformations.

1.2 Purpose of the research

The aim of this research has been the pursue of a method for studying historical cartographic documents through a scientific procedure of analysis and data processing, facilitating a multidisciplinary approach for understanding cartographical techniques used in the past. Nowadays cartographical data is an extremely effective and easily understandable message for a wider public; that's why it could be considered a didactic and a valuable tool for territorial analysis.

The cartographical data can be found in various forms to be analysed in different ways: here two cases were studied. The first one focuses on data that can't be found today on any support but on some historical description: it is the case of a navigational guide from the end of the XII century, the *Liber de Existencia Riveriarum et Forma Maris Nostri Mediterranei* (Gautier Dalché, 1995). The second case involves data that preserve its semantic and metric content: six oval projections from the XVI century where analysed. With the method of the strain analysis the projective system used by renaissance cartographers was examined (Balletti *et al.*, 2017).

The work presented here is therefore divided in two sections: based on the given data, different methods were used for processing and handling the historical cartographic heritage.

The first part discusses the study of the *Liber*; after a short historical introduction, the measures of distance from the text will

* Corresponding author

we can calculate that the first one enlarged the values of longitude as much as he contracted the size of the earth: this has to be considered as two aspects of the same error (Russo, 2013). From the coordinates of the places, the distances have been calculated using the spherical trigonometric formula of the haversine and subsequently compared to the *Liber* and the actual measurements. In this analysis there has been no correction of the coordinates given from the *Geography*: the results show even more the issue of the earth size reduction and the error of the values of longitude found in the *Geography*, giving credit to the correction of the Ptolemaic coordinates.

2.3 Numerical analysis of the *Liber*

This section describes the methodological procedure applied for the analysis of the *Liber*'s distances. First of all, in order to perform this study, it is necessary to recognise the toponyms used at the end of the XII century for the identification of port areas. The toponyms identification is a very complex operation and it requires an extensive historical knowledge. At the end of Gautier Dalché's essay two modern maps are presented, with the redrawing of some *Liber*'s distances and the relative harbours names: the first map focuses on the Italian peninsula and on the Aegean islands; the second one, instead, gives a complete description of the Mediterranean Sea basin. Therefore, the first step consisted in the spatial georeferencing of the two maps in a GIS environment, in order to implement the data of ports and distances based on those already studied by Gautier Dalché and his research group (Fig. 2).

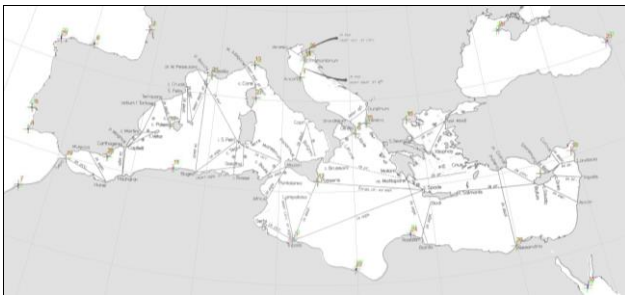


Figure 2. One of the two Gautier Dalché's maps georeferenced.

For the georeferencing procedure the ArcGIS software (ArcGIS Website) was used: the maps were georeferenced with respect to an actual cartography of the Mediterranean area in a Lambert conform conical projection with the central meridian set at 15°. The procedure was applied to easily identify some toponyms in their respective geographic area to obtain a reference base for the accurate localization of all the harbours. At the end of this procedure, a total of 124 distances and 158 toponyms were identified (Fig. 3).



Figure 3. The Mediterranean basin with the redrawing distances.

Moreover, the names of 138 of these places were also found in Ptolemy's *Geography*. In this case, many issues were encountered: although, in fact, the catalogue compiled by Tsorlini reports the subdivision of localities divided by geographical regions, the identification of ancient toponyms presupposes a very elevated historical knowledge.

At the end of this first analysis all the lengths that presented the distance information in nautical miles have been catalogued and related to toponyms and current distances; these values were also associated with some information derived directly from the essay of Gautier Dalché, such as the orientation of the *Liber*, the *Carta Pisana* and a modern map, the toponyms of the *Compasso da Navigare* and its miles. Finally, these data were also related to the names indicated by Ptolemy, their respective regions and the coordinates λ and φ described in the Tsorlini catalogue.

Given the number and complexity of catalogued information, immediately it was clearly necessary to implement all the data in a GIS environment (Fig. 4), that can relate heterogeneous data from different sources, allowing further queries and analyses. In fact, the modern Geomatics tools can offer a necessary support for the analysis of historical information and for its representation in a defined cartographic system (Gatta *et al.*, 2016; Carrion *et al.*, 2013; Gregory *et al.*, 2007). The potentiality of GIS as a tool for managing and cataloguing heterogeneous data is now widely established: for this study a complex database has been created, on which it is possible to carry out spatial analysis and make queries concerning the represented entities. Although in recent years there has been a high development of collaboration between multidisciplinary knowledge, GIS tools are still little used in Italy in the humanities, fortunately with some exceptions. This tool does not pretend to be an alternative to historical research, but rather wants to underline the importance of using complementary methods with respect to the more traditional ones in order to obtain a complete knowledge process (Barzaghi *et al.*, 2012).

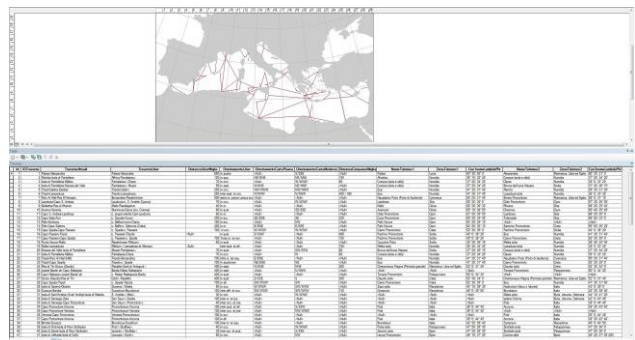


Figure 4. The GIS system with the catalogued historical information.

Once the harbours and distances have been redrawn, it has been decided to divide the Mediterranean basin into its smaller seas, in order to connect each port to the respective belonging sea. This choice was planned to spatially localize the differences between the measurements and to verify a possible concentration of errors in specific areas.

The subdivision shown in Fig. 5 refers, in order, to the following minor seas of the Mediterranean basin: 1) Alboran Sea; 2) Southern Balearic Sea; 3) Northern Balearic Sea; 4) Gulf of Lion; 5) Ligurian Sea; 6) Tyrrhenian Sea; 7) Sardinia Channel; 8) Strait of Sicily; 9) Libyan Sea; 10) Ionian Sea; 11) Adriatic Sea; 12) Sea of Crete; 13) Aegean Sea; 14) Levantine Sea.

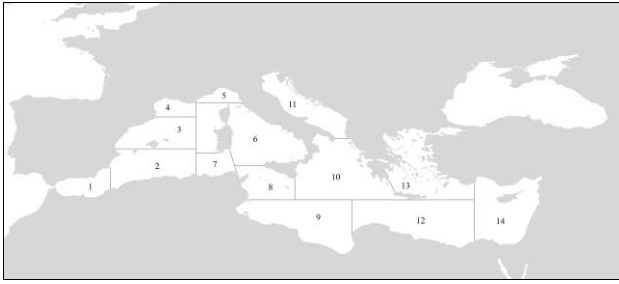


Figure 5. The subdivision of the Mediterranean basin into its smaller seas.

The Ptolemaic distances were calculated from the given coordinates, assuming as a reference surface a unitary sphere, through the spherical trigonometric formula of the haversine: in this way, the great-circle distance (i.e. the geodetic distance) was calculated between two points on the earth's surface. In the current case, this distance has been obtained directly from the ArcGIS software. The measures were finally included in a table containing the distances of the *Liber* (nm), the current ones (km), and the Ptolemaic ones (km). All the analyses described and the graphics shown have been realized with the SPSS statistical analysis software (IBM Website).

After analysing the distributions of the distance measurements of the three different sets, a consideration was required between the values in kilometres and those given in nautical miles, in order to allow an efficient and correct comparison. The first interpretation problem has concerned precisely the conversion of the nautical mile in the *Liber* era: in fact, historical information on this topic is heterogeneous. In literature, the most supported hypothesis associates the value of nautical mile with a 5:6 ratio compared to the Earth mile, i.e. equal to 1.233 km.

In order to choose the conversion, the ratio *current km/Liber's miles* was analysed: the results are concentrated around an average value of 1.34 km/nm and are characterized by a median value of 1.17 km/nm. For the visualization of the calculated ratio from a geographical point of view, the values were also associated to the distances in the GIS environment. In the image below (Fig. 6), the 36 purple distances are characterised by $0.45 \leq km/nm \leq 1.09$, while the red ones (28) are characterised by $1.10 \leq km/nm \leq 1.39$; finally, for the black ones (27) we have $1.40 \leq km/nm \leq 4.37$.

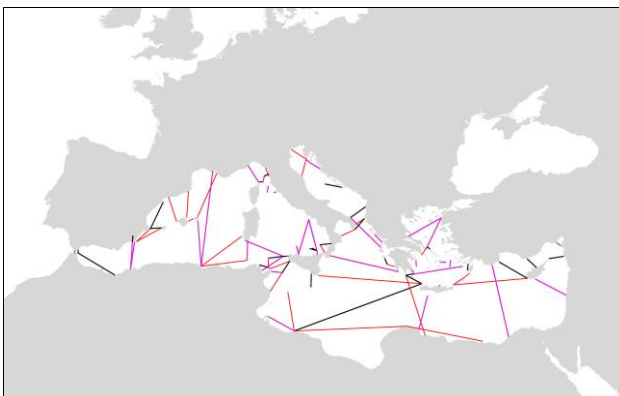


Figure 6. The ratio *current km/Liber's miles* visualized in the GIS environment.

Since the first elaborations, we noticed the different factors that occurred in the identification of the uncertainty of the data studied, starting from the order of magnitude used in the *Liber*. In fact, analysing the distances distribution, we noticed a leap in

the level of approximation for long distances (between 200 and 700 nm) equal to 50 nm, while for shorter distances equals to 10 nm.

This approximation led to the necessity of a subdivision of the data collected into two main classes, one for the short and medium distances, the other characterized by high values of length. Moreover, confirmed that in many cases it is difficult to precisely identify the current location of the harbours reported in the *Liber*, it was decided to treat in a different manner the shorter distances, for which even a slight error in the localization of the actual location would have created a too high relative uncertainty. Due to this consideration, we have subdivided the *Liber's* distances into three classes: 1) small distances (between 10 and 50 nm); 2) medium distances (between 60 and 160 nm); 3) long distances (between 200 and 700 nm). The first class is characterized by 26 cases, the second one by 37 and the third one by 28 cases (Fig. 7).

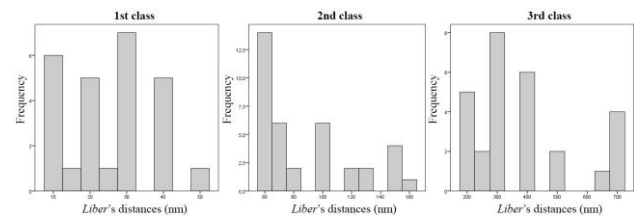


Figure 7. Distribution of distances of the *Liber* divided into the three classes.

Progressively, we have attempted to define a general descriptive model able to distinguish between the different factors affecting the uncertainty of the analysed measures, formulating the following hypothesis:

$$Liber = current\ measure (R + m_1 + m_2 + m_3) \quad (1)$$

where:

- R is the ratio *current km/Liber's nm*;
- m_1 is the uncertainty of current measure in relation to short distances. In this case, the uncertainty deriving from the identification of modern harbours' location in relation to those used in the *Liber* plays a significant role;
- m_2 is the measures' uncertainty in the *Liber*;
- m_3 is the accuracy for the measures in the *Liber*, that corresponds to the level of approximation used.

Of course, any of the three classes is characterized by a different set of uncertainty factors. In order to estimate the conversion ratio and the relative error of the *Liber's* measures with respect to the current ones, it has been applied a linear regression analysis for each class. We started from the less complex set of cases, the second class, as the factors m_1 and m_3 relate only to the two classes 1 and 3.

The regression line of the second class (Fig. 8) shows a positive relation between the two distance measures which is highly significant from a statistical point of view (R^2 is equal to 0,7) and it suggests a ratio between current km and *Liber's* miles equal to 1.3 km/nm. Even more interesting are the results from the regression analysis of the third class: the angular coefficient of the regression line is approximated to 1.2 km/nm (very similar to the ratio suggested in the scientific literature) and the function is even more significant from a statistical point of view, as it helps explaining 85% of the relative variability of the measures.

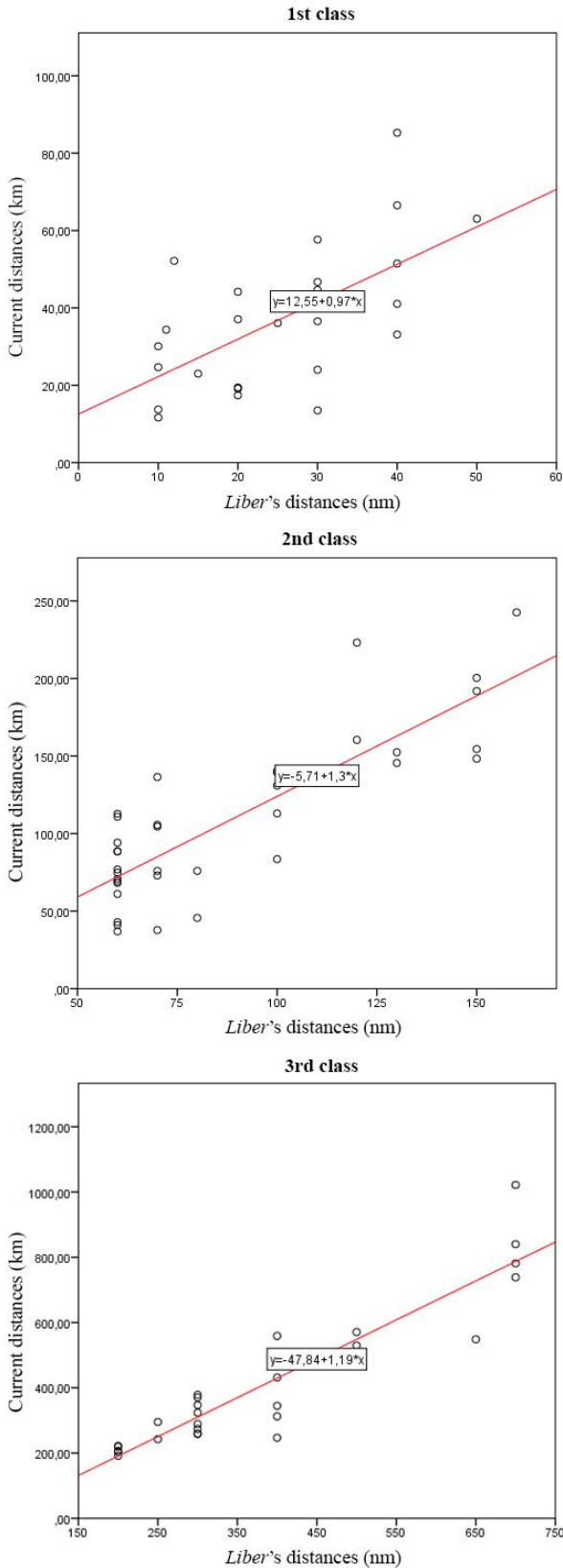


Figure 8. The angular coefficients detected for the three classes.

The linear regression analysis showed less substantial results for the first class cases. Here, though, the uncertainty factors are very high and it is difficult both to identify and to interpret them: for example, for short distances, a small uncertainty on the

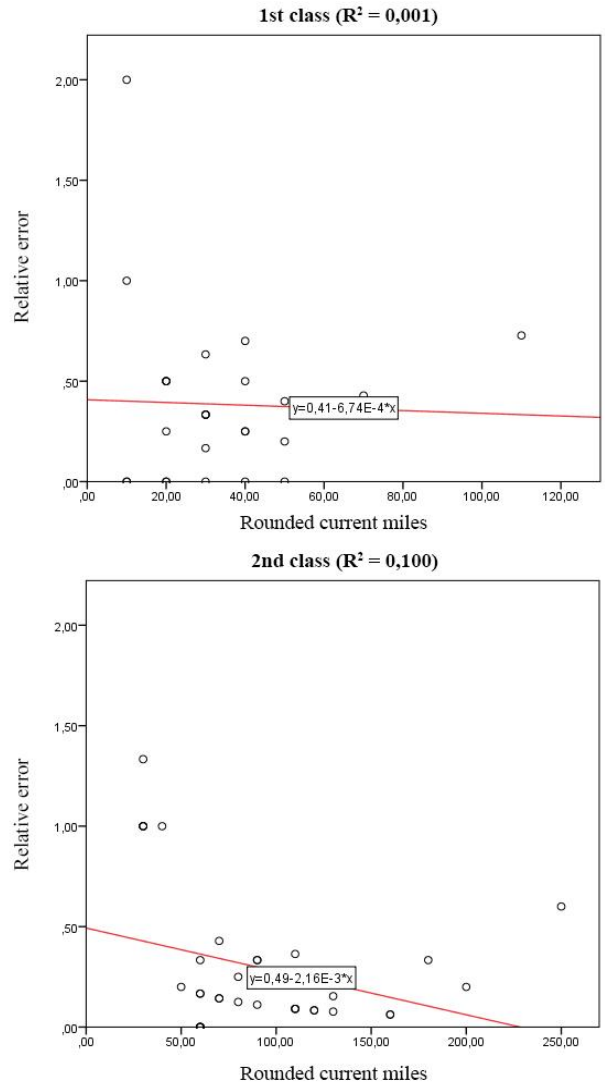
localization of harbours leads to higher differences between current measurements and those from the *Liber*.

Supposing a conversion ratio between km and nm among 1.233 and 1.3, we can estimate the difference between the two sets of measurements, the current ones and the *Liber*'s. The difference is represented by the relative error's measure between the nm described by the anonymous Pisan author and the current nm, classified with the measuring scale of the *Liber*. In fact, all the current values were rounded to 10 nm for the distance up to 160 nm and rounded to 50 nm for longer distances in order to compare the two different sets of measures.

The relative error is quite high for all the three classes: at the end of this performed analysis, we noticed that relative errors are always lower if we use the ratio equals to 1.233 km/nm (Fig. 9) instead of the one of 1.3 km/nm.

Given the conversion factor equals to 1.233 km/nm, consequently:

- for the cases of the first class, the relative error is on average 33% and it varies within the range 21%-56%;
- for the cases of the second class, the relative error is on average 26% and it varies within the range 18%-41%.
- for the cases of the third class, the relative error is on average 20% and it varies within the range 13%-31%.



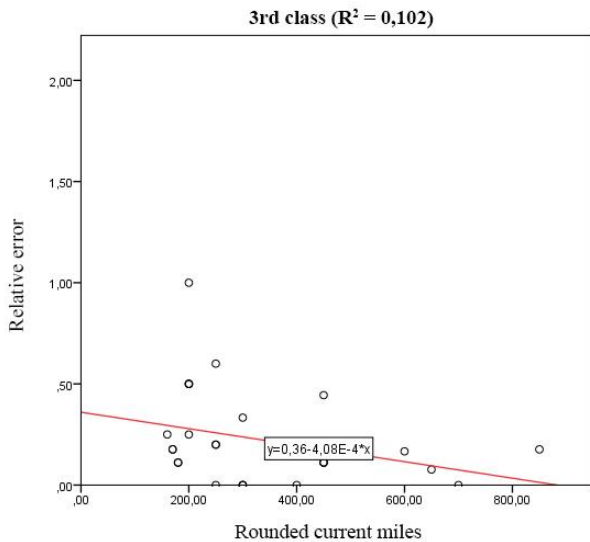


Figure 9. The relative error of the *Liber*'s measures with respect to the current distances (1.233 km/nm).

Therefore, it seems that there is a relationship between relative error and distance length, even if with very low intensity.

Trying to explain the error found in the measures of the *Liber*, other possible causes were investigated, including a value of uncertainty related to the part of the distance that can be travelled at sight rather than using a compass. To carry out this process, the raster images provided by the USGS (USGS Website) with information on the areas' elevation in the Mediterranean basin have been used. After creating a DEM in ArcGIS, the visibility area was calculated using the horizon distance formula; in this way, it was possible to determine the dimension of the distance that can be travelled on sight and that which can be travelled using a compass. However, also for this comparison, there are no evident linear statistical relationships between the distribution of the relative error and the maximum distance of the length that can be travelled with the visible coastline.

Subsequently, the relationship between the current distances (km) and the distances calculated starting from the coordinates provided by Ptolemy was also analysed. In this case there seems to exist a negative relation between the quantity of error and distance, but the results, i.e. the coefficient of the line and R^2 , are statistically not very significant.

Finally, it was decided to set up a comparison between the *Liber* and Ptolemy in order to investigate the origin of the portolans and their existence before the Middle Ages. The error of Ptolemy's measurements was compared with the error of *Liber* in order to look for a possible connection between the two data sets: in fact, if *Liber* derives from *Geography*, there should be a perpetuation of the same errors.

However, in this case, the relationship between *Liber* and Ptolemy is very low, but this is also due to the fact that this is only a preliminary analysis and it wants to be a starting point for a possible future development of the research. The fields that have to be investigated are several and complicated, since there is a lot of uncertainty about the Ptolemy's values, not only with regard to toponyms and their difficult identification but, above all, regarding the coordinates, especially with respect to the longitude. At the moment, the analysed coordinates have not been corrected yet and the distance has been calculated from the latitude and longitude information provided directly by *Geography*; the differences that emerged suggest, once again, the need for a correction of Ptolemaic longitude coordinates.

The statistical study analysed in this part of the research did not reveal any particular causes that could explain the uncertainty and relative error of the *Liber* measures, although we can notice a similar macroscopic trend between the medieval data compared to the current ones. An interesting consideration was made on a possible pattern within the Mediterranean, i.e. if the harbours with greater uncertainty were located in a specific sea within the basin.

In this case, an index was calculated in order to measure the error of ports and seas with respect to the *Liber* and Ptolemy; as can be seen, the measurement of the difference is relative. The analytical formulation of this index is expressed as:

$$I = \frac{|\sum x - \sum y|}{\sum y} \quad (2)$$

where x stands for the distances from the *Liber* (or Ptolemaic ones) which refer to one harbours (or all the harbours of one particular sea), whereas y stands for current distances.

What emerges from this research is that there are indeed seas where the error is greater: for example, if we analyse the relative error of the *Liber* sea compared to the current one (with the conversion 1.233 km/nm) it is possible to notice that the maximum error is concentrated in particular in the Italian seas (especially in the Tyrrhenian Sea, in the Sardinia Channel and in the Ligurian Sea), while the lower uncertainty is in the North Balearic Sea, in the Strait of Sicily and in the Libyan Sea. In the same way, errors relating to harbours have also been analysed, both for the *Liber* and for Ptolemy: this error was also graphically represented by associating the calculated values to the toponyms identified in the GIS (Fig. 10).

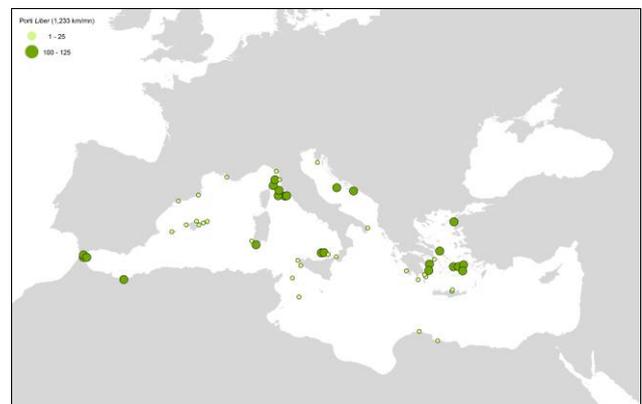


Figure 10. The error of the *Liber*'s harbours in the GIS environment (1.233 km/nm).

It is interesting to note that the results of the error analysis compared to the seas and ports reveal a coherence with what affirmed Gautier Dalché regarding some inaccurate directions located in the Italian and in the Aegean Seas: some areas are clearly affected by errors and approximations both as regards the description of the direction and the distance measure. At this point, it would be interesting to investigate whether the results obtained from a numerical and statistical analysis also indicate and describe the knowledge of seas and ports in the *Liber*'s era from an historical point of view.

With this research a methodological procedure for analysing historical cartographic data was set up; through a statistical analysis of information, it was possible to allow comparison, on one hand, with the actual situation and, on the other, with an ancient case study. One of the final results of this research is represented by a complex information system that allows

scholars from different research groups and disciplinary fields to visualize the data in a defined spatial context and to be able to re-use it for different purposes. In conclusion, the modern tools of Geomatics have allowed an accurate study of the medieval manuscript of the *Liber* applying a linear regression analysis on this particular document's data, comparing them with the current ones and introducing a new field of investigation in the future on the possible pre-medieval origin of the portolans.

3. THE ANALYTICAL STUDY OF SIXTEENTH CENTURY OVAL PROJECTION

3.1 The oval projection of the XVI century

Oval projections characterized the entire sixteenth century, starting from the map of Giovanni Matteo Contarini, engraved by Francesco Rosselli in 1506, followed by that of Benedetto Bordone (1528), Battista Agnese (1544), Giacomo Gastaldi (1546), until the end of the century and the early seventeenth century with the cartographic representations of Abraham Ortelius (1570) and Matteo Ricci, who will introduce the oval projective system for the first time in China. This cartographic graticule was progressively abandoned and forgotten until the early twentieth century, thanks to the theorization of pseudo-cylindrical projections by Max Eckert.

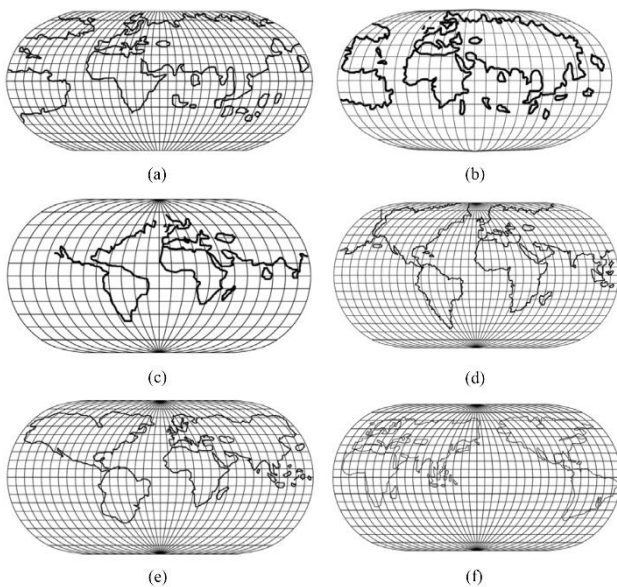


Figure 11. The analysed oval graticules: (a) Contarini-Rosselli; (b) Bordone; (c) Agnese; (d) Gastaldi; (e) Ortelius; (f) Ricci.

The research presented here is based on the study of the six Renaissance described maps (Fig. 11), icons for that historical period: starting from the formulations of the pseudo-cylindrical representation found in literature, the first analysis concerned the study of the projective system used by the Renaissance cartographers.

In the last decades some variants of the analytical formulation have been elaborated and proposed to define the model of the sixteenth century projection: in literature there is the formulation associated to Bordone and Ortelius's grid (Snyder *et al.*, 1994; Snyder, 1987; Tobler, 1966). Moreover, the historical maps have been studied also through the tools provided by the strain analysis in order to calculate some fundamental scalars associated with the evaluation of metric properties and the related deformations of the projection (Dermanis *et al.*, 1983a).

The constant and recurrent characteristics in the oval projections are mainly two: first, the ratio between the length of the Equator and the central meridian is equal to 2:1, then, the parallels are straight lines equidistant to each other and parallel to the Equator. Instead, some characteristics are depending on the analysed map: the meridians are symmetrical with respect to the Equator and the central meridian and are either elliptic or circular sections connected to the poles; moreover, the grid step is variable according to the choice of the cartographer and it is not always the same between meridians and parallels.

The first historical map studied was drawn by the Venetian Giovanni Matteo Contarini, with the help of the engraver Francesco Rosselli, in 1506; it is the first map that uses the oval projection and wants to be an advancement with respect to the Ptolemy's second projection. The equal distance step of the meridians and parallels is 10°. The second map was drawn by Benedetto Bordone in 1528: the equal distance step of the meridian is 20° and 11°15' (11.25°) is the step of the parallels. This grid is now associated with an analytical model described as a special case of the pseudo-cylindrical loximuthal projection (Snyder, 1993), but this model deviates from the historical graticule. In literature, also a graphic elaboration of this grid is provided (Anderson, 2002), close to the Bordone's original oval, with a 15° equal distance step between parallels and meridians. The third map was drawn by the Genoa native cartographer Battista Agnese in 1544. The analytical formulation associated with the Ortelius projection also describes the projective grid of Agnese: in this case, the step is constant and equal to 15°. Giacomo Gastaldi, a Venetian of Piedmont origin, is the author of the fourth map, dating back to 1546: here, the meridians and parallels step is equidistant and equal to 10°. Abraham Ortelius is the only non-Italian cartographer among the six cases studied, certainly the best known, thanks to the impact that the publication of his cartographic work had at his time. The step, visible on the map of 1570, is also in this case equidistant and equal to 10°. Finally, the Chinese planisphere by Matteo Ricci (1602) was analysed, in which the step is equidistant and equal to 10°. The main characteristic of this map is the unusual geographical location of the American continent, placed to the east of the European continent. This choice is explained due to the Ptolemaic cultural heritage: in fact, the classic world used to represent the *Ecumene*, i.e. the known world, from 0° to 180°, positioning each new extension always in the east direction (Livieratos, 2016).

The six projections were divided into three different cases: a) the Contarini-Rosselli map, a unique case to be treated individually, whit the unknown analytical formulation; b) the Bordone map, also to be treated as an isolated case. In fact, since the analytical model does not correctly describe the used grid, this case will be treated like an unknown projection; c) the 'Agnese set', which includes, in chronological order, the maps of Agnese, Gastaldi, Ortelius and Ricci, associated with the same mathematical model. In fact, the analytical formulation from the literature and associated with the Ortelius projection describes the projective grid also used by the three Italian cartographers. The formula is different for $\lambda \leq 90^\circ$ e $\lambda > 90^\circ$: in the first case, the meridians are elliptic segments while, in the second case, they are circular. Assuming a unit sphere, for the meridians with the values of longitude $0^\circ \leq \lambda \leq 90^\circ$, the formula is:

$$\begin{aligned} x &= \lambda - k + l \\ y &= \varphi \end{aligned} \tag{3}$$

with the replacements: $k = \pi^2/8\lambda + \lambda/2$; $l = \sqrt{k^2 - \varphi^2}$. For the meridians with $90^\circ < \lambda \leq 180^\circ$:

$$\begin{aligned} x &= \sqrt{m} + \lambda - \frac{\pi}{2} \\ y &= \varphi \end{aligned} \quad (4)$$

with the replacement: $m = \pi^2/4 - \varphi^2$.

Starting from these formulas, the x and y coordinates have been calculated maintaining the meridian and parallel steps as shown in the maps (15° for Agnese, 10° for Gastaldi, Ortelius and Ricci); the geographic grid was subsequently redesigned in AutoCAD (AutoCAD Website).

For the two cases of unknown projection, respectively the Contarini-Rosselli map and the Bordone map, the graticule has been redesigned directly from the maps. As anticipated, the Bordone grid is associated to a special case of the pseudo-cylindrical projection of the XX century: when we calculate the coordinates to redraw the parallels and meridians with the step of the historical maps, we obtain a curvature of the meridians that deviates when compared to the original one. For this reason, the study of Anderson was taken as reference for the Bordone graticule (Fig. 12).

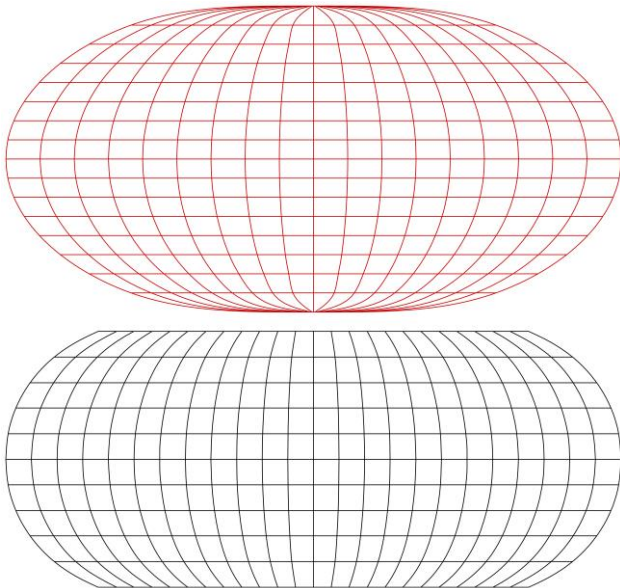


Figure 12. The Bordone's graticule derived from the formula (in red) and the redrawn one (to 75°N and 75°S).

Once the projective graticule of the three sets of maps have been redrawn, an analysis has been planned in order to study the spatial distribution of the grid and, in particular, the angular deviation of the meridians from orthogonality with respect to the parallels.

In general, the angular deviation from orthogonality is varying from 0° to ca. 5° in the areas close to the central meridian and the Equator, it is ca. 25° (± 10°) in the mid-distant areas from the zero meridian and the Equator and ca. 50° (± 10°) in further areas from central meridian and the Equator.

As it can be seen from Fig. 13 (Surfer Website), the trend of the angular deviation of the Contarini-Rosselli map and the 'Agnese set' is very similar, highlighting a pattern in the angular deviation from the perpendicular. On the other hand, Bordone's projective grid allows larger areas relatively closer to the orthogonality in the zones nearby the zero-meridian and the Equator.

Due to the lack of analytical formulation for the cases of Contarini-Rosselli and Bordone, it was not possible to derive directly the mathematical parameters for the calculation of the metric tensors to apply the subsequent analysis of the deformations. The implementation of a method for the study of

unknown projections starting from the graphic redrawing of the graticule is certainly a fundamental topic for the knowledge of the XVI century projections and it allows a possible future development in this research field.

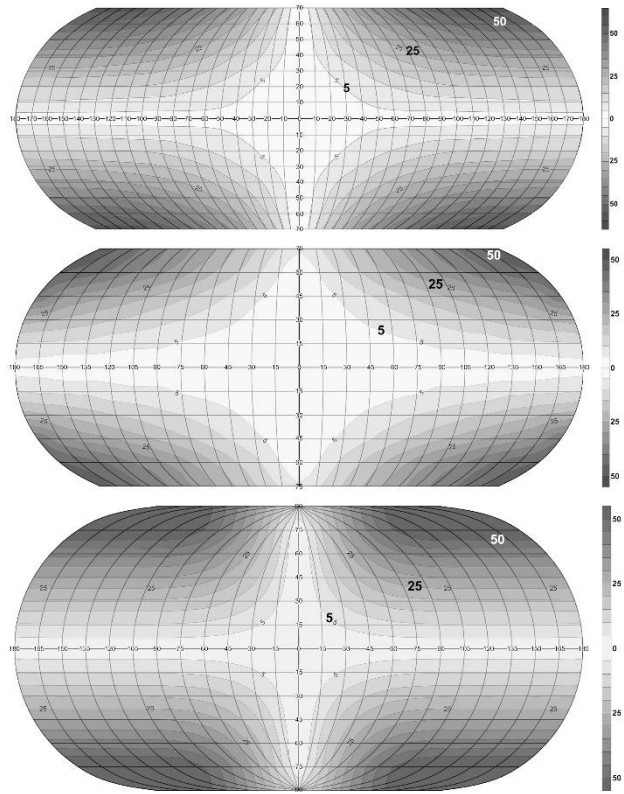


Figure 13. The spatial distribution of the graticule angular deviation from orthogonality. From the top: the Contarini-Rosselli's, the Bordone's and the 'Agnese set' graticules.

3.2 The metric properties and the oval deformation

As it is well known from differential geometry of surfaces, the three Gaussian forms g, f, e , fully describe the metric intrinsic properties of a surface, alias the metric tensor, at any point, given from the following matrix product:

$$\mathbf{J}^T \mathbf{J} = \begin{bmatrix} g & f \\ f & e \end{bmatrix} = \begin{bmatrix} \left(\frac{\partial x}{\partial \lambda}\right)^2 & \frac{\partial x \partial x}{\partial \lambda \partial \varphi} \\ \frac{\partial x \partial x}{\partial \varphi \partial \lambda} & 1 + \left(\frac{\partial x}{\partial \varphi}\right)^2 \end{bmatrix} \quad (5)$$

where \mathbf{J} is the Jacobian matrix 3x3 of the partial derivatives of the general system of equations representing the oval and \mathbf{J}^T its transpose. It is now possible to calculate the three parameters:

$$\begin{aligned} g &= \left(\frac{\partial x}{\partial \lambda}\right)^2 \\ f &= \frac{\partial x \partial x}{\partial \lambda \partial \varphi} \\ e &= 1 + \left(\frac{\partial x}{\partial \varphi}\right)^2 \end{aligned} \quad (6)$$

From these formulations, an important general condition is derived concerning the first differential form parameters of the ovals:

$$f = \sqrt{g(e-1)} \tag{7}$$

For the computation of the metric parameters of historical maps with known analytical representation, we started from the formulas described in the previous paragraph, applying the appropriate replacements for the ‘Agnese set’.

Two different sets of metric tensor (g, f, e) were calculated respectively for the meridians up to 90° and for the meridians from 90° to 180° . For the meridians with the longitude condition $0^\circ \leq \lambda \leq 90^\circ$, the metric tensors are:

$$\begin{aligned} g &= \frac{k^2}{l^2} \left(1 + \frac{l-k}{\lambda}\right)^2 \\ f &= \frac{\phi k}{l^2} \left(1 + \frac{l-k}{\lambda}\right) \\ e &= 1 + \frac{\phi^2}{l^2} \end{aligned} \tag{8}$$

whereas, for the meridians with the longitude condition $90^\circ < \lambda \leq 180^\circ$ the metric tensor are:

$$\begin{aligned} g &= 1 \\ f &= \frac{\phi}{\sqrt{m}} \\ e &= 1 + \frac{\phi^2}{m} \end{aligned} \tag{9}$$

In this case, it is interesting to notice that the metric properties of the graticule section $90^\circ < \lambda \leq 180^\circ$, in the ‘Agnese set’ of ovals, is independent of the longitude, which is varying increasingly only to the increase of latitude.

In recent years, a detailed study of crustal surface deformation, in terms of dilatation and shear, was proposed (Livieratos, 1980) to show how appropriate tools of deformation strain analysis can be used for the computation of specific invariant strain criteria associated with the intrinsic metric properties of map projections. These strain criteria can describe, in terms of elasticity, the deformation of a sphere while represented on a plane under the mapping conditions (Rastbood, 2014). This methodology was proposed as an alternative to the classical use of the well-known *Tissot’s* Indicatrices: the strain analysis give a ‘mechanical-type’ description of the alterations of linear and areal entities thanks to the parameters as dilatation and shear component (Truesdell *et al.*, 1965).

Following the Lagrangian approach in describing the metric differences of two surfaces, as the sphere and its representation under a specific mapping, a Lagrangian 2x2 strain tensor, in a matrix representation E , has to be computed (Dermanis *et al.*, 1984). Solving the characteristic equation of E matrix, it is possible to derive the invariant maximum and minimum strains (E_{max} , E_{min}) in order to calculate some invariant scalars, as Δ and γ , described respectively as dilation and maximum shear; these two values represent respectively the isotropic and the anisotropic part of deformation in the infinitesimal proximity of the point of interest.

In other words, Δ represents the areal change per unit area, equal in all directions (isotropic), positive ($\Delta > 0$) for areal increase (expansion), negative ($\Delta < 0$) for areal decrease (shrinkage);

instead, γ represents the shear across the direction of its maximum value (maximum anisotropy), always positive, indicating alteration in shape independently of magnification or reduction. The Lagrangian strain tensor E computed for a map point (λ, ϕ) with orthogonal reference directions, is written as (Dermanis *et al.*, 1983b):

$$E = \frac{1}{2} (Q^{-1} J^T J Q^{-1} - I) \tag{10}$$

where I is the unit matrix. In explicit form:

$$E = \frac{1}{2} \begin{bmatrix} g \sec^2 \phi - 1 & f \sec \phi \\ f \sec \phi & e - 1 \end{bmatrix} \tag{11}$$

from which Δ, γ, ψ are calculated as:

$$\begin{aligned} \Delta &= \frac{1}{2} (g \sec^2 \phi + e) - 1 \\ \gamma &= \frac{\sec^2 \phi}{2} \sqrt{(g - e \cos^2 \phi)^2 + (2f \cos \phi)^2} \\ \psi &= \frac{1}{2} \arctan \left(\frac{-2f}{g \sec \phi - e \cos \phi} \right) \end{aligned} \tag{12}$$

where the value ψ is the reference strain direction of the E_{max} . For the analysed ovals, the three scalars Δ, γ, ψ , with the expressions of g, f, e , allow the description of the strain induced by the metric properties of the projection in the close vicinity of points on the maps. The strain induced in the ‘Agnese set’ of ovals is described in terms of dilatation Δ (isotropic areal expansion), maximum shear γ (the percentage of alteration in shape) and the direction of maximum strain ψ in the Lagrangian sense (Fig. 14).

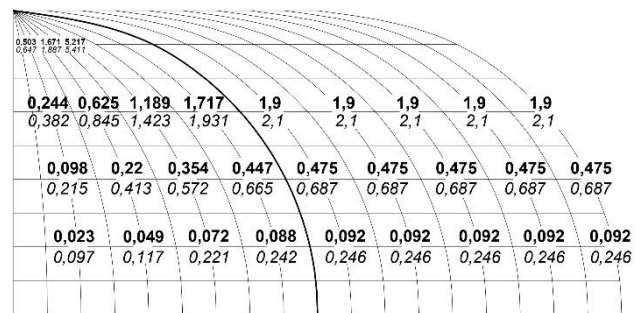


Figure 14. The distribution of dilatation Δ (bold) and maximum shear γ (italics) in the ‘Agnese set’ of ovals.

In the Table 1 are summarised the percentage values of isotropic and anisotropic deformation computed for the ‘Agnese set’. The directions ψ of the maximum strain E_{max} are varying within the North – North-Northeast (NNE) and Northeast (NE) orientation sector, with assigned values close to 40° nearby the Equator, ca. 35° in the mid-latitudes and ca. 30° in the higher latitudes in the entire longitude area.

Longitude Zone	$0^\circ \leq \lambda \leq 90^\circ$	
	Δ areal expansion (%)	γ maximum shear (%)
Close to Equator	2 - 9	10 - 25
Mid Latitudes	10 - 45	20 - 70
High Latitudes	25 - 170	35 - 200

Longitude Zone	$90^\circ < \lambda \leq 180^\circ$	
	Δ areal expansion (%)	γ maximum shear (%)
Close to Equator	10	25
Mid Latitudes	50	70
High Latitudes	200	200

Table 1. The distribution of the areal isotropic dilatation and of anisotropic maximum shear (per unit area).

From the deformation's analysis, it was therefore possible to see that the oval projective system introduces large alteration in shape, mainly characterized by an anisotropic factor. Moreover, the direction of the maximum deformation has a NNE-NE and NNW-NW orientation in the northern hemisphere, while it is characterized by an SSE-SE and SSW-SW orientation in the southern hemisphere.

3.3 The semantic content of the oval projections

Although this part of the research focused on the analysis of metric properties and deformation of the oval projections, during the process some interesting results about the semantic content of the maps were brought out; the six oval projections were converted in equirectangular projections (*plate carrée*) with the aim of facilitating the comparison of the drawn coastlines of the different continents.

The Contarini-Rosselli and Bordone maps reflect coastlines very similar to the ones from the second Ptolemaic projections and are very similar one another from a morphological point of view especially for the case of the Americas, even though they have a different grid (Fig. 15).

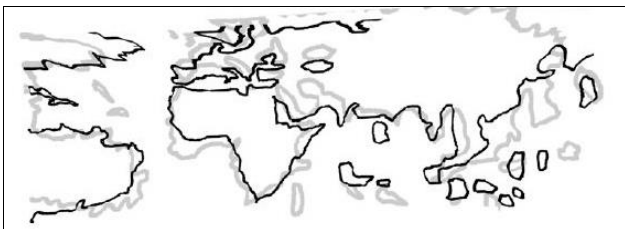


Figure 15. The coastline comparison realized between Bordone (grey) and Contarini-Rosselli (black).

The 'Agnese set' maps were also compared: the results show that the coastlines from the Ortelius's representation are very different from the Gastaldi's (Fig. 16) and Ricci's, which relate to one another quite accurately (Fig. 17).

A morphologic similarity of the grid is not necessarily connected to a similar semantic content. This can be seen particularly in the representation of the coastline of south America.

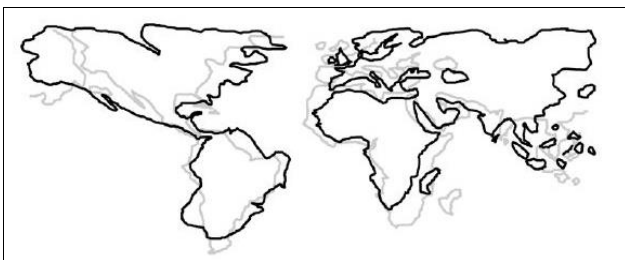


Figure 16. The coastline comparison between Ortelius (black) and Gastaldi (grey).

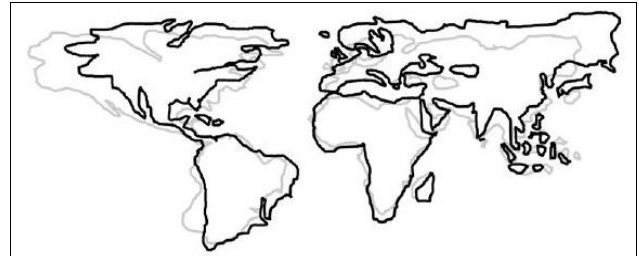
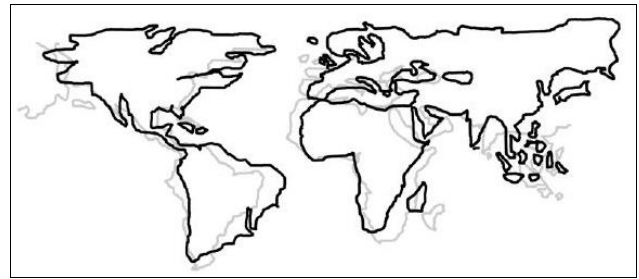


Figure 17. The coastline comparison realized. From the top: Ricci (black) and Gastaldi (grey); Ricci (black) and Ortelius (grey).

One of the main topic is the similarity, seen especially in the coastlines of South America, between Ortelius's map and Mercator's (Fig. 18). His projection set a revolution in navigation and became a necessity for bigger explorations later on.



Figure 18. The comparison of the South American coastlines. From left to right: Agnese, Gastaldi, Mercator and Ortelius.

This similarity underlines on one side the affinity of Ortelius with the *Euro-Atlantic* cartographic representations and on the other the semantic autonomy of the Flemish cartographer which distinguishes himself from the Italian ones and the *Euro-Mediterranean* such as Agnese, Gastaldi and Ricci.

Thanks to this research the continuum between information and knowledge through time has been underlined: this can be clearly seen in the reference to the historical cartography and to the second Ptolemaic projection. Using the strain analysis, a new strict method has been defined as long as a possible key for studying historical projections.

4. CONCLUSIONS

In this research two different methods have been applied starting from the different type of data given, either numerical or graphical. Two possible paths were tested with the aim of defining a methodological procedure for each case.

Modern Geomatics tools made the examination of the medieval *Liber* possible, through an analysis that hadn't been tested yet; this set the base for a future investigation on the probable pre-medieval origin of the portolans.

Also, thanks to an innovative method, already tested by the research group from the University of Venice and Thessaloniki, a particular type of historical map (the XVI century oval projections) was deeply studied. This leads to possible

developments in the research as far as identification and study of unknown projections are concerned.

It is obvious that this research doesn't set the end point of all the different methods that can apply to such data, but wants to be a starting point to future developments: Geomatics techniques give a scientific key to data reading and analysis, but they need a collaboration with wider research groups in order to reach a better understanding of the analysed information.

In the future, research will focus more on the issues found during the development of this work: further studies will be conducted on the relation between portolans and medieval nautical charts and ancient traditional cartography; also a numerical method will be implemented to study renaissance maps with unknown projection.

As said before, the importance of the individuation of toponyms is always a complex and actual theme for the analysis: it will be necessary to relate to historians and researchers for the identification of toponyms, in particular those from the Ptolemaic era. The research proposes a methodological procedure for the analysis of historical data. Thanks to that, additional modifications to whatever toponym will be followed by further implementation to the standardized procedure, with the addition of more correct values.

This research develops giving credit to the importance of historical cartography not only for the study of the territory, but also for the knowledge of the evolution of cartography throughout the centuries. In nowadays society, where visual communication is vital, cartography could be an effective and straight way of communicating to a wider range of people (not only the ones involved in such researches). That is the reason why it should be valued as an important didactic tool and an efficient base for examinations of the territory and its several representations from different ages.

The results of the research underline the importance of sharing this knowledge to be used in different fields of application: key to this is the accessibility of this work that should take advantage from the integration of different fields of knowledge and the collaboration of various researchers in order to obtain new educational and didactic tools.

REFERENCES

- Adami, A., Fregonese, L., Guerra, F., Livieratos, E., Tsioukas, V., 2007. Digital representations and analysis of deformations induced in map supporting materials. In: *Proceedings of CIPA International Symposium*, Athens, Greece.
- Anderson, P.B., 2002. *Map Projections b/w pdf graphics optimized for 'printing' from the browser*. Center for Spatially Integrated Social Science, University of California, Santa Barbara, on-line website: <http://www.csiss.org/map-projections>
- Ballarin, M., Balletti, C., Gottardi, C., 2015. Automatic systems for digitizing historical maps. In: *e-Perimtron*, vol. 10, n. 1, pp. 21-29.
- Balletti, C., 2000. *Metodi analitici e quantitativi per lo studio del contenuto geometrico delle carte storiche*. PhD Thesis in Scienze Geodetiche e Topografiche, 13° cycle, Politecnico di Milano.
- Balletti, C., Ceregato, A., Gottardi, C., Rizzi, F., Vianello, A., 2016. 3D digitizing and web publishing of an ISMAR Cartographic Heritage: historical maps of Venice Lagoon. In: *e-Perimtron*, vol. 11, n. 2, pp. 47-56.
- Balletti, C., Gottardi, C., 2015. Analytical methods for the projective content of Coronelli's central Europe maps. In: *Proceedings of Venezia e l'Europa Orientale tra il Tardo Medioevo e l'Età Moderna*, ed. by Corila Editore, Venice, pp. 22-33.
- Balletti, C., Gottardi, C., Guerra, F., Livieratos, E., 2017. Revisiting sixteenth-century oval maps with a cartographic strain analysis. In: *International Journal of Cartography*, pp. 1-16. DOI: 10.1080/23729333.2017.1370860
- Barzaghi, R., Carrion, D., Migliaccio, F., Minini, G., Zambrano, C., 2012. Strumenti GIS per il supporto agli studi storici: una proposta per l'innovazione dei metodi di ricerca. In: *Proceedings of 16th Conferenza Nazionale ASITA*, Vicenza, Italy, pp. 167-170.
- Bellomo, E., 2008. Sapere nautico e geografia sacra alle radici dei portolani medioevali (secoli XII-XIII). In: *Dio, il mare e gli uomini*, Quaderni di storia religiosa, vol. 15, pp. 215-241.
- Boutoura, C., Livieratos, E., 1986. Strain analysis for geometric comparisons of maps. In: *The Cartographic Journal*, vol. 23, n. 1, pp. 27-34.
- Campbell, T., 1987. Portolan charts from the late thirteen century to 1500. In: *History of Cartography*, vol. 1, ed. by J. B. Harley e D. Woodward, Chicago, University Press.
- Cantile, A., 2013. Lineamenti di storia della cartografia italiana. Volume primo: dalle origini al Cinquecento. Roma, Geoweb, pp. 134-146.
- Carrion, D., Migliaccio, F., Minini, G., Zambrano, C., 2013. Rappresentazione cartografica e condivisione di dati storici in ambiente GIS. In: *Proceedings of 17th Conferenza Nazionale ASITA*, Riva del Garda, Italy, pp. 379-384.
- Ceregato, A., Vianello, A., Balletti, C., Campiani, E., Gottardi, C., Menegon, S., Rizzi, F., Trincardi, F., 2014. Le mappe e i portolani dell'Istituto di Studi Adriatici: valorizzazione di un patrimonio storico per la ricerca e la divulgazione. In: *Proceedings of 18th Conferenza Nazionale ASITA*, Firenze, pp. 331-337.
- Dermanis, A., Livieratos, E., 1984. Deformation analysis of isoparametric telluroid mappings. In: *Bollettino di Geodesia e Scienze Affini*, vol. 43, n. 4, pp. 301-312.
- Dermanis, A., Livieratos, E., 1983a. Dilatation, shear, rotation and energy analysis of map projections. In: *Bollettino di Geodesia e Scienze Affini*, vol. 42, n. 1, pp. 53-68.
- Dermanis, A., Livieratos, E., Paraschakis, I., 1983b. Applications of strain criteria in cartography. In: *Bulletin Géodésique*, vol. 57, pp. 215-225.
- Gatta, Giorgia, 2010. Valorizzazione di cartografia storica attraverso moderne tecniche geomatiche: recupero metrico, elaborazione e consultazione in ambiente digitale. PhD Thesis in Scienze Geodetiche e Topografiche, 22° cycle, Alma Mater Studiorum Università di Bologna.
- Gatta, G., Bitelli, G., 2016. A historical GIS for the comparison of past and present views: Bologna, yesterday and today. In: *Proceedings of 11th ICA Conference on Digital Approaches to Cartographic Heritage*, Riga, Latvia, pp. 125-131.

- Gautier Dalché, P., 1995. Carte marine et portulan au XIIe siècle. Le Liber de Existencia Riveriarum et Forma Maris Nostri Mediterranei (Pise, circa 1200). Roma, Publications de l'École Française de Rome, vol. 203.
- Gregory, I., Healey, R., 2007. Historical GIS: structuring, mapping and analysing geographies of the past. In: *Progress in Human Geography*, vol. 31, n. 5, pp. 638–653.
- Guerra, F., 1999. *Trasformazioni geometriche locali: trasformazione versus corrispondenza*. PhD Thesis in Scienze Geodetiche e Topografiche, 12° cycle, Politecnico di Milano.
- Livieratos, E., 2016. The Matteo Ricci 1602 Chinese World Map: the Ptolemaean Echoes. In: *International Journal of Cartography*. DOI: 10.1080/23729333.2016.1184553
- Livieratos, E., 2006. On the study of the geometric properties of historical cartographic representations. In: *Cartographica*, vol. 41, n. 2, pp. 165-175.
- Livieratos, E., 1980. Crustal deformations from geodetic measurements. In: *Bollettino di Geofisica Teorica ed Applicata*, vol. 22, n. 88, pp. 255-260.
- Nicolai, R., 2015. The Premedieval Origin of Portolan Charts: New Geodetic Evidence. In: *The History of Science Society*, vol. 106, n. 3, pp. 517-543.
- Ptolemaeus, C., 1516. La Geografia di Claudio Tolomeo Alessandrino, Nuouamente tradotta di Greco in Italiano da Girolamo Ruscelli. Venezia, Valgrisi, ETH-Bibliothek Zürich, Rar 414. DOI: 10.3931/e-rara-1861
- Rastbood, A., 2014. Strain Analysis of Common Map Projections in Iran Using Continuum Mechanics Concepts. In: *Proceedings of International Conference on Research in Engineering, Science and Technology*.
- Russo, L., 2013. L'America dimenticata. I rapporti tra le civiltà e un errore di Tolomeo. Mondadori, 2nd ed.
- Snyder, J.P., 1993. *Flattening the Earth: Two Thousand Years of Map Projections*. Chicago – London, University of Chicago Press.
- Snyder, J.P., 1987. *Map Projections – a Working Manual*. USGS Professional Paper 1395, Washington DC, US Government Printing Office.
- Snyder, J.P., Voxland, P.M., 1994. *An Album of Map Projections*. USGS Professional Paper 1453, Washington DC, US Government Printing Office.
- Tobler, W., 1966. Notes on two projections. In: *Cartographic Journal*, vol. 3, n. 2, pp. 87-89.
- Truesdell, C. and Noll, W., 1965. The non-linear field theories of mechanics. In: *Encyclopedia of Physics*, Vol. III/3, ed. by S. Fluegge, New York, Springer.
- Tsorlini, A., 2011. Claudius Ptolemy Geōgrafikē Yfēgēsis (Geographia): digital analysis, evaluation, processing and mapping the coordinates of Greece, the Mediterranean and the Black Sea, based on 4 manuscripts and 15 printed editions, from Vaticanus Urbinas Gr. 82 (13th cent.) until today. The new Catalogue "GeoPtolemy-9". PhD Thesis in Engineering, Aristotle University of Thessaloniki.
- ArcGIS Website:
www.esri.com
- AutoCAD Website:
<https://www.autodesk.it/products/autocad/overview>
- IBM Website:
www.ibm.com/analytics/it/it/technology/spss
- Surfer Website:
www.goldensoftware.com/products/surfer
- USGS Website:
www.usgs.gov

INNOVATIVE USE AND INTEGRATION OF REMOTE SENSED GEOSPATIAL DATA FOR 3D CITY MODELING AND GIS URBAN APPLICATIONS

A. Lambertini

Dept. of Civil, Chemical, Environmental and Materials Engineering (DICAM),
University of Bologna, Viale Risorgimento 2, 40136 Bologna Italy – alessandro.lambertini@unibo.it

KEY WORDS: Remote Sensing, LIDAR, UAV, Point cloud, 3D city model, Smart City, GIS, Open Source, Open Data

ABSTRACT:

Modern remote sensing instruments, mounted on aerial platforms and assisted through the use of automated procedures are now capable of acquiring data over a vast area in a short timeframe. Thanks to innovative processing methods and algorithms it is then possible to rapidly deliver results with a high detail and accuracy. The paper provides an overview, through different case studies and examples, on the evolving complete pipeline required to survey, process, store, integrate, analyse and deliver data in the form of a 3D city model for GIS application in the urban environment. A comprehensive 3D city model is, in fact, the necessary multi-disciplinary backbone for the ubiquitous sensors of a Smart City.

1. INTRODUCTION

Nowadays, modern remote sensing instruments, mounted on aerial platforms and assisted with automated procedures are capable of acquiring data over a vast area in a short timeframe and deliver results with a high detail providing even on-demand acquisition in case of necessity. Information acquired by these systems is processed with different kind of workflow that convert the initial raw data into meaningful products with further processing. This output can be further visualized, analysed and delivered to other researchers, professionals or stakeholders in general. However, it is necessary to consider the importance of precision and accuracy especially when there is an overload of data but sometimes lack of reliable information and metadata.

Furthermore, a deep knowledge of the urban structure geometry is today essential for a significant number of applications such as urban planning, cadastre, environmental analysis, communication, and navigation.

In particular, Geographic Information System (GIS) are now more widespread than ever as they became mission critical tools in different applications and are used in various fields of scientific research. Therefore, precise, linked, detailed and updated geographic data is needed. This research focuses on some very promising techniques used to obtain geographic information.

In the last decades, in a standard surveying task, the main instrument used to be the total station. Nowadays new geographic data acquisition technologies brought different tools in the field of topographic mapping and the use of photogrammetry or laser scanning has become a viable choice. The presented paper is focused on remote sensing in urban areas, paying particular attention to the pipeline concerning the surveying, processing and analysis of data acquired over buildings (Table 1). The selection of the appropriate platform for such survey in urban areas is discussed among satellite data, airborne data, or data collected from an unmanned aerial platform. Each platform is studied based on the context and the objective of the analysis, adapting the choice at different scales ranging from the whole urban area to the detail of individual buildings. Then the attention is focused on several sensors suitable for acquiring data in urban areas, fitted on different platforms, with a resolution and accuracy suitable for

three-dimensional modelling of buildings. Several techniques are then examined for the acquisition of data in the form of point clouds, in particular, laser scanner and photogrammetric processing, considering the latest respective developments. Following the acquisition process, the performance and characteristics of different software and algorithms used to process the previously detected data are studied. Particular attention is paid to the possibility to increase the automatic processing of data identifying new workflows that may produce a result in an efficient and rigorous way. The innovative analysis made possible by the three-dimensional models constructed from point clouds are discussed and models that integrate data from different sensors, considering the relative accuracy, are studied with varying levels of detail depending on the context. Finally, the analysis moves on the best methodologies to structure the data collected and processed within tested Geographic Information System (GIS), useful to allow sharing of derived products with the scientific community and stakeholders. In fact, geospatial analysis can help institutions and local municipalities in urban planning to give better and more efficient results to their citizens.

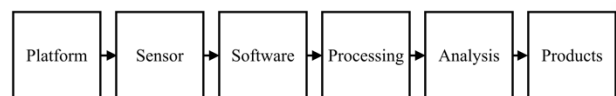


Table 1. The complete pipeline for geospatial data.

The research project aim is to study a reliable workflow that begins from the raw 3D point cloud. It is possible to process a first automatic classification, distinguishing the points of the cloud surveyed over buildings from those acquired over vegetation or terrain, employing advanced algorithms. Further analysis by semi-automatic procedures is possible to recreate the surfaces accurately oriented in space creating a true representation for each slope of the roof of each building. On these new data it is straightforward to perform further analysis such as a reliable estimate of solar radiation on each slope, depending on its orientation and area, and therefore an estimate of the potential use of a photovoltaic system installed on every building in a city.

Being able to produce a highly accurate and semantically complete 3D building model at urban scale is an essential

support in managing the urban infrastructure with a greater level of efficiency, better addressing any critical issues caused by the rapid pace of urbanization (Rottensteiner et al., 2014). A complete 3D city model is the necessary multi-disciplinary backbone for the ubiquitous sensors of a Smart City. In fact, the growing technological evolution will enable a great number of possibilities in sensing data in an urban environment for critical topics such as building and infrastructure monitoring, distribution and transport system (Hancke et al., 2013).

Remote sensed data are widely used in different applications and studies, some of them in urban areas, such as land use/cover mapping, updating of existing maps, detection of buildings and their characterization, urban growth, urban planning, emergency response and even web representations for citizens (Meixner and Leberl, 2011). A great effort in research is currently devoted to the automatic reconstruction of building models from remotely sensed data. Therefore, a multitude of case studies and procedures at different scales in an urban environment will be presented in the following chapters, trying to compose the big picture of remote sensing for 3D city modelling in the urban environment, with the latest innovation, some new algorithm proposals, and critical issues that are yet to be resolved.

2. PLATFORMS AND SENSORS

In the field of remote sensing, various platforms can be considered, based on user needs, as the best point of view defined to capture data with a particular sensor. In general terms, remote sensing defines the use of techniques to measure objects from a sensor mounted on a distant platform from the object itself, without any contact between the sensor and the surveyed object (Richards, 2013).

2.1 Analysis of the Proper Platform for Urban Applications

Satellites, as a spaceborne platform controlled by governments or commercial entities, have been used worldwide as remote sensing tool and gained always more importance over the years as a privileged platform for Earth observation. Among the advantages of the satellite over other remote sensing platforms it is possible to cite its ability to cover large areas thanks to its high altitude and can be therefore considered very cost-effective when used to acquire data over large areas.

The use of airborne platforms, such as a manned aircraft or helicopter, in order to carry a different kind of sensors such as laser scanners or digital cameras, can help to produce more accurate models and thematic maps for various applications covering even large areas with a minimum of ground control points. This platform has been the primary source of geospatial data for the developed part of the world until the most recent introduction of commercial remote sensing satellite. When government restriction on satellite imagery resolution was lifted and imagery with a high spatial resolution was finally sold, the difference between airborne and satellite imagery has been reduced (Toth and Józków, 2016). However, aerial platforms still maintain an order of magnitude advantage in spatial resolution over spaceborne platforms and therefore they guarantee good performances when needed, such as in urban context. Moreover, they can carry different kind of sensors, not only passive but also active such as laser scanners or radar.

The last aerial platform that will be examined is the commonly called drone: aircraft without a human pilot

onboard in which the control is remotely provided using a controller sending navigation command wirelessly. These platforms are worldwide known through different acronyms: Unmanned Aerial System (UAS), Unmanned Aerial Vehicle (UAV), Remotely Piloted Aircraft System (RPAS).

The choice of the correct platform for a survey in an urban area is not trivial. A unique answer does not exist, the choice should be based upon the specific requirements for the final products to obtain after the processing. In this chapter all the main remote sensing platform were described with their characteristics, capabilities, efficiency and limitations, impacting mainly the spatial and temporal resolution for the survey (Table 2). Another clearly linked topic that will be discussed in the following chapter is about the sensors that could be installed on different platforms and some of them could also be structured as a multi-sensor system.

	Spaceborne	Airborne	UAV
Cost	High	Medium	Low
Operation	Global	Regional	Local
FOV	Narrow	Wide	Wide
Spatial Res.	Low	Medium	High
Temporal Res.	Days	Hours	Minutes

Table 2. Comparison between some parameters among different remote sensing platforms

2.2 Sensors for Data Acquisition

Remote sensing instruments can be at least divided into two main categories: passive and active sensors.

Passive sensors can record energy emanating from earth’s surface, or the acquired object in general terms. This energy, such as natural solar reflected light or electromagnetic energy, is measured using different kinds of sensors mounted on an aerial platform and the measured energy is used to construct an image of the objects acquired from the platform (Richards, 2013). On the other hand, active sensors emit a signal, in the form of an energy packet, addressed directly at the object of the survey. The same signal is reflected back at the instrument and detected by a sensor. Therefore, they may be less dependent on environmental circumstances compared to passive sensors. Among the active sensors that are widely used in remote sensing it is possible to cite Radio Detection And Ranging (RADAR) and Light Detection And Ranging (LIDAR) sensors.

The rapid developments in the fields of laser scanning, photogrammetry, and computer vision give the possibility to survey highly accurate three-dimensional data. Depending on the complexity of the objects, various technologies can be applied, fused and integrated. For example, three-dimensional visualization for cultural heritage helps to preserve the memories of historic buildings and archaeological sites.

Point clouds are now the primary sources for three-dimensional information. LiDAR sensors have been the primary system to acquire point cloud data for many years, but recent advances in the field of computer vision have allowed a rapid generation of detailed point clouds processed from uncalibrated cameras with Dense Image Matching (DIM) algorithms, used to generate point clouds from aerial images.

With recent advancements in sensor technology and UAV payload capabilities, the LIDAR market for UAV is expanding. UAV platforms are in fact being increasingly used as a low-cost alternative to other aerial platforms in order to obtain valuable data for small areas or individual buildings, in order to produce maps and 3D models (Nex and Remondino,

2014). Both LIDAR and UAV technologies are evolving and the union of the two is still at its beginning. As the technology will advance in both sectors, it will lead to new developments and applications. Until some years ago, LIDAR sensors were confined to manned platforms such as airplanes and helicopters due to the weight of those sensors and the power needed to operate them. Only recently, some compact, lightweight, and low-energy LIDAR instruments have become available and every year active sensors and high-grade IMU are getting smaller and cheaper (Colomina and Molina, 2014). A promising segment of the market is today related to UAV-mounted camera sensors due to recent developments. Having to deal with a constrained payload, weight is a fundamental parameter for UAV photogrammetry, while it is not a strict limit for photogrammetry from a manned airplane or helicopter. It must be limited in order to maintain flexibility in the selection of flight height, duration, and speed.

Especially in rotary-wing platforms, the sensor is not directly connected to the aircraft. Instead, a gimbal is used to support the sensor, as a pivoted mechanism allowing rotation of the supported sensor around a certain number of axis. The use of gimbals in remote sensing allow the computation of a pre-determined path and trajectory to keep the line of sight of the camera targeted to the surveyed object (Sun et al., 2008). In particular, gyrostabilized gimbals are also employed in order to free the sensor from any vibrations transmitted by the UAV platform. Furthermore, maintaining a remote control on the gimbal movements, the ground operator can choose where to aim the sensor in order to acquire nadiral or oblique imagery. The ability to observe also the façades of buildings allow to generate a complete 3D city model containing details and texture data for each element of the surveyed structures, developing specific methods to avoid problems arising from occlusions (Rau and Chu, 2010).

The UAV platform can guarantee the possibility to maintain a close distance from the sensor to the object to survey when it is needed. Thanks to the control over the gimbal it is possible to acquire in a single flight both vertical and oblique imagery in a short timeframe. It is verified that the simultaneous use of images with a vertical and inclined axis in the generation of a dense 3D point cloud has reduced the uncertainty of the final model (Bolognesi et al., 2014).

2.3 Discussion and Integration of Data

The described sensors are in some cases complementary regarding the survey detail, survey coverage and spectral information. In some studies, such as in Stal et al. (2013), data acquired from aerial imagery is compared to products derived from LIDAR and compared qualitatively and quantitatively.

With the combination of the good height assessment accuracy of the laser scanner and good planimetric accuracy of aerial images, both high accuracy and higher automation in data processing can, in theory, be obtained (Shan and Toth, 2008).

From LIDAR surveys, for instance, it is possible to obtain a cleaner point cloud and a complete information regarding vegetation and objects below it. Furthermore, it is a sensor not dependent on light conditions.

Regarding the case studied in the context of this paper in urban applications, a few critical issues such as occlusions and irregular point density have an impact on the final quality of 3D city models.

Regarding occlusion, it is a common problem for sensors mounted on airborne platforms applied in surveys for urban areas. As previously said, the laser scanner can acquire data even from objects hidden behind vegetation, penetrating the

foliage. Nevertheless, the final result depends on the leaf surface and foliage density. Furthermore, neither LIDAR or photogrammetry techniques can avoid occlusions due to solid objects that pose in between the sensor and the complete acquired scene. In order to have complete data for the area, even for the building facades, sometimes a terrestrial survey or a low-height flight must be taken into account, with an oblique acquisition.

Furthermore, there are some variables that contribute in generating a point cloud with an irregular density. It must be considered that, for instance, LIDAR sensor emits a signal that is reflected by the surveyed surface and the final size of each pulse footprint or distance measured on the ground between consecutive pulses is correlated to the platform altitude and technical specification of the LIDAR instrument. Furthermore, some returns are discarded for their weak intensity caused by an unfavourable angle of the surveyed surface. The final result is a point cloud with irregular displacement of surveyed measures and the 3D models that are later generated from the dataset can suffer from fragmentations and holes lowering the global accuracy of the results. Regarding possibilities for direct survey and georeferencing from an aerial platform, without the use of Ground Control Point (GCP), it is feasible if supported by accurate Inertial Measurement Units (IMU) (Mostafa and Hutton, 2001).

One of the key points of the research here described is data fusion in order to find the proper way to use any data available in the case study area inside the interpretation processing. As it was illustrated in previous sections, it is possible to process different data acquired with different sensors at a different distance from the desired object. For instance, a point cloud acquired with LIDAR sensors can be integrated with aerial thermal imagery and ground surveys in order to determine a better model for the environmental conditions of the area studied, providing a DSM with a high spatial resolution and a detailed model for Sky-View Factor (Mandanici et al., 2016). Point clouds acquired from airborne platforms can be integrated with information obtained from high-resolution images acquired from satellite and other laser scanner data acquired from a terrestrial platform. Furthermore, other possibilities are now offered by sensors that can be mounted on a UAV. One of the challenges in data fusion is considering the accuracy of different data, that vary mainly depending on the distance of acquisition and generally it is inversely proportional to how wide is the area covered by the acquisition.

One of the topics of research concerns the study of best practice to integrate geospatial data with different characteristics, acquired from different surveys. Use of accurate data and updated metadata is mandatory, within the same spatial and temporal reference system. Both the scientific community and technicians need precise and up to date geographical data for different purposes.

A case study (Franci et al., 2014) considers data acquired in two areas within the city of Bologna integrating data from: a very high-resolution multispectral satellite image, a 3D point cloud acquired by aerial laser scanner and a digital cartography, generated through aerial photogrammetry and updated by the Municipality of Bologna, used as a geometric reference. It was possible to produce a workflow for the simultaneous use of heterogeneous techniques such as satellite imagery and the aerial laser scanner in order to update an existing database while providing new information at urban scale. Furthermore, the use and integration of multispectral data from the WorldView-2 sensor have been indispensable to classify the materials of each building roof. The obtained map

with the building's classification, according to their roofing material, have been further used to derive an additional level of information in the available numerical cartography. The experience described shows different thematic maps produced in a GIS environment from the integration of data acquired from different platforms and sensors for an urban application. One of the critical issues was to properly co-register all the different geospatial data. This created an added value updating and enriching a pre-existent numerical cartography, delivering precious information useful in a Smart City perspective, where accurate and up-to-date databases are crucial for a number of applications at urban scale such as energy performance indicator, traffic analysis, environmental monitoring (noise, pollution) and sustainable planning.

3. PROCESSING ALGORITHMS

Nowadays, even if sensors described in the previous chapter can rapidly acquire enormous quantities of precise geospatial data, there is still a great challenge in the scientific community in order to study efficient and accurate automatic detection and interpretation algorithms. In raw geospatial data obtained from remote sensing instruments there isn't any semantic information associated. Consequently, the previously acquired data must pass through different steps of processing in order to become meaningful for researchers and stakeholders. In particular, point clouds collected in urban areas contain a great number of points at a variable density collected over objects with a different level of complexity and variability, creating a great challenge for an automatic procedure for filtering, classification, and modelling.

In recent years, great efforts have been made in the scientific community in order to develop a workflow of efficient and automated procedures in order to extract, from acquired data in the urban environment, roof lines and slopes in a complete automated processing (Rottensteiner et al., 2014).

The vast size of the data acquired during an aerial survey, make it impossible to carry out a manual processing within a reasonable time and with reduced costs. It is thus necessary to study and develop new automatic or semiautomatic methods for processing such data. In addition, a further advantage in the use of these procedures is that the products obtained by processing through an algorithm will be of constant quality over time because of their deterministic nature.

3.1 Software Comparison

New techniques and procedures for automatic and semi-automatic extraction of information from remote sensing data are increasingly developed, following a great scientific and commercial interest. Several algorithms are subjects for the experimentation here described and they are implemented in different software, COTS (Commercial Off-The-Shelf) or FOSS (Free and Open-Source Software), able to detect the geometry of buildings inside a point cloud. This kind of data can be acquired from aerial LiDAR or photogrammetric survey. Point cloud processing is a non-trivial issue: processed data can indicate great differences depending on the precise workflow followed with a specific software and therefore on different algorithm procedures. Alternative implementations can, in fact, deliver different performance improving processing speed, memory efficiency or reliability of the results. In this chapter, different algorithms to process dense point clouds will be compared for the extraction and classification of thematic information. The algorithms are implemented in different software, both COTS and FOSS:

GRASS GIS, ENVI LiDAR, and LAsTools. These different software are structured to meet different needs in the processing workflow for geospatial data. The procedures have been tested with a common dataset and the results are analysed in a GIS environment. Additional considerations are carried out to evaluate different software functionality, comparing its performance and features.

In the case studied different software is used and each one shows advantages and drawbacks related with their different approach and design.

1. ENVI LiDAR (Harris Geospatial Solutions, 2017): a software designed for LiDAR data analysis with fast and simple processing that can deliver precise results. It is a commercial software and their algorithms are not in public domain, and also the scientific community has no further information about the methodology for processing. Only some parameters can be changed in order to adapt the processing to the specific case study.
2. LAsTools (Isenburg, 2018): a suite of various software, each developed specifically for a specific task in LiDAR data processing. Some of the algorithms are open source and it was possible to achieve good results within a brief processing time. Several parameters can be set in order to adapt the processing to the specific case study.
3. GRASS GIS (Neteler et al., 2012): an Open Source Geographic Information System software that can rely on a large number of algorithms and plugins extending its original capabilities in order to adapt the processing also to point cloud data. It is not the most efficient solution, considering that the software is not designed for LiDAR data processing. The processing time is usually longer and it is also longer the preliminary phase needed to import the point cloud. Being Open Source, it uses well known and defined algorithms that can be analysed and therefore it is possible to have a complete control on the result.

3.2 Dense Point Cloud Processing

A point cloud used for the comparison was acquired in the urban area of the city of Vaihingen, in Germany. It is a dataset acquired and published with the aim to create a common benchmark in order to evaluate different algorithms to process data acquired by airborne sensors, within the initiative "ISPRS Test Project on Urban Classification and 3D Building Reconstruction" (Rottensteiner et al., 2012). In particular, the point cloud here analysed was acquired by Leica ALS50 airborne laser scanner and the entire test subject area is contained in 5 strips with a flight altitude of 500 meters above the city. The result is a point cloud with an average density of almost 7 points per square meter, and a minimum of 4 points per square meter in those areas where there is no overlap between adjacent strips. These strips were processed in advance removing georeferencing systematic errors.

The surveyed area furthermore divided into three smaller parts, the test areas, which present different features. The area "1" is located in the heart of the city and is characterized by a number of historic buildings close to each other and consist of complex geometries. The area "2" is instead characterized by some high residential buildings, surrounded by vegetation. The area "3" is also residential, and instead includes buildings with more compact dimensions, well-spaced, but equally surrounded by vegetation.

3.3 Processing Results

The results have been analysed in the form of digital cartography in a GIS environment. In a first qualitative analysis, it has been observed that in some cases different geometries of the same building have been produced, in particular highlighting how some algorithms produce an incorrect footprint in the most critical circumstances such as those of tall vegetation proximity, or when the building geometry is, in fact, more complex. Comparing different procedures, it is possible to perform further considerations based on the total number of buildings properly reconstructed for the great part of their surface in the different areas analysed for the city of Vaihingen. The area marked as 1, with data acquired over the city centre, comprehends a total of 27 buildings. The area marked as 2, with high residential structures, has 9 separate structures. The area number 3, which is also residential, is characterized by 40 well-spaced compact buildings. It was possible to distinguish three cases: the buildings completely correctly recognized marked as “correct”, the buildings recognized only in some part of the structure with minor problems and marked as “partial”, and lastly the building that haven’t been recognized at all or whose surface were wrongly overestimated and therefore marked as “missed” (Table 3).

Area	GRASS GIS			LAStools			ENVI LIDAR		
	1	2	3	1	2	3	1	2	3
Correct	51.9	77.8	57.5	59.3	100	87.5	59.3	100	77.5
Partial	25.9	11.1	12.5	33.3	0.0	2.5	7.4	0	2.5
Missed	22.2	11.1	30.0	7.4	0.0	10.0	33.3	0	20.0

Table 3. Quantitative analysis for percentage of buildings modelled from the point cloud.

As it is possible to observe from the results, a better performance was achieved in particular in residential areas ("2" and "3"), by specialized software in the processing of LiDAR data: LAStools and ENVI LiDAR. It is also possible to highlight additional considerations related to the various software features. In fact, performance and capability of user intervention in selecting the appropriate parameters for the data processing were compared. Also, the products generated as output from the different software differ by type and purpose. For example, a peculiarity for the ENVI LiDAR software regards the greater control in the process of Quality Assurance that allows a trained human operator to review the results obtained from the automatic analysis.

In Figure 1 it is possible to observe the results of the processing with ENVI LIDAR after the extraction of several buildings from the 3D point cloud and the derived 3D city model as discussed in Lambertini et al., 2016.

Nevertheless, in all the cases analysed, it was still possible to export vector geo-referenced polygons representing the footprints of buildings and overlap this new layer produced with other geographical information. The experimentation was carried out as a methodology for software and procedures comparison, looking for a tool that can be effectively inserted into a workflow for the analysis of large amounts of data. It was possible to verify that the procedure for the automatic extraction of buildings from point clouds, with all the software analyses in this work, is accessible for users with enough experience in the treatment of geographic data. In particular, it was evident that any application that shows to the user a more simplified and immediate interaction, on the other hand, shows less chance for deep analyses by means of a complete choice over variables and parameters calibrated according to different needs. This is especially true for the most specialized

software. They give more control to the user on the final result and therefore requiring a steep learning curve and a greater experience to complete the required workflow.

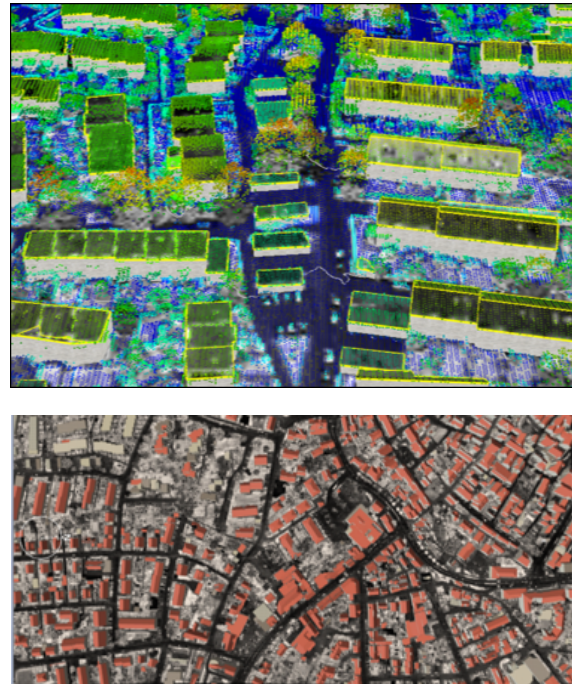


Figure 1. Three-dimensional visualization of building extracted with ENVI LIDAR (top) and the derived 3D city model (bottom).

4. ANALYSIS AT DIFFERENT URBAN SCALES

4.1 Level of Detail

The Level Of Detail (LOD) of a 3D city model may be considered as the most relevant parameter. It represents the correspondence of the model to the real-world (Biljecki et al., 2014). The CityGML standard from the Open Geospatial Consortium defines five different levels of detail. The concept is intended for different thematic classes of objects. Nevertheless, its primary focus are buildings, which are described through five classes with increasing geometric complexity.

In this chapter, a number of case studies will be presented and described in detail with their different workflow aimed to produce 3D models with a required LOD based on context. Therefore, different techniques to reach the desired LOD will be discussed.

First of all, it is necessary to introduce a definition of the different LOD as described by Kolbe (2009) in CityGML: LOD0: a simple representation of footprints, typically used in a GIS environment; LOD1: a simple prismatic model that can be obtained with the height extrusion of the building footprint contained in a LOD0 model using the elevation of the object as the only further parameter, without any definition of the roof structure; LOD2: a slightly more complex model with schematic roof shape. In particular different model, components can be classified in semantic classes such as facades, roof slopes, etc.; LOD3: an architecturally detailed model which comprises small items such as windows or doors and is overall more complex than LOD2; LOD4: it completes the previous level of detail including not only the exterior part

of the model but also interior items such as internal walls and furniture.

4.2 Roof Slopes from Point Cloud

The case study here presented is an area within the city of Düsseldorf, the capital city of North Rhine-Westphalia (NRW) state in Germany. The point cloud is currently available as Open Data in NRW website. The data contained in the files is delivered in tiles aligned in a grid, differentiated between raw data for DSM and filtered data for DTM. The DSM dataset contains also only first pulses (FP). The files are compressed in a ZIP folder when downloaded from the repository. Inside the compressed folder, the data is delivered in a simple ASCII file in text format with Est, North, Elevation coordinates rounded to centimetre resolution with two decimal digits.

It was possible to observe and process all the data for the case study. The density of the data isn't constant along the surveyed area, reaching higher values in the overlapping of adjacent strips. As a first step, the DSM and DTM were computed for the entire area of interest (Figure 2).

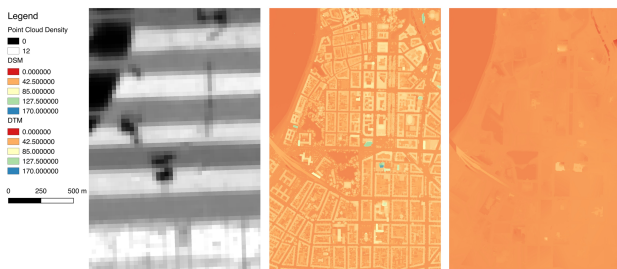


Figure 2. Data processed for the study area, from left to right: point cloud density, digital surface model, digital terrain model.

In a detail for a specific building, it is possible to observe the full pipeline of processing, starting from the raw point cloud data, highlighted with colours proportional to the elevation of the data, to a sequential step of classification of the point cloud in points surveyed over the building roof (yellow), ground (orange) and vegetation (green). Finally, a 3D model is computed on the points attributed to the building slopes (Figure 3).

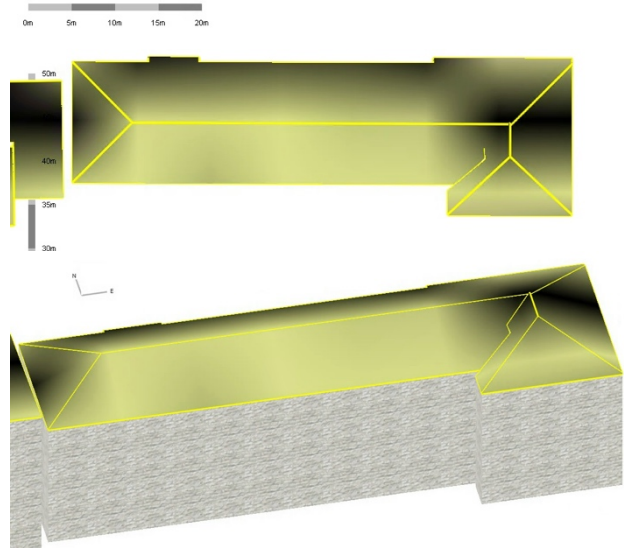
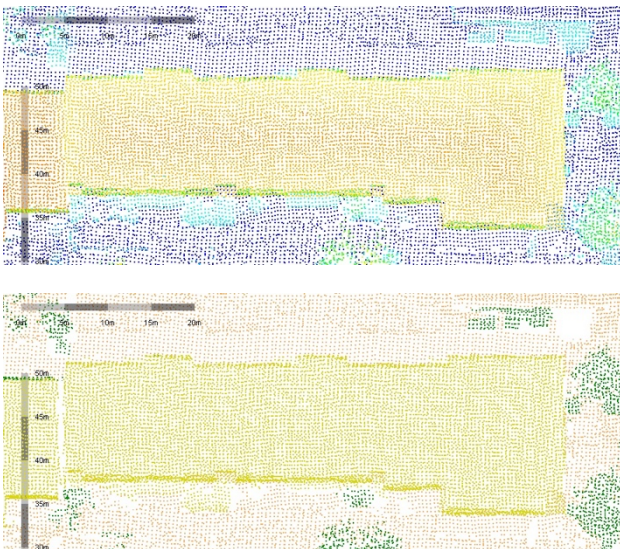


Figure 3. The full pipeline of processing described in the sequence of workflow for a specific building.

Data belonging to the facades is also recorded in the FOV of the LIDAR sensor, as can be seen in detail from cross sections (Figure 4). The highlighted data is partially recorded over balconies and partially over wall surfaces.

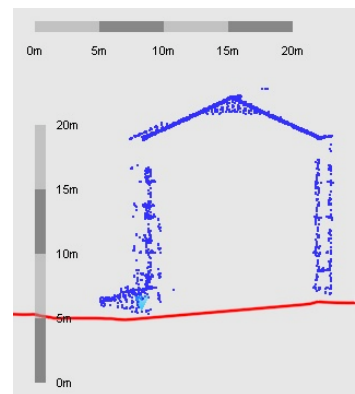


Figure 4. Reference building and its cross section from the analysed point cloud.

The structure of the urban texture in the study area is compact and regular, as it is possible to observe from the enlarged detail of the DSM extracted in Figure 5.

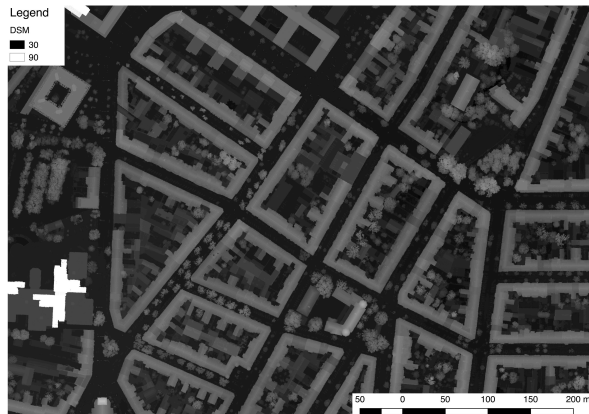


Figure 5. DSM for a central area of the city.

The reference data used in the Düsseldorf case study is ALK NRW, the cadastre map delivered and maintained by North Rhine-Westphalia State (Figure 6) showing a good comparison with the data extracted from point cloud processing.

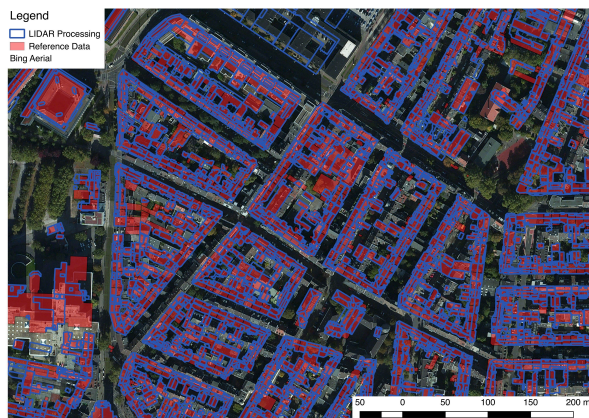


Figure 6. Building slopes processed from LIDAR data against reference data for buildings and aerial image in the background.

A final LOD2 model is computed with the data processed from the LIDAR survey (Figure 7).



Figure 7. LOD2 3D City Model.

4.3 Solar Radiation on Roof Planes

Identifying the right roofs to install solar panels inside an urban area is crucial for both private citizens and the whole local population. It is not an easy procedure because it depends on a large number of parameters: insolation, orientation of the surface, size of the surface, shading due to topography, shading due to taller buildings next the surface, shading due to

taller vegetation and other possible problems typical of urban areas like the presence of chimneys. Accuracy of data related to the analysed surfaces is indeed fundamental, and also the detail of geometric models used to represent buildings and their roofs. The complexity that these roofs can reach is elevated. This work was possible with the collaboration of technicians from Comune di Bologna and published in the International Archives of the Photogrammetry, Remote Sensing and Spatial Information Sciences (Africani et al., 2013). It uses LiDAR data to obtain, with a semi-automatic technique, the full geometry of each roof part complementing the pre-existing building data in the municipal cartography. With this data it is possible to evaluate the placement of solar panels on roofs of a whole city analysing the solar potential of each building in detail. Other traditional techniques, like photogrammetry, need strong manual editing effort in order to identify slopes and insert vector on surfaces at the right height. Regarding LiDAR data, in order to perform accurate modelling, it is necessary to obtain a high-density point cloud. The method proposed can also be used as a fast and linear workflow process for an area where LiDAR data are available and a municipal cartography already exist: LiDAR data can be furthermore successfully used to compare to a pre-existent digital cartography.

Knowing that a city is a central hub of energy consumption, among useful applications for GIS and 3D city models there is the study for energy consumption and production. This analysis can be conducted at an urban scale even to single buildings in detail. One example is Bologna Solar City, from Municipality of Bologna (Italy): a web application created to evaluate the placement of solar panels on roofs. It will be discussed in detail in the following section. Another example is to use LiDAR data and a derivative Digital Surface Model to produce a true orthophoto (Günay et al., 2007) that is useful in order to refine a detailed energy map relative to each building. This kind of analysis at building level was performed within EnergyCity, a project from Central Europe, to better understand the actual energy management and support strategies from the urban municipalities in order to reduce energy consumption and CO₂ emissions (Bitelli et al., 2015).

The Municipality of Bologna has a long experience in cartography and a good collection of data over the years in digital format. These data are continuously updated through different sources: georeferenced CAD drawings from executive projects, manual extraction of features from aerial orthophoto taken every year and surveys on the field are used to update the original large scale numerical cartography (CTC) made by aerial photogrammetry. In 2010, in order to help its inhabitants to reduce energy costs and save the environment, Bologna SIT office created a web application called Bologna Solar City to search for renewable energy systems applied in the Bologna territory and to evaluate the placement of solar panels on roofs. The basic idea was to estimate the solar energy available on roofs. This evaluation is the sum of direct and diffuse solar energies and it was calculated with ArcGIS tools. The algorithm applied required several elements in input. First of all, a DSM of the city territory developed with a large number of altimetric information deduced from the municipal cartography. The other factors considered are, on a raster-based model, weather conditions, position, and shade of each location (Minghetti et al., 2011).

The main simplification in Bologna Solar City was to consider all the roofs as flat, because in 1:2000 municipal cartography there are only two height information for each building: the bottom line and the height of the rain gutter. Unfortunately,

the greatest part of roofs in Bologna, as well as in many other cities, are composed of a complex arrangement of different slopes, with many ridges and valleys. In order to perform an accurate analysis, different parameters must be considered: insolation, orientation of the surface, size of the surface, shading due to topography, taller buildings, taller vegetation and other possible problems typical of an urban area like the presence of chimneys.

The accuracy of data relative to analysed surfaces is indeed fundamental, and also the detail of geometric models used to represent buildings and their roofs. For this reason, the precise geometry has to be acquired in order to have a good evaluation of the solar potential of each part of the roof. To obtain this kind of information a DSM of the city could be very useful. This is obtained, in the presented work, from LiDAR data using point clouds acquired from airborne laser scanning. These points are loaded in ENVI LiDAR. This software can classify and also directly extract 3D features (Figure 8) from the point cloud if the data density is adequate.

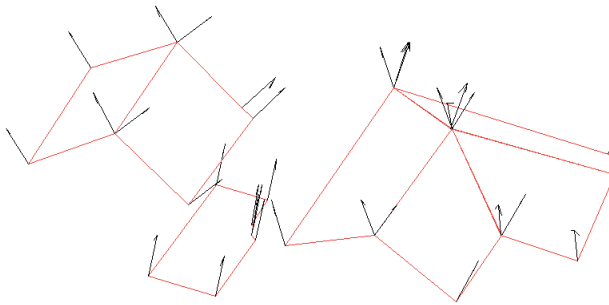


Figure 8. Vector roof models extracted from LIDAR data, displayed in a 3D visualization with the normal vectors applied to each separate slope.

To obtain slope and aspect values in GIS environment, using a 3D vector exported from ENVI LiDAR, the best option is to transform 3D data to a raster. Generating a DSM allows running 3D analysis tools like line-of-sight, viewsheds or solar radiation calculations. This transformation is performed creating first a Triangular Irregular Network (TIN) using the roof polygons as breaklines and using constrained Delaunay triangulation where no densification occurs and each breakline segment is added as a single edge. Then it's used a tool to generate a raster linearly interpolating cell z-values from the input TIN at the specified resolution of 0.5 meters that should be adequate given the instrument accuracy. Then Extract by Mask function is performed to delete values outside the modelled buildings, using the building's perimeter polygons obtained from ENVI LiDAR as a mask. With this final raster is possible to create derivative products like aspect and slope maps and use the resulting DSM to perform solar radiation analysis (Figure 9).

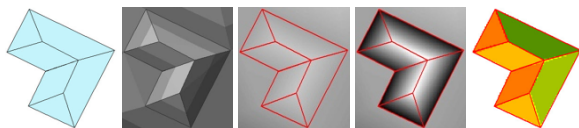


Figure 9. 3D vector obtained from LIDAR data processing, TIN model, raster model, masked model, aspect analysis

4.4 Rooftop Detailed Analysis

In order to take into account each element on the most complex rooftop, a high LoD is needed to model larger structures such as dormers and chimneys (Biljecki et al., 2014). In the example of solar panels placement, in order to assess the precise contribution in photovoltaic performance and displacement from each rooftop, a very high-density point cloud with great accuracy is needed to model and take into account for each element surveyed over the analysed roof: chimneys, dormers, etc (Figure 10).



Figure 10. Examples of a complex roof in the case of study.

This problem can be solved stressing simple GIS procedures in a specific iterative workflow in order to find any possible combination of solar panels with a certain dimension, fitting the area identified by the slope, avoiding any interference with pre-existing structures standing over the roof. Nevertheless, the source dataset must have the necessary elements to carry out the described analysis. An example is provided by the case study of Düsseldorf in which a building roof has been selected, containing numerous chimneys, dormers and other particular elements that contribute increasing the overall complexity of the slopes. It is possible to observe that in such cases if the point cloud is not sufficiently dense, it is impossible to produce an accurate model of the increased number of slopes for the building roof (Figure 11).



Figure 11. Results carried out over a building with a roof composed of complex slopes highlight the necessity of high density and accurate point clouds (aerial image on the left, slopes reconstructed from the point cloud on the right)

Some researchers have highlighted the need for an enhanced version for certain LOD in order to explicit more details in the modelling of the roof slopes, bringing improvements in the

overall accuracy of the building reconstructed. However, in order to reconstruct 3D models with such level of detail, both airborne and terrestrial surveys are needed (Biljecki et al., 2016).

The lack of information on the facades from data acquired with nadir-mounted sensors can amplify the problem related to occlusions, that can be solved with oblique imagery or oblique LIDAR survey in order to record data in the visible facades. In the vast majority of cases, oblique imagery may be sufficient to reconstruct information for the facades of a building (Rau and Chu, 2010), but still, the final model can benefit from an integration of data acquired with a terrestrial survey (Figure 12).



Figure 12. Explanation of building data acquired with different survey techniques

Furthermore, if there is not available a high-density dataset it is then not possible to precisely set the gutter line displacement, therefore the resulting slope will still be under-dimensioned as the 3D model will consider only the latest point acquired over the slope. The two described issues have an impact in the computation of building volumes and footprints.

5. CONCLUSIONS

The paramount importance of remotely sensed geospatial data has been highlighted through experimental results and analysis of various case studies. The presented work has been focused on the use of remotely sensed data in urban areas, paying particular attention to the analysis concerning the data surveyed over buildings, in order to propose a complete and reliable pipeline for data acquisition and processing.

In particular, the research begins with an examination of the available combinations of platforms and sensors used to acquire data in urban scenes, discussing the motivation behind the choice. A description of the possibilities for an efficient data processing, through the analysis of results carried out in many software environments, is provided, followed by a discussion regarding the critical issues related to the integration and processing of different datasets, providing few examples of future research topics and directions. The subsequent part is devoted to various case studies at different urban scales described with some degree of detail, from 3D city models of a whole area to a more accurate analysis of a single building. In contexts extending beyond the topics of this paper, these models have several critical applications such as assessment of solar radiation over an entire city or structural analysis for each building.

The growing trends in data continuously acquired from a larger number of platforms and sensors lead to a significant challenge in storage and processing of the surveyed data. If we are not able to transform this vast amount of data in derived products that are meaningful providing accurate information, then we have failed the primary goal of remote sensing. Despite the efforts spent in data acquisition, the availability of high-quality models is limited by the cost and the time needed to create them. Therefore, we need to support further research in and stress the related critical issues. It has been

demonstrated that it is now possible to efficiently create models of an entire city after a proper survey carried out from a remote sensing platform with the appropriate sensor. In fact, as we have seen in the state of the art review carried out through the entire paper, a significant part of research topics concerns the development of robust semi-automatic and automatic methods for 3D city models. The goal is to reduce the subjectivity of human-driven interpretation tasks, thus also reducing any time-consuming intervention that generates higher costs and delays in the delivery of a final product. Updated city models are in some cases urgent, such as in emergency scenarios, considering that a significant number of urban centres with a population high density are located in areas prone to natural disasters. Through the use of such models, it is possible to predict and mitigate the impact of emergency events.

All the approaches described can be applied to an even large number of different case studies, supporting the scientific community by defining best practices. In particular, stressing and examining some of these critical issues highlighted in the previous chapters such as point cloud density, precision, and accuracy. The urgent need for 3D city model, precise information and coherent metadata regarding building structures and their properties has been highlighted through the various chapters.

Nevertheless, some critical issues, particularly related to the production of 3D city models with a high level of detail, are still open and further research will be needed to address those topics and many procedures presented in this work will benefit from further improvements. However, the results presented here have proven to be promising and highlighted the clear advantages of creation and updating of a 3D city model in a Smart City perspective.

ACKNOWLEDGEMENTS

I would like to express my gratitude to Prof. Gabriele Bitelli, Prof. Luca Vittuari and Prof. Gil Gonçalves. Thanks to their assistance in this study and their guidance during these years I have had the opportunity to see the edge of knowledge in many connected topics, gain experience working on different projects and obtain a broader vision.

REFERENCES

- Africani, P., Bitelli, G., Lambertini, A., Minghetti, A., Paselli, E., 2013. Integration of LiDAR data into a municipal GIS to study solar radiation. *ISPRS - Int. Arch. Photogramm. Remote Sens. Spat. Inf. Sci.* XL-1/W1, 1–6. doi:10.5194/isprsarchives-XL-1-W1-1-2013
- Biljecki, F., Ledoux, H., Stoter, J., Vosselman, G., 2016. The variants of an LOD of a 3D building model and their influence on spatial analyses. *ISPRS J. Photogramm. Remote Sens.* 116, 42–54. doi:10.1016/j.isprsjprs.2016.03.003
- Biljecki, F., Ledoux, H., Stoter, J., Zhao, J., 2014. Formalisation of the level of detail in 3D city modelling. *Comput. Environ. Urban Syst.* 48, 1–15. doi:10.1016/j.compenvurbsys.2014.05.004
- Bitelli, G., Conte, P., Csoknyai, T., Franci, F., Girelli, V.A., Mandanici, E., 2015. Aerial thermography for energetic modelling of cities. *Remote Sens.* 7, 2152–2170. doi:10.3390/rs70202152

- Bolognesi, M., Furini, A., Russo, V., Pellegrinelli, A., Russo, P., 2014. Accuracy of cultural heritage 3D models by RPAS and terrestrial photogrammetry. *ISPRS - Int. Arch. Photogramm. Remote Sens. Spat. Inf. Sci.* XL-5, 113–119. doi:10.5194/isprsarchives-XL-5-113-2014
- Colomina, I., Molina, P., 2014. Unmanned aerial systems for photogrammetry and remote sensing: A review. *ISPRS J. Photogramm. Remote Sens.* 92, 79–97. doi:10.1016/j.isprsjprs.2014.02.013
- Franci, F., Lambertini, A., Bitelli, G., 2014. Integration of different geospatial data in urban areas: a case of study, in: Hadjimitsis, D.G., Themistocleous, K., Michaelides, S., Papadavid, G. (Eds.), *Proc. SPIE 9229, Second International Conference on Remote Sensing and Geoinformation of the Environment (RSCy2014)*, 92290P (August 12, 2014). doi:10.1117/12.2066614
- Günay, A., Arefi, H., Hahn, M., 2002. True orthophoto production using lidar data. *Int. Soc. Photogrammetry Remote Sens.*
- Hancke, G.P., de Silva, B. de C., Hancke, G.P., 2013. The role of advanced sensing in smart cities, *Sensors (Switzerland)*. doi:10.3390/s130100393
- Lambertini, A., Pastorello, E., Bitelli, G., 2016. Tecniche per l'estrazione automatica di edifici da nuvole di punti con software proprietari ed open source, in: *Atti 20a Conferenza Nazionale ASITA 2016*. pp. 835–840.
- Mandanici, E., Conte, P., Girelli, V.A., 2016. Integration of Aerial Thermal Imagery, LiDAR Data and Ground Surveys for Surface Temperature Mapping in Urban Environments. *Remote Sens.* 8. doi:10.3390/rs8100880
- Meixner, P., Leberl, F., 2011. 3-Dimensional building details from aerial photography for Internet maps. *Remote Sens.* 3, 721–751. doi:10.3390/rs3040721
- Minghetti, A., Africani, P., Paselli, E., 2011. Bologna solar city, a web application for the analysis of potential energy: from estimating solar radiation to the realization of the application, in: *17th Building Services, Mechanical and Building Industry Days - Urban Energy Conference*. Debrecen, Hungary, pp. 25–30.
- Mostafa, M., Hutton, J., 2001. Airborne remote sensing without ground control, in: *IGARSS 2001. Scanning the Present and Resolving the Future. Proceedings. IEEE 2001 International Geoscience and Remote Sensing Symposium (Cat. No.01CH37217)*. IEEE, pp. 2961–2963. doi:10.1109/IGARSS.2001.978222
- Neteler, M., Bowman, M.H., Landa, M., Metz, M., 2012. GRASS GIS: A multi-purpose open source GIS. *Environ. Model. Softw.* 31, 124–130. doi:10.1016/j.envsoft.2011.11.014
- Nex, F., Remondino, F., 2014. UAV for 3D mapping applications: A review. *Appl. Geomatics* 6, 1–15. doi:10.1007/s12518-013-0120-x
- Rau, J.Y., Chu, C.Y., 2010. Photo-Realistic 3D Mapping From Aerial Oblique Imagery, in: *International Archives of the Photogrammetry, Remote Sensing and Spatial Information Sciences - ISPRS Archives*.
- Richards, J.A., 2013. *Remote Sensing Digital Image Analysis*. Springer Berlin Heidelberg, Berlin, Heidelberg. doi:10.1007/978-3-642-30062-2
- Rottensteiner, F., Sohn, G., Gerke, M., Wegner, J.D., Breitkopf, U., Jung, J., 2014. Results of the ISPRS benchmark on urban object detection and 3D building reconstruction. *ISPRS J. Photogramm. Remote Sens.* 93, 256–271. doi:10.1016/j.isprsjprs.2013.10.004
- Rottensteiner, F., Sohn, G., Jung, J., Gerke, M., Baillard, C., Benitez, S., Breitkopf, U., 2012. The ISPRS Benchmark on Urban Object Classification and 3D Building Reconstruction. *ISPRS Ann. Photogramm. Remote Sens. Spat. Inf. Sci.* I-3, 293–298. doi:10.5194/isprsannals-I-3-293-2012
- Shan, J., Toth, C.K., 2008. *Topographic Laser Ranging and Scanning: Principles and Processing*. CRC Press.
- Stal, C., Tack, F., De Maeyer, P., De Wulf, A., Goossens, R., 2013. Airborne photogrammetry and lidar for DSM extraction and 3D change detection over an urban area – a comparative study. *Int. J. Remote Sens.* 34, 1087–1110. doi:10.1080/01431161.2012.717183
- Sun, M., Zhu, R., Yang, X., 2008. UAV path generation, path following and gimbal control. *Proc. 2008 IEEE Int. Conf. Networking, Sens. Control. ICNSC* 870–873. doi:10.1109/ICNSC.2008.4525338
- Toth, C., Józków, G., 2016. Remote sensing platforms and sensors: A survey. *ISPRS J. Photogramm. Remote Sens.* 115, 22–36. doi:10.1016/j.isprsjprs.2015.10.004

RIVERS HYDROMORPHOLOGICAL CHARACTERIZATION FROM HIGH RESOLUTION REMOTELY SENSED DATA

M. Niroumand-Jadidi

Department of Civil, Environmental, and Mechanical Engineering, University of Trento, Via Mesiano, 77 - 38123 Trento

KEY WORDS: Remote Sensing, River, Sub-Pixel Mapping, Bathymetry, Riverbed, Spectroscopy, Radiative Transfer Modeling, HRSI

ABSTRACT:

Remote sensing of hydromorphology can play a decisive role in a wide range of river science and management applications including habitat modeling and river restoration. This research aims to develop advanced methodologies for processing high resolution satellite imagery (HRSI) to map and quantify a set of key hydromorphological attributes including: river boundaries, bathymetry and riverbed types and compositions. To deal with the problem of boundary mixed pixels, optimal band analysis for normalized difference water index (OBA-NDWI) and modified binary pixel swapping (PS) are proposed for unmixing and super resolution mapping (SRM), respectively. The proposed sub-pixel mapping methodology improved user/producer accuracies on the order of 10% with respect to conventional hard classification in mapping the Sarca River (Italy) using WorldView-3 (WV-3) imagery. In the context of bathymetry and riverbed mapping, three different data sources are examined which include spectroscopic measurements in a hydraulic laboratory, radiative transfer simulations, and WV-3 image. This research introduces multiple optimal depth predictors analysis (MODPA) that combines previously developed depth predictors along with other measures such as the intensity components of HSI color space. The results indicated the robustness of MODPA with respect to heterogeneity of bottom types, inherent optical properties (IOPs) and atmospheric effects. Following retrievals of depth and diffuse attenuation coefficient (k_d), bottom reflectances are then estimated using a water-column correction method. The results demonstrated significant enhancements in streambed mapping based upon retrievals of bottom reflectances when compared to those using above-water spectra. It is also found that the WV-3's red-edge (RE) band, i.e., 724 nm, considerably improves the characterization of submerged aquatic vegetation (SAV) densities from both above-water or retrieved bottom spectra using WV-3 imagery.

1. INTRODUCTION

Consistent, accurate, and timely hydromorphological information is critical for managements of fluvial systems (Ashworth and Ferguson, 1986; Westaway et al., 2001; Woodget et al., 2014). Remote sensing approaches provide an efficient means of characterizing fluvial systems across large spatial and temporal extents (Legleiter et al., 2009). In spite of sound background in coastal studies, remote sensing of riverine systems still requires significant amount of research (Visser et al., 2013; Legleiter et al., 2016). With the increasing availability of high resolution satellite imagery, applications of satellites have recently been expanded to riverine environments as well (Legleiter and Overstreet, 2012; Hugue et al., 2016; Legleiter et al., 2016; Niroumand-Jadidi and Vitti, 2017b).

This research is focused on mapping and quantification of a set of hydromorphological attributes which are discussed in three groups hereafter: (1) sub-pixel mapping of river boundaries, (2) river bathymetry, and (3) mapping of riverbed types and compositions.

1.1 Sub-pixel mapping of river boundaries

Extraction of river area is the primary task required for a wide range of remote sensing applications in fluvial systems spanning from hydrological, ecological, and morphological studies to mapping the habitat suitability for different aquatic species (Legleiter et al., 2004; Marcus and Fonstad, 2010). Thresholding on spectral bands (e.g. NIR band) or on water indices such as normalized difference water index (NDWI), as well as image classification (supervised or unsupervised) are the

main techniques for delineation of water bodies from optical imagery (Jiang et al., 2014). However, most of the available techniques consider a hard labeling approach for producing the water mask. This means that mixtures within the pixels are considered very roughly so that each pixel can be assigned to only a single water/non-water class which represents the most abundant class within the pixel. The spectral mixture can occur at every spatial resolution, particularly in the boundary pixels (Foody, 2006). This point deserves more attention in terms of remotely mapping of rivers, as the boundaries of river channels are inevitably subject to uncertainties concerned with mixture of water with surrounding land covers. Mixed boundary pixels can suppress the extraction of river area, geometric features, as well as construction of cross-sections. To address the problem of spectral mixture, this research aims first at the estimation of water fractions within the mixed pixels, i.e., unmixing, and then at the spatial allocation of corresponding sub-pixels, i.e., super resolution mapping (SRM) in order to map river boundaries at the sub-pixel level. To this end, NDWIs are leveraged for the estimation of water fractions. As different combinations of spectral bands can be used in the structure of NDWI, a full search approach is proposed to identify the optimal pair of bands leading to the highest correlation of NDWI values with water fractions. The effectiveness of a regression model is explored for estimation of water fractions from NDWI values. The accuracy of the proposed method is compared against an advanced unmixing method, namely fully constrained simplex projection unmixing (SPU). A thorough investigation is carried out on the performance of SRM techniques in the context of river mapping. Several SRM techniques are focused which include pixel swapping (PS) and interpolation-based

algorithms. Furthermore, the PS algorithm is modified to speed up the binary water/non-water classification. Both semi-simulated and the fractions derived from real imagery are used for evaluation of SRM techniques. The first of these provides the possibility of accuracy assessment of the sole spatial allocation of sub-pixels task, while the latter considers also the uncertainties involved in estimation of water fractions.

1.2 River bathymetry

Bathymetry is one of the key applications of remote sensing to fluvial systems that facilitates understanding the river form, process and function (Shintani and Fonstad, 2017). Information on water depth can play a decisive role in, for instance, mapping in-stream habitats (Carbonneau et al., 2012; Hugue et al., 2016), parameterization and analysis of hydro-morphological processes (Flener et al., 2012) as well as flood modeling and management (Adnan and Atkinson, 2012).

Three main objectives are followed in the context of river bathymetry: (1) developing a new method called multiple optimal depth predictors analysis (MODPA) for bathymetry retrieval by identifying and incorporating optimal image-derived depth predictors; (2) assessing the robustness of proposed MODPA compared to existing models with respect to heterogeneity in substrate types, inherent optical properties (IOPs) and atmospheric effects; (3) assessing the efficacy of WV-3 sensor’s additional spectral bands compared to traditional 4-band (RGB-NIR) high resolution satellite imagery (HRSI) such as GeoEye (Table 1).

1.3 Mapping of riverbed types and compositions

Most of the previous research concerned with mapping of riverbed types and compositions have been based upon above-water reflectance data where water-column attenuation is not accounted for (Legleiter et al., 2016). The above-water reflectances/radiances are influenced by attenuation of light through the water column that can be a limiting factor for characterizations and classifications of substrate types from optical imagery (Visser et al., 2013). More recently, Legleiter et al. (2016) examined the possibility of retrieving bottom reflectances by accounting for depth and IOPs of water column. They measured the diffuse attenuation coefficient (k_d) directly in the field and then retrieved the bottom reflectances to classify sediment facies and algal density in Snake River (Wyoming, USA) from field spectra and airborne hyperspectral imagery. Although their preliminary results indicated no improvements in a riverbed classification exercise using bottom reflectance versus above-water reflectance, there is still a need to further investigate the effects of water-column attenuations in various environmental conditions, i.e., IOPs, bottom types, and water depths (Legleiter et al., 2016). The primary goal of this part of

research is to perform comprehensive analyses on impacts of water-column correction in fluvial remote sensing. In this context, three different data sources are examined, which include radiative transfer simulations, spectroscopic measurements at a hydraulic laboratory and WV-3 imagery. More specifically, our objectives are to (1) evaluate retrievals of k_d and bottom reflectances, (2) assess the bottom-type mapping and SAV retrievals before and after accounting for water-column attenuation, (3) examine the utility of WV-3’s eight spectral bands with respect to GeoEye, and (4) identify SAVs characterized with different densities in riverine environments using WV-3 imagery.

2. PROPOSED METHODS

2.1 Sub-pixel mapping of river boundaries

In this research, image-derived spectra for major land-cover types (i.e. water, vegetation and bare earth/soil) are mixed linearly with all the possible fractions of the classes with one percent intervals (Figure 1). This approach has been adapted from Ji et al. (2009); however, in the case of presence of an outstandingly different major class (endmember), number of classes can be increased. However, the mentioned three major classes which can be derived from grouping the sub-classes with similar spectral characteristics are representative for a wide range of applications and particularly for the riparian zones (Ji et al., 2009; Wetherley et al., 2017).

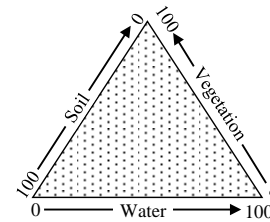


Figure 1. The scheme for linear spectral mixture of three dominant endmembers of land surface. Each point inside the triangle represents a possible combination of fractions; adapted from Ji et al. (2009).

After producing the synthetic spectra with all the possible fractions of the three classes, the NDWI values of the spectra are regressed against known water fractions. In this regard, an optimal band analysis for NDWI (OBA-NDWI) is proposed to identify the pair of bands for which the corresponding NDWI values yield the highest correlation with the water fractions. All the possible combinations of spectral bands are considered to calculate NDWI (Equation 1) in order to examine their potential for estimation of water fractions by assessing the coefficient of determination (R^2) and RMSE of the regression models.

Band	GeoEye		Band	WV-3	
	Center wavelength (nm)	Bandwidth (nm)		Center wavelength (nm)	Bandwidth (nm)
Blue	484	76	Coastal-Blue (CB)	426	60
(B)	547	81	Blue (B)	481	72
Green	676	42	Green (G)	547	79
(G)	851	156	Yellow (Y)	605	49
Red (R)			Red (R)	661	70
NIR			Red Edge (RE)	724	51
			NIR1	832	134
			NIR2	948	182

Table 1. Multispectral band designations for GeoEye and WV-3 sensors.

$$NDWI_{proposed} = \frac{b_i - b_j}{b_i + b_j} \quad (1)$$

$i = \{1, 2, \dots, \text{number of bands} - 1\}, \quad j = \{2, 3, \dots, \text{number of bands}\}$

After identification of the optimal combination of bands to be used for calculation of NDWI, the corresponding regression model is used to predict the water fractions of the image pixels. The regression-based approaches are previously used for estimation of fractional vegetation coverage using vegetation indices (Elmore et al., 2000; Xiao and Moody, 2005) but have not been explored yet for estimation of water fractions based on water indices.

The number of sub-pixels corresponding to the fraction of a given class within each pixel can be calculated based on the desired zoom factor (ZF) according to the following equation:

$$N^k = \text{round}(F^k \times ZF^2) \quad (2)$$

where N^k = sub-pixels' number for class k within a pixel
 F^k = fraction of the class k within the pixel
 ZF = zoom factor

For the binary water/non-water classification, the number of sub-pixels is calculated for water class based on the Equation 2, and then its subtraction from ZF^2 gives the number of sub-pixels for the non-water class.

The PS algorithm (Atkinson, 2005; Thornton et al., 2006) allocates sub-pixel labels in random positions within each pixel. Then, the attractiveness of each sub-pixel with respect to a particular class is predicted as a distance-weighted function of its neighbors according to the following equation:

$$A^k = \sum_{i=1}^n \frac{F_i^k}{d_i} \quad (3)$$

where A^k = attractiveness of a sub-pixel towards class k
 F_i^k = fraction of class k in the i -th neighbor pixel
 n = number of neighbor pixels
 d_i = distance of the i -th neighbor pixel

Considering the attractiveness values of the class k in a pixel, the least attractive sub-pixel location initially allocated to the desired class (e.g. water) should be identified as well as the most attractive location initially allocated to the other class (e.g. non-water). If the attractiveness of the least attractive location is less than that of the most attractive location, then the classes are swapped, otherwise no change is made (Niroumand-Jadidi and Vitti, 2015). After applying the swapping process on all image pixels, this process should be iterated until reaching a point that the algorithm is not able to perform anymore swaps. An example of the swapping process is illustrated in Figure 2 where the central pixel with 58% water fraction is divided to nine sub-pixels ($ZF=3$) and the attractiveness of each sub-pixel is calculated based on the eight neighboring pixels.

After calculation of the attractiveness values for sub-pixel locations, the original PS algorithm commences with a random allocation of sub-pixels and then maximizes the spatial dependency in an iterative manner. This can be a barrier in terms of computational time when applying the algorithm on large extents. To tackle this problem, a simple non-iterative solution is examined for the spatial allocation of binary classes (e.g. water and non-water). The proposed method suggests to simply allocate the sub-pixels of the desired class (water) in the N^k locations with the highest attractiveness values toward that class. The remaining sub-pixel locations are then directly

assigned to the non-water class. The proposed modified binary PS (MBPS) method is applied on the same example discussed in Figure 2. Here, resultant sub-pixel map is the same as that of the original PS algorithm (Figure 3).

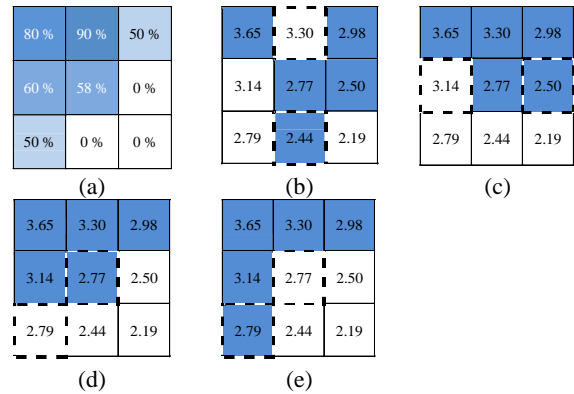


Figure 2. Water fractions and the PS process for spatial allocation of sub-pixels for a given pixel; (a) water fractions, (b) random allocation of sub-pixels, (c, d, e) swaps (candidate sub-pixels for swapping are highlighted by dash-lines); values of sub-pixels represent their attractiveness toward water class.

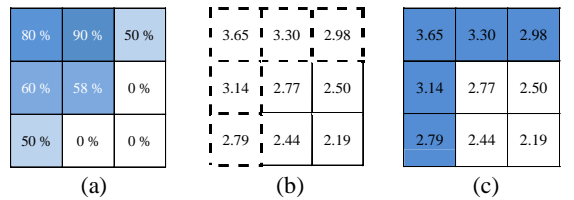


Figure 3. Proposed MBPS for spatial allocation of sub-pixels; (a) water fractions, (b) identification of sub-pixel locations with highest attractiveness, highlighted by dash-lines, (c) allocation of water and non-water sub-pixels; values of sub-pixels represent their attractiveness toward water class.

The interpolation methods can be also employed to develop non-iterative SRM. Assigning the fractions of classes to the center of the corresponding pixels, sub-pixel fractions can be estimated using common interpolation methods. Here, several techniques including bilinear, bicubic and lanczos3 are tested. A hard labeling process can be applied then on interpolated points (i.e. sub-pixels) to assign each sub-pixel to the class with the highest estimated fraction. The main advantage of this technique is that the labeling procedure can be done in a single step which can improve the computational efficiency.

2.2 River bathymetry

The total radiance reaching to the sensor at a given wavelength i.e., $L_T(\lambda)$, can be formulated as (Legleiter et al., 2004):

$$L_T(\lambda) = L_b(\lambda) + L_c(\lambda) + L_s(\lambda) + L_p(\lambda) \quad (4)$$

where $L_b(\lambda)$ = bottom reflected radiance

$L_c(\lambda)$ = water-column reflected radiance

$L_s(\lambda)$ = water-surface reflected radiance

$L_p(\lambda)$ = atmospheric radiance

Aside from $L_p(\lambda)$, each of the above-mentioned radiance components can be associated with a specific property of the

water body. For instance, the surface-reflected component of the radiance can be linked to the roughness of the water surface which in turn is a function of local hydraulics in riverine environments and can potentially reveal information about the flow velocity (Overstreet and Legleiter, 2017). The bathymetry information is embedded in the bottom-reflected component of radiance which is affected not only by water depth but also the bottom type (Lee et al., 1998; Stumpf et al., 2003; Niroumand-Jadidi and Vitti, 2016b).

Lyzenga's model (1978, 1981) is built upon the Beer-Lambert law to describe the exponential attenuation of light travelling through the water-column. This model (see Equation 5) includes a deep-water correction ($L_{\infty}(\lambda)$ i.e., radiance observed over optically-deep water) to account for the radiance reflected from the water column, the water surface and the atmosphere. The bottom-reflected radiance can be considered negligible for radiances observed over optically-deep waters. Therefore, subtraction of $L_{\infty}(\lambda)$ from all water pixels leaves the bottom-reflected radiance which contains bathymetry information. According to Lyzenga's model, the water depth (d) depends linearly on the predictor (X) derived from image values in a given spectral band:

$$X = \ln(L_T(\lambda) - L_{\infty}(\lambda)), \quad L_{\infty} = L_C + L_S + L_p \quad (5)$$

$$d = aX + b$$

The unknown parameters (a , b) can be estimated by means of a simple regression between X and in-situ depths (d). However, these parameters depend on IOPs of the water-column and the bottom reflectance, which may vary within a given scene. To deal with these problems, a linear combination of the predictors (X_i) derived from multiple (n) spectral bands has been suggested to estimate the depth (Lyzenga et al., 2006):

$$d = \sum_{i=1}^n a_i X_i + b \quad (6)$$

The water-surface roughness, i.e. surface-reflected radiance, can also be significantly variable for rivers within an image scene (Legleiter et al., 2009). These effects cause variations in near-infrared signals, which do not contain significant bottom-reflected signals because of the large water attenuation in these bands. Thus, scaled versions of the near-infrared signals can be used to correct for variations in the surface-roughness as well as atmospheric effects (Lyzenga et al, 2006). Stumpf et al. (2003) proposed to use a ratio model for depth retrievals to mitigate the undesirable effect of variations in bottom reflectance (Equation 7). Their model relies on the fact that different substrates at the same depth have approximately equal values of the ratio between total radiances at two different wavelengths.

$$X = \ln \left[\frac{L_T(\lambda_1)}{L_T(\lambda_2)} \right] \quad (7)$$

Such a ratio can be used as a single and to some extent robust depth predictor with respect to substrate variability (Stumpf et al., 2003; Flener, 2013). Note that Equation 7 is a special case of Equation 6, with $n=2$ and $a_2 = -a_1$. So this method is in principle equivalent to that of Lyzenga, although a different procedure is used to determine the parameters. Legleiter et al. (2009) extended the idea of ratio model in the form of optimal band ratio analysis (OBRA). This model examines all the possible pair of bands through the ratio model to identify the pair that provides the highest R^2 .

The bathymetric models are originally developed for coastal environments and they are just recently being translated to the fluvial systems particularly using HRSI (Niroumand-Jadidi and Vitti, 2016a). The key distinctive feature of riverine environments would be the thinner water-column compared to the coastal settings. Therefore, a relatively high contribution from river substrate and a relatively low contribution from the water column can be expected particularly for shallow and clearly flowing streams. Although this is a promising point for depth retrievals due to having strong desired signal (i.e. bottom radiance), the pronounced effect of the substrate variability can make the depth retrieval complicated. Note that the deep-water correction required for Lyzenga's model demonstrated to be negligible for shallow rivers (Flener et al., 2012; Flener, 2013). This is mainly because the bottom signal is the dominant component of radiance reaching to the sensor particularly for the atmospherically corrected imagery.

The existing bathymetric models individually employ single/multiple Lyzenga predictors or a single ratio predictor. Although OBRA identifies the optimal ratio predictor, the model is based on a sole ratio predictor. The selection between predictor types (Lyzenga or ratio) can be challenging in practice as the results of previous studies indicate that each type of predictors can possibly lead to more accurate results than the other depending on the case study. For instance, Jawak and Luis (2016) reported that the Lyzenga model derived the bathymetry of a shallow lake more precisely (with 15% higher R^2 and 0.98 m lower RMSE) than the ratio model using WV-2 imagery. On the other hand, the regression type (simple or multiple) defines the number of predictors in the linear regression model. The bathymetry models relied on simple regression (e.g. OBRA) explains the dependent variable (i.e., depth) by only one predictor where other informative predictors can potentially be neglected.

This research aims at extending the initial depth predictors by considering all of the possible Lyzenga and ratio predictors rather than relying upon one of predictor types. In addition, some extra predictors can be considered from the RGB to HSI (hue, saturation, intensity) color space transformation. In this regard, the intensity component of the HSI space is added to the original image feature space and the associated Lyzenga and ratio predictors are included in the predictors. Note that the color space transformation can be applied to each combination of three spectral bands so that several intensity bands can be added to the feature space (e.g. four intensity bands can be derived for a 4-band GeoEye image). A multiple regression approach is then considered to keep most of the variability of predictors. However, making use of all the predictors increase the possibility of high correlation among the predictors. For example, 36 initial predictors can be derived from 8-band WV-3 imagery (8 Lyzenga predictors and 28 ratio predictors) while this number can be even increased by considering extra predictors. Therefore, performing a dimensionality reduction on all the possible predictors is appropriate. This study suggests to select the optimal predictors by using three different regression methods of partial least square (PLS), stepwise and principal component (PC). The resultant optimal predictors can then be a combination of Lyzenga, ratio and the extra predictors (Niroumand-Jadidi et al., 2018b).

2.3 Mapping of riverbed types and compositions

Bottom mapping is poorly studied in the context of fluvial systems and has mostly been based on above-water reflectances, which neglect the attenuation effects of water column. The first attempt to apply existing water-column correction techniques in

a riverine environment is the very recent work by Legleiter et al. (2016) wherein limited field and spectral measurements have been applied. Their results demonstrated that sediment facies and algal densities can be characterized based on spectral information while retrievals of bottom reflectances were unnecessary.

The remote sensing reflectance (R_{rs}), defined as the ratio of water-leaving radiance and total downwelling irradiance just above water, is an apparent optical property needed essentially for interpretation of optical imagery over water bodies (Mobley, 1999). Radiometric and atmospheric corrections are required to derive R_{rs} from top of atmosphere (TOA) radiance values. Note that reflectances/radiances and also k_d are all wavelength (λ) dependent, however, we drop λ for brevity in the text while it has been presented in the equations. Remote sensing reflectance just beneath the water surface (r_{rs}) can then be estimated to account for the transmission and refraction at the air-water interface (Lee et al., 2002; Legleiter et al., 2016):

$$r_{rs}(\lambda) = \frac{R_{rs}(\lambda)}{[0.52 + 1.7R_{rs}(\lambda)]} \quad (8)$$

Thereafter, the remote sensing reflectance of bottom (r_{rs}^B) can be estimated according to the following equation (Maritorena et al. 1994; Legleiter et al. 2016):

$$r_{rs}^B(\lambda) = \frac{r_{rs}(\lambda) - R_{rs}^\infty(\lambda)[1 - e^{-2k_d(\lambda)d}]}{e^{-2k_d(\lambda)d}} \quad (9)$$

where R_{rs}^∞ denotes remote sensing reflectance of optically-deep water. The parameter k_d is the spectral diffuse attenuation coefficient that characterizes the propagation of light through the water column (Lee et al., 2005). Legleiter et al. (2016) estimated k_d by directly measuring the vertical profile of downwelling irradiance within water column using a spectroradiometer with waterproof accessories. In this study, we solve for k_d using water-leaving reflectances observed for different known depths and a homogenous bottom type adapted from (Maritorena, 1996; Fritz et al., 2017; Niroumand-Jadidi et al., 2018a). Considering a small reach of river with homogenous bottom types, the changes in bottom reflectances can be assumed negligible for a given pair of pixels, i.e., $r_{rs}^{B1} = r_{rs}^{B2}$. Then, k_d can be estimated by rearranging Equation 9 for each pair of pixels with different water depths (d_1, d_2):

$$k_d(\lambda) = \frac{\ln\left(\frac{r_{rs2}(\lambda) - R_{rs}^\infty(\lambda)}{r_{rs1}(\lambda) - R_{rs}^\infty(\lambda)}\right)}{2(d_1 - d_2)} \quad (10)$$

This approach requires R_{rs} coupled with corresponding depth information. Water depth can be measured in the field or inferred from the image using bathymetry models. This study estimates depths within the river channel using the proposed MODPA.

Deep-water correction (R_{rs}^∞) can be dispensed in bathymetry of shallow rivers particularly when the image is atmospherically corrected (Flener, 2013). However, in the context of riverbed mapping, Legleiter et al. (2016) collected the spectra over the deepest part of channel (~ 2 m deep) as an estimation of R_{rs}^∞ to perform the water-column correction. However, this assumption is subject to uncertainties in having effects from bottom particularly in clear or very shallow streams. Flener (2013)

proposed an iterative procedure to estimate L_∞ or R_{rs}^∞ in the absence of optically-deep waters in shallow rivers: the L_∞ or R_{rs}^∞ can be estimated by starting with an initial value and then its modification in an iterative process in such a way that the correlation between image/spectra-derived quantities (X) and the water depths (d) to be maximized. This research utilizes Flener's method (2013) for deep-water correction and then the impact of correction is examined on retrieving k_d and bottom reflectances.

This research investigates also the effectiveness of main terrestrial and aquatic VIs for detection of SAVs in shallow rivers (Table 2). In this regard, vegetation indices (VIs) with different band combinations are used to identify the SAVs before and after water-column correction.

VIs	Original formula	Alternative WV-3 band combinations
Terrestrial	$NDVI = \frac{R_{NIR} - R_R}{R_{NIR} + R_R}$	(NIR1, R) (NIR2, R) (RE, R)
Aquatic	$WAVI = (1 + L) \frac{R_{NIR} - R_B}{R_{NIR} + R_B + L}, L = 0.5$	(NIR1, B) (RE, B)

Table 2. Vegetation indices (VIs) used to study SAV.

The VIs such as the NDVI are widely used as indicators for fractional vegetation coverage (Elmore et al., 2000; Xiao and Moody, 2005). To evaluate the effectiveness of VIs for quantifying SAV densities, regression analyses are performed between VIs and SAV fractions where detailed fractions are known using the synthetic data. In addition, clustering of VIs are analyzed on laboratory and WV-3 data for detection of SAV density classes. The k-means algorithm, a frequently used unsupervised classifier, is applied to both above-water and retrieved bottom reflectances to map the riverbed classes. Then, statistics derived from confusion matrix are used for accuracy assessment, which include overall and user/producer accuracies as well as kappa coefficient.

3. STUDY AREA AND DATASETS

The Sarca River located in northeast Italy is selected as the case study. Sarca is a very shallow river in Italian Alps supplied with melting from the Adamello glaciers and flowing down into Lake Garda. The riverbed in the study area is composed of gravels (dolomite as the dominant material) with patches of SAV. The mean width of channel is about 30 m and the water depth < 1 m with an average of about 0.5 m in the study region.

To perform a comprehensive assessment of bathymetry and bottom reflectance retrievals methodologies, this study applies three different radiometric datasets, measured in laboratory, simulated using Hydrolight radiative transfer modeling (Mobley and Sundman, 2008), and collected by satellite sensors like WV-3. The laboratory experiments allow for controlled measurements of surface reflectances for flowing water with different SAV densities. The simulated spectra enable assessments of streambed mapping in a range of bottom types, water depths and IOPs representative of the Sarca River. The multispectral WV-3 image of the Sarca River is also used to classify SAV densities to assess the feasibility and effectiveness of water-column correction from space (Table 3). The measured and simulated reflectances are convolved with spectral responses of WV-3 and GeoEye sensors to allow for performing a consistent analysis.

3.1 Spectroradiometric experiments

A set of spectral reflectances is collected in an indoor hydraulic laboratory to test bathymetry and bottom reflectance retrievals models under controlled conditions of illumination, water level, IOPs and bottom properties. These experiments are, to the best of our knowledge, first of this kind that integrate spectroscopic and hydraulic facilities in an indoor laboratory.

Spectral reflectance measurements were acquired in a darkroom with an Analytical Spectral Devices (ASD) HandHeld 2 spectroradiometer operating within the 325–1075 nm spectral range. A standard ASD illuminator is used to produce highly stable light across the full visible/NIR spectral range (350 – 2500 nm). The spectral data were recorded by pointing a fiber optic jumper cable in a near-nadir viewing angles from 30-cm above water surface. The sensor’s field of view was adjusted to sample a cell centered across the channel to observe the spectral response of the flow avoiding any probable adjacency effects. The illumination geometry was modified to remove the instrument self-shadings over the flume (Gordon and Ding, 1992). Three spectra were recorded for each flow condition by averaging 25 individual samples. Radiometric calibrations including white reference and dark current observations were updated for recording each reflectance data to obtain the reflectance values. Four sets of data were collected over different bottom types, including non-vegetated gravel bed and three SAV densities (high, medium and low). For each set, dry bottom reflectance (representing exposed material) was first measured as the reference bottom reflectance. Then measurements were continued with 1 cm increments of water level up to 40 cm. Figure 4 shows the hydraulic flumes and the configuration of spectroradiometric measurements.

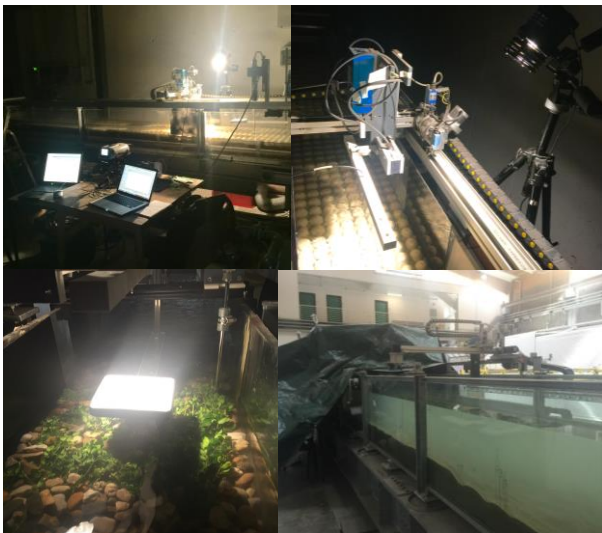


Figure 4. Hydraulic flumes and configuration of spectroradiometric experiments.

3.2 Radiative transfer simulations

This study utilizes radiative transfer simulations to gain more insights on bathymetry and streambed mapping in shallow riverine environments. The R_{rs} as well as the associated k_d are simulated using the widely used Hydrolight radiative transfer model (Mobley, 1994; Mobley and Sundman, 2008) for three different bottom types (i.e., macrophyte, dark sediment and dolomite) as well as a range of IOPs representative of the Sarca River and similar alpine rivers. Maximum and minimum values of the IOPs are selected based on long-term observations of water quality indicators documented by local environmental agencies. A database of simulations including more than 20,000 individual spectra was produced (see Table 3).

3.3 WV-3 image and in-situ measurements

To gauge the performance of the bottom reflectance retrieval methodology for SAV-density mapping, an 8-band WV-3 image (equivalent to WV-2 bands) over the Sarca River is employed. In-situ water depths and also information on SAV densities were recorded using a real-time-kinematic (RTK) GPS rover (Figure 5). The in-situ depth measurements were conducted along cross-sections in three reaches. To link field depths to image pixels, an ordinary kriging is used to interpolate the measured depths at pixel level (Legleiter and Overstreet, 2012). One-half of the data is used for calibration of the bathymetry model and the second half as validation for the accuracy assessment. For each patch of SAV, approximate areal coverage is documented to further evaluate the performance of clustering SAV-density classes.



Figure 5. Field observations using RTK GPS to record water depths and location of SAVs in the Sarca River.

4. IMPLEMENTATIONS AND RESULTS

4.1 Sub-pixel mapping of river boundaries

The semi-simulated as well as real water fractions are used as inputs for SRM algorithms. For instance, the sub-pixel maps obtained from the semi-simulated fractions are represented for a river segment in Figure 6. As it is clear from the illustrations, hard classification is very rough on the river boundaries, while the SRM techniques reconstruct boundaries with sub-pixel details.

Datasets	Spectral characteristics	Bottom types	Water depths	IOPs
Laboratory	Spectroradiometry with 1 nm resolution convolved to WV-3 and GeoEye bands	Non-vegetated gravel, SAV with different densities	0 to 0.4 m with 1 cm intervals	Clear water with low TSS (~ 2 g/m ³)
Synthetic	Hydrolight simulations with 10 nm resolution convolved to WV-3 and GeoEye bands	Sediment, Macrophyte and Dolomite	0 to 1 m with 2 cm intervals	TSS = 2-6 g/m ³ Chl-a = 1-5 mg/m ³ $a_{CDOM}(440) = 0.07-0.22 \text{ m}^{-1}$ TSS ~ 3 g/m ³
Satellite	8-band WV-3 image	SAV with different densities	0 to 0.8 m	Chl-a ~ 2 mg/m ³ $a_{CDOM}(440) \sim 0.09 \text{ m}^{-1}$

Table 3. Datasets used in this study and their specifications.

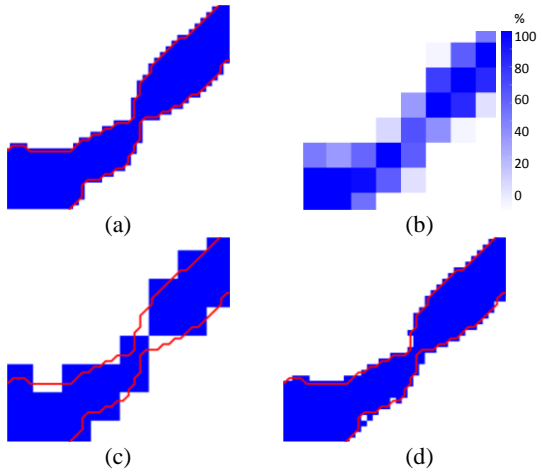


Figure 6. (a) Reference map, (b) semi-simulated water fractions ($ZF = 5$), (c) hard classified map, and (d) sub-pixel map derived from proposed MBPS method. Reference river boundaries are represented by red lines on each map.

Figure 7 shows user and producer accuracies of the river area extracted from hard classification and SRM methods.

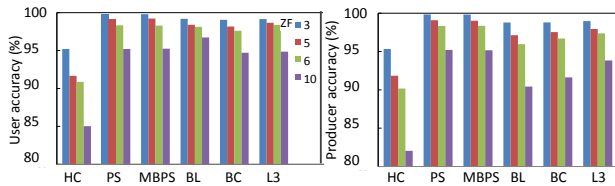


Figure 7. User and producer accuracies of hard classification and SRM algorithms using semi-simulated water fractions across a range of ZF; (HC: hard classification, PS: pixel swapping, MBPS: modified binary PS, BL: bilinear, BC: bicubic, L3: lanczos3).

The user/producer accuracies of hard classification are remarkably lower than that of sub-pixel maps. This issue gets worse with higher ZF where the difference between the accuracies of hard classification and SRM methods reaches above 10%. Interpolation-based SRM and MBPS lead to comparable accuracies with respect to the PS algorithm except at higher zoom factors ($ZF = 10$) where the producer accuracies of interpolation-based techniques are lower.

4.2 River bathymetry

The parameters of the bathymetric models are estimated using random half of the spectra observed over two flumes to get insights into the robustness of models with respect to substrate variations between the flumes. The depth retrieval models are validated using second half of the spectra and associated bathymetry information as of independent check points. Figure 8 represents the predicted vs. observed depths using laboratory spectra convolved with WV-3 band passes. As evident, the retrievals from OBRA are sensitive to the substrate types of the two flumes. This would be interpreted as relatively bright substrate of the flume-1 which is confused with shallower depths while the darker bottom-type of the flume-2 caused to an overestimation of depths. However, MODPA is very robust with respect to substrate variability.

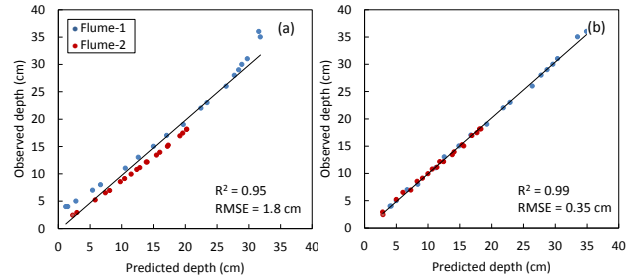


Figure 8. Validation of depth retrieval from WV-3 laboratory spectra based on (a) OBRA, and (b) MODPA using PLS regression.

Radiative transfer simulations are then used to test the performance of proposed MODPA in optically complex shallow waters with variable bottom-types and IOPs (Figure 9). MODPA leads to the highest correlation with known depths ($R^2 = 0.98$ and $RMSE = 6$ cm without considering extra predictors). Including the extra predictors enhances further the depth retrievals using MODPA ($RMSE = 3$ cm). This demonstrates the effectiveness of extra predictors for improving the robustness of bathymetry models in optically-complex waters. Matchups indicate significant improvement (i.e. 17 cm better RMSE) of depth retrievals using MODPA compared to the MODPA.

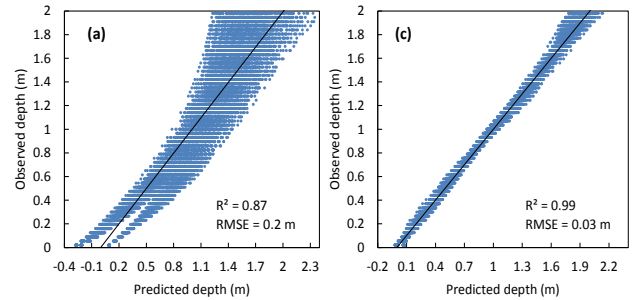


Figure 9. Match-up validation of depth retrievals based on (a) OBRA, and (b) MODPA with extra predictors for the optically complex spectra with variable IOPs and bottom types.

In Figure 10, bathymetry maps obtained from TOA reflectances of WV-3 image are compared with the in-situ depths within a reach of Sarca River. The accuracy statistics of bathymetry models with and without extra predictors are compared for WV-3 image and its convolution to GeoEye bands. In addition, AComp reflectances are examined against the TOA reflectances using the WV-3 image (Figure 11). In general, the AComp reflectances yielded higher accuracies than TOA reflectances. However, the accuracy enhancement is more pronounced for OBRA while the MODPA is less affected by atmospheric effects. Again, the three approaches for selection of optimal predictors provided comparable results whereas the method based on PLS regression is to some extent more accurate than others. This model applied on WV-3 image is composed of three Lyzenga predictors derived from CB, G and RE bands and two ratio predictors derived from G/R and G/NIR1.

Figure 12 illustrates the bathymetry map retrieved from WV-3 image for about five km long reach using the proposed MODPA and based on PLS regression.

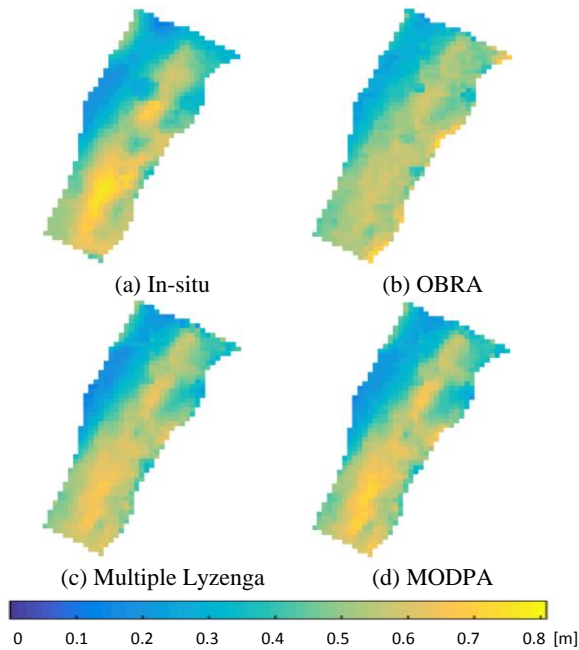


Figure 10. Comparison of in-situ depths with bathymetry maps derived from different models.

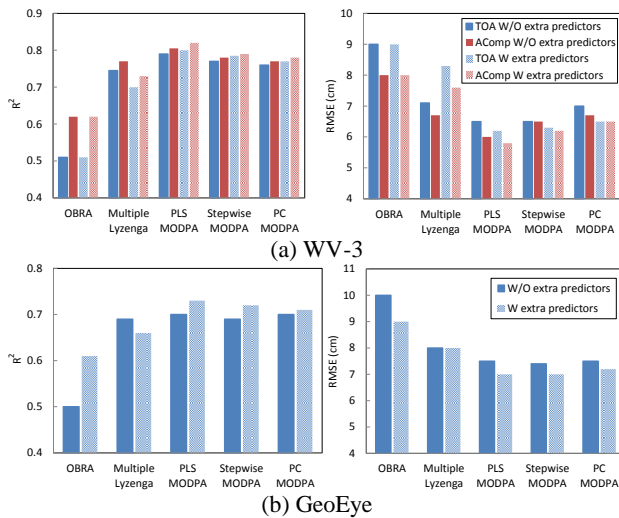


Figure 11. Accuracy statistics (R^2 and RMSE) of bathymetry models with (W) and without (W/O) extra predictors applied on (a) WV-3 and (b) GeoEye images. The comparison also performed for the TOA and AComp reflectances of the WV-3 image.

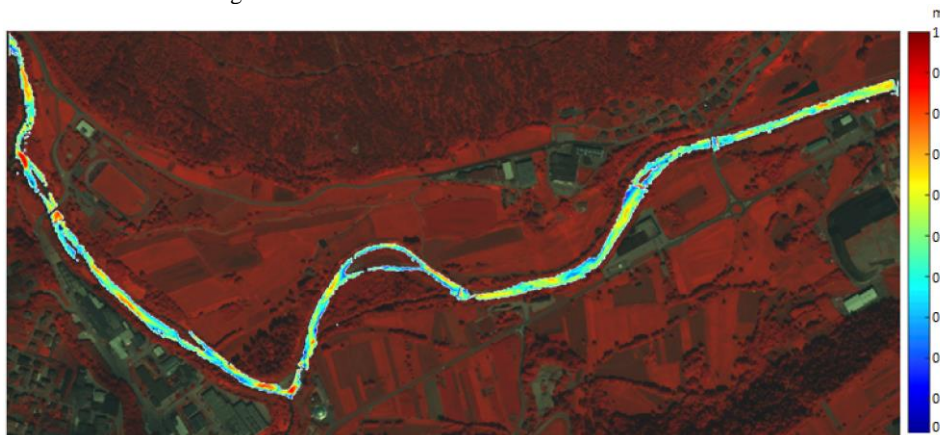


Figure 12. Bathymetry map derived from the proposed MODPA based on PLS regression using WV-3 image

4.3 Mapping of riverbed types and compositions

The retrieved bottom reflectances show good agreements with the measured reflectances at the laboratory particularly across the visible spectrum and the deep-water correction slightly improves the results (Figure 13). The error bars indicate the effects of changing water level, i.e., the smaller the error bars, the better the water-column correction is.

Figure 14 indicates the RMSEs for inferred bottom reflectances across a range of water depths considering constant IOPs. In general, bottom reflectances within the visible bands are retrieved with high accuracies and the water depth has less effect on RMSEs. The RMSEs for the NIR bands increase sharply with water depth particularly without applying deep-water correction. The effect of deep-water correction is pronounced for relatively deep water (depth > 0.5 m) where improves the bottom reflectance retrievals particularly in NIR spectrum.

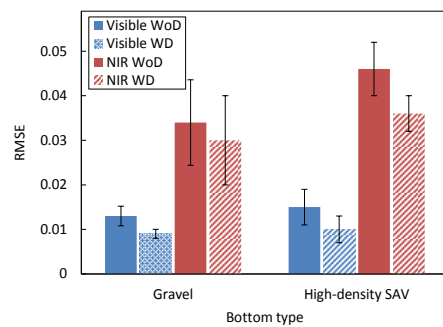


Figure 13. RMSEs for the retrieved bottom reflectances with (WD) and without (WoD) applying deep-water correction across visible and NIR bands using laboratory measured spectra.

The areal coverage of SAV patches gathered in the field was converted to a density index by dividing the observed area of a patch by the sensor's nominal spatial resolution (1.6 m \times 1.6 m for the WV-3 data used in this study). Then, the index values were clustered using k-means algorithm to three density classes used as a reference map (Figure 15a). The image-derived VIs (either before or after water-column correction) are clustered using k-means algorithm and compared with the reference map. The best results are achieved when the (RE, R) band combination is used, i.e., before and after water-column correction (Figures 15b and 15c).

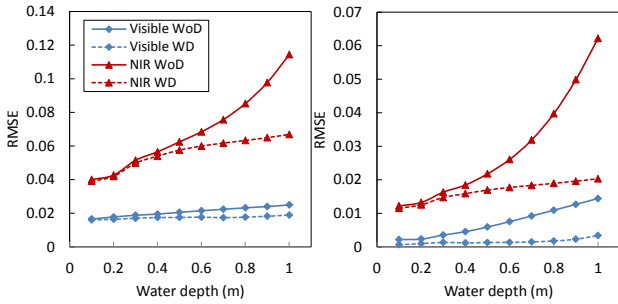


Figure 14. RMSEs of bottom reflectance retrievals across a range of water depths and three bottom types with and without deep-water correction (WD, WoD) using simulated spectra convolved to WV-3 spectral bands. IOPs are constant (TSS = 4 g/m³, Chl = 3 mg/m³, a_{CDOM}(440) = 0.14 m⁻¹).

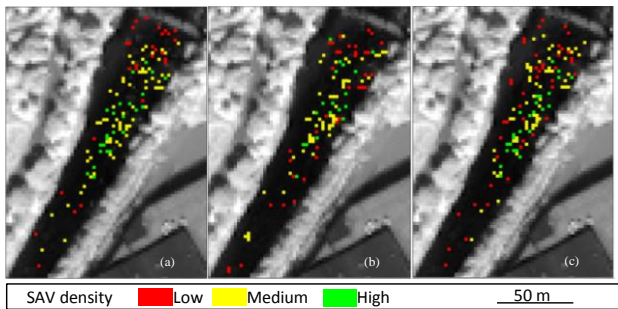


Figure 15. (a) In-situ map of SAV densities vs. maps derived from clustering VI with (RE, R) band combination (b) before and (c) after water-column correction.

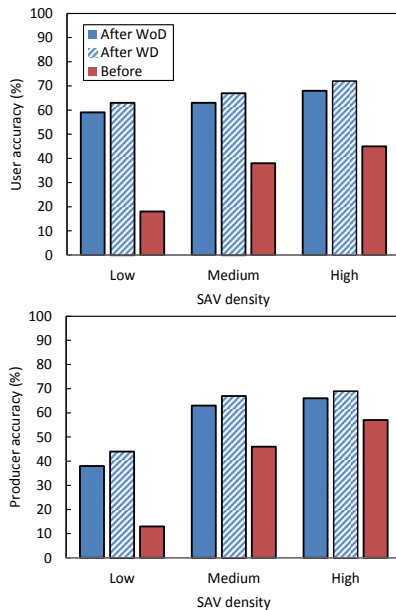


Figure 16. User and producer accuracies of SAV density clusters derived from WV-3 image based on VI with (RE, R) band combination before and after water-column correction with and without applying deep-water correction (WD, WoD).

The user and producer accuracies of SAV-density clusters indicate that the retrieved $r_{rs}^{B,WV-3}$ yield remarkably higher accuracies than R_{rs}^{WV-3} for all the SAV densities. However, the accuracies of clustering from R_{rs}^{WV-3} increase by increasing the

SAV density (45% user accuracy and 57% producer accuracy for high-density SAV). This is also valid for clustering from $r_{rs}^{B,WV-3}$ with a lower magnitude (Figure 16).

5. CONCLUSIONS

5.1 Sub-pixel mapping of river boundaries

Addressing the problem of mixed boundary pixels can enhance the accuracy of remote sensing applications in river sciences. Unmixing and SRM are key tools, respectively, for the spectral and spatial decomposition of the mixture in river boundaries. The former estimates the water fractions and the latter allocates the fractions in proper sub-pixel locations. Both of these steps have been the focus of this study in order to examine and develop the techniques for mapping of river boundaries at the sub-pixel resolution. Two different testing approaches are considered to survey the efficiency of SRM algorithms, while accounting for the absence and presence of uncertainty in the input data (i.e. fractions obtained from unmixing). Semi-simulated fractions are used as a contrived input with known fractions which provide a unique means of assessing the performance of the spatial allocation of sub-pixels. In the second testing approach, real water fractions are estimated based on a proposed method, namely OBA-NDWI, as well as using the fully-constrained algorithm of SPU. The OBA-NDWI performs the NDWI with all the possible combinations of spectral bands to identify the pair of bands for which the NDWI values yield the highest correlation with water fractions. To analyze the relation of NDWI values and water fractions through OBA-NDWI, a linear mixture of image-derived spectra is used to simulate all the possible mixing fractions of selected endmembers. The proposed OBA-NDWI method permits a systematic approach to find the optimal combination of bands for calculation of NDWI which can also be instrumental for images with high spectral resolution. This benefits both the hard and soft classification of water features where the highly-correlated NDWI to water fractions can enhance the accuracy of the extraction of water features either at the pixel or sub-pixel level. The semi-simulated and real fractions are employed for SRM based on the PS algorithm, as well as interpolation-based techniques. Moreover, the MBPS algorithm is developed to provide a non-iterative alternative to the traditional PS.

The proposed OBA-NDWI demonstrated that additional spectral bands of WV-3 imagery provide a couple of choices for selecting the proper pair of bands to form NDWI equation. Although the (CB, RE) pair is selected as the optimal combination of bands for the Sarca River, other combinations, such as (CB, NIR2), (B, RE), and a few other combinations also demonstrated a strong relation with water fractions. In this regard, making use of several NDWIs to establish a multiple regression for the prediction of water fractions can potentially lead to maximum benefit from spectral bands which can be an area of investigation for future studies. Furthermore, the number and quality of endmembers can affect the results of unmixing methods. In case of presence of an obviously different endmember in the riparian/buffer zone of the river, the number of endmembers can be increased through the unmixing process using OBA-NDWI. In this case, identification of the optimal bands would be performed locally. The OBA-NDWI method can be applied in a segment-based approach to identify the optimal bands for each desired segment of the channel.

The proposed OBA-NDWI method has the potential for selecting the proper threshold for hard classification using NDWI values which requires more investigation. OBA-NDWI

can be investigated further for sub-pixel mapping of any other land/water classes, such as coastlines, road and farm boundaries. Although the focus of this study was on HRSI due to the small size of the rivers, the proposed methodology can be applied on any other sensor (e.g. Landsat-8 and Sentinel-2).

5.2 River bathymetry

This research introduced MODPA to take the advantages of both Lyzenga and ratio depth predictors and also to integrate extra predictors obtained from the intensity component of HSI color space. In this regard, all the possible Lyzenga and ratio predictors derived from original image as well as the intensity bands of HSI color space are considered as initial predictors. A set of optimal predictors are then selected based on one of PLS, PC or stepwise regressions.

Lyzenga's single predictor is demonstrated to be very sensitive to variation between substrate types. Although this predictor is not appropriate for depth retrieval, it might have the potential for classification of riverbed compositions. The OBRA also showed a poor robustness with respect to substrate variability. Despite identification of optimal pair of bands for the ratio model, OBRA is a single predictor model and most likely neglects other explanatory variables. Multiple Lyzenga predictors enhanced the robustness of model with respect to variable bottom types. However, this model does not account for any process to select optimal predictors that most likely lead to having correlation among regression parameters. This problem would arise more significantly when hyper-spectral imagery or extra predictors are used. As it can be inferred from the results, the multiple Lyzenga model with extra predictors is less accurate than that of without any extra predictor using WV-2 data. This suggests making use of extra predictors when a selection process is performed on the predictors. As OBRA and proposed MODPA identify the optimal predictor/s, they yield improved results with extra predictors. More specifically, the single predictor of OBRA for the GeoEye image is resultant from extra predictors. This shows the effectiveness of extra predictors for bathymetry mapping from the imagery with low spectral resolution. The results of bathymetry models applied on simulated spectra suggest the robustness of MODPA with respect to changes in each of IOPs (TSS, Chl-a and CDOM) and also in optically-complex rivers where all the IOPs as well the bottom types are variable. The extra predictors improved the results of MODPA in the testing scenario associated with the optically-complex rivers (3 cm improvement of RMSE for depths up to 2 m). The simulated spectra comprise high concentrations of IOPs which are representative for turbid rivers in the study area (alpine rivers such as Sarca). However, more research should be dedicated to study other turbid rivers to further explore the potentials of bathymetry models.

The enhanced spectral resolution of WV-3 showed benefits for mapping the bathymetry of shallow rivers. For instance, the long-wavelength bands including RE and NIR-1 demonstrated to be useful as Lyzenga predictors or as denominator of ratio predictors. This is mainly because the attenuation of light in shallow and clear rivers does not get saturated even for long/highly-absorbing wavelengths. On the other hand, short-wavelength bands (e.g. B, CB, G and Y) performed as appropriate numerator bands for the ratio predictor. In summary, WV-3 sensor provides wealth of options for selecting either Lyzenga or ratio predictors and leads to higher accuracies than when using conventional 4-band HRSI (e.g. improvements of R² and RMSE respectively on the order of 9% and 1 cm using TOA reflectances without extra predictors). AComp reflectances yield relatively higher accuracies than TOA data

which is more pronounced for OBRA (improvements of R² and RMSE on the order of 11% and 1 cm, respectively). However, multiple-predictor models particularly MODPA showed robust bathymetry retrievals with respect to atmospheric effects. The first tests on DigitalGlobe AComp indicate the effectiveness of this product for mapping the bathymetry of shallow and clearly flowing rivers. However, more studies should be dedicated to comprehensively analyze the quality of AComp product for remote sensing of inland waters.

The proposed MODPA provided promising results and improvements for bathymetry retrieval in Sarca River using WV-3 image. The best result derived from MODPA based on PLS regression using AComp reflectances where R² and RMSE are estimated as 0.82 and 5.8 cm, respectively. Although three investigated regression methods provided very comparable results, the PLS-based regression showed slightly accurate results. Additional extra predictors can possibly be considered (e.g. spectral water indices) particularly for low spectral resolution imagery or for studies on optically-complex waters which requires more investigations.

5.3 Mapping of riverbed types and compositions

In this research, retrievals of bottom reflectances and mapping riverbed types and compositions are addressed comprehensively. Unlike bulk of the literature (Visser et al., 2013; Flynn and Chapra, 2014), a water-column correction approach is pursued to map the bottom properties by retrieving the bottom reflectances rather than using the above-water spectra. The methodology accounts for the water-column attenuation by estimating k_d for which some known depths are required over a homogenous bottom type. Water depth for each pixel is needed along with the k_d parameter to retrieve the bottom reflectance. A multiple linear regression method was used to derive the bathymetry which uses all the spectral bands and provides robust depth retrievals for different substrates and various IOPs. Then, a portion of in-situ depths used for calibration of the bathymetric model and/or image-derived depths over a homogenous bottom type can be used for estimating k_d , i.e., the key parameter for bottom reflectance retrieval, so that no further in-situ efforts are required for direct k_d measurements.

Here, the bottom reflectance retrievals and substrate-type mapping have been explored via three independent experiments. The spectroscopic measurements in the hydraulic laboratory and simulations from radiative transfer modeling provided the study with a thorough understanding of streambed mapping and the driving factors, such as water depth, IOPs, deep-water correction, and choices of spectral bands. Further, in a first attempt to map substrate properties from space, an 8-band WV-3 image of a reach in the Sarca River analyzed for classifying SAV densities. The results from spectroscopic measurements and simulations suggest that k_d and bottom reflectance retrievals are more accurate in the visible bands than in the NIR bands, particularly for relatively deep waters (> 0.5 m). This is attributed to the rapid light attenuation towards longer wavelengths the NIR region, in particular, for "thicker" waters. However, deep-water correction demonstrated to be effective to enhance the retrievals in NIR spectrum when the water becomes deeper. This is reasonable as the main effect of deep-water correction is when the bottom reflectance approaches to zero. However, the effect of deep-water correction is negligible for visible bands in the range of water depths discussed in this study (< 1 m) as well as for the NIR bands in very shallow depths (< 0.5 m). Moreover, the effect of IOP variability is investigated on the bottom reflectance retrieval of the simulated

channel. It is inferred that when the sampled pixels for k_d retrievals are chosen from an area well representative of the IOPs of the stream, the streambed clusters are slightly more accurate (~ 2-3 %). However, the results of clustering are subjective to the level of spectral discrepancy of the bottom types. Further analyses of IOPs using synthetic data revealed that turbidity has less impact on r_{rs}^B retrievals in the visible bands. This is why increasing the turbidity reduced the accuracy of r_{rs}^B retrievals in the NIR bands. However, the deep-water correction again mitigates the effect of turbidity on retrievals of r_{rs}^B . Another key finding is that the water-column correction significantly improves riverbed mapping. This is also demonstrated in making distinction among SAV densities based on analyses of VIs where retrievals of bottom reflectances yielded VIs strongly correlated with macrophyte fractions. Of all band combinations used for terrestrial and aquatic VIs, the terrestrial VI with (RE, R) band combination was found to provide the highest correlation with the SAV fractions using either inferred r_{rs}^B ($R^2 = 0.85$ and $RMSE = 0.07$) or R_{rs} ($R^2 = 0.48$ and $RMSE = 0.2$). This band combination also yielded the most accurate clusters of SAV densities in the laboratory setting as well as in the WV-3 image analysis. In general, the R_{rs} showed potentials for detecting high-density SAVs in the Sarca River (user accuracy= 45% and producer accuracy= 57%). This indicates the effectiveness of WV-3's RE band (i.e., 705-745 nm) for mapping SAV densities. Moreover, enhanced spectral resolution of the WV-3 compared to the GeoEye provided higher accuracies (on the order of 5%) in mapping the streambed using synthetic data. Note that the k_d retrievals using the NIR2 band is slightly less accurate than that derived from GeoEye's NIR band. This can be attributed to the strong water-column attenuation in the NIR2. Nevertheless, the improved accuracies gained in the clustering experiment using WV-3 image indicated the overall efficacy of enhanced spectral resolution of this sensor compared to the traditional 4-band high resolution satellite imagery to map bottom compositions. This research demonstrated the effectiveness of spectroscopic experiments in an indoor environment of a hydraulic laboratory to study the bathymetry and bottom properties of very shallow waters. Experiments of this kind can be extended to study further attributes of fluvial systems such as grain size mapping (Niroumand-Jadidi and Vitti, 2017a), flow velocity and water quality indicators.

ACKNOWLEDGEMENTS

This work was carried out within the SMART Joint Doctorate (Science for the Management of Rivers and their Tidal systems) funded with the support of the Erasmus Mundus programme of the European Union. The author would gratefully appreciate ASD Inc. for awarding a short-term usage of HandHeld 2 spectroradiometer as of Alexander Goetz Instrument Support program.

REFERENCES

Adnan, N.A., Atkinson, P.M., 2012. Remote sensing of river bathymetry for use in hydraulic model prediction of flood inundation. Proc. – 2012 IEEE 8th Int. Colloq. Signal Process. Its Appl. CSPA 2012 (2012), pp. 159–163.

Ashworth P.J., and Ferguson, R.I., 1986. Interrelationships of channel processes, changes and sediments in a proglacial braided river. *Geografiska Annaler*, 68: 361–371.

Atkinson, P.M., 2009. Issues of uncertainty in super resolution mapping and their implications for the design of an inter-comparison study. *Int. J. Remote Sens.*, 30, 5293–5308.

Atkinson, P.M., 2005. Sub-pixel target mapping from soft-classified remotely sensed imagery. *Photogramm. Eng. Remote Sens.*, 71, 839–846.

Carboneau, P., Fonstad, M.A., Marcus, W.A., Dugdale, S.J., 2012. Making riverscapes real. *Geomorphology*, 137 (1),74–86.

Elmore, A.J.; Mustard, J.F.; Manning, S.J.; Lobell, D.B., 2000. Quantifying vegetation change in semiarid environments: Precision and accuracy of spectral mixture analysis and the normalized difference vegetation index. *Remote Sensing of Environment*, 73, 87–102.

Flener, C., 2013. Estimating deep water radiance in shallow water: adapting optical bathymetry modeling to shallow river environments. *Boreal Environment Research*, 18: 488–502.

Flener, C., Lotsari, E., Alho, P., Käyhkö, J., 2012. Comparison of empirical and theoretical remote sensing based bathymetry models in river environments. *River Research and Applications*, 28 (1), 118-133.

Foody, G., 2006. Sub-Pixel Methods in Remote Sensing. In: *Remote Sensing Image Analysis*; Springer: New York, NY, USA.

Fritz, C.; Doernhoefer, K.; Schneider, T.; Geist, J.; Oppelt, N. 2017. Mapping Submerged Aquatic Vegetation Using RapidEye Satellite Data: The example of Lake Kummerow (Germany). *Water*, 9, 510.

Gordon, H. R., and Ding, K., 1992. Self-shading of in-water optical instruments, *Limnology and Oceanography*, 37 (10).

Hugue, F., Lapointe, M., Eaton, B.C., Lepoutre, A., 2016. Satellite-based remote sensing of running water habitats at large riverscape scales: Tools to analyze habitat heterogeneity for river ecosystem management. *Geomorphology*, 253, 353–369.

Jawak, S.D., and Luis, A.J., 2016. High-resolution multispectral satellite imagery for extracting bathymetric information of Antarctic shallow lakes ", Proc. *SPIE 9878, Remote Sensing of the Oceans and Inland Waters: Techniques, Applications, and Challenges*, 987819.

Ji, L.; Zhang, L.; Wylie, B. 2009. Analysis of Dynamic Thresholds for the Normalized Difference Water Index. *Photogramm. Eng. Remote Sens.*, 75, 1307–1317.

Jiang, H.; Feng, M.; Zhu, Y.; Lu, N.; Huang, J.; Xiao, T., 2014. An Automated Method for Extracting Rivers and Lakes from Landsat Imagery. *Remote Sensing*, 6, 5067–5089.

Lee, Z.P., Carder, K.L., Mobley, C.D., Steward, R.G., and Patch, J.S., 1998, Hyperspectral remote sensing for shallow waters: 1. A semi-analytical model, *Applied Optics*, 37, 6329 – 6338.

Legleiter, C.J., and Overstreet, B.T. 2012. Mapping gravel-bed river bathymetry from space. *Journal of Geophysical Research-Earth Surface*, 117(F04024).

- Legleiter, C.J., Roberts, D.A., and Lawrence, R.L. 2009. Spectrally based remote sensing of river bathymetry. *Earth Surface Processes & Landforms*, 34(8): 1039-1059.
- Legleiter, C.J., Roberts, D.A., Marcus, W.A., Fonstad, M.A., 2004. Passive optical remote sensing of river channel morphology and in-stream habitat: Physical basis and feasibility. *Remote Sensing of Environment*, 93: 493–510.
- Legleiter, C.J., Stegman, T.K., and Overstreet, B.T. 2016. Spectrally based mapping of riverbed composition. *Geomorphology*, 264: 61-79.
- Lyzenga, D.R., 1978. Passive remote sensing techniques for mapping water depth and bottom features. *Applied Optics*, 17, 379–383.
- Lyzenga, D.R., 1981, Remote sensing of bottom reflectance and water attenuation parameters in shallow water using aircraft and Landsat data, *International Journal of Remote Sensing*, 2:1, 71-82.
- Lyzenga, D.R., Malinas, N.P. and Tanis, F.J., 2006. Multispectral bathymetry using a simple physically based algorithm, *IEEE Transactions on Geoscience and Remote Sensing*, 44(8), 2251-2259.
- Marcus, W. A., and Fonstad, M.A., 2010. Remote sensing of rivers: The emergence of a subdiscipline in the river sciences, *Earth Surface Processes & Landforms*, 35(15), 1867–1872.
- Maritorena, S. 1996. Remote sensing of the water attenuation in coral reefs: A case study in French Polynesia. *International Journal of Remote Sensing*, 17, pp. 155–166.
- Mobley, C.D., 1994. *Light and water: Radiative transfer in natural waters*. Academic: San Diego, USA.
- Mobley, C.D., 1999. Estimation of the remote-sensing reflectance from above-surface measurements. *Applied Optics*, 38 (36), 7442–7455.
- Mobley, C.D., and Sundman, L.K., 2008. *Hydrolight 5, Ecolight5 User Guide*, Sequoia Scientific, Inc., Bellevue.
- Niroumand-Jadidi, M. and Vitti, A., 2015. Sub-Pixel Mapping of Water Boundaries Using Pixel Swapping Algorithm (Case Study: Tagliamento River, Italy), *Proc. SPIE 9638, Remote Sensing of the Ocean, Sea Ice, Coastal Waters, and Large Water Regions 2015*, 96380G.
- Niroumand-Jadidi, M. and Vitti, A., 2016a. Optimal Band Ratio Analysis of WorldView-3 Imagery for Bathymetry of Shallow Rivers (case Study: Sarca River, Italy), *ISPRS- International Archives of the Photogrammetry, Remote Sensing and Spatial Information Sciences*, Volume XLI-B8, 2016, pp. 361-364. doi:10.5194/isprsarchives-XLI-B8-361-2016.
- Niroumand-Jadidi, M. and Vitti, A., 2017a. Grain Size Mapping in Shallow Rivers Using Spectral Information: A Lab Spectroradiometry Perspective, *Proc. SPIE 10422, Remote Sensing of the Ocean, Sea Ice, Coastal Waters, and Large Water Regions 2017*, 104220B.
- Niroumand-Jadidi, M., and Vitti, A., 2016b, Improving the accuracies of bathymetric models based on multiple regression for calibration (case study: Sarca River, Italy), *Proc. SPIE 9999, Remote Sensing of the Ocean, Sea Ice, Coastal Waters, and Large Water Regions 2016*, 99990Q.
- Niroumand-Jadidi, M., and Vitti, A., 2017b. Reconstruction of River Boundaries at Sub-Pixel Resolution: Estimation and Spatial Allocation of Water Fractions. *ISPRS International Journal of Geo-Information*. 6(12):383.
- Niroumand-Jadidi, M., Pahlevan, N. and Vitti, A., 2018a, Bottom reflectance retrieval in shallow rivers: Findings from laboratory experiments, radiative transfer modeling, and high-resolution imagery, *Remote Sensing of Environment* (under revision)
- Niroumand-Jadidi, M., Vitti, A. and Lyzenga, D.R., 2018b, Multiple Optimal Depth Predictors Analysis (MODPA) for River Bathymetry: Findings from Spectroradiometry, Simulations and Satellite Imagery, *Remote Sensing of Environment* (under revision)
- Overstreet, B.T., and Legleiter, C.J. 2017. Removing sun glint from optical remote sensing images of shallow rivers. *Earth Surf Processes & Landforms*, 42(2): 318-333.
- Shintani C., and Fonstad, M.A., 2017. Comparing remote-sensing techniques collecting bathymetric data from a gravel-bed river, *International Journal of Remote Sensing*.
- Stumpf, R. P., Holderied, K., and Sinclair, M., 2003. Determination of water depth with high-resolution satellite imagery over variable bottom types. *Limnology and Oceanography*, 48, pp. 547–556.
- Thornton, M.W.; Atkinson, P.M.; Holland, D.A., 2006. Super-resolution mapping of rural land cover objects from fine spatial resolution satellite sensor imagery. *International Journal of Remote Sensing*, 27, 473–491.
- Visser, F., Wallis, C., Sinnott, A.M., 2013. Optical remote sensing of submerged aquatic vegetation: opportunities for shallow clear water streams. *Limnologica Ecol. Manag. Inland Waters*, 43 (5), 388–398.
- Westaway, R.M., Lane, S.N., and Hicks, D.M., 2001. Airborne remote sensing of clear water, shallow, gravel-bed rivers using digital photogrammetry and image analysis. *Photogrammetric Engineering and Remote Sensing*, 67: pp. 1271–1281.
- Wetherley, E.B.; Roberts, D.A.; McFadden, J. Mapping spectrally similar urban materials at sub-pixel scales. *Remote Sensing of Environment*, 2017, 195, 170–183.
- Woodget, A.S., Carbonneau, P.E., Visser, F., and Maddock, I.P., 2014. Quantifying submerged fluvial topography using hyperspatial resolution UAS imagery and structure from motion photogrammetry. *Earth Surface Processes and Landforms*, 40: 47–64.
- Xiao, J.; Moody, A., 2005. A comparison of methods for estimating fractional green vegetation cover within a desert-to-upland transition zone in central New Mexico, USA. *Remote Sensing of Environment*, 98, 237–250.

SENSEABLE SPACES: FROM A THEORETICAL PERSPECTIVE TO THE APPLICATION IN AUGMENTED ENVIRONMENTS

Roberto Pierdicca^{1, *}

¹ Università Politecnica delle Marche, Dipartimento di Ingegneria Civile, Edile e dell' Architettura - r.pierdicca@staff.univpm.it

Commission N/AWG N/A

KEY WORDS: Geomatics, Digital Cultural Heritage, AR/VR, Geolocalization, GIS, Photogrammetry, Geosciences, Space Sensing

ABSTRACT:

Given the tremendous growth of ubiquitous services in our daily lives, during the last few decades we have witnessed a definitive change in the way users' experience their surroundings. At the current state of art, devices are able to sense the environment and users' location, enabling them to experience improved digital services, creating synergistic loop between the use of the technology, and the use of the space itself. We coined the term *Senseable Space*, to define the kinds of spaces able to provide users with contextual services, to measure and analyse their dynamics and to react accordingly, in a seamless exchange of information. Following the paradigm of *Senseable Spaces* as the main thread, we selected a set of experiences carried out in different fields; central to this investigation there is of course the user, placed in the dual roles of end-user and manager. The main contribution of this thesis lies in the definition of this new paradigm, realized in the following domains: Cultural Heritage, Public Open Spaces, Geosciences and Retail. For the Cultural Heritage panorama, different pilot projects have been constructed from creating museum based installations to developing mobile applications for archaeological settings. Dealing with urban areas, app-based services are designed to facilitate the route finding in a urban park and to provide contextual information in a city festival. We also outlined a novel application to facilitate the on-site inspection by risk managers thanks to the use of Augmented Reality services. Finally, a robust indoor localization system has been developed, designed to ease customer profiling in the retail sector. The thesis also demonstrates how Space Sensing and Geomatics are complementary to one another, given the assumption that the branches of Geomatics cover all the different scales of data collection, whilst Space Sensing gives one the possibility to provide the services at the correct location, at the correct time.

1. INTRODUCTION. A THEORETICAL PERSPECTIVE FROM AUGMENTED SPACES TO SENSEABLE SPACES

“Do we end up with a new experience in which the spatial and information layers are equally important?” With this question, Lev Manovic was introducing, in 2006, the revolutionary concept of *augmented spaces*; in (Manovich, 2006), the author synthesizes the space that we leave, made up of two layers: the physical (or tangible) dimension, and the digital (or intangible) one. The dissertation provides a very simple and clear definition of this paradigm: “augmented space is the physical space overlaid with dynamically changing information. This information is likely to be in multimedia form and it is often localized for each user”. Now, ten years later, we can witness to the realization of this concept in our daily life. The two dimensions seem to mesh-up, in a seamless relation between real and virtual. This is mostly because latest improvements on mobile devices capabilities are changing the way people interact with their surroundings. Nowadays, devices are able to sense the environment and users' location, enabling them to experience improved digital services. But this is not the only reason. In fact, mobile devices alone can just provide the users with tools (e.g applications) and services that can facilitate them in performing single tasks. Instead, along with the growing ubiquity of mobile technologies, they can be enabled to interact with the space, or better, with the objects that fit that space. And more, other data are produced from this interaction, creating a sort of loop between the use of the technology, and the use of the space itself. Starting from this assumption, this thesis addresses the topic of understanding the relation between the

space, people and technologies and investigates how the ubiquity of digital tools can augment our environments and can leverage new ways of interaction. It uncovers how data from sensors can be presented to the observer in an intuitive manner, in the context of the observed environment. In a focal role of this dissertation there is, of course, the user. Modern technological applications can dynamically deliver different kind of data to the users, or extract data from them, transforming the space from augmented to *Senseable*. In other words, the delivery of information to users in space, and the extraction of information about those users, are closely connected and pave the way towards the “*ability to sense and make sense*” of it.

1.1 Thesis outline

This research (here briefly summarized) was experienced with a multidisciplinary approach, covering a wide spectrum of domains and topics, addressing the problem of defining new methods of observing the dynamics of a space, collecting data and using them with the twofold purpose of providing services, and enhancing the space itself. The present work is aimed at providing a wide overview about the concept of *Senseable Space*, starting from the growing connection between the space and the technology and highlighting the importance of data, regardless the type of data we are dealing with. We generally use to think that every discipline has its own kind of data, like compartments that cannot mesh up and support each other. But so often we forget that because of its nature, a data represent a measure. If we deal with spatio-temporal data, or geo-spatial data, we are measuring an event. In this, Geomatics plays a pivotal role in terms of data acquisition from different data sources. For long

*Corresponding author

time, Geomatics has been considered the discipline to take measurement, rather than to measure an event. The provisioning of affordable data, their management, their loss less simplification is essential to provide users with services that improve their experience of a *Senseable Space*. The core idea behind this work was inspired by the new vision of *Space Sensing*, developed by the Senseable City lab that Carlo Ratti founded in 2003 at the MIT in Boston, USA. As the author of this thesis, Carlo Ratti is an architect which fulfilled the cause of interweaving his background of planner and designer with the usage of digital methods to uncover spaces' dynamics, analysing them in real time and predicting their changes. For the sake of brevity due to space constraints, the complete literature review has been omitted, even if interested readers can find the complete version published in (Bekele et al., 2018), where is reviewed the state of art about technologies and application that, more than others, have demonstrated of being suitable for the development of new kinds of interaction and to make a space *Senseable*. Among the others, Augmented Reality (AR) is the cutting edge technology in which we decided to investigate, since it embraces both the concepts of sensing the space and giving information. Complementary to the theoretical introduction, a wide set of use cases has been experienced. It represents the summa of different experiences, activities and best practices which can help to contribute, compared with the state of art, to better understand the paradigm of a *Senseable Space* in different research areas. For the Cultural Heritage panorama, different pilot projects have been constructed from creating museum based installations to developing mobile applications for archaeological settings. Dealing with urban areas, app-based services are designed to facilitate the route finding in a urban park and to provide contextual information in a city festival. We also outlined a novel application to facilitate the on-site inspection by risk managers thanks to the use of Augmented Reality services. Finally, a robust indoor localization system has been developed, designed to ease customer profiling in the retail sector. Building up such scenarios and architectures, we have attempted to address the following statement of the problem: are we able to design a space, regardless the domain, capable of bidirectional exchange of data between the space and the user? The thesis also demonstrates how Space Sensing and Geomatics are complementary to one another, given the assumption that the branches of Geomatics cover all the different scales of data collection, whilst Space Sensing gives one the possibility to provide the services at the correct location, at the correct time. Each use case have been divided, to facilitate the reader, into a hierarchical scheme: *Scenario, System Architecture, Results*. In this way we thought to better highlight the benefits that the different approaches (in different domains), brought to the users. Besides arguing over the possibilities that the proposed paradigm opens up in different topics, challenges, open issues and limitations have been broadly discusses. Finally, it is fair to say that, due to large amount of tests conducted and the number of publication came out from the thesis, this document will not provide details about each experiment and results, but relevant citation will be provided.

1.2 The relation between spaces, users and technologies

While this new research paradigm of *Senseable Spaces* have been outlined, what is still missing is a description of the "components" that could make it possible. Manovic gave several examples of applications and technologies widely adopted to dynamically deliver data to, or extract data from, physical space. Video surveillance for instance have become ubiquitous. Cameras, are able to serve several purposes: real time tracking, recognition, localization. As well, even if in a completely different way, mobile

phones act exactly in the same direction. Using the logs of a devices, we can understand the devices' position (via wireless connections in indoor, via GPS in outdoor) and from it give contextual information. But while the technologies imagined by these research paradigms accomplish their intentions in a number of different ways, the end result is the same: "overlaying dynamic data over the physical space". An old timeless quote by Mark Weiser (Weiser, 1991) affirms that the most profound technologies are those that disappear. Despite it was coined more than a decade ago, this sentence is still an important guideline for the development of smart objects. In the early nineties the idea of an environment with pervasive (but not intrusive) computing laid the foundations for Ubiquitous Computing. In the recent years, we witnessed to an improvement in the use of handy smart devices (e.g. mobile phones), insomuch that they are naturally extended to all areas of science like education, health, cultural heritage, entertainment, sports, transportation and many more, into a collaborative way of interaction. The key aspect for *Ambient Intelligence* lays in the possibility to provide services not for user request, but based over the intelligence of the system; this will allow the automatic provision of services depending of the profile and the position of the user experiencing a task. Consequently, the interaction between spaces and users should be done through natural interfaces adapting to them habits and behaviours. To allow this interaction, it is enough to pair with their mobile devices. A network of sensor allows processing the context through the user interaction in real time (Heidemann and Govindan, 2005), (Fernández et al., 2011). Besides, provides analytic taken from users' interaction with spaces; in the retail sector for instance, it can give many information about customers, allowing the retailer to customize the shop to their needs and adapting product arrangements, expositions, design according to their behaviours. Data extracted in this way are objective; indeed, this kind of decision-making process is lead to an objective and reliable data collection. Intellectual approaches are not able to explain the complexity of consumer behaviours, because they arise from many aspects such as cultural context, habits and so on. Several aspects of these problems are currently solved using artificial intelligence and, in particular, vision (Mancini et al., 2013). Notwithstanding, the efforts backed to provide and obtain data, are joint by a fundamental action: to measure. We witnessed to the tremendous growth of localization, even thought with different methods and aims. But localize means measure. Moreover, the main task demanded to a *Senseable Space*, is to measure a certain event and, if possible, to react on it through the provisioning of services to the user. Obviously, those actions are possible just with the use of data, measured data. And it is exactly in this dichotomy that geomatics plays a pivotal role, the science of collecting and providing data, that, in turns, have been measured as well. In the following, a brief dissertation about the "new" meaning of Geomatics will be given: Geomatics as a fundamental source of data

1.3 Geomatics: a fundamental source of data

We have described, up to know, the new possibilities offered by devices, sensors and technologies to *sense* the environment; the data exchange among the user and the space proved to be a winning solution for several domains: urban planning, indoor spaces (e.g. museums), geography, retail and many more. We also described some of the services that can be provided to the user according to their location. However, the service for the users cannot be seen just like a notification in a phone or just the number of visitor of a space. The services for the users come from data that they can: interact with, manage and that can improve their knowledge about that specific space. To provide users

with contents, there is the need to collect information, from different data sources, and to present them in the right form to be managed. Taking into account the introductory statement that a *Senseable Space* is such, just if we are able to measure it, along with the changing dynamics in it, the applied science which brings a strong contribution in this direction is geomatics. A revolutionary turning point about the concept of geomatics was brought by the research paper titled "Geomatics and the new Cyber-Infrastructure" (Esche and Blais, 2008). Authors state that geomatics deals with multi-resolution geospatial and spatio-temporal information for all kinds of scientific, engineering and administrative applications. This sentence can be summarized as follows: geomatics is far from the concept of simply measuring distances and angles. A few decades ago, surveying technology and engineering involved only distance and angle measurements and their reduction to geodetic networks for cadastral and topographical mapping applications. Survey triangulation, trilateration and even precise levelling have now largely been replaced by Global Positioning System (GPS) applications for positioning and navigation in various modes of implementation. Satellite imagery of various types and specifications are becoming available globally in near real-time for environmental and related applications. Multi-resolution geospatial data (and metadata) refer to the observations and/or measurements at multiple scalar, spectral and temporal resolutions, such as digital imagery at various pixel sizes and spectral bands which can provide different seasonal coverages. Surveying still plays a leading technological role, but it has evolved in new forms: positioning and navigation can be obtained with several devices that were not properly conceived to accomplish these tasks; topographical mapping, one time conducted with bulky instruments requiring complex computation made by the workers, has now become a byproduct of Geospatial or Geographical Information Systems (GIS); digital images, obtained with different sensors (from satellite images to smartphones), can be used to accomplish both the tasks of classifying the environment or make a virtual reconstruction. Survey networks and photogrammetric adjustment computations have largely been replaced by more sophisticated digital processing with adaptive designs and implementations, or ready to use equipments like Terrestrial Laser Scanners (TLS). The transition from analogue to digital methodologies, moreover, has not only resulted from the availability of ubiquitous computers, but has shown to be superior in just about every aspect of data processing and information extraction and identification. Furthermore, as in many other fields of endeavour, computation is now regarded as a primary driver of innovation. This scenario makes it clear that the digitalization of information enables a rapid and wide dissemination of knowledge, increasing the number of people that can have access to data, improving the sharing and enhancing the quality and the accuracy of the knowledge itself (Condotta and Borga, 2012). Moreover, the actual amount of sensors and measuring systems of physical and environmental phenomena allows us to talk easily about "Space Sensing" as a widespread and pervasive approach to understanding the dynamics of the contemporary environments (both indoor and outdoor). What is still missing is the possibility to provide the user with these data in a complete form, and more, how the physical conformation of the space can be changed from the information extracted from it. A huge help can be exploited from geomatics applications, which are able to cover different working scales (Lambers and Remondino, 2008), as well as to produce different outcomes that are useful for the whole meaning of a *Senseable Space*. Analysis tasks can be performed at a regional level thanks to the use of high resolution images from satellite or aerial images; inferring information is pos-

sible thanks to land usage classification (Malinverni et al., 2011), as well describing the shape thanks to ranging techniques like LiDAR and Radar pulse. Dealing with architectural scale complex objects, the possibilities offered by new acquisition devices are wide. Low cost equipments (i.e. cameras, small drones, depth sensors, and so on) are capable to accomplish reconstructions tasks. Of course, there is also the accuracy issue to take into account; in fact, geo-referencing complex models requires more sophisticated and accurate data sources like GNSS (Global Navigation Satellite System) receiver or TLS. In the case of small objects or artefacts, terrestrial imagery and close range data are the best solution to obtain detailed information about them. Thus, since we live in an almost well connected digital world, geomatics can play a new role in research and development involving geospatial and related information, as well as creating entrepreneurial opportunities. The following are listed some potential areas of application that are closely related to geomatics, emerged from the previous analysis: natural environment, quality of life in rural and urban environments, predicting, protecting against and recovering from natural and human disasters, archaeological sites documentation and preservation, just to mention some. We can summarize that geomatics is able to cover the spectrum of almost every scale; even though there is no panacea, the integration of all these data and techniques is definitely the best solution for 3D surveying, positioning and feature extraction. This concept will become more clear in the Chapter 3, where the set of scenarios described demonstrates that the winning solution for the different domain is the merging of data from different sources. Data fusion, or data integration, refers to the process of merging data (and knowledge) coming from different sources (or sensors) - and, generally, at different geometric resolution - but representing the same real-world object in order to produce a consistent, accurate and useful representation. Data fusion processes are often categorized as low, intermediate or high, depending on the processing stage at which fusion takes place. Low level data fusion combines several sources of raw data to produce new raw data. The expectation is that fused data is more informative and synthetic than the original inputs (Ramos and Remondino, 2015). As well, data visualization has to be considered a core step of the system. If, for example, we are dealing with environmental monitoring tasks, the starting point is a map, obtained with well established processes. From it, it is possible to infer information and extract knowledge of a large scale territory. And, it can also be managed into a GIS environment to add (meta)data to it. However, the map can be fully exploited directly on site, where the operator have the possibility to perform his task with the help of the real environment. The task of the *Senseable Space* is to provide this information to the operator in real time, for instance with his own mobile device. But it is not enough; for completing the system, it is necessary that the user is able to visualize the map, to update its own information, and in the meanwhile to be monitored in his task (for instance by using his Digital Footprints), so that the bidirectional process of providing/getting information can be accomplished. The same example can be done for indoor spaces. If we imagine a space where some sensors (e.g. beacons) are able to track people movement, one of the main task delegated to geomatics is to perform his/her geo-location into the WSN built. If we know the position of this user (e.g. visitor in the case of a museum, a customer in the case of a retail mall), we can provide him with contextual information. These information are always asked to be produced with geomatics techniques (3D reconstructions for instance), that need both acquisition and computation tasks to be visualized in the proper way. Finally, the knowledge of the visitor path provides useful insights to re-arrange the space, if, for

instance, some of these data are not visualized or some areas are not visited. The ones given above are just few examples of how spatial data are a fundamental component of a *Senseable Space*. All the scenarios that have been implemented move in this direction; a multidisciplinary work, experienced in different domains, with the main thread of providing/extracting data, with the user at the center, computer science as the link, and Geomatics as the mean.

2. BACKGROUND

Summarizing all the above-mentioned topics, researches and technologies into one laboratory, in 2003 Carlo Ratti founded the *Senseable* city lab at the MIT of Boston, USA. The core activities of the lab are oriented towards a pervasive data collection from users, from different data sources, to uncover humans dynamics and to support planners. In fact, since the spaces are generally designed for humans activities, the planning community should be interested from this gathering of information. As stated by Carlo Ratti “the way we describe and understand cities is being radically transformed, alongside the tools we use to design them and impact on their physical structure”. Human activities, nowadays, are strictly related to the use of their mobile phones. From them it is possible for instance, in different way that we will describe in the following, to extract data about vehicles. By tracking the single identifier (ID) of each device, or just analysing the phone calls by cells, we can monitor vehicle origins and destinations that is fundamental for the planning process of the infrastructures of a city. Several critical issues, like for instance patterns of congestion, can be derived. Moreover, to understand the benefits from a new area, will be useful to get the pedestrian flows (Bojic et al., 2015) for inferring patterns from humans tracking (e.g. via GPS positioning services). The main project of the lab have been reviewed, in order to enhance the knowledge and move the applications developed from the city scale to smaller ones but in multiple scenarios. Some projects, developed for outdoor environments, deals with Location Based Services (Ratti et al., 2006), (Grauwin et al., 2015), other with the monitoring and tracking the so-called User Generated Data (UGDs) (Golder and Macy, 2014), other (Outram et al., 2010). Some experiences have been even conducted for indoor environments, and especially for museums, like in (Yoshimura et al., 2014). From the above emerged that the use of data collected from humans’ activity, monitored through different kinds of connections and technologies, is possible to embrace an incredible number of domains (tourism, urban planning, environmental monitoring) and to address different needs (contextual services, planning criterion establishment, hazards identification). The use of large-scale datasets enables managers to discover and analyze frequent patterns in human activities. Such analyses have been conducted in the specific spatio-temporal range. All these information are needful to improve the space layout and eventually intervene in a more reliable and efficient way. The analysis of the works by the *Senseable City* lab demonstrates that this research topic is emerging and could bring its benefits in almost every domain in which the planning process is required.

3. USE CASES AND RESULTS. APPLICATIONS OF SENSEABLE SPACES

As showed in the previous Sections, the augmentation of the space is entrusted to the ability of developing a bidirectional interaction between the users and the space they live. The aim of the

research activity conducted during the years of the Ph.D. studies by the author, is oriented towards the use of sensors, devices and technologies able to make the concept of *Senseable Space* real. The goal of understanding the dynamics of a space starting from the knowledge of the users was experienced in different domains of applications. This for two reasons: first of all, even if the main activities where conducted into the CH domain, it was not sufficient to understand the limits and benefits of this paradigm only by exploring a single topic. Secondly, different domains have different needs, so that to understand the potential of *Senseable Spaces*, it was fundamental to face with different scenario and, eventually, to outline points of contact. Following the paradigm of *Senseable Spaces* as the main thread, we selected a set of experiences carried out in different fields; at the center of this investigation there is of course the user, in the double meaning of end-user and manager. Besides, both indoor and outdoor scenario have been explored, since the knowledge of the operational condition of a space is a mandatory requirement to use the technology in the most proper way. The main topics of investigation have been the following: **Cultural Heritage**, described through several applications in both museums and archaeological settings, **Public Open Spaces**, where the core activities where performed within the framework of the European project *CyberParks*, **Geosciences** through the case study of an ad-hoc application for environmental monitoring and finally **Retail Environments** that, because of its nature of being a pervasive environment, a *Senseable Space* can be built in its whole meaning. Only one case for each domain have been chosen, referring the reader to the related publication for a deepen analysis.

3.1 Senseable Spaces and Digital Cultural Heritage

In the CH valorisation and communication, ICT offer an easier access and a multi-perspective view of artefacts and can also increase education, thanks to the use of innovative learning/teaching methods (Ott and Pozzi, 2011). Visitors of a museum can interact with the content in the most interesting way thanks to the introduction of ICT. In the last years, many researches have been aimed at providing museums with interfaces and software tools. Their intention is to develop web-based virtual museum devices integrating 3D computer graphics and augmented reality (AR). The purpose of making a heritage site *Senseable*, can be reached with the twofold approach of giving services to the visitors and collecting their insights to improve the service provided. In this specific domain of course, a fundamental step to provide high quality content is demanded to Geomatics applications. In fact, dealing with complex architectures and spatial data in general, the data collection phase, that seems to be just a preliminary phase, become essential. TLS, Multi-view Stereo (MVS) matching, GPS and other sources are, up to now, well established solutions that could bring a great benefit. However, the management of the quality, as well as the construction of an affordable workflow that ranges from the acquisition to the visualization in a *Senseable Space*, is not totally established so far. The interaction with virtual contents, their visualization in different devices, the ability of devices to sense the environment in order to provide contextual information are all elements that play a pivotal role. And more, since the curators have the need to understand if the services provided are accessible and usable for the users, there is also the necessity to analyze their behaviour for the improvement of these services. Given the above, in the following we show different use cases, selected as the more relevant among the works conducted in the CH domain, experienced for both museums and archaeological settings and demonstrating,

in the results sections, how the use of the developed digital tools have increased the value of the scenario where they have been used.

3.1.1 Real case exhibitions in museums environments Exhibitions are becoming ever more interactive. Museums undertaken the strategy of offering technological services to its visitors; furthermore, insiders are increasing their awareness about the need to provide visitors innovative solution of experiencing art. The spreading of advanced digital tools (e.g. mobile applications, addictive interaction systems and multimedia contents) made possible a new paradigm for art installations. New trends in the international panorama demonstrate how such innovative tools are the best (and only) way to enhance the fruition of CH. Through digital tools, the museum experience becomes a lay experience of culture and then the art seems democratic. The taxonomy proposed in this thesis about the use of AR in different sub-areas of CH demonstrate this trend. Up to now, what is missing, is the real exploitation of the pervasive nature of mobile devices. In fact, so often digital installations require cumbersome equipment that place the user in another dimension (like for instance with the use of Virtual Reality (VR) experiences) and that need skilled staff to train the users to perform the task. Mobile devices and simple interfaces have the capabilities to reach the vast majority of the public, in an interaction that move from a “one to one” to a “one to many” experience. But this is not the only issue. The knowledge of the users’ insights is needed, if we want the evolution of the digital product itself. The study cases proposed in the following go in this direction. Starting from the famous painting “La città ideale”, we developed, tested and delivered several AR tools that are able to give new hints to the exhibition without the need of further equipments, apart from the device that single visitor have at his disposal. A specific focus was also devoted on the user behaviour understanding, using both classical direct interviews and eye tracking technology. For the purpose of the present document, this latter part will not be detailed, referring the reader to the related publication (Naspetti et al., 2016). Moreover, for the sake of completeness, AR technology has been implemented for other scenario, dealing respectively with complex architectures and in relation with GIS environment. These works can be found in (Clini et al., 2016) and (Quattrini et al., 2016).

3.1.2 Scenario 1: Augmenting paintings through AR. The usefulness of a *Senseable Museum* is to provide cultural institutions with the best practices of digital interactions efficiently and with low budgets. Hence, this work started with the main objective of developing a low cost method for high-resolution acquisition of paintings that is used as a base of knowledge for the development of an AR application. The case study chosen was the famous painting “La città ideale”, preserved at the “Galleria Nazionale delle Marche” in Urbino. Starting from this experience, the work was extended and installed in a temporary exhibition about Piero della Francesca, that will be detailed in the following. The first problem we faced during the development of the AR application was the lighting condition inside the museum. In fact, artificial lights and protecting glass generate abrupt reflections that generally cause instability during the feature extraction phase (see the enabling technologies discussed in Chapter ??). Experimental results demonstrate the robustness of the proposed approach with extensive use of the AR application in front of the painting. The first step was to obtain a low cost acquisition way for high-resolution images. The acquired image was then used for the development of the mobile application and, later, for the installation described. Users tests in the real scenario were also

conducted to prove the usability and ensure a good user experience.

3.1.3 System architecture The first stage of this experience was the development of an AR tool, based on the whole painting image, designed to augment the painting. Once the app is launched, the device’s camera is activated and ready to recognize a target. Each of these points is represented as a marker and a billboard containing the name of the painting. This system shows the user the direction to follow to reach the painting through AR. For further information on how to reach a point of interest, the user has to only tap the corresponding geometry. This will display the path on the museum map from the current user position to the selected painting. The meaningful steps for the creation of the Ducale AR experience are the content creation, the web, and the final visualization. This last is the more challenging, since it is related to the lighting issue described above; the proposed methodology for the development of the AR tool consists of an improved SIFT extractor for real time image using a robust matching. The other novelty of this work is the multi-point probabilistic layer. Details about the methodology can be found in (Clini et al., 2014). The application was then required to be part of the real case exhibition *PIERO DELLA FRANCESCA. Il disegno tra arte e scienza*¹. The whole installation system (see Figure 1) is composed by a faithful (and real-scale) facsimile of the “Ideal City” painting and a touch-screen. The artwork is flanked by tablets which allow visitors to interact with multimedia contents thanks to the applications, already installed; inside the touch-screen the HR image of the painting is installed (refer to Figure 1 for a comprehensive overview of the installation). The

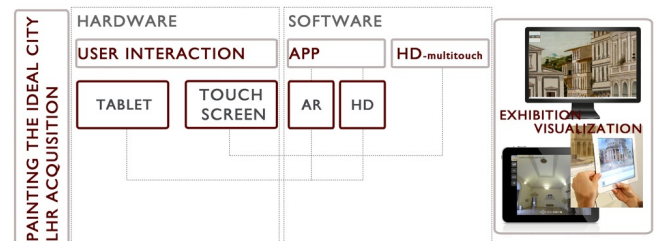


Figure 1. Phases and connections between elements: the production chain from the LHR acquisition to the exhibition.

different “visions” of the same artwork, here accessible, form a new way to communicate paintings and to facilitate its disclosure with edutainment practices. The HD makes more evocative looking at the painting, because it allows to watch it as well as the artist and to enter the will of representation. The “Città Ideale” app facilitates the link with the painting thanks to the technology, but the tool still needs the real art work, in its physical dimension, in a close relationship between art and technology.

3.1.4 Results A first result of this work is the successful creation and the validation of an easy work flow for HD images. The use of the “Città Ideale AR” macrophotography in mobile and web-based applications has shown good performances of the image, obtained in our process. “Città Ideale AR” app, starting from the aforementioned work, proposes an innovative solution of experiencing paintings, allowing to interact with all the available multimedia contents realized for this project. Some key aspects of the application are:

- augmented view of the artwork;

¹<http://www.palazzomagnani.it/2014/11/piero-della-francesca-il-disegno- tra-arte-e-scienza>

- improvement of knowledge and curiosity about the painting;
- stable POI selection for different lighting conditions.

Besides, we also performed a user test. In order to know the characteristics of the interviewed sample preliminary questions relating to age, academic qualifications, work, and the use of technology in general were initially asked. The system was tested on 15 different human subjects with age between 22 and 48, with different academic qualification and expertise. The question where oriented to understand the relation between the technological skills of the panellists and their knowledge about AR, in relation with the usability of the application (see (Clini et al., 2014)). Notwithstanding, our purpose was also to make the improvements based on a more rigorous approach, understanding in automatic way the behaviour of the users looking at the paintings. For this reason, the further step was to test eye-tracking technology and collect visitors data, as described in the following scenario.

3.1.5 AR and Geomatics to support Archaeology Archaeology underlies complexity and limitations that make the use of new media (and technologies) unavoidable. Two kinds of users can take advantage from this approach: the first ones being the insiders, like archaeologists, experts and conservators. They have access to innovative acquisition techniques allowing a quick and low cost data gathering. The second ones are the visitors, who can exploit the potentials of new ways of communication to improve their knowledge. However, particularly in this field, emergencies, on site conditions and economic limitations makes the exploitation of the media communication particularly difficult. The use of AR technology can give a strong contribution. Because of its nature, in fact, AR allows to make *visible the invisible* (Pierdicca et al., 2015a), allowing an archaeological site, or the museum of the site, to become a *Senseable Space* with the enrichment provided by multimedia tools. Nonetheless, computation, processing and management of 3D data are the core components of the system. And more, 3D digital acquisition techniques represent the most popular means for the documentation and digitization of archaeological heritage. That said, in the following we provide an overview of the developed systems to support archaeological settings to be more appealing, informative, and *Senseable*. The proposed scenarios have been experienced within the framework of two research projects; the first one within MIPE (Italian mission in Peru) project in cooperation with CNR-ITABC from Rome that is part of a broader project named PECACH (Proyecto Especial Complejo Arqueologico Chan Chan), for the safeguard, documentation and digitization of the UNESCO archaeological site of Chan Chan, Peru. The second, a national project named Archeofano project, mainly aimed at improving collection, organization and management of a GIS data structure for the designing of the urban-archaeological Roman centre of Fano town. The latter will not be here described, but more information can be found in and (Pierdicca et al., 2015b).

3.1.6 Scenario 2: The virtualization of ancient buildings

The proposed approach provides a complete pipeline of survey for the safeguarding, documentation and the fruition of archaeological remains. In particular, the proposed workflow is based on the combination of different technologies. Specifically, we have firstly built the overall frame of an historical building by spherical photogrammetry; hence we completed the survey by using dense reconstruction techniques. The main contribution of the aforementioned approach lies in the integration between Multi-Image Spherical Photogrammetry (MISP) and Structure from Motion -

Multi-View Stereo (SfM-MVS) workflow. MISP is a photogrammetric technique based on spherical panoramas, which is the cartographic representation of the sphere where the projected images are taken at the same point (Fangi, 2011). SfM-MVS techniques have been adopted because they are needful to augment virtual reconstructions with high photorealistic contents. Some geometrical constrains and the precarious conditions in which we operated, made impossible the reconstruction of some parts; to overcome this issue, a close cooperation between 3D modellers and archaeologists (together with ancient drawings and documents) led to a progressive refinement of the reconstructive hypotheses, documented in the paper. The aforementioned approach was tested on Chan Chan archaeological site, which is probably the largest pre-columbian archaeological site built in adobe. The detailed description of the method was published and can be found in (Pierdicca et al., 2016a). The outputs of this specific case, as well as other acquisitions conducted by the authors, have been processed and exploited in a real case exhibition at the museum of the site, in order to make them visible to the majority of the visitors. In fact, Chan Chan vastness and its impervious conditions make the visit limited to a little amount of findings. The architecture proposed in the following attempt to overcome all the aforementioned issues.

3.1.7 System architecture The importance of the whole set of data gathered is twofold: first of all a complete metrical reconstruction of the site provides conservators with a fundamental starting point for restoration works. Secondly, these data give the possibility to create a virtual corner for their exposition, moving from the scheme of a classical exposition of findings towards a digital and interactive visualization. The scheme reported in Figure 2 shows the complete pipeline of work that includes data acquisition of many complexes of the site, data processing and content creation for the exhibition. This last, installed into the Chan Chan museum, is composed of three main installations. The first one is an AR application that was developed to discover the archaeological findings hidden by earth. In (Pierdicca et al., 2015a) a location-based solution was developed to test the performances in outdoor scenario (in this specific case the app was developed to visualize the central entrance door of the main square of Palacio Rivero). However, the site is not opened to the public, hence we propose a marker-less solution of the same artefact, supported by a wall mounted poster displaying a high-resolution image. The final result is the overlapping of the 3D model (gained with Structure from Motion techniques) of the rests in the corresponding position. The second is the visualization of a virtual tour of the site, created with a previous research work (Colosi et al., 2013). The third section consists on the visualization of the 3D model of a temple and the related bas-reliefs, which embellish the structure, through the use of an advanced web-browser.

3.1.8 Results The work conducted for the development of the museum's installation is backed, as referenced in the previous pages, by several research works. However, it is not the purpose of this thesis to describe the details of the single methodologies, rather than to provide a general overview of how the single applications can become part of a wider installation; hence, the results should be intended as the final set-up, which embraces all the computation performed for the digitization of the site. In the exhibition it is possible to use a web-browser to navigate among the virtual 3D reconstruction of the whole complex and its bas-reliefs. The final result is reached with a wall-mounted poster containing the 3D model representation of Huaca Arco Iris, with the correct position of the decoration (Figure ??). This last was labelled with the same code of the web browser, so that the user

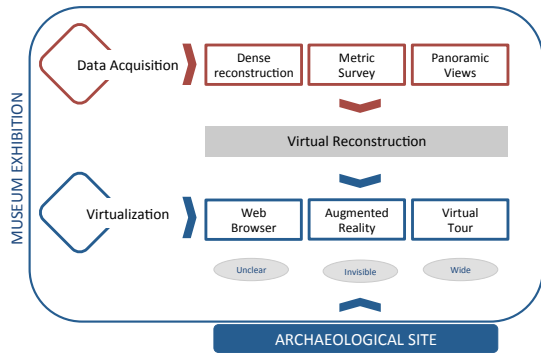


Figure 2. Pipeline of digital object development, management and exploitation in multimedia applications. Oval labels represent the problem that each technology is able to solve for a complete fruition of heritage goods.

can interact between the artwork and the digital tool. The 3D reconstruction displayed in the poster arose from the methodology previously described. The work has been realized through the use of some basic libraries for the 3D Web rendering: WebGL, Three.js and Tween.js. The first is needed for the real time visualization of the scene. In order to be able to display 3D objects in a proper manner with Three.js, a scene, a camera and a renderer are needed, so that the model can be rendered in real time. The scene variable is a container that is used to store and keep track of all the objects that we want to display. More details about the complete methodology can be found in (Pierdicca et al., 2016d).

3.2 Senseable Public Open Spaces

Internet, wireless networks, tablets and smart phones, bluetooth and others represent the main communication mediums. Among all possible opportunities opened by ICT, one of the most important for the *Senseable Spaces* concept is the communication aspect. New ICT devices not only enable new forms of interaction, but also strongly attract people to communicate in real-time with others. ICT also enable gather information about places in a bigger scale. The digital footprints, left by individuals in their daily activities can be used as data for statistics, and extracting metrics about socio-spatial behaviours, directly from the source (public space users). This information are geolocated and embody numerous opportunities, as they offer the possibility of working with high spatial and temporal data, always available and always updated. The advantage of collecting digital footprints (Girardin et al., 2008) ranges among different domains. One field, which can benefit from better ICT-space interaction, is the tourism sector. As it is very much related to the quality of place, on-site information and analysis of visitors' motivations and behaviour. All the scenario reported in the following, have been experienced within the framework of "Cyberparks - Fostering knowledge about the relationship between Information and Communication Technologies and Public Spaces" is a network of 70 experts from different working fields and scientific domains, coming from 29 different European countries and financed for four years (June 2014-May 2018) under the COST Framework (Khromova et al., 2016). Also in this case, several cases have been experienced; however, we are here summarizing the one performed in Cardeto park, referring the reader to (Frontoni et al., 2016) for a specific focus on how sensors can be used in a

Public Event for collecting data and providing contextual information to the user.

3.2.1 Scenario: experiencing CyberParks The development of AR applications for outdoor scenario implies the use of built in sensors, handy and spread for the majority of devices, but error-prone in terms of accuracy.

The main objective of this work is the development of an AR experience for cultural communication, designed for mobile devices in outdoor environments. The project aims at enhancing the Cardeto Park (Ancona, Italy), focusing on personal experience to provide tourists and visitors with an interactive tool to discover the hidden secrets of the park. This research underpins two main aspects. The first one, theoretical, is that AR and mobile technologies would represent the milestone for the promotion, the use and the conservation of archaeological parks. We propose a shift, through new technological tools and new contents, with the twofold objective of making the visit experience easier and complete, with a greater involvement of visitors, bridging the gap between existing and accessible, between visible and invisible. The second aim, more technical, is to challenge the development of an application by merging a well established state of art location-based services with an edge-based tracking system. The idea is to use a hybrid approach, integrating into the same application the two aforementioned tracking techniques. Our test demonstrates that the latter is a performing tracking system also in outdoor scenarios, where lighting condition and the variety of landscape hamper an affordable use of marker-less solutions based on image matching. We also outlined best practices suitable to be adopted for further exploitations of open-air cultural heritage.

3.2.2 System architecture This project is concerned with the proposal of a change in the use of the park: new technological tools and new contents communicate with the dual objective of making the visit easier and straightforward, improving the involvement of visitors. Actually, the park presents some weaknesses such as the complete lack of orientation and the inaccessibility for the majority of the buildings. With the introduction of digital service, the expectation is that there will be a change in the use of the park, bridging this way the gap between existing and accessible, between the visible and invisible. The app, accessible by smartphone or tablet, allows visitor to choose from different visit trails. Accordingly with his position, the tourist can chose among different pathways. By different tracking techniques, further information are made available every time a user gets close to a specific POI. For the development of the proposed application, we have chosen to adopt two tracking systems. Location-based tracking and edge-based tracking. The first one is based on the user location and enables the smartphone retrieving context information accordingly. The second one is an *Object-centric* approach categorized as marker-less tracking, based on geometrical edge features (Petit et al., 2013). The reason why we have chosen to merge two tracking system into the same application, lies in the possibility to exploit the potentials of both systems. Location-based helps way finding, triggering services only at a specified distance from the POI. Furthermore, in absence of signals, as for this study case, it helps a visitor to follow his preferred path according to the POIs typology. On the contrary, once the tourist is close to the cultural good, the location-based service cannot provide in-depth analysis of cultural objects. The development of Augmented Reality experiences, in fact, is strictly dependent on the type of registration (i.e. overlaying of virtual contents) that one chooses. Delivering in-depth analysis of specific objects, requires robust tracking techniques able to anchor the real object with the one displayed in the camera of the device. The detailed

description of the architecture can be found in (Pierdicca et al., 2016b).

3.2.3 Results The particular case selected for this work encompasses a various CH, including Romans relics, as well as buildings dated the Second World War. By categorizing all the POIs, we have given the possibility to follow specified trajectories among the park. The recognition of contours (edge feature detection) is the second tracking technology used for the presented application. This tracking technique is particularly suitable to augment:

- a previously defined solid 3D object from any view angle on a non-planar environment;
- different objects independently of their texture;
- the scene to obtain the scale of the environment;
- objects in an unpredictable environment where motions and changing lighting conditions make image matching difficult.

To obtain this function, the following steps have been implemented into the application. First of all we have built the 3D model of an historical building within the park and preloaded it into the system as a tracking object. In this case an ancient barrack. Within the app, the edge detection process has been implemented with Canny algorithm running once the device's camera is enabled. All images and reports about the described application can be found in (Pierdicca et al., 2016b). It is worth to mention that, within the framework of the project, an interesting application have been developed for analysing visitor's behaviour and to perform multivariate analysis about their movement based on GPS tracking. Results are under undergoing publication process and will be published by the end of 2018.

3.3 Senseable Spaces and Geosciences

The ability to use GPS receivers, remotely stored information into GIS platforms and connections to upload new information will contribute to make the maintenance of our landscape more affordable; in the following is demonstrated how natural environment (made of hillsides, rivers, basins and more) can become a *Senseable Space*. In the agricultural landscape and over wide rural territories, the modern approach of water protection is based, among others, on the use of linear Buffer Strips (BS) along watercourses. These conservation buffers are small bands of land in permanent vegetation, designed to reduce the run-off, the accumulation of bank-top sediments and the leaking of pesticides into fresh-waters. To achieve effective protection, the network of vegetated strips must be designed with a carefully installed and well maintained stringent scheme. The protective network needs to comply with two main conditions: the integrity of the spatial continuity of the protecting belt and constant man-hours of maintenance of riverbanks. The monitoring over a wide network of vegetated linear features, whose pattern stretches across thousands of miles, is a hard task. Despite the potentialities

of GIS in managing geo-datasets and delivering relevant thematic maps are well known, the use of specific applications is still broadly missing; indeed, geographical visualization of wide datasets directly in the field require costly and specialized equipment. In particular, viewing the physical real world "augmented" by computer-generated sensory inputs represents a powerful tool to deliver supplementary information about the surrounding environment and its objects, enriching the human perception. This kind of visualization can be achieved using AR, that could trigger smarter watershed control and riverbank maintenance with less time-consuming during on-site inspections; furthermore, it can be used to cope with the technological limitations that cannot be overcome by using GIS as a stand alone platform. By merging these technologies into a single platform, data become available in real time. The main actors who can benefit from this are the on site inspectors, that have at their disposal a quick and agile tool for monitoring and updating tasks, and the managing authorities, who can remotely check the data collected on site in real time.

3.3.1 Scenario: monitoring river banks buffer strips This case study is particularly suitable for the visualization of information on mobile devices; vegetated BS are constantly evolving because of the sudden growth of surrounding vegetation and because riverbanks are continuously changing. Besides, since BS are disseminated among wide areas, on-site monitoring is a challenging activity. Given the above, the only way to ensure their correct maintenance by the owner is on-site inspection using tools that can identify the POI in the correct location in the real world. In this light, our purpose is to provide management authorities, land managers and insiders with an intuitive and dynamic real-time visualization tool. The proposed solution combines an existing GIS with the use of relevant AR technology.

3.3.2 System architecture The visualization of buffer strips directly on-site is fundamental; as a matter of fact, farmers who want to step-up into the Common Agriculture Policy funding scheme and claim for the payments of subsidies, must compel with a set of conditions (Good Agricultural Environmental Conditions), among which the maintenance of vegetated strips (BS) along watercourses is compulsory. Local authority has to ensure that the network of BS is kept and maintained over the time by the farmer. The faster way to monitor the operational state of the network is to identify the linear pattern and verify its maintenance status. In the following section a mobile AR application for GIS data visualization is described. Our tool provides the necessary information to properly inspect the area of investigation and to visualize in real time the BS. Buffer strips are contextualized within the real environment once the camera is on and placed in the correct location where they are located in the GIS cartography. The purpose is to provide a geo-visualization method for real time and on-site data visualization, particularly suitable for this case study, but that could be used for many other GIS datasets. Details of the development phases, libraries and functionality of the application are presented in the following section. To move from GIS model to AR Geo-layer, we designed a workflow based on several items:

- availability of geo-referenced data from the GIS;
- contents to be overlaid once the user is on-site;
- a tracking system;
- link to sending data to a cloud-based data processing environment;
- interaction with the superimposed contents.

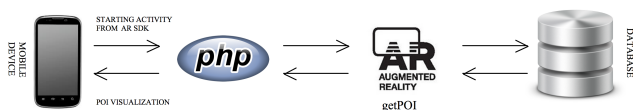


Figure 3. The steps of the architecture during on site visit.

To do so, the developed tool is composed of the following functionalities;

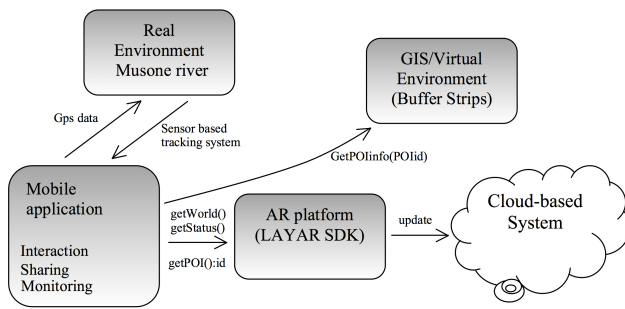


Figure 4. System architecture diagram and test-bed.

- **Augmented reality tool:**
this functionality allows the user to exploit the augmented reality browser to search for the buffer strips closer to him/her.
- **The use of the map:**
the map function is a key tool to have a quick overview of all the relevant POIs of a specific area, keeping trace about previous comments associated to it.
- **Management of Points of Interest:**
each time a specific buffer strip is selected by clicking on it, users can choose between two alternative actions: to “add a comment” or to “enrich” the scene with AR contents.
- **Data Management:**
this functionality copes with the need of updating POI comments also in case of lack of network connection; data are locally stored into a mobile device (i.e., tablet or smartphone).

3.3.3 Results We have designed different test cases under different conditions. The tests were made in real scenarios, with different daytime, mainly focusing on the usability and positioning accuracy. During the testing phase we observed that the application retrieved and displayed the buffer strips in less than a second. The system proved to be responsive to user commands, having a quick access the database. Furthermore, all the 3D models linked with the GIS system where displayed correctly in the landscape. For testing the accuracy of the tracking system, we tried different 3D models of the buffer strips, in different locations and times. The current state of sensor-based and marker-less AR technology is mainly limited by positioning accuracy; moreover, the spreading of geospatial applications will depend on the growth of the customer market for more accurate positioning systems. It is important to highlight that the developed tool can serve monitoring and maintenance tasks at the same time. In fact, the proposed solution, besides allowing monitor and supervise reporting area (in our specific case, the buffer strips at collection basin scale), also allows to share observations and surveyed data in real time, by uploading and linking this information in a GIS environment. In particular, the cycle of maintenance can be re-iterated endlessly: the health-check status of buffer strips can be monitored and verified at any time and the environment constantly maintained. The complete description of this work has been published in (Pierdicca et al., 2016c).

3.4 Senseable Spaces and Retail

The specific domain of Retail Environments deserve a focus of attention; because of its nature of being an attractive space for

humans, the *Senseable Space* paradigm get an increased meaning. The design of a point of sales, the monitoring of its performances and also the capability to engage customers attention are, up to know, the most important challenges the Retail sector is facing. But it is important not to forget that the spatial dynamics we described in the previous section, brings always to the same added value. Giving information to the users (the customers) and getting information from them for planning/decision making (the retailers). Heading all these assumption, there is the data collection task, that is to say measuring what is really happening in a space (the store). “Measure to design”, “measure to react” thanks to the help of Ambient Intelligence (AmI). The key aspect for AmI into retail environments lays in the possibility to provide services not only guided by user request, but also based over the intelligence of the system; this will allow the automatic provision of services depending on the profile and the position of the user inside the store. Consequently, the interaction between spaces and consumers should be done through natural interfaces adapting to their habits and behaviour. Nowadays, this process has been enhanced thanks to the tremendous improvement of sensors, actuators and processing units that are increasingly cheaper and smaller. One time, stores were only the places for searching and buying products; nowadays it has become the place where consumers spend time, test products in real time or just inquire about the recent products or trends. Because of this, the research about consumers’ behaviour are strictly related with in-store features for the retailers.

3.4.1 Intelligent Retail Environment Localization and people tracking in an indoor environment (e.g., stores, museums, hospitals, public and private buildings in general) is an interesting challenge for AmI applications. If the location of monitored subjects is well known, a smart system can provide them with correct and proper information about the surrounding environment. For indoor localization the main common approaches are based on received strength of radio signals, by evaluating the Received Signal Strength Indication (RSSI) of stationary satellites used to evaluate distances. An important aspect is to develop algorithms that can filter several position information derived from multiple sensors. Some of these methods previously introduced, such as Kalman filter or particle filter, improve the localization accuracy. The choice of using one filter rather than another depends on the type of sensors used, the available power of processing and the given environment. Another possible improvement is to combine different fusion filters by exploiting multiple data sources generating a more precise tracking. In literature an application of this method is proposed in (Krach and Robertson, 2008), where the Kalman filter and particle filter are combined by obtaining a more accurate estimation of the trajectory detected by the tracking system. Our approach is based on distance evaluation from received of strength radio signals of stationary beacons, enhanced by Kalman filtering as technique to combine data from RGB-D camera.

3.4.2 Scenario: customer profiling by vision and radio beacon sensor fusion The main purpose of the project is to evaluate, in a not empirical way, the success of marketing strategies, investigating over the decision-making process which drives consumers towards choices. The aim of the proposed solution is to provide retailers with useful information, analysing consumer activities inside the store, made “intelligent” with a WSN based on Active Beacons and RGB-D camera. The main contribution lays on the multi sensor integration based on different technologies that are usually installed in modern retail environments (cameras and beacons) and that alone are not suitable for a comprehensive

and precise people tracking: from one side beacons are not precise enough to correctly analyse people behaviours, while from the RGB-D camera point of view a full coverage of the store is not economically affordable. The research described in this scenario demonstrates that this multi-sensor fusion technique is suitable and results coming from real test in a retail scenario are satisfactory. Other novelties are introduced: the action-reaction data scheme and the ability to scientifically prove effectiveness of communication and general “call to action” in intelligent retail environment. Finally we tested also a simple Human Behaviour Analysis (HBA) approach able to classify users’ behaviour, with the goal of designing a proof of concept of the whole data flow going from sensors to tracking and from semantic maps to consumer behaviours.

3.4.3 System architecture The proposed system architecture consists of an active WSN, arranged among the store, composed of active beacons and an RGB-D camera. The user’s smartphones, with a BLE module, can receive and interpret radio signals from beacons. The installed application sends Beacon’s raw data to the server that compute Kalman filter with position estimation received from RGB-D camera. The server can provide this more accurate localization to the smartphone allowing also a more precise context awareness. A schematic explanation of the whole system can be found in Figure 5.

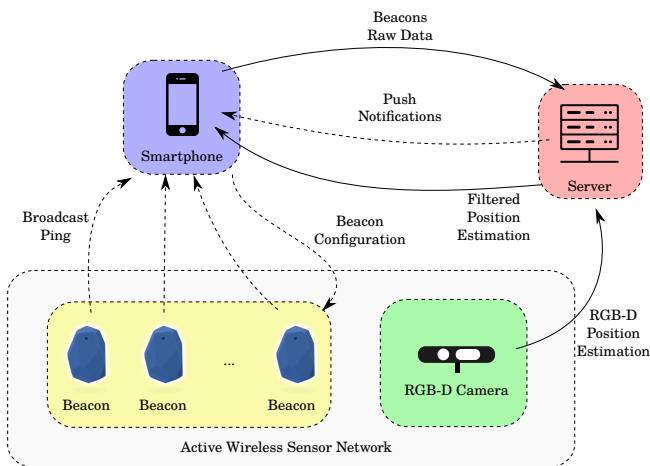


Figure 5. System architecture with main components and exchanged data.

Beacons have been preferred to other available wireless technologies because they present many advantages such as cross-platform development, low costs, long-life (thanks to low battery consumption), simple installation in the store and compact design. For the set up of the system we have used Estimote Beacons which are commercially available sensors with a built-in bidirectional BLE radio. Beacons can be fixed in a pre-defined location and they are able to send the identity information (MAC address, programmable UUID, major and minor numbers) to the smartphones around them, implementing a broadcasting service. Devices into the range of action of a single beacon, between 5m to 70m depending on the arrangement of the spaces and broadcasting power (configurable from $-30dBm$ to $+4dBm$), can pick up the BLE radio signal (without previous pairing), and the distance can be obtained with the measure of the received signal strength (RSSI). To achieve a better customer experience, as well as a more affordable data analysis, the signal frequency can be switched between 1 times (1Hz) to 10 times a second (10Hz), increasing the battery consumption. Beacons are also configurable to transmit tiny amounts of information, hence contents

(e.g., texts, pictures, etc.), implementing a light push/notification service. To deliver more context information, the mobile application can query a device-stored database or retrieve data from a web-service on a server or cloud-based storage space. The mobile application represents the crucial node of this AmI architecture, acting as the linking element between the space, the customer and the information. The Estimote SDK allows to manage intercepted beacons’ broadcasting ping. The environment is described as JSON map file containing both space boundaries and beacons’ position (identified by MAC address). In the meanwhile, an RGB-D sensors system is configured to control an area and to track people. Our positioning framework is defined in a real showroom. However, the method is general to be ported to other environments configuring location map and installing a number of active beacons sufficient to cover the area and obtain the requested accuracy. It is important to remark the presence of an electromagnetic source of disturbance from electrical panel near the entrance and a window with steel studs on the left wall. We arranged a network of beacons attached on the walls (at middle high of 2.0m) and one RGB-D camera, with a top-view configuration, placed on the ceiling at the entrance (with a coverage area of $4.0m \times 3.0m$). The evidence of benefits introduced by this approach, permit to get more reliable datasets and is the starting point to track consumer path inside the store, as discussed in the following.

3.4.4 Results Experimental tests demonstrate that our positioning framework, based on sensor fusion, allows consumer path tracking, providing useful input information to perform automatic customer behaviour analysis. At a first stage, we analysed all customers tracks, calculating a posteriori probabilities for people presence in an “area of interest” and for transitions between adjacent areas. These probabilities can be used to analyse movement trends inside the shop and comparing them with a priori expected behaviour, they can provide insights to improve product displacement and store layout. We then proceeded with a path clustering, to point out correspondences that should exist between recorded paths and range of ages. Even if the number of samples is not enough to evaluate the clustering method by itself, this approach show the potentiality of identifying different customer behaviour and the suitability of the proposed methodology in an integrated data flow going from consumer tracking to consumer behaviour analysis and classification. More details about the complete methodology can be found in (Sturari et al., 2016).

4. DISCUSSION, CONCLUSION AND FUTURE WORKS

The examples illustrated and the use cases described so far, have proved that the new paradigm of *Senseable Spaces*, is able to solve both sides of the problem. The data collection from the space, along with the objects in it, has the twofold purpose of providing the users with contextual information which improve their knowledge of the space and to enrich the perception of the space itself. The increased knowledge of the users, that depends on the usage that they do about the services provided, opens up future scenario of improvement that are made not only with subjective analysis, but performed with an increased awareness, thanks to the data collected. Even if each scenario presents different features and needs, in every ambit it is possible to outline the dualism between the provisioning of data and the collection of data, regardless to the domain we are facing with. The different declination of *Senseable Spaces* experimented and showed, demonstrated that it is possible to cope with these needs. For

the Cultural Heritage domain, broadly experienced for both museums and archaeology, emerged the need to set up fast and agile procedures allowing art curators to digitize their collections, present them in a digital form to the visitors, and to understand their insights. Besides, we witnessed to a tremendous change in which it is possible to exploit the potentials of UGD for a better understanding of Public Open Spaces; tourists, or more in general citizens leave traces of their activities thanks to the use of their devices, while municipalities have the obligation to investigate these dynamics and provide planners with more efficient methods of urban design. Environmental changes are very difficult to be monitored; providing on site inspectors with suites of digital tools that ease the inspections, will facilitate the process and, moreover, will give the possibility to the decision makers to have more updated databases and GIS for a more constant monitoring and for a more aware policy making. Also the retail sector demonstrated to be a suitable domain to tackle; from one side, there is the need to engage customers with pervasive solutions, from the other to understand the performances of the space, of which the retailer is the owner, and plan, rearrange and redesign accordingly.

4.1 Conclusion

In this thesis, the new paradigm of *Senseable Spaces* was outlined. To fulfil this new vision, use cases and experimental set-up where implemented to demonstrate the possibility to apply the concept of a *Senseable Space* in several domains; it was also the opportunity to outline points of contact among disciplines apparently different, but that can be joined thanks to this common thread.

4.2 Thesis contributions

The main contribution of this thesis can be summarized in the following aspects: first of all, the new paradigm of *Senseable Spaces* was applied in different research settings, verifying for each one the real feasibility. The innovation introduced by the present study is demonstrated by several scientific publications in the domains described. We proved, by developing innovative mobile applications, that AR can be experienced in front of a painting (Clini et al., 2014) as well as in large archaeological settings (Pierdicca et al., 2016e); complex contents have been developed in order to make them suitable for different output, experiencing data fusion techniques to achieve relevant output suitable for different platforms (Pierdicca et al., 2016a). Notwithstanding, monitoring user behaviour remain the best practice to be used in order to improve the services to the users. The example of using eye tracking technology as a data enrichment for AR application is a clear demonstration (Naspetti et al., 2016). As well, POS today are not fully exploited as a collector of information. The experiences developed demonstrate that we are able, thanks to the use of pervasive solutions like sensors or beacons, to address the problem. The pilot project set up during the Mogliano Festival (Frontoni et al., 2016) demonstrates how is possible to collect UGD and provide users with transportation data in real time. And with different needs and purposes, indoor spaces can be designed and redesigned accordingly. The development of the novel indoor localization system, in a experimental setup achieved with the combination of radio beacons and RGB-D camera (Sturari et al., 2016), allowed to achieve the objective of tracking customers' movements (and clustering them with a Markov Chain model), analysing the performances of a space and to providing contextual information. And more, a standardization of data, arising from GIS, processed to be used in AR for environmental in-

spection (Pierdicca et al., 2016c) was validated in real scenario, demonstrating the huge potential offered by a *Senseable Space* to be measured by providing users with multimedia solutions and applications. Now, at the end of this dissertation, is more clear what is needed to make a space *Senseable*: the space, the technology, the users. Every solution described had, at the center of the experimentation, the end user, in different meanings: sometimes a visitor, sometimes a customer, sometimes a citizen. And from the results section of each scenario also emerged that, if we were able to reach the objectives of providing services and to collect data from the user, what is still missing to this chain to be accomplished is the ability to react to these information. Future works will be steered toward these directions. Scenarios where the users are the active part of the system, measuring and being measured at the same time. As stated by Carlo Ratti, "we can analyze the pulse of the city, moment to moment. Over the past decade, digital technologies have begun to blanket our cities, forming the backbone of a large, intelligent infrastructure; it becomes an ideal lab to study the link between technology and city planning".

REFERENCES

- Bekele, M., Pierdicca, R., Frontoni, E., Malinverni, E. and Gain, J., 2018. Survey of augmented, virtual and mixed reality for cultural heritage. *Journal on Computing and Cultural Heritage* pp. – . In Press.
- Bojic, I., Massaro, E., Belyi, A., Sobolevsky, S. and Ratti, C., 2015. Choosing the right home location definition method for the given dataset. In: *International Conference on Social Informatics*, Springer, pp. 194–208.
- Clini, P., Frontoni, E., Quattrini, R. and Pierdicca, R., 2014. Augmented reality experience: From high-resolution acquisition to real time augmented contents. *Advances in Multimedia* 2014, pp. 18–27.
- Clini, P., Frontoni, E., Quattrini, R., Pierdicca, R. and Nespeca, R., 2016. Real/not real: Pseudo-holography and augmented. *Handbook of Research on Emerging Technologies for Digital Preservation and Information Modeling* p. 201.
- Colosi, F., Gabrielli, R., Malinverni, E. and Orazi, R., 2013. Strategies and technologies for the knowledge, conservation and enhancement of a great historical settlement: Chan chan, peru. In: *Proceedings of Conference Built Heritage*, pp. 56–64.
- Condotta, M. and Borga, G., 2012. "sensing" the "city model" to improve effectiveness of digital resources. *Territorio Italia. Governo del Territorio, Catasto, Mercato immobiliare. Periodico di Informazione tecnico-scientifica* 12(2), pp. 85–93.
- Esche, H. and Blais, J. R., 2008. Geomatics and the new cyber-infrastructure. *Geomatica*.
- Fangi, G., 2011. The multi-image spherical panoramas as a tool for architectural survey. *CIPA HERITAGE DOCUMENTATION, BEST PRACTICES AND APPLICATIONS XXXVIII-5/C19*, pp. 21.
- Fernández, S., Gualda, D., García, J. C., García, J. J., Ureña, J. and Gutiérrez, R., 2011. Indoor location system based on zig-bee devices and metric description graphs. In: *Intelligent Signal Processing (WISP), 2011 IEEE 7th International Symposium on*, IEEE, pp. 1–5.
- Frontoni, E., Mancini, A., Pierdicca, R., Sturari, M. and Zingaretti, P., 2016. Analysing human movements at mass events: A novel mobile-based management system based on active beacons and avm. In: *Control and Automation (MED), 2016 24th Mediterranean Conference on*, IEEE, pp. 605–610.

- Girardin, F., Calabrese, F., Dal Fiore, F., Ratti, C. and Blat, J., 2008. Digital footprinting: Uncovering tourists with user-generated content. *IEEE Pervasive computing* 7(4), pp. 36–43.
- Golder, S. A. and Macy, M. W., 2014. Digital footprints: Opportunities and challenges for online social research. *Sociology* 40(1), pp. 129.
- Grauwin, S., Sobolevsky, S., Moritz, S., Gódor, I. and Ratti, C., 2015. Towards a comparative science of cities: Using mobile traffic records in new york, london, and hong kong. In: *Computational approaches for urban environments*, Springer, pp. 363–387.
- Heidemann, J. and Govindan, R., 2005. Embedded sensor networks. In: *Handbook of Networked and Embedded Control Systems*, Springer, pp. 721–738.
- Khromova, A., Costa, C. S., Erjavec, I. Š., Pierdicca, R., Malinverni, E. S., Galli, A. and Marcheggiani, E., 2016. Is the mediated public open space a smart place? relationships between urban landscapes and ict—the cost action tu 1306 cyberparks. *SCIRESI-SCIENTIFIC RESEARCH AND INFORMATION TECHNOLOGY* 6(2), pp. 17–28.
- Krach, B. and Robertson, P., 2008. Integration of foot-mounted inertial sensors into a bayesian location estimation framework. In: *Positioning, Navigation and Communication, 2008. WPNC 2008. 5th Workshop on*, IEEE, pp. 55–61.
- Lambers, K. and Remondino, F., 2008. Optical 3d measurement techniques in archaeology: recent developments and applications. In: *Proceedings of the 35th International Conference on Computer Applications and Quantitative Methods in Archaeology (CAA)*, Vol. 10, Posluschny, A., K. Lambers and I. Herzog, pp. 27–35.
- Malinverni, E., Tasseti, A., Mancini, A., Zingaretti, P., Frontoni, E. and Bernardini, A., 2011. Hybrid object-based approach for land use/land cover mapping using high spatial resolution imagery. *International Journal of Geographical Information Science* 25(6), pp. 1025–1043.
- Mancini, A., Frontoni, E., Zingaretti, P. and Placidi, V., 2013. Smart vision system for shelf analysis in intelligent retail environments. In: *ASME 2013 International Design Engineering Technical Conferences and Computers and Information in Engineering Conference*, American Society of Mechanical Engineers, pp. V004T08A045–V004T08A045.
- Manovich, L., 2006. The poetics of augmented space. *Visual Communication* 5(2), pp. 219–240.
- Naspetti, S., Pierdicca, R., Mandolesi, S., Paolanti, M., Frontoni, E. and Zanoli, R., 2016. Automatic analysis of eye-tracking data for augmented reality applications: A prospective outlook. In: *International Conference on Augmented Reality, Virtual Reality and Computer Graphics*, Springer, pp. 217–230.
- Ott, M. and Pozzi, F., 2011. Towards a new era for cultural heritage education: Discussing the role of ict. *Computers in Human Behavior* 27(4), pp. 1365–1371.
- Outram, C., Ratti, C. and Biderman, A., 2010. The copenhagen wheel: An innovative electric bicycle system that harnesses the power of real-time information and crowd sourcing. In: *EVER Monaco International Exhibition & Conference on Ecologic Vehicles & Renewable Energies*.
- Petit, A., Marchand, E. and Kanani, K., 2013. Augmenting markerless complex 3d objects by combining geometrical and color edge information. In: *Mixed and Augmented Reality (ISMAR), 2013 IEEE International Symposium on*, IEEE, pp. 287–288.
- Pierdicca, R., Frontoni, E., Malinverni, E. S., Colosi, F. and Orazi, R., 2016a. Virtual reconstruction of archaeological heritage using a combination of photogrammetric techniques: Huaca arco iris, chan chan, peru. *Digital Applications in Archaeology and Cultural Heritage* 3(3), pp. 80–90.
- Pierdicca, R., Frontoni, E., Zingaretti, P., Malinverni, E. S., Colosi, F. and Orazi, R., 2015a. Making visible the invisible. augmented reality visualization for 3d reconstructions of archaeological sites. In: *International Conference on Augmented and Virtual Reality*, Springer, pp. 25–37.
- Pierdicca, R., Frontoni, E., Zingaretti, P., Malinverni, E. S., Galli, A., Marcheggiani, E. and Costa, C. S., 2016b. Cyberarchaeology: Improved way findings for archaeological parks through mobile augmented reality. In: *International Conference on Augmented Reality, Virtual Reality and Computer Graphics*, Springer, pp. 172–185.
- Pierdicca, R., Frontoni, E., Zingaretti, P., Mancini, A., Malinverni, E. S., Tasseti, A. N., Marcheggiani, E. and Galli, A., 2016c. Smart maintenance of riverbanks using a standard data layer and augmented reality. *Computers & Geosciences* 95, pp. 67–74.
- Pierdicca, R., Malinverni, E., Cline, P., Mancini, A., Bozzi, C. and Nespeca, R., 2015b. Development of a gis environment for archaeological multipurpose applications: the fano historic centre. In: *XIII International Forum Le Vie dei Mercanti*, pp. 588–597.
- Pierdicca, R., Malinverni, E. S., Frontoni, E., Colosi, F. and Orazi, R., 2016d. Esquina multimedia—museum exhibition for the visualization of chan chan archaeological site. In: *8th International congress on archaeology, computer graphics, cultural heritage and innovation*, Editorial Universitat Politècnica de València, pp. 274–276.
- Pierdicca, R., Orazi, R., Colosi, F., Frontoni, E. and Malinverni, E. S., 2016e. 3d visualization tools to explore ancient architectures in south america. *VAR Virtual Archaeology Review* 7(15), pp. 44–53.
- Quattrini, R., Pierdicca, R., Frontoni, E. and Barcaglioni, R., 2016. Virtual reconstruction of lost architectures: from the tls survey to ar visualization. *ISPRS-International Archives of the Photogrammetry, Remote Sensing and Spatial Information Sciences* pp. 383–390.
- Ramos, M. M. and Remondino, F., 2015. Data fusion in cultural heritage—a review. *The International Archives of Photogrammetry, Remote Sensing and Spatial Information Sciences* 40(5), pp. 359.
- Ratti, C., Frenchman, D., Pulselli, R. M. and Williams, S., 2006. Mobile landscapes: using location data from cell phones for urban analysis. *Environment and Planning B: Planning and Design* 33(5), pp. 727–748.
- Sturari, M., Liciotti, D., Pierdicca, R., Frontoni, E., Mancini, A., Contigiani, M. and Zingaretti, P., 2016. Robust and affordable retail customer profiling by vision and radio beacon sensor fusion. *Pattern Recognition Letters*.
- Weiser, M., 1991. The computer for the 21st century. *Scientific american* 265(3), pp. 94–104.
- Yoshimura, Y., Sobolevsky, S., Ratti, C., Girardin, F., Carrascal, J. P., Blat, J. and Sinatra, R., 2014. An analysis of visitors' behavior in the louvre museum: A study using bluetooth data. *Environment and Planning B: Planning and Design* 41(6), pp. 1113–1131.

PhD Supervisors:

Prof. Emanuele Frontoni and Prof. Eva Savina Malinverni



c/o CIRGEO, Centro Interdipartimentale di Ricerca di Geomatica - Università degli Studi di Padova

Viale dell'Università 16, 35020 Legnaro (PD)

Prof. Antonio Vettore tel. 049-8272688

e-mail antonio.vettore@unipd.it

con il supporto di



ISBN 978-88-942926-4-0

Luglio 2018